Scanning Electrical Mobility Methods for Aerosol Characterization

Thesis by

Huajun Mai

In Partial Fulfillment of the Requirements for the

Degree of

Doctor of Philosophy

CALIFORNIA INSTITUTE OF TECHNOLOGY

Pasadena, California

2018

Defended May, 24, 2018

Huajun Mai
ORCID: 0000-0002-0616-1986

I would like to thank my thesis advisor, Professor Richard C. Flagan, for his guidance and support throughout my Ph.D. career. He is one of the most creative, resourceful scientist I ever worked with. I highly appreciate for the freedom he provided, allowing me to explore various projects, from the atmospheric nucleation to the novel instrument developments, in the past five years. I can not even remember exactly how many times I have detoured before I found out the subjects for my thesis, with the following projects I ever explored but not presented in this thesis: novel particle counter, binary nucleation theory, Titan atmospheric nucleation, transfer function of OMAC, nucleation experiments at CERN. Every time I got stuck with the projects, Professor Flagan is always there to encourage me and try his best to support my research.

It is my pleasure to work with Professor John H. Seinfeld in my first year. With his input and mentorship, I completed the project on the gas-particle partitioning time scales. He is the most dedicated scientist I ever worked with. I still remember, when he edited my manuscript, he always gave me feedback in less than three days, even in the weekend. I would also like to thank him for being my thesis committee member and the help he and his group provided throughout these years.

I would like to thank the other two members of my thesis committee, Professor Paul O. Wennberg and Professor Mitchio Okumura. They gave me invaluable suggestions for my thesis and future career.

Professor Michel Attoui, from University of Paris XII, is always doing what he could do to make my life easier. He is the most considerate, also the most humorous person I ever know in the field of aerosol science. The first time I met him dates back to 2013, when he came to Tsinghua University and equipped me all sorts of fundamental experimental skills that I needed to complete my thesis. He fixed an optical detector for me when I was working on a new particle counter two year ago, and he built two aerosol electrometers on his own and sent them to me, which allowed me to complete the characterization of scanning ROMIAC. At the time when I was struggling on the CLOUD experiments, he sent me a heat exchanger so that I could keep my instrument running properly.

All my colleagues from the Flagan and Seinfeld group are very friendly and give me emotional support during my stay at Caltech, especially Amanda Grantz, Paula Popescu, Jill Craven, Natasha Hodas, Johannes Leppä, Changhyuk Kim, Stavros Amanatidis, Xiaohan Xue, Xuan Zhang, Yuanlong Huang, Sophia Charan and Weimeng Kong. My labmate, Wilton Mui, taught me the necessary

skills to conduct experiments when I joined the group.

I would like to thank Julie Lee, the administrative assistant in the GPS division, for her immense encouragement, support and care.

The chamber music group at Caltech fills my life with warmth and love. I am grateful to Delores Bing, Maia Jasper White and Michael Kreiner for organizing and coaching my teams. Playing chamber music in my third and fourth year is one of the best memories at Caltech.

I would like to express my deep gratitude to my fiancée, Zhangjun Zhou. She is my best listener, and the one who knows me the best in the world. This summer marks our nine-year-long-distance relationship. The bonding between Zhangjun and me is the best gift I have ever received.

My family has been unconditionally supportive to me since I was born. My mom, Fengling He, took care of everything for me before I moved away from my hometown to Beijing. To me, she is a mentor with great patience. My dad, Wenguang Mai, made great sacrifices to support the whole family. When he graduated from college, he gave up the chances to pursue a higher degree, and chose to go back to hometown to support the family when my paternal grandmother, Xia Liang, suffered from heart disease, and my paternal grandfather, Yaoyi Mai, made a living from repairing bicycles.

It was a great fortune for me to grow up in an extended family with my grandparents, my aunt and my cousin. My paternal grandfather spent a lot of time teaching me math and Chinese handwriting before I went to school. As a role model to me, his perseverance and righteousness always inspired me. I dedicate this thesis to my grandfather.

ABSTRACT

The scanning electrical mobility measurement is the most common tool used to characterize the size distribution of fine particles in the atmosphere. This thesis develops the methods for retrieving the particle size distribution from scanning electrical mobility measurement data for two systems: (1) the scanning electrical mobility spectrometer (SEMS; also known as the scanning mobility particle sizer, SMPS), which measures particle size distribution ranging from 15 - 1000 nm; (2) the scanning radial opposed migration ion and aerosol classifier (ROMIAC) system, which uses a two-stage condensation particle counter as particle detector to complete the 1 - 20 nm particle size distribution measurements.

SEMS / SMPS data have traditionally been inverted to determine the particle size distribution by solving a Fredholm integral equation in which the kernel function is based upon constant-voltage operation of the mobility classifier. The viscous boundary layer within the classifier renders that model invalid. This thesis determines, for the first time, the transfer function for a real differential mobility analyzer (DMA) that is operated in the scanning mode. The flow and electric fields within the instrument were obtained by finite element simulations taking into account its detailed geometry. Brownian dynamics simulations were then used to simulate diffusive particle trajectories within the instrument as the voltage was scanned. There results were coupled with empirically-derived response-time functions for the condensation particle counter that serves as a detector in the SEMS / SMPS to obtain integrated system transfer function that substantially improve the fidelity of the SEMS / SMPS data inversion.

This approach was also applied to adaptation of the radial opposed migration ion/aerosol classifier (ROMIAC) for scanning-mode operation. The transfer function obtained through simulation of the scanning ROMIAC was used in the experimental validation of this new measurement method. This new instrument was then used to measure wall loss rates for 1.6 nm to 20 nm particles in the Caltech environmental chamber.

Mui, Wilton, Huajun Mai, Andrew J. Downard, John H. Seinfeld, and Richard C. Flagan (2017). "Design, simulation, and characterization of a radial opposed migration ion and aerosol classifier (ROMIAC)". In: *Aerosol Science and Technology* 51.7, pp. 801–823. DOI: 10.1080/02786826.2017.1315046.
H.M. derived the instrument transfer function, developed the electrospray system for the experiments.

Wagner, R. et al. (2017). "The role of ions in new particle formation in the CLOUD chamber". In: *Atmospheric Chemistry and Physics* 17.24, pp. 15181–15197. DOI: 10.5194/acp-17-15181-2017. URL: https://www.atmos-chem-phys.net/17/15181/2017/.
H.M. prepared the instruments and carried out the experimental measurements.

Mai, Huajun, Manabu Shiraiwa, Richard C. Flagan, and John H. Seinfeld (2015). "Under what conditions can equilibrium gas–particle partitioning be expected to hold in the atmosphere?" In: *Environmental science & technology* 49.19, pp. 11485–11491. DOI: 10.1021/acs.est.5b02587.
H.M. developed the analytical solution, ran the numerical models, performed the analysis, created the figures and tables, and wrote the paper.

Mai, Huajun and Richard C. Flagan (In review). "Scanning DMA Data Analysis I. Classification Transfer Function". In: *Aerosol Science and Technology*.
H.M. modeled the instrument performance, analyzed the data, created the figures and tables, and wrote the paper.

Mai, Huajun, Weimeng Kong, John H. Seinfeld, and Richard C. Flagan (In review). "Scanning DMA data analysis. II. Integrated DMA-CPC instrument response and data inversion". In: *Aerosol Science and Technology*.
H.M. developed the models, designed the experiments, carried out the experiments, analyzed the data, created the figures and tables, and wrote the paper.

Number *Page*

INTRODUCTION

The atmospheric aerosol remains one of the most uncertain component in shaping the Earth's energy balance. Aerosol particles can scatter the solar radiation, while some types of aerosol, such as black carbon, absorbs the radiation in the so-called direct effect. Aerosol particles can also serve as the cloud condensation nuclei (CCN) for cloud formation, and enhance the radiation reflection (indirect effect). Whether atmospheric particles can become CCN depends on their physicochemical properties, such as chemical composition, saturation ratio, and particle size (Petters and Kreidenweis, 2007). Understanding particle formation and growth mechanisms is important in constraining the uncertainty in the climate effect of aerosol particles, as new particle formation (NPF) via nucleation can contribute global CCN concentration as much as 50 % (Spracklen et al., 2008; Merikanto et al., 2009).

Recent research shows that sulphuric acid, ammonia, amines, and highly oxygenated molecules contribute to the nucleation process and to the initial particle growth (Kirkby, Duplissy, et al., 2016; Kirkby, Curtius, et al., 2011; Almeida et al., 2013). Further condensation of organic molecules allows particles to grow to sufficiently large sizes that they can serve as cloud condensation nuclei. Measurements of the time evolution of the particle size distribution in both controlled experiments and field campaigns can provide key insights into these dynamic processes, but the required high time-resolution poses serious measurement challenges. Electrical-mobility-based classification of aerosol particles is the most commonly used method for particle size distribution measurements. This size characterization is primarily accomplished using the condensation particle counters (CPC) to detect sub-micron particles.

To increase the time resolution of size distribution measurement, Wang and Flagan (1990) introduced the scanning operation of particle classifier, which continuously changes the electrode voltage during the measurements. The instrument performance of the scanning classifier and the downstream CPC are required to retrieve the particle size distribution.

My primary research at Caltech has focused on data analysis of scanning electrical mobility measurement systems. In Chapter 2, the instantaneous transfer function of the scanning differential mobility analyzer (DMA), one of the most commonly used commercial aerosol classifier, is determined by using the Brownian dynamics simulation of particle trajectories within the instrument.

These simulations were performed for the conditions that are used in controlled chamber measurements to determine aerosol yield from the condensation of oxidized organics. The measured electrical mobility equivalent size range in this operation condition is 15 - 800 nm. The detailed simulations of the scanning DMA shows distortions of the transfer function from the idealized model developed in the previous studies.

Based on the instantaneous scanning transfer function of DMA, Chapter 3 presents the associated asymmetric instrument response of DMA-CPC, and it is validated with experimental measurements. The distortions of the instrument response are mainly attributed to the distorted scanning DMA transfer function and the time delay effect within the CPC. Both up-scan (exponentially increasing voltage) and down-scan (exponentially decreasing voltage) instrument responses are presented, although the particle size distribution inversion is only explored for the up-scan in Chapter 3.

The uncertainty in retrieving particle size distributions from scanning electrical mobility measurements could be minimized by increasing the classifier resolution and reducing the response time of the particle detector. Chapter 4 explores the potential of scanning the radial opposed migration ion and aerosol classifier (ROMIAC) (a novel mobility classifier whose design limits diffusional degradation of classifier resolution) thereby expanding the measurement range to lower voltage than is possible in DMAs. Despite the distortions of the scanning ROMIAC transfer function, particularly in the down-scan operation, which shows deviation from the expected single-mode distribution, the scanning ROMIAC is able to classify aerosol in 3 s scan with reasonable total transmission efficiency. Based on the finite-element simulated particle trajectory, the aggregated distortions of down-scan transfer function results from the asymmetric design of the instrument, which introduces the aerosol into the classification region at the upper electrode. Regardless the non-idealized transfer function of the scanning ROMIAC, it enable measurements of the 1-20 nm particle size distribution when a high time-resolution is desired, such as flight measurements and new particle formation events.

Both Chapter 2 and 4 uses the finite-element analysis method to derive the scanning transfer function of DMA and ROMIAC, respectively. While this method does provide accurate characterization of the instrument, as it captures all the details of the instrument geometry and the non-ideality of the flow- and electric-fields, it is computationally expensive. Chapter 5 describes an alternative to complete the size distribution data inversion by measuring the instrument responses on the upstream polydisperse particles. The kernel function of the data inversion is then derived based on these experimental measured results. In Chapter 5, this method is used for the scanning ROMIAC system, with a two-stage CPC as the particle detector, but it can be extended to other scanning

electrical mobility measurement systems as well.

Chapter 6 shows the experimental measured 1 - 20 nm particle deposition rate within the environmental chamber using the scanning ROMIAC measurement system and the scanning data inversion methods described in Chapter 2 - 5. The particle deposition in this size range is important for determining the particle nucleation rate when the environmental chamber is used to investigate the nucleation mechanism.

Gas-particle interactions are also an important process in the atmosphere, aside from the nucleation process, which involves the gas molecule interaction. Condensation of gas molecules onto the pre-existing particles lead to the changes of particle sizes and its physicochemical properties. Chapter 7 investigates the gas-particle partitioning process from a transport perspective. The equilibration time scale of gas-particle partitioning can range from minutes to months, depending on the volatility of gas-phase molecules, accommodation coefficients and particle sizes.

References

Almeida, João et al. (2013). "Molecular understanding of sulphuric acid–amine particle nucleation in the atmosphere". In: *Nature* 502.7471, p. 359. DOI: 10.1038/nature12663.

Kirkby, Jasper, Joachim Curtius, et al. (2011). "Role of sulphuric acid, ammonia and galactic cosmic rays in atmospheric aerosol nucleation". In: *Nature* 476.7361, p. 429. DOI: 10.1038/nature10343.

Kirkby, Jasper, Jonathan Duplissy, et al. (2016). "Ion-induced nucleation of pure biogenic particles". In: *Nature* 533.7604, p. 521. DOI: 10.1038/nature17953.

Merikanto, J. et al. (2009). "Impact of nucleation on global CCN". In: *Atmospheric Chemistry and Physics* 9.21, pp. 8601–8616. DOI: 10.5194/acp-9-8601-2009. URL: https://www.atmos-chem-phys.net/9/8601/2009/.

Petters, M. D. and S. M. Kreidenweis (2007). "A single parameter representation of hygroscopic growth and cloud condensation nucleus activity". In: *Atmospheric Chemistry and Physics* 7.8, pp. 1961–1971. DOI: 10.5194/acp-7-1961-2007. URL: https://www.atmos-chem-phys.net/7/1961/2007/.

Spracklen, D. V. et al. (2008). "Contribution of particle formation to global cloud condensation nuclei concentrations". In: *Geophysical Research Letters* 35.6. DOI: 10.1029/2007GL033038.

Wang, Shih Chen and Richard C. Flagan (1990). "Scanning Electrical Mobility Spectrometer". In: *Aerosol Science and Technology* 13.2, pp. 230–240.

SCANNING DMA DATA ANALYSIS I. CLASSIFICATION TRANSFER FUNCTION

By Huajun Mai, and Richard C. Flagan

This Chapter is submitted to, and is currently under review by, *Aerosol Science and Technology* as:

Mai, Huajun and Richard C. Flagan (In review). "Scanning DMA Data Analysis I. Classification Transfer Function". In: *Aerosol Science and Technology*.

2.1 Abstract

The scanning electrical mobility spectrometer (SEMS; also known as the scanning mobility particle sizer, SMPS) enables rapid particle size distribution measurements with a differential mobility analyzer (DMA)/condensation particle counter (CPC) combination by ramping the classifier voltage, and continuously counting particles into time bins throughout the scan. Inversion of scanning measurements poses a challenge due to the finite time response of the CPC; the distorted data can be deconvoluted to improve the fidelity of size distributions obtained with the SEMS/SMPS. Idealized models of the classification region have shown that, for rapid voltage scans, the non-diffusive transfer function deviates significantly from that at constant voltage. Nonetheless, most SEMS/SMPS data analyses employ the constant voltage transfer function, a result that is valid only for plug flow in the classification region. This paper develops the scanning-mode transfer function for the actual geometry of the TSI Model 3081 DMA. Finite element calculations are used to determine the flow and electric fields through the entire DMA. The instantaneous scanning-DMA transfer function for diffusive particles is determined using Brownian dynamics simulations. Comparisons of the results from this simulation of a real instrument to those from the idealized models reveal the shortcomings of prior models in describing the instantaneous scanning-DMA transfer function. A companion paper (Part II) combines this scanning-mode transfer function with response functions for the other components of a SEMS/SMPS measurement system in order to derive the response function for the integrated measurement system.

2.2 Introduction

The differential mobility analyzer (DMA; Knutson and Whitby, 1975) has become the primary method for physical characterization of submicron aerosol particles owing to its ability to resolve details in the particle size distribution over a range that, today, extends from 1 μm to as small as 1 nm diameter. Key to that quantitation is detailed knowledge of the instrument response to particles of different sizes. In their landmark paper Knutson and Whitby (1975) derived an expression for the probability that a particle would be transmitted through the classification region as a function of the applied voltage. Stolzenburg (1988) extended that "transfer function" to include the effects of diffusion away from the nondiffusive trajectories used to derive the Knutson and Whitby transfer function, greatly improving the fidelity of inferred size distributions for small particles, *i.e.*, those that are classified at low voltage. Most applications of this theory resort to a highly idealized geometry in which the electric field is assumed to be strictly perpendicular to the electrodes; we label this type of model the parallel-flow DMA (PFDMA). Both uniform velocity, *i.e.*, plug-flow, and fully-developed laminar flow versions of the PFDMA model have been reported, denoted here as PFDMA-P and PFDMA-L, respectively.

To measure the size distribution with a constant voltage DMA, particle concentrations are recorded as the DMA voltage is stepped through the measurement range. The measurement at each voltage requires waiting for particles to pass through the classifier, plumbing, and the internal flow passages of the detector before they can be counted. The differential mobility particle sizer (DMPS; Fissan, Helsper, and Thielen, 1983; Ten Brink et al., 1983) embodied this stepping mode, and continues to be used by some researchers to this day, but the long delays between successive size/mobility measurements required to obtain a steady-state signal make the DMPS inappropriate for systems in which aerosol properties change at all rapidly.

The scanning electrical mobility spectrometer (SEMS, Wang and Flagan, 1990; also known as the scanning mobility particle sizer, SMPS) accelerates mobility-based size distribution measurements by classifying particles in a time-varying electric field; transmitted particles are continuously counted into time bins, thereby eliminating delays between measurements at different sizes. Employing an exponential ramp ensures that particles of different mobilities experience the same relative change in migration velocity with time during their passage through the classifier.

The time responses of all components of the measurement system may, however, influence the acquired data and its interpretation. Russell, Flagan, and Seinfeld (1995) found that the signals obtained from the SEMS were distorted by the slow response of the CPC detector, and developed a model based on the particle residence time distribution within the CPC to describe the effect.

While the early model was quite complex, Collins, Flagan, and Seinfeld (2002) developed a simpler, and efficient deconvolution algorithm to correct data for the slow detector response. Numerical simulations of trajectories of particles during their passage through the scanned DMA revealed a change in shape of the transfer function associated with changes in the particle trajectory through the PFDMA when the voltage is allowed to vary with time (Collins, Cocker, et al., 2004). Subsequently, Mamakos, Ntziachristos, and Samaras (2008) and Dubey and Dhaniyala (2008) independently derived an analytical expression for the non-diffusive transfer function for the laminar flow PFDMA operated in scanning mode, obviating the need for the numerical simulation of the non-diffusive particle trajectories for this idealized geometry. Dubey and Dhaniyala (2011) applied Brownian dynamics (Monte Carlo) simulations to this model to elucidate the effects of diffusional broadening of the transfer function of the SEMS. The parallel-flow model does not, however, capture the influence of flow and field distortions in the entrance and exit regions of the cylindrical DMA that, as we will show below, can be important.

Only when all of the factors that distort the DMA measurements are addressed can the size distribution be quantitatively recovered from measurements; the coupling of time and migration in the SEMS complicates the analysis in ways that have only partially been addressed through characterization of the time response of the detector. The resulting distortions are apparent in the number distributions; consideration of higher moments, such as aerosol mass, amplifies the effects of these distortions on the tails of the size distributions. Thus, previously unaccounted deviations from the ideal, steady-state PFDMA transfer function limit the ability of traditional SEMS data analysis methods to quantify time variations in such quantities as $PM_{2.5}$ (mass concentration of particles smaller than 2.5 μm diameter), or aerosol yield in atmospheric chamber studies (the fraction of reacted hydrocarbon vapors that contribute to secondary organic aerosol mass). In the present work, detailed numerical simulations are used to fill in gaps in our understanding by determining the transfer function of a real DMA when operated in scanning mode. In this paper, we focus on that portion of the transfer function considered in previous studies, which we will label the *c*lassifier transfer function. To invert SEMS data, these models of the DMA must be integrated with models of downstream plumbing and particle detection apparatus to determine the response function that takes into account all components of the integrated SEMS instrument; the integrated instrument transfer function is the subject of a companion paper.

To examine the influence of DMA design on the transfer function, we replace idealized models of the DMA geometry, electric fields, and flow paths with finite element simulations of the fluid flow and electric field within each region of a real DMA, and then use the resulting fields in a Brownian dynamics simulation of particle transmission through the scanning DMA. The simulations have

been performed for the TSI Model 3081A long-column, cylindrical DMA (hereafter denoted TSI DMA); details of the DMA design that have not been considered in previous studies will be shown to significantly affect the transfer function when the DMA voltage is scanned. While the present study focuses on one particular instrument and a limited range of operating conditions, the lessons learned have important implications for the interpretation of scanning (or fast-stepping) measurements with any DMA.

2.3 Methods

While the conceptual approach toward deriving the DMA transfer function based upon stream functions and electric flux functions is quite general, quantitative evaluation of the transfer function has been based upon idealized models (Knutson and Whitby, 1975; Stolzenburg, 1988). Detailed numerical simulations of the flows and fields within a DMA have aided in understanding small deviations from the predictions of those simplistic models for steady-state DMA operation (Da-Ren Chen and D. Y. Pui, 1997), and in the design of new instruments (*e.g.*,D-R Chen et al. (1998) and Mui et al. (2017)). Since our purpose is to enable quantitative interpretation of scanning DMA measurements, we follow this approach by numerically solving the Navier-Stokes and Maxwell equations to determine the flows and electric fields, taking into account the full 3-dimensional geometry of the instrument used to make measurements. The flow in the DMA is steady; the electric field changes only slowly, so it can be assumed to be in a quasi-steady-state, such that the electric field within the classification region of the DMA can be expressed as

$$E(r, z, t) = E_0(r, z) f(t) \tag{2.1}$$

where $E_0(r, z)$ is the electric field at the start of a scan, $t = 0$, when the applied voltage is $V(t = 0) = V_0$. $f(t)$ is the prescribed time variation of the voltage applied to the central electrode of the DMA; for the exponential voltage ramp that is commonly used in the SEMS, $f(t) = e^{\pm \frac{t}{\tau_s}}$, where

$$\tau_s = \frac{t_{\text{ramp}}}{\ln \frac{V_{\text{high}}}{V_{\text{low}}}} \tag{2.2}$$

is the e-folding time for a ramp of duration t_{ramp}, and V_{high} and V_{low} are the maximum and minimum magnitudes of the voltages of that ramp, respectively.

In DMA operation, particles enter through one electrode, which, in the TSI DMA, is electrically grounded, and exit through the counter-electrode (usually at high-voltage). As the classified aerosol exits the DMA, it must pass through a transition from high-voltage to ground that results in an adverse potential gradient that retards the motion of the classified particles and may enhance losses

(Kousaka et al., 1986; Zhang and Flagan, 1996); the adverse gradient may be at the aerosol entrance in other DMAs. In the TSI DMA studied here, the adverse gradient occurs when particles move from the central high-voltage electrode to the grounded exit region in the exit flow passage, causing some electrophoretic losses of classified particles. Because the strength of the fields in this region is determined by the time-varying voltage applied to the central electrode, $V_0(t)$, this portion of the exit is logically included in the classifier simulations, forming part of an extended classification region. The exact geometry of the DMA classification region that is modeled is shown in Fig. 2.1(b).

The PFDMA models used in previous studies have assumed that the particles are uniformly distributed across a portion of the flow between the two electrodes. On the other hand, particles enter the classification region of the TSI long column DMA after passing through a narrow annular channel where boundary layers distort that distribution, so the velocities at which particles enter the classification region vary along the width of an entrance port in the outer electrode wall. Because of the way that the annular channel alters the spatial distribution of particles entering the DMA, we include that channel as part of an extended classification region in the simulation, as shown in Fig. 2.1(a). We start the sheath flow simulation immediately downstream of the sheath flow mesh screens that are used to uniformly distribute the flow. The simulation of the flow between the coaxial, cylindrical electrodes thus extends from the mesh to the plane of the exhaust flow exit holes, though the details of those holes are not modeled; the exhaust flow exit boundary condition is treated as an atmospheric pressure boundary condition.

In that portion of the classified-aerosol outlet downstream of the adverse-gradient region, and in the entrance region, there is no electric field to drive migration, but the complexities of the flows in both of these regions contribute to particle losses, and may introduce a distribution of delays beyond those associated with the classification region or the detector. Since the classified sample flow is discharged from the DMA through a side port, and the DMA entrance region includes an off-center inlet, the flows in these regions are simulated using the full, three-dimensional geometry.

The performance of a DMA is described by a transfer function that allows one to predict the signals produced when sampling an aerosol with a known size distribution or, alternatively, to infer the size distribution of the sampled aerosol from the signals (particle counts) in the different measurement channels. Knutson and Whitby, 1975 defined the constant-voltage DMA transfer function, $\Omega_{ss}(Z_p, Z_p^*)$, as the probability that a particle of mobility Z_p will be transmitted through the classification region of the DMA when the DMA voltage and flows are set such that the mobility of the particle that passes from the centroid of the incoming aerosol flow to the centroid of the

classified sample flow is $Z^*_{\mathrm{p,ss}} = (Q_{\mathrm{sh}} + Q_{\mathrm{ex}})/4\pi LV$. Hereafter, the mobility of the particle that passes from centroid to centroid will be called the "centroid mobility". Under these conditions, and with a constant aerosol source, the value of the transfer function is simply the ratio of the flow of particles of mobility Z_{p} that leaves in the classified aerosol outlet flow at operating condition $Z^*_{\mathrm{p,ss}}$ to that present in the incoming aerosol flow, *i.e.*,

$$\Omega(Z_{\mathrm{p}}, Z^*_{\mathrm{p}}) = \frac{Q_{\mathrm{c}} N_{\mathrm{e}}}{Q_{\mathrm{a}} N_{\mathrm{i}}}, \tag{2.3}$$

where Q_{a} and Q_{c} are the flow rates of the incoming polydisperse aerosol, and the outgoing classified aerosol sample, respectively, and N_{i} and N_{e} are the corresponding incoming and exiting particle number concentrations.

If we similarly define the centroid mobility for the scanning DMA, the centroid mobility continuously changes with time during the scan, *i.e.,* $Z^*_{\mathrm{p}} = Z^*_{\mathrm{p}}(t)$, so the transfer function must be expressed in terms of time. For plug flow (uniform velocity) within the DMA, $Z^*_{\mathrm{p}}(t) = Z^*_{\mathrm{p,ss}}\,|_{\bar{V}(t_{\mathrm{e}})}$, where $\bar{V}(t_{\mathrm{e}})$ is the average voltage experienced by a particle that exits at time t_{e} as it transits through the DMA on the centroid trajectory (Wang and Flagan, 1990). Because particles are counted after leaving the DMA, the appropriate time to relate to particle mobility is the time at which the particle exits the classification region of the DMA, t_{e}; thus, we denote the centroid mobility as $Z^*_{\mathrm{p}}(t_{\mathrm{e}})$. Note that the voltage at t_{e} is higher than $\bar{V}_{\mathrm{transit}}$ during an up-scan, and lower during an down-scan, so the mobility evaluated at any time differs from that derived by Wang and Flagan (1990) for the plug-flow SEMS model.

Variations in the velocity across the flow channel in fully-developed laminar flow, or in the real instrument alter the trajectory through the DMA from that of plug flow, thereby shifting the distribution of times at which particles of a given mobility will exit, and changing $Z^*_{\mathrm{p}}(t)$. For present purposes, it is sufficient to note that the centroid trajectory ending at time t_{e} for a particular scan lies in the range

$$Z^*_{\mathrm{p,ss}}\Big|_{\min(|V(t_{\mathrm{i}})|,|V(t_{\mathrm{e}})|)} \le Z^*_{\mathrm{p}}(t_{\mathrm{e}}) \le Z^*_{\mathrm{p,ss}}\Big|_{\max(|V(t_{\mathrm{i}})|,|V(t_{\mathrm{e}})|)}, \tag{2.4}$$

where t_{i} is the time at which the particle enters the classification region. Theoretical derivations of the non-diffusive transfer function for the scanning DMA reveal that particles that are included in the classified aerosol outlet flow experience a range of transit times due to the coupling of the time variation of the field within the classification region with the nonuniform axial velocity (Dubey and Dhaniyala, 2008; Mamakos, Ntziachristos, and Samaras, 2008). This added complexity requires a

different approach to determination of the transfer function of the scanning DMA from that used in earlier, steady-state DMA studies.

In the present study, we do not attempt to derive a theoretical model to account for this variation; instead, we seek to capture the effects of the scan on the transfer function through Brownian dynamics simulations. To include all of the factors that affect the transfer function, we have examined a particular scanning DMA, the TSI Model 3081A long-column DMA, simulating flows and electric fields for the exact geometry of that instrument, including its entrance and exit regions, using COMSOL Multiphysics^{TM} to obtain a finite-element solution of the Navier-Stokes equations for the flow field, and of Maxwell's equations for the quasi-steady-state electric field. Brownian dynamics (Monte Carlo) simulations of particle Brownian motion were used to account for the effects of diffusion on the transmission of particles through the DMA.

We have subdivided the internal geometry of the DMA into three regions: (*i*) an upstream entrance region where we probe losses as the flows are brought into the classifier; (*ii*) the extended classification region described above; and (*iii*) the grounded portion of the DMA exit downstream of the adverse gradient. To elucidate the effects of the off-axis aerosol sample inlet and classified aerosol outlet ports, 3-dimensional models were used to simulate the flows in the grounded portions of the entrance and exit regions; the flow and electric fields in the classification region were represented using a 2-dimensional, axisymmetric model to reduce computation time. The electric field and fluid motion within each of these regions were calculated once; the results are stored in a gridded format for use in the study of particle trajectories.

As noted above, comparison between traditional classifier transfer functions become more complex for scanning-mode operation than for steady-state operation. When the voltage is constant, losses of particles during passage through the entrance and exit regions that we have excluded from the classification region can be addressed using empirically-derived transmission efficiency functions since these regions do not directly impact the classification process.

To place the present work in context relative to the previous, simplified, parallel-flow models of the classification region between the coaxial, cylindrical electrodes, we also represent particle transmission for fully-developed laminar flow using the traditional, idealized, parallel-flow DMA model (PFDMA-L). We note that, for the flow rates considered here, the flow within the DMA rapidly approaches fully-developed laminar flow, so this is a reasonable model to the extent that the PFDMA model accurately describes the DMA. Because non-diffusive particle classification during plug flow has previously been shown to attain the same transfer function as that for the constant voltage DMA (Wang and Flagan, 1990), we do not simulate the plug flow limit, but, rather apply

the Stolzenburg, 1988 model to predictions for that idealized representation.

Once the flow and electric fields are obtained, diffusional trajectories through each of these regions are modeled using a Brownian dynamics (Monte Carlo) simulations. For a small time step, the incremental change in the variance from the position that a particle would reach by advection and electrophoretic migration is given by the Einstein relation,

$$\mathrm{d}\sigma_\chi^2 = 2\mathcal{D}\mathrm{d}t \tag{2.5}$$

where χ denotes one of the Cartesian coordinates, x, y, or z. Within the entrance and exit regions, 3-dimensional Brownian motion is simulated wherein, in a time step $\mathrm{d}t$, the particle motion is described by

$$\chi(t+\mathrm{d}t) = \chi(t) + \int_t^{t+\mathrm{d}t} v_\chi(x,y,z,t)\mathrm{d}t + g(\sqrt{\mathrm{d}\sigma_\chi^2}) \tag{2.6}$$

where $g(\sigma)$ is a random variable in a Gaussian distribution with standard deviation σ, and zero mean. The integral terms describe advection and electrophoretic migration; the Gaussian term accounts for Brownian motion. The axisymmetric, two-dimensional model employed here combines the Brownian contributions in the x and y directions into the r component (see Supplementary Information for derivation), so that

$$r(t+\mathrm{d}t) = \sqrt{\left[r(t) + \int_{\mathrm{t}}^{t+\mathrm{d}t} v_r(r,z,t)\mathrm{d}t + g\left(\sqrt{\mathrm{d}\sigma_x^2}\right)\right]^2 + g\left(\sqrt{\mathrm{d}\sigma_y^2}\right)^2}. \tag{2.7}$$

The kinematic velocity in each direction is the sum of the local fluid velocity and that due to electrophoretic migration, $\mathbf{v}(r,z,t) = \mathbf{u}(r,z) + Z_\mathrm{p}\mathbf{E}(r,z,t)$, which can be obtained using the flow and electric field data obtained from the finite element calculations.

To enable coupling of the models of the classification and exit regions, the aerosol outlet boundary of the classification region is subdivided into 100 radial bins to record the exit radial distribution $p(r)$ of the transmitted particles, which are fitted to three-term Gaussian model, *i.e.*,

$$p(r) = \sum_{i=1}^{i=3} a_i \exp\left[-(\frac{r-b_i}{c_i})^2\right], \tag{2.8}$$

where a_i, b_i and c_i are fitting coefficients. These spatial distribution fits were then used as input to simulation of the exit region. Steady-state, 3-dimensional, laminar flow simulations with the COMSOL Multiphysics$^{\mathrm{TM}}$ particle tracing module were performed for the entrance and exit regions.

Flow and electric field data from the COMSOL Multiphysics^{TM} simulations were imported into Igor Pro to evaluate individual particle trajectories in the 2-dimensional simulations. At each time step of the simulation, a fixed number of new particles was introduced into the classification region; they were distributed with radial position so that the number concentration in the flow was constant. The times at which particles pass through the aerosol outlet boundary were recorded, as were their entrance times.

Simulations were performed for the conditions that are used in our chamber measurements of aerosol yield; these conditions, which are summarized in Table 2.1, correspond to a nominal nondiffusive resolving power of $\mathcal{R}_{nd} = \beta^{-1} = 5$, and span a particle size range of 15.3 nm $< D_p <$ 1130 nm. Scan times of $t_{ramp} = 10,\ 20,\ 45,\ 90,$ and 240 s were simulated (our chamber measurements have typically been employed $t_{ramp} = 45$ s) in order to explore the effect on differences between the SEMS transfer function and that of the classic, stepping mode (DMPS) operation of the DMA.

2.4 Results and discussion

COMSOL^{TM} simulations

Figure 2.2 shows the results of the COMSOL^{TM} simulations of the flow and electric fields within the DMA classification region for the operating conditions indicated in Table 5.1, focusing on the aerosol inlet and outlet regions. The fluid streamlines in the classification region and the fluid flow velocity magnitude are shown in Fig. 2.2(a) and (b). The entrance disturbance to the flow in the space between the electrodes is clearly seen on the right-hand-side of Fig. 2.2(a), as is the smaller disturbance near the aerosol outlet at the bottom of the main flow channel (Fig. 2.2(b)). Figures 2.2(c) and (d) show the electric flux lines and normalized potential. The distortion of the field near the entrance slot in the outer electrode has previously been identified as the cause of a small deviation from the predicted value of $Z^*_{p,ss}$ (Da-Ren Chen, D. Y. H. Pui, et al., 1999).

Figures 2.3(a-c) show representative trajectories of 147 nm particles in the entrance, classification, and exit regions of the DMA, respectively; due to their low diffusivities, such large particles directly reveal the effects of voltage scanning on particle paths through the different regions of the DMA. This particular simulation considers a measurement cycle that begins with a constant low voltage for 20 s, followed by an exponential, 45 s up-scan. Since no electric field is present in that portion of the entrance shown in Fig. 2.3(a), these trajectories persist throughout the measurement cycle. The particles enter through a bent tube at the top of the instrument that discharges them into a plenum where a recirculation is induced (see Supplementary Information for the flow fields solution in the entrance and exit regions).

Trajectories of 147 nm particles that enter the inlet annulus at a particular instant in the measurement cycle are shown in Fig. 2.3(b). For this simulation, the particles enter the inlet annulus close to the peak in their transmission efficiency at $t - t_0$ =42 s, where t_0 denotes the time at the start of the voltage ramp. The particle trajectories depend upon their initial radial position in the annulus. Particles that enter in the core of the flow in the annulus, dashed lines in Fig. 2.3(b), are rapidly advected through the classification region, and exit it with the excess air discharge flow. Those that enter the inlet annulus at smaller radii at this same instant of time (solid lines in Fig. 2.3(b)) may be transmitted to the classified sample outlet flow. Those that enter near the outer radius of the inlet annulus (dotted lines in Fig. 2.3(b)) pass through the annulus slowly due to the boundary layer, and enter the region between the electrodes when the voltage is high. As a result, they migrate quickly toward the central electrode, where they deposit. For particles in this boundary layer to be transmitted, they must enter the annulus earlier in the scan when the electric field strength is lower.

This snapshot of particles that enter the annulus at one instant of time shows that both the entrance time and the position of the particle within the aerosol inlet determine whether it can successfully penetrate through the classification region and be included in the classified sample outlet flow. Particles entering on any trajectory can be efficiently transmitted to the classified aerosol outlet flow, provided they enter the annular region at the appropriate instant of time. The transfer function must, therefore, account for all particles of a given mobility that exit the classifier at time, t_e, regardless of their entrance times.

After passing through a downstream exit port in the central electrode, classified particles are transmitted into a cylindrical channel along the axis of that electrode; particle migration in the adverse potential gradient in this region affects their transmission efficiency (Kousaka et al., 1986). The radial distribution, shown in Fig. 2.4, is the cumulative result for particles in a complete up-scan. The particle beam sweeps through the particle exit slot slowly at the beginning of the up-scan owing to the low electric migration velocity. Thus, the time-weighted particle penetration will be higher at r >1 mm compared to that near the centerline (r = 0). Because the primary deposition mechanism in the adverse gradient region is electrophoretic migration, these losses are similar for particles of very different mobilities (Zhang and Flagan, 1996). The radial distribution was fitted to Eq. (2.8) for use in the exit region simulations. At the bottom of the exit channel, particles enter a plenum where another recirculation zone exists, shown in Fig. 2.3(c). Ultimately, the surviving particles exit through a cylindrical port to one side at the base of the instrument.

In contrast to the real instrument, the PFDMA-L simulation, shown in Fig. 2.3(d), distributes the incoming particles across the flow between the electrodes without distorting the velocity profile, so

much less trajectory crossing takes place; that which does occur happens as the particles approach an annular sample extraction portion of the space between the electrodes in this simplistic model, which captures particle behavior only in the region between the electrodes. Those particles that enter the PFDMA-L classification region near the inner (small radius) limit of the sample flow, *e.g.*, $r_{in} \leq 14.5$ mm, where the fluid velocity is high, experience relatively short residence times compared with those that enter on the corresponding streamlines of the real DMA where the boundary layer in the inlet annulus slows the flow.

Scanning DMA transfer function for low diffusivity particles

Simulations of the entrance, classification, and exit regions of the DMA operated under the conditions indicated in Table 5.1 were performed for 52 logarithmically-spaced electrical mobilities ranging from $Z_p = 8.64\times10^{-7}\mathrm{m}^2\mathrm{V}^{-1}\mathrm{s}^{-1}$ ($D_p = 15.3$ nm) to $Z_p = 9.30\times10^{-10}\mathrm{m}^2\mathrm{V}^{-1}\mathrm{s}^{-1}$ ($D_p = 1130$ nm). Particles of each size were introduced into the classifier at a constant rate of 200 particles per time step throughout the scan. The transfer functions were obtained by locally-weighted scatterplot smoothing (LOESS; Cleveland, 1979) of the raw data using second order polynomials. The error bars show the root-mean-square sum of residuals of the raw data from this fitted function.

Accurate estimation of the transfer function using Brownian dynamics simulation requires a short time step, but the computational cost increases dramatically with decreasing step size. The approach of an asymptotic form for the transfer function was explored by performing simulations with time steps, dt, ranging from 1.25 ms to 20 ms. The resulting ratio of the flow of particles contained in the classified aerosol outlet flow (number/s) to the entering particle flow rate is shown as a function of time-in-scan in Fig. 2.5. Decreasing the time step from 20 ms to 10 ms increased the peak transmission two-fold; the peak value approaches an asymptotic limit as dt approaches 1.25 ms for small, high-diffusivity, 24.5 nm particles. Long time steps increase the likelihood that, during a single time step, simulated diffusional motion will bring a particle to a flow boundary, particularly during the low voltage portion of the particle's transit through the classification region when particles are advected close to, and nearly parallel to an electrode surface, *i.e.*, the outer electrode in the up-scan, and the inner electrode in the down-scan. Shorter time steps make it possible to better track the particle trajectories through this critical portion of their time in the classification region, and, therefore, yield higher transmission probabilities. As particle size increases, diffusivity and σ_r decrease, enabling longer time steps. With time step of 1.25 or 2.5 ms, the total number of transmitted particles in the simulated scans were 2.25×10^5 and 1.10×10^5.

The steady-state, three-dimensional simulation of flow in the entrance region produced the penetration efficiency as a function of the mobility-equivalent diameter shown in Fig. 2.6. For these

operating conditions, diffusional losses become significant as particle diameter decreases below about 70 nm, though transmission was high, even for the smallest particles.

That portion of the exit within the central electrode and the downstream insulator have been included in the classification region in order to account for the adverse potential gradient, so its effects are part of the classification region transfer function reported here. While steady-state can be assumed for the region upstream of the entrance annulus, the distribution of delay times during passage through the exit region can distribute the particles into different counting bins. Therefore, the exit region analysis considers the time-dependent penetration through the exhaust plenum where the strong recirculation seen in Fig. 2.3(c) occurs, and the lateral exit tube. The efficiency of particle penetration through this region is shown as a function of particle size in Fig. 2.7(a). The overall penetration efficiency within the exit region is close to unity, ranging from 96% to 99.5% as shown in Fig. 2.7(b); penetration decreases with decreasing size due to diffusion. The mean residence time within this region for those particles that are transmitted through it, shown in Fig. 2.7(c), ranges from 0.20 s to 0.22 s, and increases with particle size because diffusion reduces the concentrations of the smallest particles in the boundary layer where velocities are low. While these times are short compared to that in the classifier for the low flows considered in this study, they could become important in measurements of smaller particles.

To determine the scanning DMA transfer function, the entrance and exit times of each particle that is successfully transmitted are stored. Because the clearest indication of the effect of scan time on the DMA transfer function is found in simulations of large, low diffusivity particles, we first consider relatively large ones.

The entrance times of successfully transmitted 147 nm particles for a 45 s up-scan exhibit a highly skewed distribution, and differ dramatically between the geometric model (G-DMA) and the idealized, laminar and parallel flow model (PFDMA-L), as seen in Fig. 2.8(a). The long tail toward the small entrance-time limit of the distribution results from particles that enter near the wall, where the velocity is low. Particles that enter where the velocity is high have quite uniform transit times, so there is no tail for late entering particles. This distortion of the entrance time distribution in the geometric model of the real DMA results from the two boundary layers in the entrance annulus, while particles entering the PFDMA-L model experience only a single boundary layer region. While the entrance time distribution of 147 nm particles during down-scan operation in the G-DMA model shows tails toward late exit times, the entrance-time distribution of the PFDMA-L model is close to triangular shape (Fig. 2.8(b)).

In contrast to the entrance time distribution, the exit time distribution for the up-scan approaches

the triangular, non-diffusive form seen for large particles in the constant-voltage DMA. As defined by Eq. (2.3), the scanning DMA transfer function describes the temporal distribution of particles exiting the classification region. Both G-DMA and PFDMA-L models show skewed exit time distributions for the down-scan operation.

Since the exit time determines into which time bin a particle is counted, the up-scan yields better behaved data than does the down-scan, a conclusion that many users have drawn from scanning DMA data. Since this corresponds most closely to the time bins into which counts are accumulated during measurements, further discussion of the results of this study will focus on the exit times.

In the limit of long scan times (large τ_s), the voltage changes little during any particle's transit through the classification region. Hence, we intuitively expect the transfer function to asymptotically approach that of the constant voltage DMA. As suggested by Wang and Flagan (1990), the non-diffusive transfer function preserves its triangular form for plug flow. We see in Fig. 2.9 that, even with the pronounced boundary layers produced by laminar flow in real DMAs, the triangular form is preserved for a wide range of scan times. On the other hand, as τ_s decreases, the shape of the transfer function becomes increasingly distorted for both fully-developed laminar flow (PFDMA-L) and the real-world flow patterns of the G-DMA. Some of the particles are artificially introduced into the high-velocity region of the flow in the PFDMA-L, so the mean residence time in that model is artificially low. In contrast, a fraction of particles in a real scanning DMA (and in the G-DMA model) must pass through the boundary layer region where the velocity is low, increasing the mean residence time slightly over that of the plug flow. The laminar and plug-flow PFDMA models exclude diffusional losses in the entrance annulus, and electrophoretic particle losses in the adverse gradient region, so the transmission probabilities estimated by both models are higher than predicted using the real DMA geometry. Indeed, the apparent transmission efficiency in the idealized laminar PFDMA can significantly exceed unity during fast scans (t_{ramp} = 10–20 s) because the particles entering late in the scan can catch up with those that entered earlier. A natural misinterpretation of the scanning-mode data is to evaluate the transfer function at the voltage at the time when particles exit the DMA, usually for the case of uniform velocity. In essence, this amounts to applying treating the scanning-mode data as though it resulted from operation of the DMA with the voltage held constant at that value. As shown in Fig. 2.9, this "static" transfer function is offset significantly from that obtained using any of the models that properly account for the time variation of the voltage during fast scans, but the discrepancy decreases in the slow scans (t_{ramp} = 240 s) as the scanning-mode transfer function asymptotically approaches the constant voltage form.

The effects of ramp time on down-scan transfer functions for the three models are shown in Fig.

2.10; the down-scan transfer function for short scan times is highly skewed to long exit times. The extent to which the down-scan transfer function exceeds unity at short scan times is lower than that for up-scans, while the tail toward small mobilities (late exit time) increases in length. During the down-scan, particles initially migrate quickly across the classification region, but their radial migration then slows, and particles spend much of their transit time in the low velocity near the inner electrode, delaying their passage through the classification region. Increasing the scan rate increases this boundary layer effect. In contrast to the up-scan, only very slow down-scans yield transfer functions that approach the triangular form of the constant-voltage DMA.

Instantaneous classification transfer function over the full range of particle sizes

To enable application of the simulated transfer function of the classification region to SEMS/SMPS data inversion, G-DMA simulations were performed for electrical-mobility-equivalent particle diameters ranging from 15.3—1130 nm in a 45 s up-scan, yielding the transfer functions shown in Fig. 2.11. The scattered dots representing the raw data from the simulation, while the curves show the LOESS-smoothed results. Particles between 15.3 nm and 19.8 nm diameter can penetrate the classification region in the first 20 seconds of the scan, when the voltage of the electrode is held at V_{low}. The transmission efficiencies of these particles remain unchanged until the voltage ramp begins, yielding a constant transfer function during this period; a similar plateau in the transmission efficiencies for large particles (800—1130 nm) starts at $t - t_0 = 71$ s, 6 seconds after the voltage reaches V_{high} and is, therefore, held constant. This time is somewhat shorter than the mean fluid residence time of 8.21 s due to rapid passage of the particles through the boundary layers of the classification region.

The variation of the transfer function with time-in-scan and mobility is shown Fig. 2.12; the continuous plot was created by interpolating the transfer functions in Fig. 2.11 over the full range of the particle sizes. The insets show the transmission efficiency at the transition from the low-voltage holding period to the voltage ramp (a), and that during the ramp (b). Because of diffusional losses, the overall transmission efficiency when the voltage is held at V_{low} is relatively low, and the transfer function is broad. Note that the electrical mobility scale is reversed so that the smallest particles appear at the bottom of the plot.

Instantaneous transfer function of the integrated scanning DMA

Thus far, we have only characterized the instantaneous classification transfer function, Eq. (2.3). The instantaneous transfer function of an actual scanning DMA must also account for particles losses in the entrance, and exit regions, as well as any delays in the classification (from its entrance

to its exit) and the exit regions, *i.e.*,

$$\Omega^{\mathrm{I}}_{\mathrm{DMA}}(Z_{\mathrm{p}}(D_{\mathrm{p}},\phi),t) = \eta_{\mathrm{ent}}(D_{\mathrm{p}})\left[\Omega(Z_{\mathrm{p}}(D_{\mathrm{p}},\phi),t) \star \eta_{\mathrm{exit}}(D_{\mathrm{p}},t)\right], \tag{2.9}$$

where $\eta_{\mathrm{ent}}(D_{\mathrm{p}})$ and $\eta_{\mathrm{exit}}(D_{\mathrm{p}},t)$ are the penetration efficiencies of the entrance and exit regions that were shown in Fig. 2.6 and 2.7, and $\star$ denotes the convolution operator, *i.e.*, $f(t) \star g(t) = \int_{-\infty}^{\infty} f(\tau)g(t-\tau)\mathrm{d}\tau$.

Figure 2.13 shows the instantaneous transfer functions of the integrated scanning DMA for 147 nm particles, *i.e.*, large, non-diffusive ones, with scan times ranging from 10 s to 90 s for both up-scan and down-scan operations. The difference between the transfer function of the integrated DMA and that of the classification region alone can be attributed to the combined effects of distribution of particle residence times within the exit region that distorts the shape of the transfer function and particle losses in both regions.

2.5 Conclusions

This study has examined the transfer function of a real DMA when operated in as part of a SEMS or SMPS. Detailed finite-element simulations of the flows and electric fields in the DMA are combined with Brownian dynamics (Monte Carlo) simulations to determine the transfer function for diffusing particles during voltage scanning. These numerical simulations reveal important differences from the idealized parallel-flow/perpendicular-electric-field models of the DMA that have been considered in most previous transfer function predictions. The effects of these differences are often small when the DMA is operated at constant voltage, but can lead to profound changes in the transfer function when operated in scanning mode, particularly for fast scans.

The present study has focused on a single instrument, the TSI Model 3081 long-column DMA, operated at flows that allow the instrument to probe relatively large particles. While the details will differ if the operating conditions are changed, or if a different classifier is used, the results of this study raise important questions about the interpretation of scanning DMA measurements. The elegant Stolzenburg transfer function (Stolzenburg, 1988) may closely approximate the instantaneous transfer function for sufficiently slow, increasing-voltage scans in a cylindrical DMA, but fails to describe the instrument when scans are fast. Further study will be needed to generalize these results to other DMAs or operating conditions.

To simulate scanning mobility particle classification, both that part of the entrance region of the DMA that influences the distribution of particles across the aerosol sample entrance into the region between the electrodes, and the region where particles pass through an adverse potential gradient

in the DMA exit were included as part of an extended classification region. The value of the classification transfer function for particles of a given mobility at exit time t_e accounts for the contributions of incoming particle that entered the DMA at all earlier times; because particles at different locations within the incoming aerosol sample experience different transit times, its value may exceed unity during fast scans. For an exponentially increasing voltage ramp (up-scan), the transfer function for non-diffusive particles is triangular in form for all but the fastest ramps, *i.e.*, smallest τ_s. In contrast, the down-scan exhibits a long tail at long time-in-scan, and yields a seriously distorted transfer function shape for all but the slowest scans. This difference in transfer function forms validates the common approach of basing scanning-DMA measurements on the up-scan, although, when the full transfer function is known, even down-scan data can be inverted to obtain the particle size distribution.

This paper has focused on obtaining the instantaneous transfer function of the DMA, and has not considered distortions of the measurements due to finite detector time response or other factors outside of the DMA. Early observations of asymmetry between up-scans and down-scans identified the slow response of the condensation particle counter used in those studies as the key factor leading to distortion in SEMS / SMPS instrument response (Russell, Flagan, and Seinfeld, 1995), though the DMA transit time distribution was later shown to be an issue (Collins, Cocker, et al., 2004; Mamakos, Ntziachristos, and Samaras, 2008; Dubey and Dhaniyala, 2008). Only the latter effects (those within the DMA) have been treated here, with the added features of particle diffusion and real DMA geometry.

While we have shown that the distortions caused by scanning the DMA voltage are more complex than previously described, SEMS/SMPS data inversion must also consider distortions due to plumbing downstream of the DMA, as well as the response-time-distribution of the detector. Therefore, data inversion requires yet another transfer function, that for the integrated SEMS/SMPS instrument that includes the effects of the DMA, downstream plumbing, and the particle detector, typically a CPC. In addition, the full SEMS / SMPS integrated instrument transfer function must account for the finite time period over which particles are counted for each time channel. This integrated transfer function for the full instrument is the topic of the companion to this paper (Mai et al., In review).

Acknowledgements

The authors thank Dr. K. Beau Farmer of TSI Inc. for providing detailed design drawings of the TSI Model 3081A DMA that made it possible to simulate flows, fields, and particle trajectories in the real instrument. We thank Yuanlong Huang, Wilton Mui, Amanda Grantz, Johannes Leppä,

Paula Popescu, and John Seinfeld for useful discussions. This work was supported by the National Science Foundation under Grant No. AGS-1602086.

Table 2.1: Operation parameters of the scanning DMA.

Parameter	Notation	Value
Length (cm)	L	44.38
Inner radius (cm)	R_1	0.937
Outer radius (cm)	R_2	1.961
Polydisperse flow rates (LPM)	Q_a	0.515
Monodisperse flow rates (LPM)	Q_c	0.515
Sheath flow rates (LPM)	Q_sh	2.510
Excess flow rate (LPM)	Q_ex	2.510
Low electrode voltage (V)	V_low	15
High electrode voltage (V)	V_high	9850
Up scan time (s)	$t_\mathrm{ramp,u}$	10,20,45,90
Down scan time (s)	$t_\mathrm{ramp,d}$	10,20,45,90
Holding time at V_low (s)	t_low	20
Holding time at V_high (s)	t_high	20

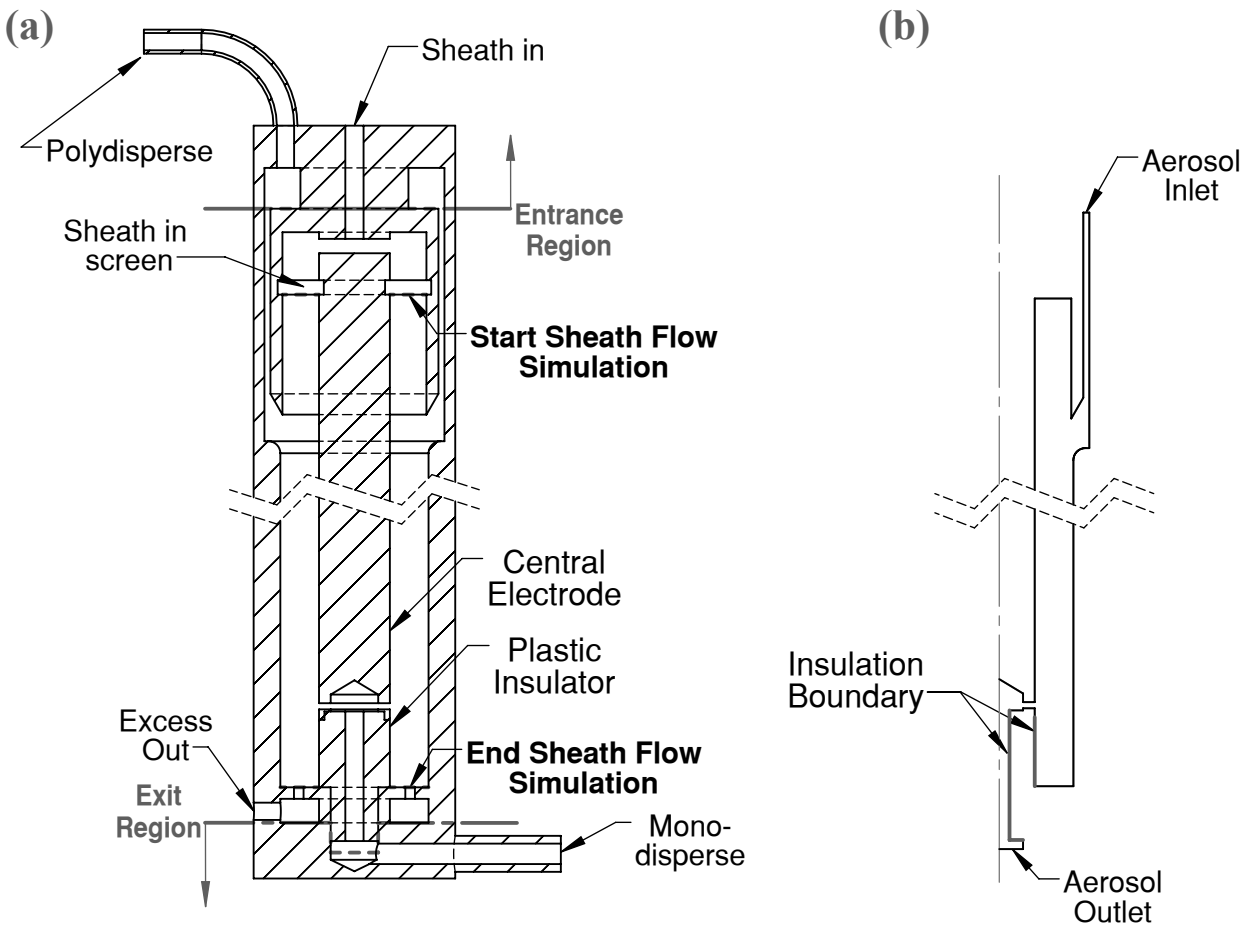

Figure 2.1: Geometry of the TSI Model 3081A long-column DMA (a) and the two-dimensional classification region (b). Details, such as the sheath in connection and the high voltage supply connection are omitted in (a), but the dimensions of the flow passages are derived directly from data by TSI, Inc., or measured in our laboratory.

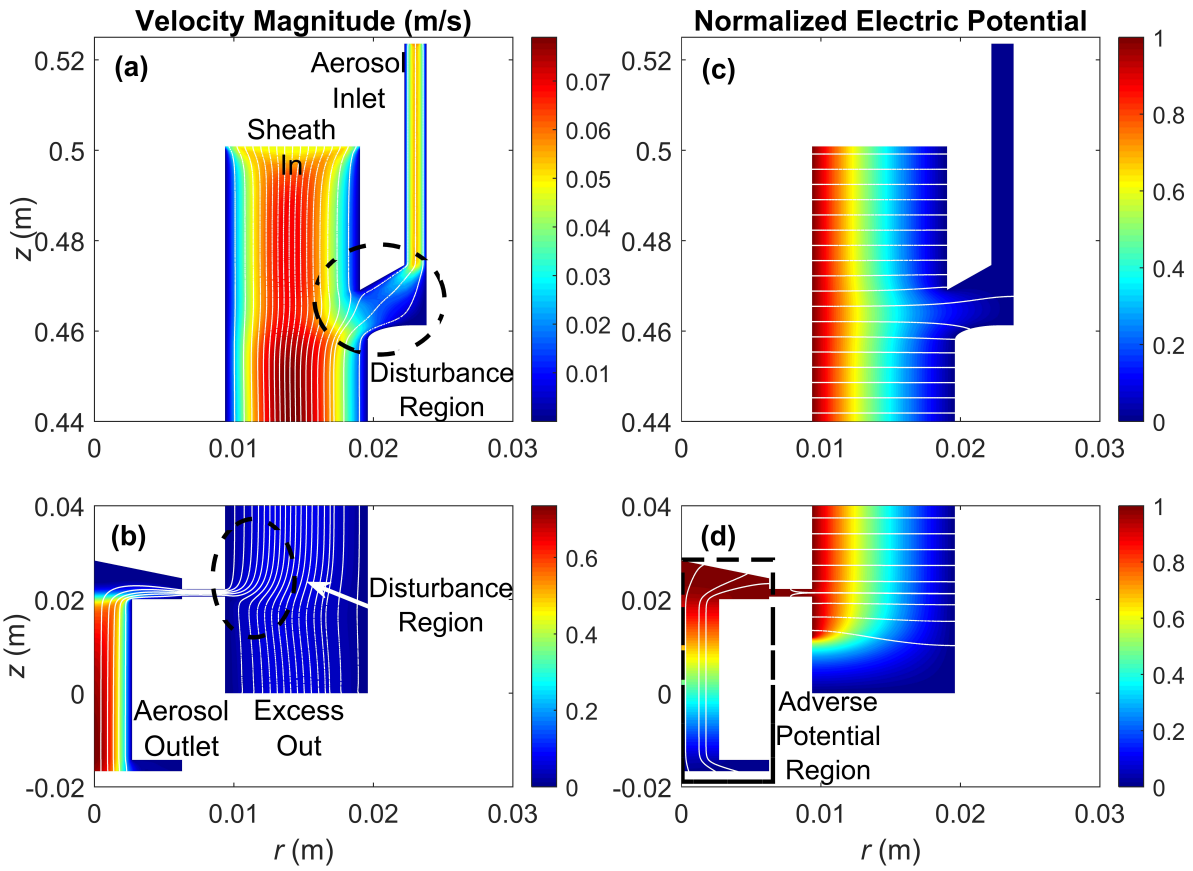

Figure 2.2: Magnitude of fluid flow velocity and electric potential within the classification region: (a) flow field in the upper region; (b) flow field in the lower region; (c) electric field in the upper region; (d) electric field in the lower region. Note that the colour scales in (a) and (b) are different. The white lines in (a) and (b) represent the fluid flow streamlines, and those in (c) and (d) are the electric field lines. The adverse electric potential gradient region is labeled in (d).

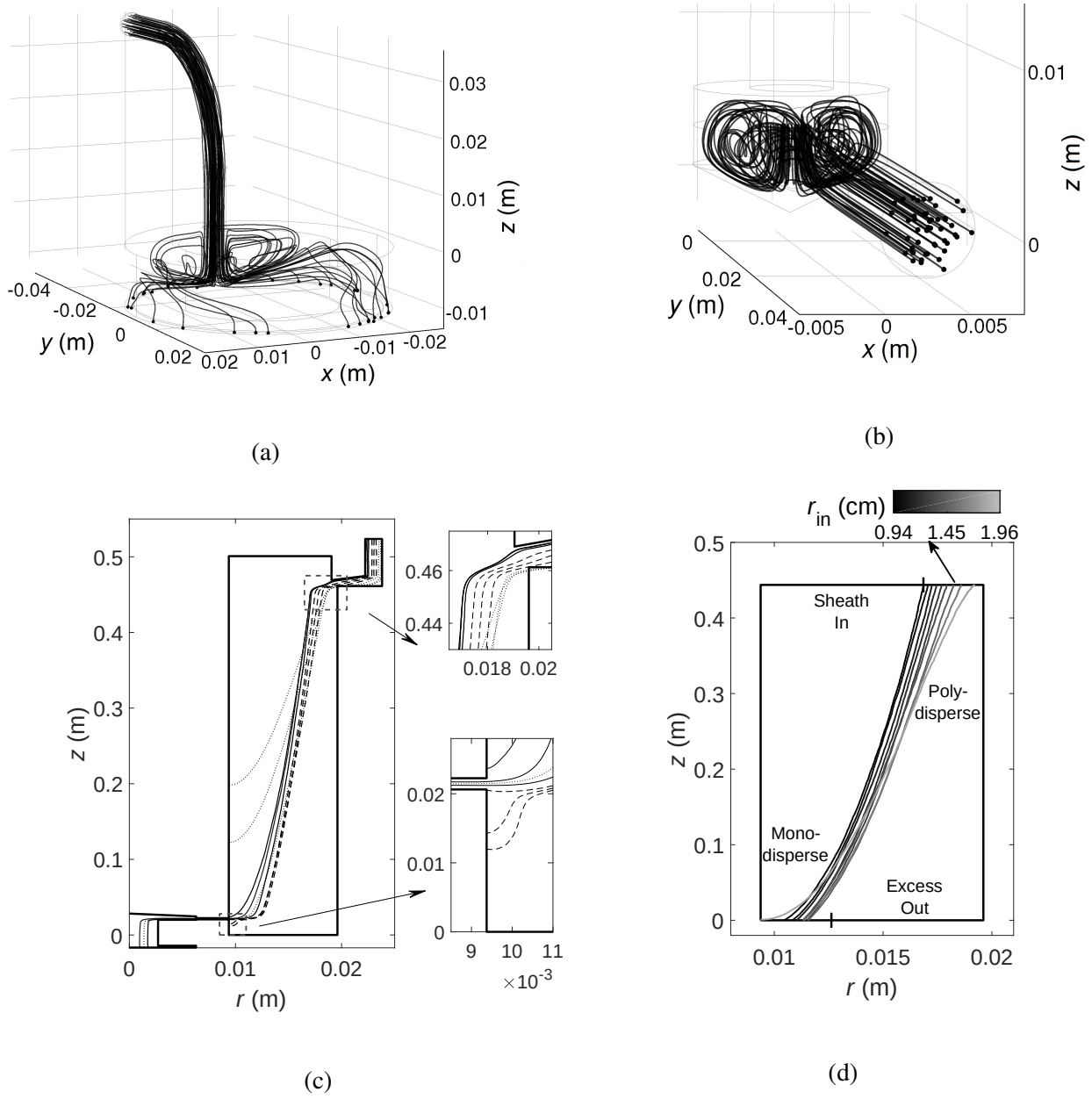

Figure 2.3: Particle trajectories within the DMA (a) entrance region, (b) exit region, (c) extended classification region for the actual DMA geometry, and (d) the idealized, parallel-flow classification region for 147 nm particles; the values of the length L, inner radius R_1, and outer radius R_2 are given in Table 5.1. The width of the aerosol sample incoming flow and classified sample outlet flow in the parallel-flow model are determined by the fraction of the total flow that corresponds to the corresponding limiting streamline.

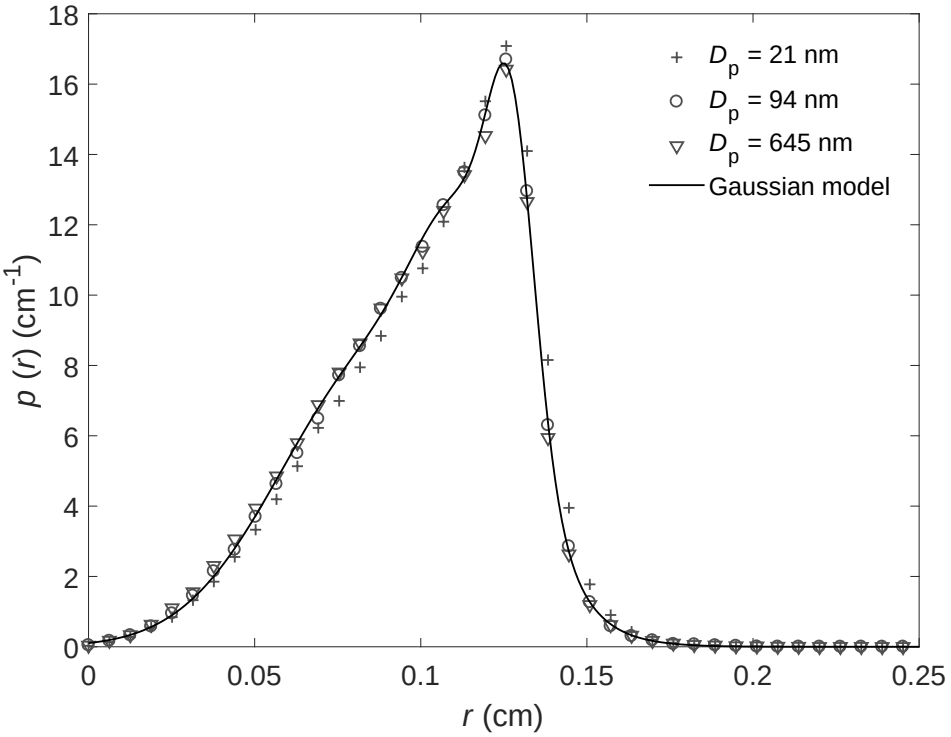

Figure 2.4: Spatial distribution of particles exiting the aerosol outlet of the DMA classification region. Data are fitted with a 3-term Gaussian model, $p(r) = \sum_{i=1}^{i=3} a_i \exp\left[-(\frac{r-b_i}{c_i})^2\right]$, where $a_i = 7.75, 7.11, 8.05$, $b_i = 0.128, 0.116, 0.087$ and $c_i = 9.77 \times 10^{-3}, 2.16 \times 10^{-2}, 4.17 \times 10^{-2}$ are the fitting parameters.

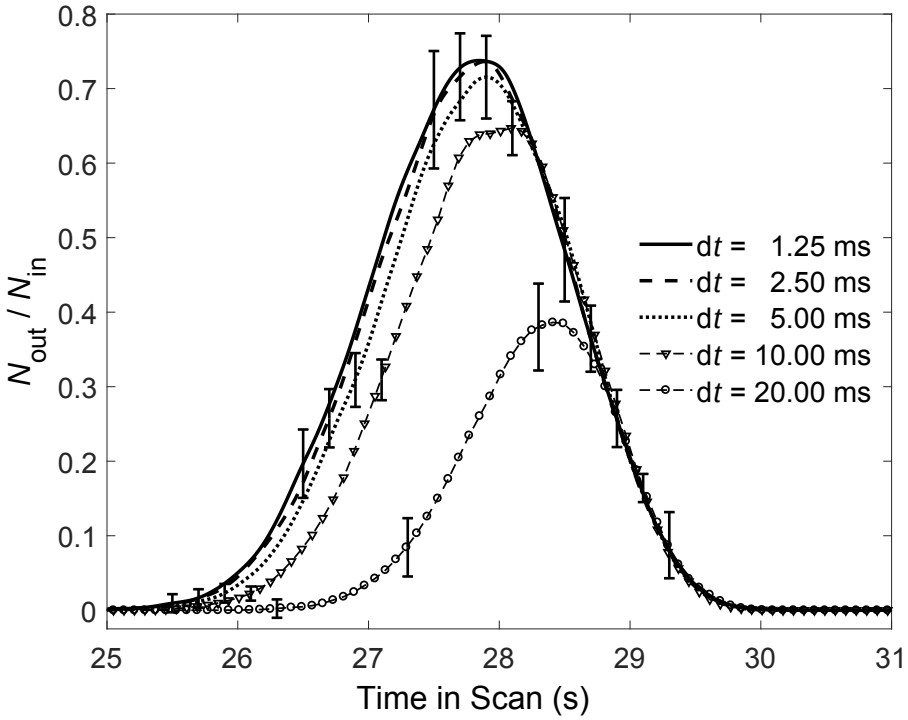

Figure 2.5: Scanning transfer functions for 24.5 nm particles through the real DMA geometry as determined using the indicated simulation time steps based for a ramp time of t_{ramp} = 45 s.

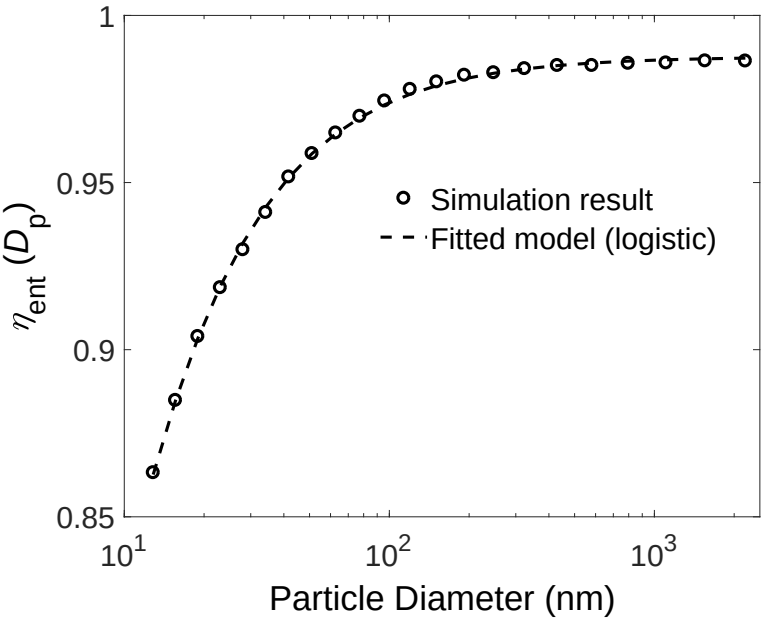

Figure 2.6: Penetration efficiency through the DMA entrance region as a function of particle diameter for an aerosol flow rate of Q_a = 0.515 LPM.

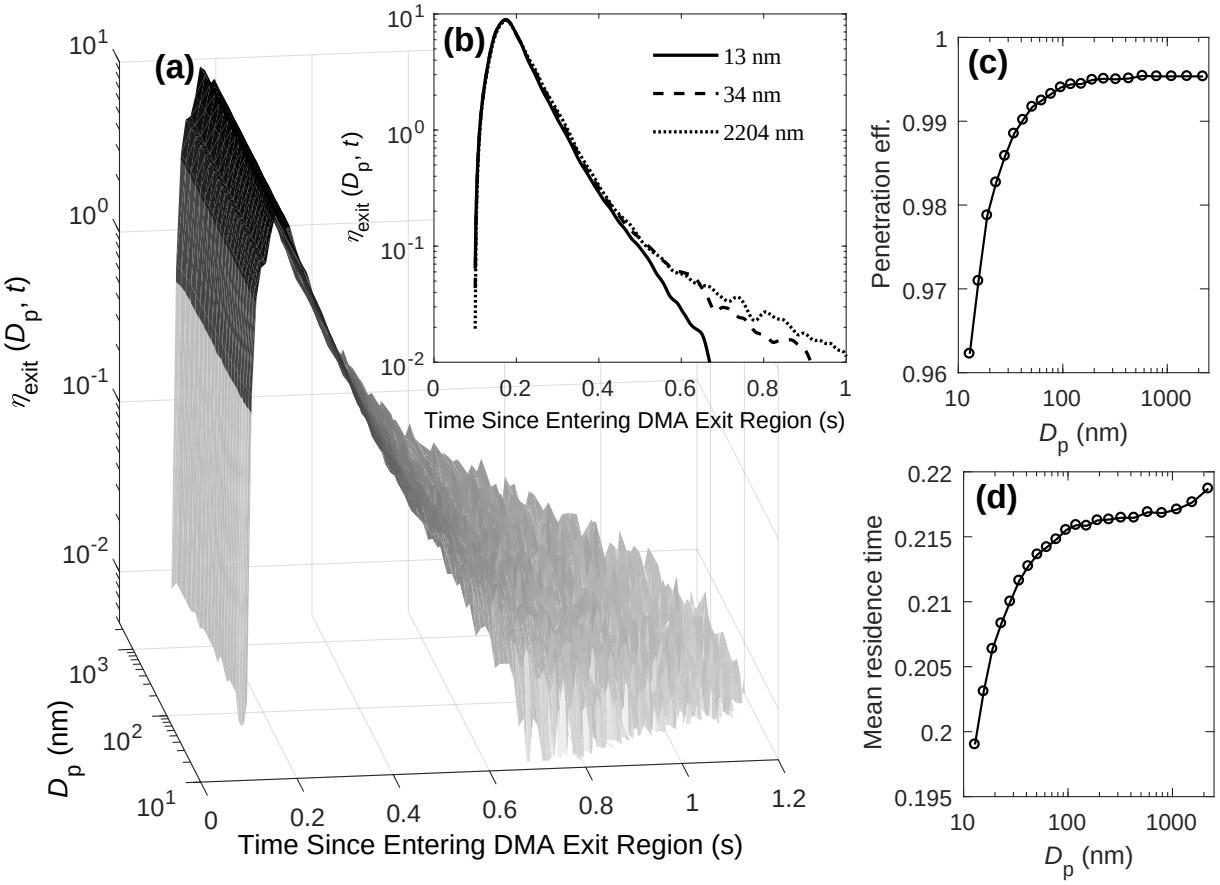

Figure 2.7: (a) Penetration distribution through the DMA exit region as a function of particle diameter and elapsed time; (b) shows the time variation of the penetration for 13, 34 and 2204 nm particles; (c) cumulative particle penetration efficiency as a function of particle diameter; (d) Mean residence time through the DMA exit region as a function of particle diameter.

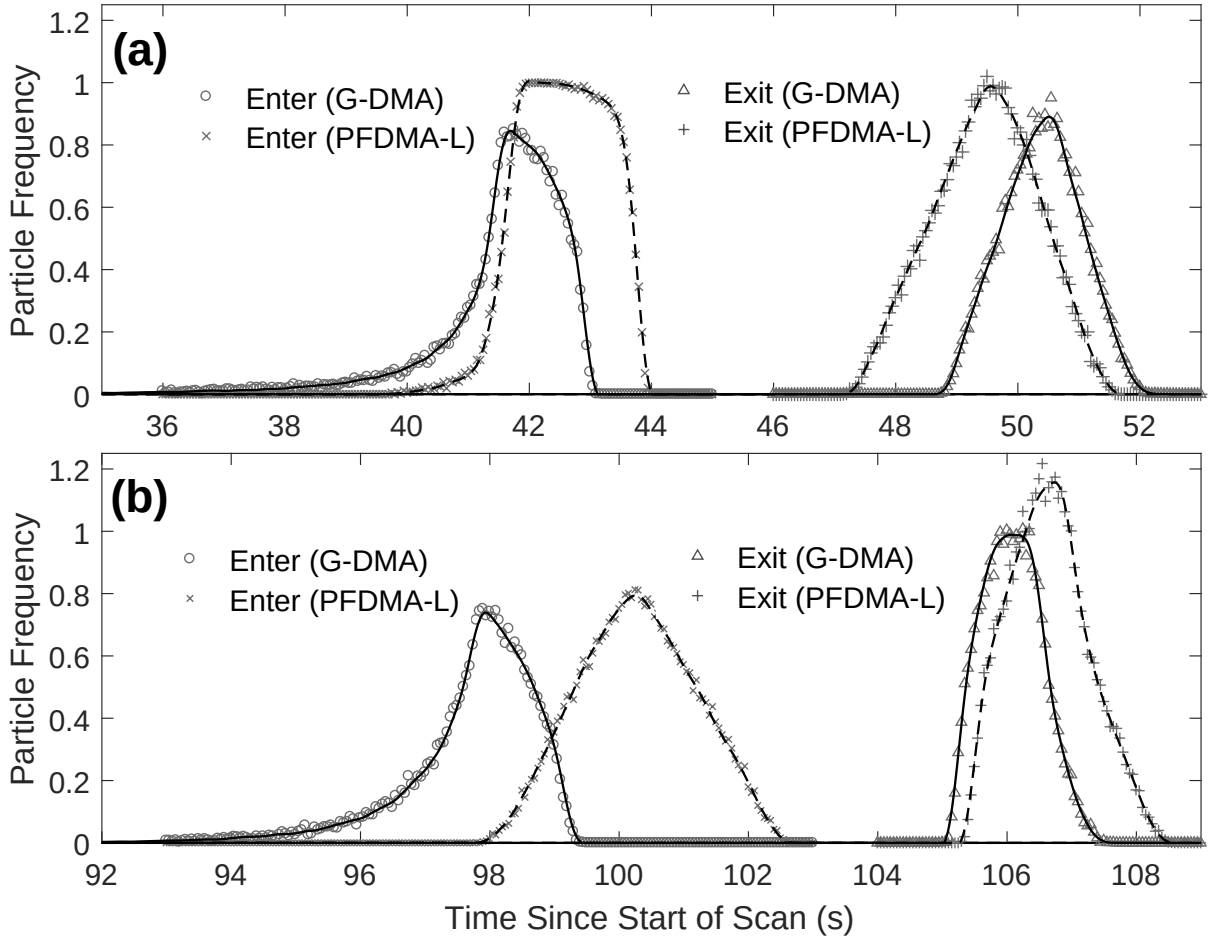

Figure 2.8: Temporal distributions of entrance and exit times for singly-charged 147 nm particles that are successfully transmitted through the DMA classification region for the geometric-DMA (G-DMA) model, or through the classification region of the parallel-laminar-flow (PFDMA-L) model. Ramp times for both upscan (a) and downscan (b) was $t_{\text{ramp}} = 45$ s ($\tau_s = 6.94$ s). The voltage was held constant for 20s before the start of each scan (up or down).

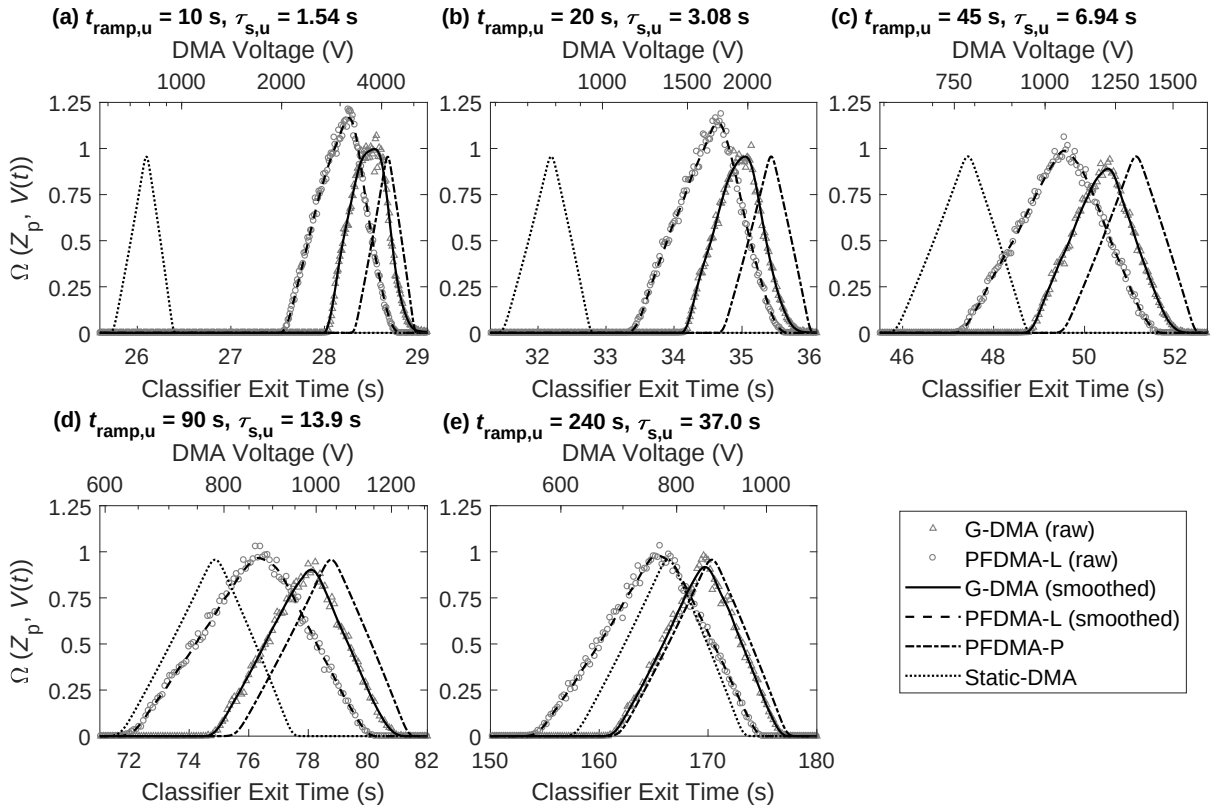

Figure 2.9: Up-scan transfer functions for 147 nm particles with a ramp time of t_{ramp} = 10, 20, 45, 90, and 240 s (corresponding to τ_s = 1.54, 3.08, 6.94, 13.87 and 37.00 s) for the geometric-DMA (G-DMA), parallel-laminar-flow (PFDMA-L) and parallel-plug-flow (PFDMA-P) models. The static-DMA model uses the constant-voltage transfer function, as in the PFDMA-P model, but evaluates the transfer function at the time at which particles exit the DMA.

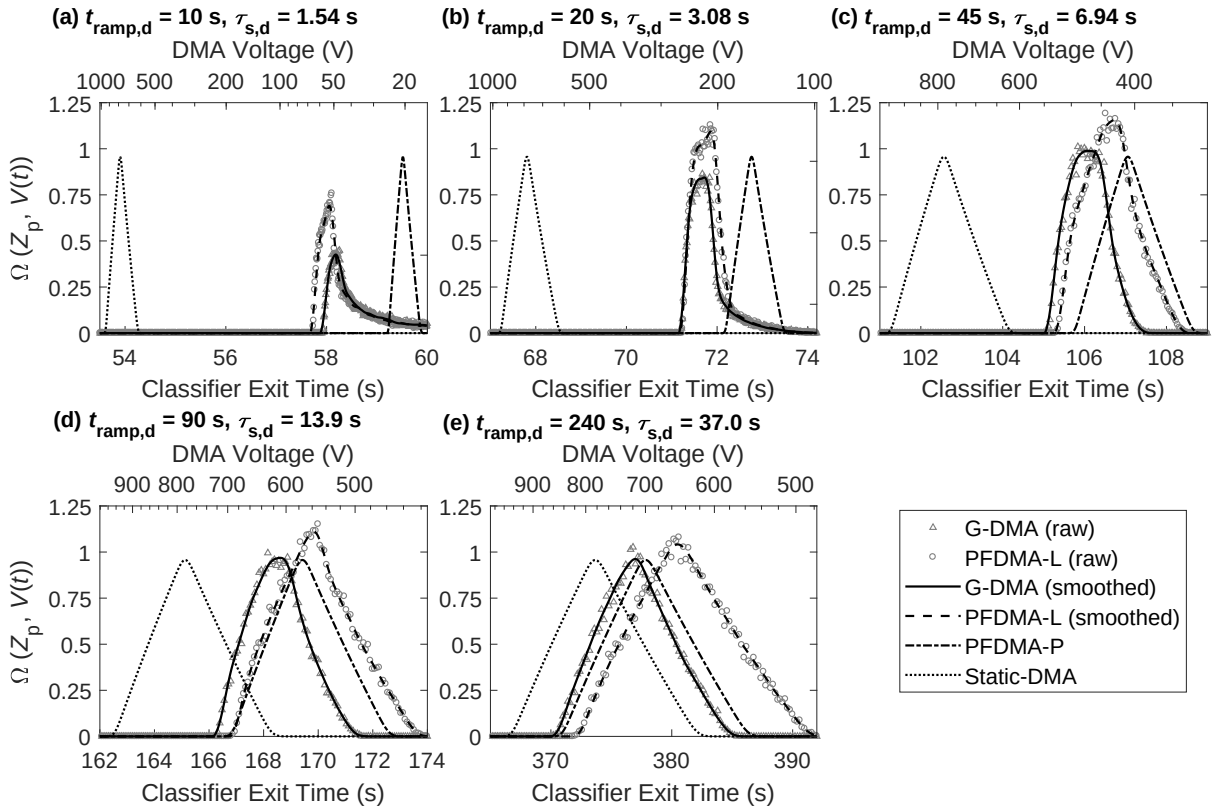

Figure 2.10: Down-scan transfer functions for 147 nm particles with ramping time t_{ramp} = 10, 20, 45, 90 and 240 s (corresponding to τ_s = 1.54, 3.08, 6.94, 13.87 and 37.00 s) for the geometric-DMA (G-DMA), parallel-laminar-flow (PFDMA-L), parallel-plug-flow (PFDMA-P), and static DMA models.

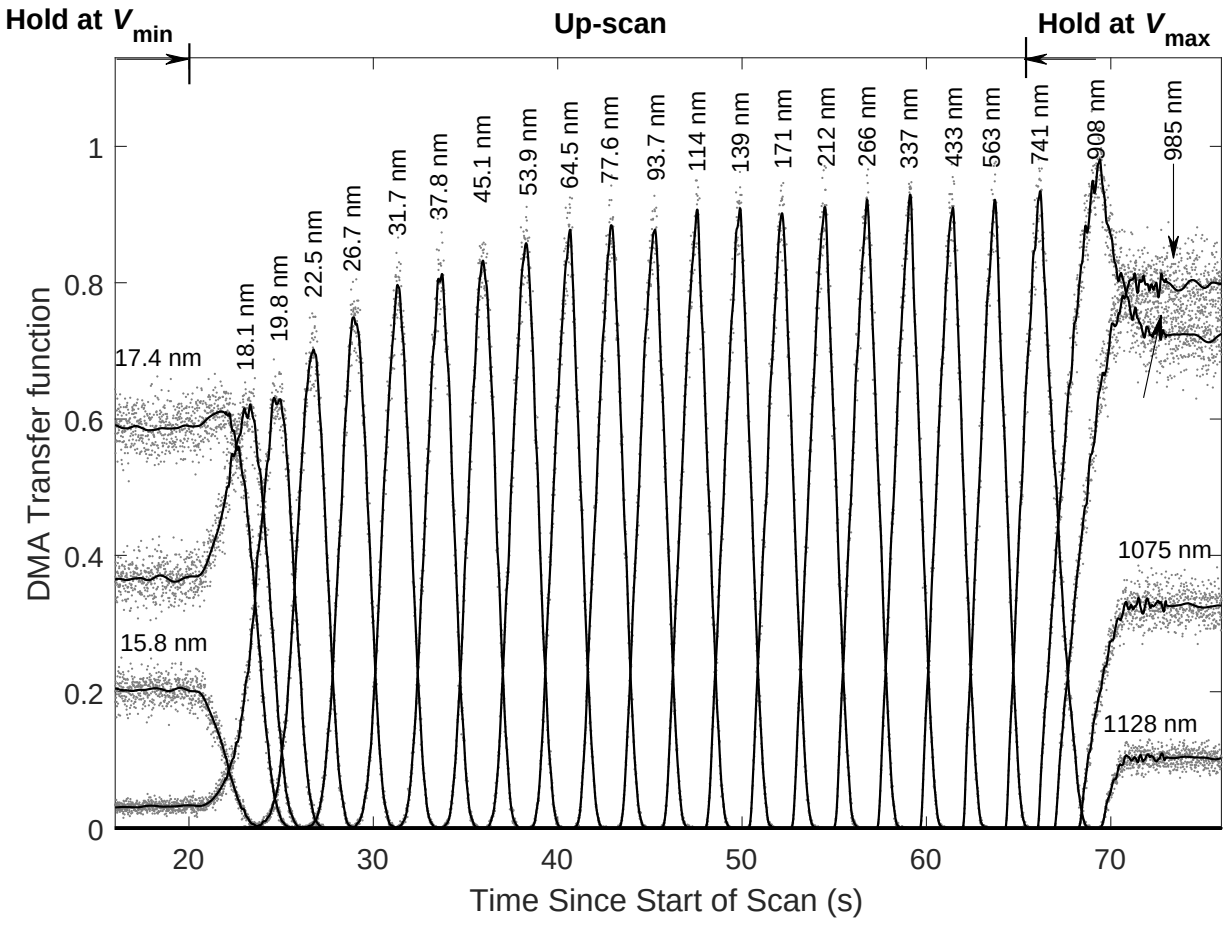

Figure 2.11: Scanning DMA transfer functions for singly-charged particles, with electric mobility equivalent diameters ranging from 15.8 nm to 1130 nm. Scattered dots represent the raw data from the simulations, while the solid lines are the result obtained by applying locally weighted scatterplot smoothing (LOESS) to the raw data.

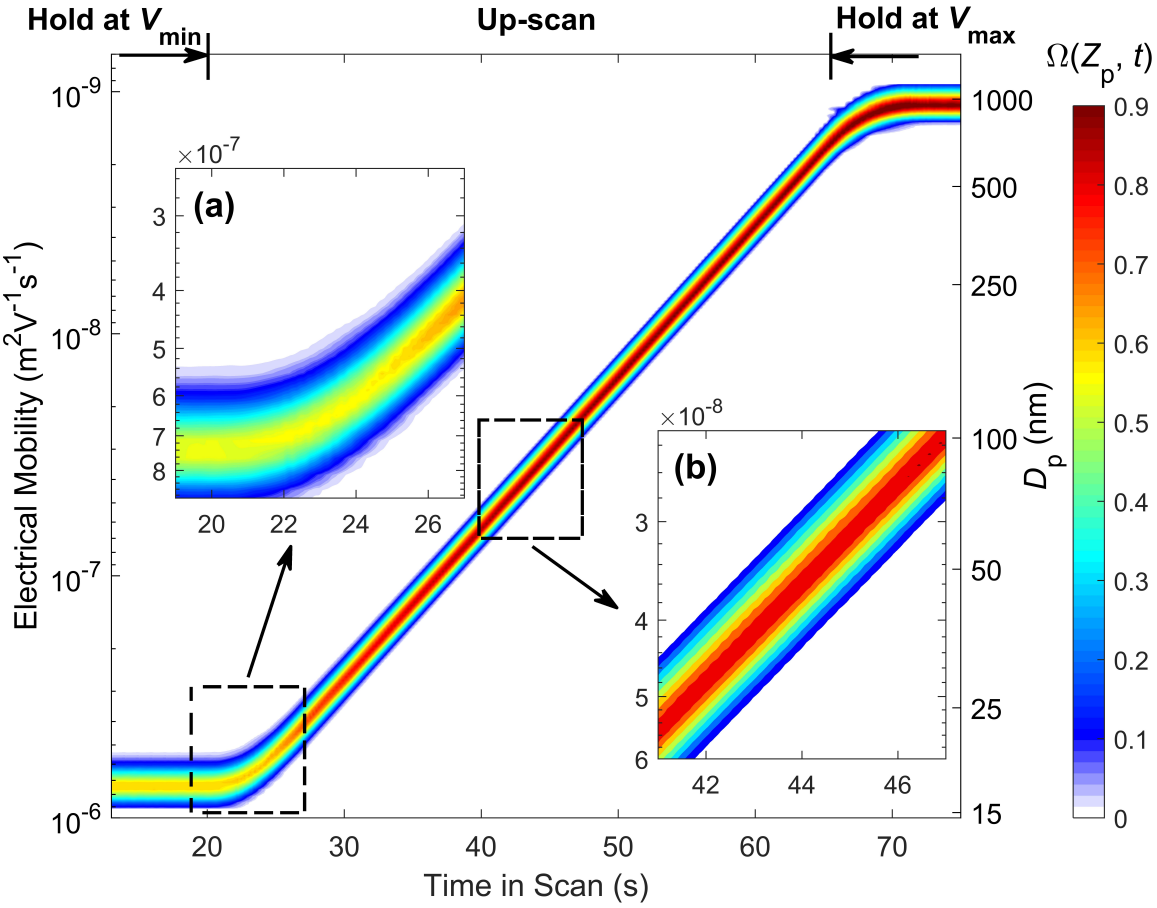

Figure 2.12: The scanning DMA transfer function as a function of the time-in-scan and the inverse particle electrical mobility. The inset (a) shows the transfer function during the transition from the low-voltage holding period to the ramp, while inset (b) shows the transfer function for particles whose transit is fully within the ramp.

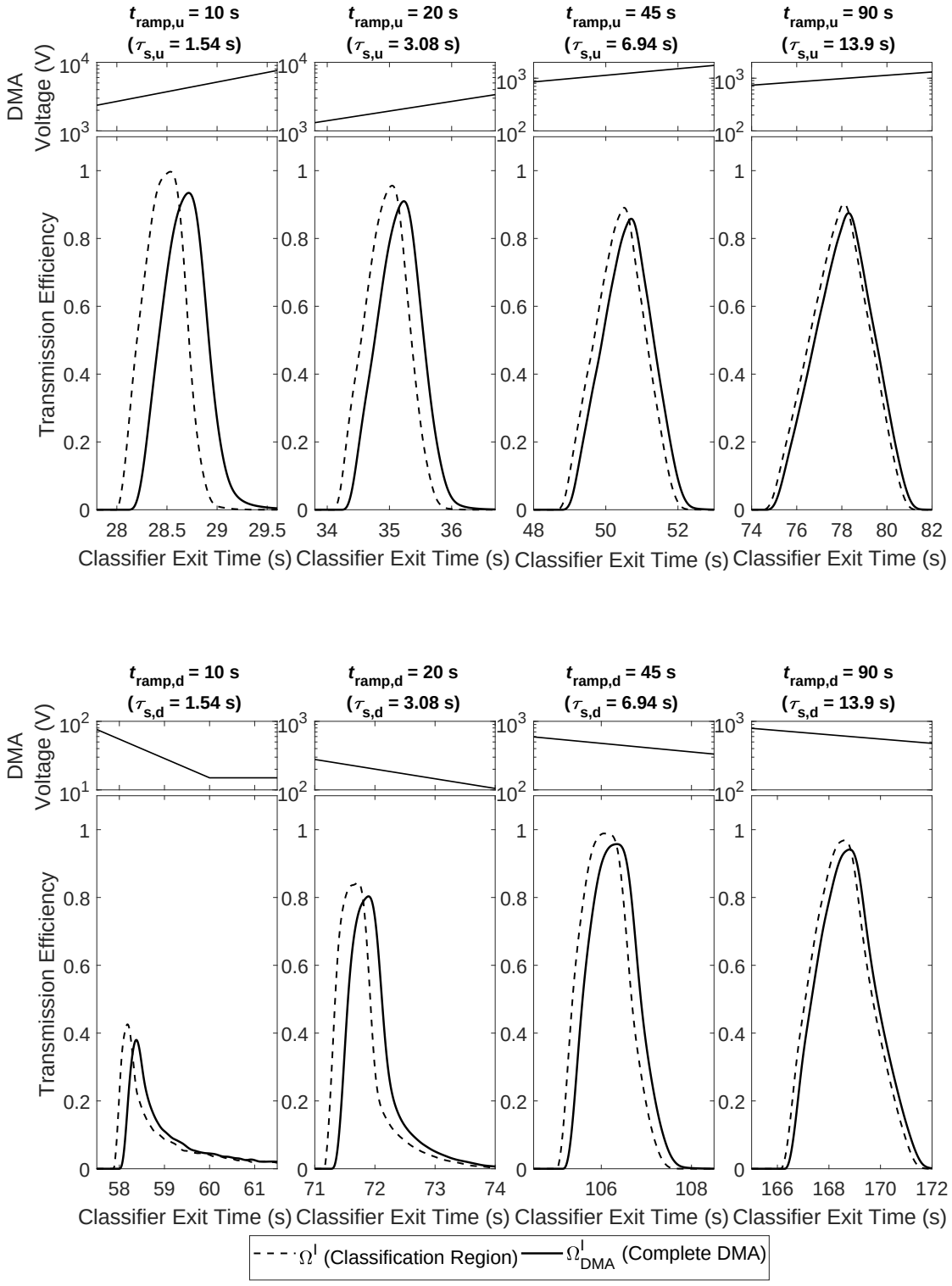

Figure 2.13: Transfer functions of the classification region and that of the complete DMA (including entrance and exit regions) for up-scan (upper panel) and down-scan (lower panel) operation for t_{ramp} = 10, 20, 45, 90 s (corresponding to τ_s = 1.54, 3.08, 6.94, 13.87 s).

References

Chen, D-R et al. (1998). "Design and evaluation of a nanometer aerosol differential mobility analyzer (Nano-DMA)". In: *Journal of Aerosol Science* 29.5, pp. 497–509.

Chen, Da-Ren, David Y H Pui, et al. (1999). "Design and Testing of an Aerosol/Sheath Inlet for High Resolution Measurements with a DMA". In: *Journal of Aerosol Science* 30.8, pp. 983–999.

Chen, Da-Ren and David YH Pui (1997). "Numerical modeling of the performance of differential mobility analyzers for nanometer aerosol measurements". In: *Journal of Aerosol Science* 28.6, pp. 985–1004.

Cleveland, William S (1979). "Robust locally weighted regression and smoothing scatterplots". In: *Journal of the American Statistical Association* 74.368, pp. 829–836.

Collins, Don R., David R. Cocker, et al. (2004). "The Scanning DMA Transfer Function". In: *Aerosol Science and Technology* 38.8, pp. 833–850.

Collins, Don R., Richard C. Flagan, and John H. Seinfeld (2002). "Improved Inversion of Scanning DMA Data". In: *Aerosol Science and Technology* 36.1, pp. 1–9.

Dubey, Praney and Suresh Dhaniyala (2008). "Analysis of scanning DMA transfer functions". In: *Aerosol Science and Technology* 42.7, pp. 544–555.

– (2011). "A New Approach to Calculate Diffusional Transfer Functions of Scanning DMAs". In: *Aerosol Science and Technology* 45.8, pp. 1031–1040. eprint: `http://dx.doi.org/10.1080/02786826.2011.579644`.

Fissan, HJ, Ch Helsper, and HJ Thielen (1983). "Determination of particle size distributions by means of an electrostatic classifier". In: *Journal of Aerosol Science* 14.3, pp. 354–357.

Knutson, E. O. and K. T. Whitby (1975). "Aerosol classification by electric mobility: apparatus, theory, and applications". In: *Journal of Aerosol Science* 6.6, pp. 443–451.

Kousaka, Yysuo et al. (1986). "Effect of Brownian Diffusion on Electrical Classification of Ultrafine Aerosol Particles in Differential Mobility Analyzer". In: *Journal of Chemical Engineering of Japan* 19.5, pp. 401–407.

Mai, Huajun, Weimeng Kong, John H. Seinfeld, and Richard C. Flagan (In review). "Scanning DMA data analysis. II. Integrated DMA-CPC instrument response and data inversion". In: *Aerosol Science and Technology*.

Mamakos, Athanasios, Leonidas Ntziachristos, and Zissis Samaras (2008). "Differential mobility analyser transfer functions in scanning mode". In: *Journal of Aerosol Science* 39.3, pp. 227–243.

Mui, Wilton et al. (2017). "Design, simulation, and characterization of a radial opposed migration ion and aerosol classifier (ROMIAC)". In: *Aerosol Science and Technology* 51.7, pp. 801–823.

Russell, Lynn M., Richard C. Flagan, and John H. Seinfeld (1995). "Asymmetric Instrument Response Resulting from Mixing Effects in Accelerated DMA-CPC Measurements". In: *Aerosol Science and Technology* 23.4, pp. 491–509.

Stolzenburg, Mark Richard (1988). “An ultrafine aerosol size distribution measuring system”. In: *Ph. D. thesis, Univ. Minnesota*.

Ten Brink, HM et al. (1983). “A high-resolution electrical mobility aerosol spectrometer (MAS)”. In: *Journal of Aerosol Science* 14.5, pp. 589–597.

Wang, Shih Chen and Richard C. Flagan (1990). “Scanning Electrical Mobility Spectrometer”. In: *Aerosol Science and Technology* 13.2, pp. 230–240.

Zhang, Shou-Hua and Richard C. Flagan (1996). “Resolution of the radial differential mobility analyzer for ultrafine particles”. In: *Journal of Aerosol Science* 27.8, pp. 1179–1200.

SCANNING DMA DATA ANALYSIS II. INTEGRATED DMA-CPC INSTRUMENT RESPONSE AND DATA INVERSION

By Huajun Mai, Weimeng Kong, John H. Seinfeld, and Richard C. Flagan

This Chapter is submitted to, and is currently under review by, *Aerosol Science and Technology* as:

Mai, Huajun, Weimeng Kong, John H. Seinfeld, and Richard C. Flagan (In review). "Scanning DMA data analysis. II. Integrated DMA-CPC instrument response and data inversion". In: *Aerosol Science and Technology*.

3.1 Abstract

Analysis of scanning electrical mobility spectrometer (SEMS) or SMPS data requires coupling to the scanning differential mobility analyzer (DMA) transfer function with the response functions for the instrument plumbing and the detector. In the limit of plug flow (uniform velocity) within the DMA, the scanning DMA transfer function is the same as that for constant voltage operation, evaluated at the mean voltage experienced by a particle during its transit through the classification region, a result that is used in most SEMS/SMPS data analysis, though previous studies have shown that, even for highly idealized DMA models, boundary layers distort the transfer function during scanning DMA measurements. Part I determined the instantaneous transfer function during scanning of the TSI Model 3081A long column DMA by modeling the flows, fields, and particle trajectories within the actual DMA geometry. This study combines that transfer function with empirical data on the efficiencies and delay time distributions of the plumbing and detector of the SEMS/SMPS to determine the instantaneous rate at which particles are counted, and integrates the count rate over the finite counting time interval to obtain the integrated SEMS/SMPS response function. The results using the geometrical model of the DMA are compared with those obtained using traditional, idealized DMA models for scan rates ranging from slow (240 s) to very fast (10 s), and with measurements of monodisperse calibration aerosols. Data inversion studies show that both up- and down-scan data can be used to determine the particle size distribution, even with fast scans.

3.2 Introduction

Measurement of particle size distributions using the differential mobility analyzer (DMA) requires knowledge of the particle behavior within the charge conditioner, DMA, particle detector, and all plumbing in between. When measurements are made in a series of constant voltage steps, as in the differential mobility particle sizer (DMPS), these components can be treated separately because the measurement is made with each component operating at steady-state. The acquired data are particle counts, $R_{i,\mathrm{DMPS}}$, measured in a finite counting time, t_c, at each of the voltage settings, V_i. For an incoming aerosol sample flow rate, Q_a, and a steady particle size distribution, $n(\log D_\mathrm{p}) \neq \mathrm{fcn}(t)$, the counts acquired using a CPC detector are

$$\begin{aligned} R_{i,\,\mathrm{DMPS}} &= Q_\mathrm{a} t_\mathrm{c} \int_{-\infty}^{\infty} n(\log D_\mathrm{p}) \sum_{\phi} \Omega(Z_\mathrm{p}(D_\mathrm{p},\phi), Z_\mathrm{p}^*(V_i), \beta, \delta) p_\mathrm{charge}(D_\mathrm{p},\phi) \\ &\times \eta_\mathrm{ent}(D_\mathrm{p},\phi)\eta_\mathrm{exit}(D_\mathrm{p},\phi)\eta_\mathrm{F}(D_\mathrm{p},\phi)\eta_\mathrm{CPC}(D_\mathrm{p},\phi)\mathrm{d}\log D_\mathrm{p}, \quad i = 1, 2, \ldots, I, \end{aligned} \tag{3.1}$$

where the so called *transfer function* of the DMA, $\Omega(Z_\mathrm{p}(D_\mathrm{p},\phi), Z_\mathrm{p}^*(V_i), \beta, \delta)$, is the probability that a particle of diameter, D_p, that carries ϕ elementary charges, and, hence, has mobility Z_p, will be transmitted through the classification region of the DMA operated at voltage V_i. If the incoming aerosol sample flow, Q_a, and outgoing classified sample flow, Q_c, are balanced, *i.e.*, $Q_\mathrm{a} = Q_\mathrm{c}$, the peak in the transmission efficiency occurs at the mobility of a particle that is transmitted from the centroid of the incoming aerosol flow, to the centroid of the classified aerosol outlet flow. Knutson and Whitby (1975) showed this centroid mobility for nondiffusive particles to be $Z_\mathrm{p}^*(V_i) = \frac{Q_\mathrm{sh}+Q_\mathrm{ex}}{4\pi L V_i}$; Q_sh and Q_ex denote the sheath and exhaust flow rates through the DMA, respectively, and L is the length of the classification region. The transfer function also depends on the flow rate ratios, $\beta = \frac{Q_\mathrm{c}+Q_\mathrm{a}}{Q_\mathrm{sh}+Q_\mathrm{ex}}$, and $\delta = \frac{Q_\mathrm{c}-Q_\mathrm{a}}{Q_\mathrm{c}+Q_\mathrm{a}}$. Stolzenburg (1988) derived an elegant expression for the transfer function that includes the effects of Brownian diffusion on the steady-state transmission efficiency through the classification region of the constant-voltage DMA. This transfer function forms the basis for DMPS data inversion to find $n(\log D_\mathrm{p})$ from the set of measured counts, $R_{i,\mathrm{DMPS}}$.

The counts recorded also depend on the efficiency of particle transmission through the entrance and exit regions of the DMA, $\eta_\mathrm{ent}(D_\mathrm{p},\phi)$ and $\eta_\mathrm{exit}(D_\mathrm{p},\phi)$, respectively, that of the flow passages upstream and downstream of the DMA (including the charge conditioner), $\eta_\mathrm{F}(D_\mathrm{p})$, the counting efficiency of the CPC, $\eta_\mathrm{CPC}(D_\mathrm{p},\phi)$, and the probability that a particle will acquire ϕ elementary charges, $p_\mathrm{charge}(D_\mathrm{p},\phi)$. The transmission efficiencies may depend on charge state because the aerosol must pass through a transition between the high voltage used in the classification and ground somewhere in the system; for the most common DMAs, that transition occurs within the exit flow passages of the DMA though some DMAs have that transition at their entrances. Charge may also affect the detection efficiency of the CPC due to its influence on particle activation.

A key challenge in measuring particle size distributions by stepping the voltage is the long time that one must wait after stepping the voltage to allow steady-state to be achieved, thereby slowing the acquisition of the particle size distribution. Scanning the differential mobility analyzer voltage eliminates those delays, enabling rapid particle size distribution measurements (Wang and Flagan, 1990). In the limit of plug flow (uniform velocity) between the classification electrodes, this scanning electrical mobility spectrometer (SEMS; also known as the the scanning mobility particle sizer, SMPS) yields the same nondiffusive transfer function as the DMPS. However, the transfer function must be evaluated at the mean field strength (voltage) experienced by a particle during its transit through the classification region of the DMA. The authors have encountered situations in which the transfer function was evaluated at the voltage corresponding to the time at which a particle exits the DMA rather than at the mean voltage. Because this closely parallels the DMPS analysis, we label this erroneous estimation the *static* transfer function; results for this evaluation will be shown to illustrate the large bias that it introduces. We also note that, due to viscous flow, the plug-flow limit can only be approximated at very high Reynolds numbers.

In the first field deployment of the SEMS, Russell, Flagan, and John H. Seinfeld (1995) observed an asymmetric response between scans in which the voltage was increased in an exponential ramp (up-scan) and those in which the voltage was exponentially decreased (down-scan); this distortion was attributed to the relatively slow response of the CPC that was used to detect the transmitted particles. Mixing within the CPC leads to a distribution of residence times that cause particle counts to be spread over many later time bins than that in which they would have been detected with an ideal, fast-response detector. The mathematical model of the system response developed in that study was quite complex; Collins, Flagan, and John H. Seinfeld (2002) later developed a much simpler deconvolution algorithm to attribute the particle counts to the proper counting-time bins. Treatment of the effects of slow detector response on the size distributions inferred from SEMS data improved the ability of the instrument to make quantitative measurements.

Most SEMS/SMPS data analysis follows the original Wang and Flagan (1990) approach, though some researchers do account for the CPC time response using the method of Collins, Flagan, and John H. Seinfeld (2002). As will be shown below, this approach is reasonable for sufficiently slow scans in which the voltage changes little during a particle's transit through the DMA. Unfortunately, correction for the slow detector response fails to capture all of the differences between the SEMS or SMPS and the DMPS. Using Brownian dynamics simulations, Collins, Cocker, et al. (2004) demonstrated that the presence of boundary layers within the classification region alters the trajectories and time required for a particle to traverse the length of the classifier. An analytical solution for the nondiffusive transfer function has been derived to describe scanning of a cylindrical

DMA(Mamakos, Ntziachristos, and Samaras, 2008; Dubey and Dhaniyala, 2008) iin the limit of the idealized, laminar, parallel-flow cylindrical DMA (PFDMA-L); the influence of particle diffusion in this model was later simulated using Brownian dynamics (Dubey and Dhaniyala, 2011) .

More recently in Part I of this two-part series of papers, Mai and Flagan (In review) used finite element simulations to capture the details of the flows and electric field within a real, cylindrical DMA (the TSI Model 3081 long column DMA). These fields were combined with Brownian dynamics simulations of diffusive particle transport through the scanning DMA. They found it necessary to extend the classification region model to include portions of the inlet and exit regions of the DMA in the numerical evaluation of the transfer function because laminar flow within the narrow aerosol inlet annulus of the TSI DMA alters the velocity distribution at the entrance to the classification region, and, thereby, some particle trajectories. The flow fields within the DMA are sufficiently complex that particles of a given mobility that enter the classification region at different times can exit a voltage-scanning DMA at the same time. In addition, the exit region introduces a range of delays between the time that a particle exits the space between the electrodes and their exit from the DMA. Hence, the transfer function for the SEMS can no longer be considered to be the probability of transmission; indeed, under some circumstances Ω^{I}_{DMA} can exceed unity. Because the field strength changes continuously throughout the voltage scan, the transfer function must be viewed as an instantaneous transfer function, which we denote below with the superscript "I".

The scanning DMA transfer function is just the starting point for describing the SEMS/SMPS, or for the analyzing data produced by these instruments. In this paper, we develop the integrated system response function and the corresponding data inversion methodology for scanning DMA measurements in the context of measurements made using the TSI Model 3081A long-column DMA with a TSI Model 3010 CPC used as the detector. The specific operating parameters considered are those employed in measurement of secondary organic aerosol yields in chamber studies at Caltech, which, because aerosol yield is a measure of mass conversion, focuses on large particles. An observed tail of the up-scan (increasing voltage) transfer function toward large particles introduces uncertainities in yield estimates that have prompted our reanalysis of the instrument response function. Nonetheless, the methodology described below is applicable to other mobility classifiers and detectors, and to measurements in other size ranges, but consideration all possible operating parameters is beyond the scope of this study. To determine the response function of the integrated measurement system, the instantaneous DMA transfer function must be known; Mai and Flagan (In review) have determined it for the particular operating conditions that we examine here. Upstream plumbing and components such as the charge conditioner also affect the ultimate detection efficiency due to losses and the charge distribution attained. All of these factors need to be integrated into the

instrument response kernel to enable data inversion for particle size distribution determination.

3.3 Methods

Instantaneous and integrated SEMS transfer functions

A particle's size and charge determine its electrical mobility, Z_p, and Brownian diffusivity, $\mathcal{D} = \frac{Z_p kT}{\phi e}$, where k, T, and e are the Boltzmann constant, temperature, and elementary unit of charge, respectively. Thus, the mobility and charge provide the information required to describe its behavior in the DMA. Assuming that the particle size distribution is steady, the instantaneous transfer function of the scanning DMA can be defined as

$$\Omega^{I}_{DMA}(Z_p(u,\phi),\beta,\delta,t_e) = \frac{n_{DMA,exit}(u,t_e)}{n(u)} \tag{3.2}$$

where $u = \log D_p$, and $t_e = t - t_0$ denotes the time-in-scan, *i.e.*, the difference between the time at which the particle exits the DMA and the time at which the measurement cycle started, t_0. Because the voltage changes continuously with time, t_e is related to the mobility of the particles that are optimally transmitted through the voltage program $V(t)$. Particle losses, as well as any delays in the transit of particles from the entrance to the exit of the classifier have also been incorporated into the instantaneous scanning transfer function of the DMA because they are affected by the voltage scan. These intra-DMA delays add to the signal smearing due to the CPC and other downstream components, and have not been considered in previous studies.

Mai and Flagan (In review) used Brownian dynamics simulations to find the instantaneous transfer functions for two DMA models: (i) the idealized laminar PFDMA in which the flow is described by the analytical solution for fully developed laminar flow between coaxial cylinders, leading to transfer function, $\Omega^{I,L}_{DMA}$; and (ii) real flow fields derived from finite element simulations of the actual geometry of the specific DMA being studied (G-DMA), the TSI Model 3081 long-column DMA, $\Omega^{I,G}_{DMA}$. Losses and time delays in the entrance and exit regions of the DMA are incorporated into $\Omega^{I,G}_{DMA}$, as are losses to the walls of the classification region. To fully capture the effects of the real geometry, the classification region was extended beyond the space between the electrodes to include portions of the entrance and exit regions of the DMA that influence classification(Mai and Flagan, In review).

The original paper on the SEMS (Wang and Flagan, 1990) considered an even simpler idealized, parallel-flow model, *i.e.*, one with uniform velocity (plug flow) for which the nondiffusive transfer function for plug-flow within the SEMS, $\Omega^{I,P}_{DMA}$ reduces to that derived by Knutson and Whitby (1975) for the DMPS; particle diffusion can be included by replacing the nondiffusive transfer function with the diffusive one (Stolzenburg, 1988), provided it is applied at the mean voltage that a

particle experiences during its transit through the classification region, making Brownian dynamics simulations unnecessary for plug flow (Mai and Flagan, In review). Rather than evaluate the mean voltage, it may tempting simplify this model by relating the mobility to the voltage at the instant of time when a particle is detected, but this introduces an additional large bias as will be shown below.

Combined Condensation Particle Counter and Plumbing Time Response

Previous studies used a continuously-stirred-tank-reactor (CSTR) model to describe the distribution of delay times within the CPC (Russell, Flagan, and John H. Seinfeld, 1995; Collins, Flagan, and John H. Seinfeld, 2002). This model predicts that the probability that a particle that enters the CSTR at time t_0 will remain within the CSTR at time t is

$$E(t) = \tau_{\mathrm{CPC}}^{-1} e^{-\frac{t-t_0}{\tau_{\mathrm{CPC}}}}. \tag{3.3}$$

Thus, for a step change in concentration from N_0 to N_1, a plot of $\ln \frac{N(t)-N_0}{N_1-N_0}$ versus time, t, is a straight line with slope τ_{CPC}^{-1}, where τ_{CPC} the mean residence time within the mixed region of the flow, *i.e.*, within the CSTR. The integrated SEMS/SMPS also exhibits size-dependent (and, possibly, charge dependent) counting and transmission efficiencies, $\eta_{\mathrm{CPC}}(u, \phi)$. Thus, the overall CPC response to particles that enter at time t_0 is $E(t - t_0)\eta_{\mathrm{CPC}}(u, \phi)$. The plumbing between the DMA outlet and the CPC inlet introduces additional delays and efficiency factors that may also depend upon charge.

The time response of a component in the SEMS measurement system can be directly measured by subjecting it to a transient source, either a step change in concentration produced by switching the flow between a particle-free one and one containing particles (Quant, 1992; Hering et al., 2005), or by producing a pulse of particles by, for example, generating a weak spark that will ablate some electrode material and nucleate fine particles in the flow (Wang et al., 2002). The latter approach minimizes perturbations to the flow, so we have employed it to measure the time response of the components downstream of the DMA outlet in our SEMS instrument, including the plumbing that connects the DMA outlet to the inlet of a TSI 3010 CPC. A computer-triggered spark-source was installed at the entrance of that plumbing (see Fig. 3.1). The detector was operated at the same flow rate, and saturator and condenser temperatures used in SEMS measurements of particle size distributions. LabView$^{\mathrm{TM}}$ software was used to control the spark and record particle counts into 0.1 s time bins. The size-dependent detection efficiency of this system was calibrated against a recently calibrated TSI 3010 CPC.

Integrated system transfer function for the SEMS

Combining the instantaneous transfer function for the scanning DMA with the response functions for the downstream components provides the information needed to describe the integrated system.

In the SEMS/SMPS, counts are acquired in successive time bins of duration t_c, but without the intervening delay between counting intervals that is required to attain steady-state in DMPS measurements. To understand the integrated system performance, the voltage program that comprises a scan must first be defined.

The time bins are defined from the start of the voltage measurement cycle, which begins at global time $T = T_\nu$ for the ν^{th} scan. The time-in-scan, t, is defined such that $t = T - T_\nu$. Initially, the voltage is held constant at the minimum voltage of the measurement cycle, V_{low} (which may be either positive or negative, depending on the polarity of the particles being classified), for time t_{low} to ensure that no particles from the previous scan remain in the classification region to be included in the counts for scan ν. The voltage is then ramped exponentially to the maximum (positive or negative) voltage, V_{high}, in time $t_{\text{ramp,u}}$, held constant at V_{high} to ensure that all particles that entered the classification region during the up-ramp are counted, and then ramped exponentially back to V_{low} in time $t_{\text{ramp,d}}$.

The applied voltage cycle is, thus,

$$V(t) = \begin{cases} V_{\text{low}}, & 0 \le t < t_{\text{low}} \\ V_{\text{low}} e^{\frac{t - t_{\text{low}}}{\tau_{\text{s, u}}}}, & t_{\text{low}} \le t < t_{\text{low}} + t_{\text{s, u}} \\ V_{\text{high}}, & t_{\text{low}} + t_{\text{ramp,u}} \le t < t_{\text{low}} + t_{\text{ramp,u}} + t_{\text{high}} \\ V_{\text{high}} e^{-\frac{t - t_{\text{low}} - t_{\text{ramp,u}} - t_{\text{high}}}{\tau_{\text{s, d}}}}, & t_{\text{low}} + t_{\text{ramp,u}} + t_{\text{high}} \le t < t_{\text{low}} + t_{\text{ramp,u}} + t_{\text{high}} + t_{\text{ramp,d}}. \end{cases} \tag{3.4}$$

The exponential ramp time constant, $\tau_{\text{s, u/d}}$, is given by $\tau_{\text{s, u/d}} = \frac{t_{\text{ramp, u/d}}}{\ln \frac{V_{\text{high}}}{V_{\text{low}}}}$. The total measurement cycle time, or scan time, is

$$t_{\text{scan}} = t_{\text{low}} + t_{\text{ramp,u}} + t_{\text{low}} + t_{\text{ramp,d}} \tag{3.5}$$

and $T_{\nu+1} = T_\nu + t_{\text{scan}}$. Owing to the asymmetry in the signals measured in the down-scan as compared to the up-scan, many users do not use results obtained from the down-scan and, therefore, make $t_{\text{ramp,d}}$ as short as possible. For convenience in data acquisition and control, the different process times, t_{low}, etc., are usually specified as integer multiples of the detector counting time, t_c.

The rate at which particles of log-mobility u are counted into a SEMS time bin results from a convolution of the rate at which particles that exit the classifier at all earlier times with the downstream delay time distribution function, assuming a quasi-steady-state size distribution,

$$\begin{aligned} \dot{R}(t) &= Q_a n(u) \sum_\phi p_{\text{charge}}(u, \phi) \eta_F(u, \phi) \eta_{\text{CPC}}(u, \phi) \\ &\times \Omega^I_{\text{DMA}}(Z_p(u, \phi), \beta, \delta, t) \star E(t), \end{aligned} \tag{3.6}$$

where $\star$ denotes the convolution operator which is defined such that

$$f(t) \star g(t) = \int_{-\infty}^{\infty} f(t')g(t-t')\mathrm{d}t'. \tag{3.7}$$

The convolution forms the instantaneous transfer function for the SEMS, *i.e.*,

$$\Omega^{\mathrm{I}}_{\mathrm{SEMS}}(Z_{\mathrm{p}}(u,\phi),\beta,\delta,t) = \Omega^{\mathrm{I}}_{\mathrm{DMA}}(Z_{\mathrm{p}}(u,\phi),\beta,\delta,t) \star E(t). \tag{3.8}$$

The total number of particles recorded in time bin i, i.e., in the time interval $(i-1)t_{\mathrm{c}} \leq t_{\mathrm{c}} < it_{\mathrm{c}}$, is obtained by integrating the particles transmitted at any instant of time over the counting-time interval, t_{c}, *i.e.*,

$$\begin{aligned} R_{i,\mathrm{SEMS}} &= Q_{\mathrm{a}} \int_{(i-1)t_{\mathrm{c}}}^{it_{\mathrm{c}}} \int_{-\infty}^{\infty} n(u) \sum_{\phi} p_{\mathrm{charge}}(u,\phi)\eta_{\mathrm{F}}(u,\phi)\eta_{\mathrm{CPC}}(u,\phi) \\ &\times \Omega^{\mathrm{I}}_{\mathrm{SEMS}}(Z_{\mathrm{p}}(u,\phi),\beta,\delta,t)\mathrm{d}u\mathrm{d}t. \end{aligned} \tag{3.9}$$

For a steady size distribution, only the instantaneous system transfer function depends upon time. Hence, a cumulative, integrated system transfer function can be defined as

$$\Gamma_{\mathrm{SEMS}}(Z_{\mathrm{p}}(u,\phi),\beta,\delta,t) = \int_{-\infty}^{t} \Omega^{\mathrm{I}}_{\mathrm{SEMS}}(Z_{\mathrm{p}}(u,\phi),\beta,\delta,t)\mathrm{d}t. \tag{3.10}$$

If t_{low} is sufficiently long for all particles that entered the DMA during previous scans to be cleared from the measurement system before the start of the voltage up-ramp, the lower bound on the integral can be taken to be $t = 0$. Substituting Eq. (3.9) into Eq. (3.10) yields

$$\begin{aligned} R_{i,\mathrm{SEMS}} &= Q_{\mathrm{a}} \int_{-\infty}^{\infty} n(u) \sum_{\phi} p_{\mathrm{charge}}(u,\phi)\eta_{\mathrm{F}}(u,\phi)\eta_{\mathrm{CPC}}(u,\phi) \\ &\times \left[\Gamma_{\mathrm{SEMS}}(Z_{\mathrm{p}}(u,\phi),\beta,\delta,it_{\mathrm{c}}) - \Gamma_{\mathrm{SEMS}}(Z_{\mathrm{p}}(u,\phi),\beta,\delta,(i-1)t_{\mathrm{c}})\right] \mathrm{d}u. \end{aligned} \tag{3.11}$$

Note that, because of the varying delays that different particles may experience, the counting bins are not synchronized with particular voltages in the measurement cycle, *i.e.*, the voltage at the instant at which a particle is counted is not simply related to its size.

Grouping all factors other than the size distribution into the kernel function, i.e.,

$$\begin{aligned} h_i(u) &= Q_{\mathrm{a}} \sum_{\phi} p_{\mathrm{charge}}(u,\phi)\eta_{\mathrm{F}}(u,\phi)\eta_{\mathrm{CPC}}(u,\phi) \\ &\times \left[\Gamma_{\mathrm{SEMS}}(Z_{\mathrm{p}}(u,\phi),\beta,\delta,it_{\mathrm{c}}) - \Gamma_{\mathrm{SEMS}}(Z_{\mathrm{p}}(u,\phi),\beta,\delta,(i-1)t_{\mathrm{c}})\right], \end{aligned} \tag{3.12}$$

the particle count becomes

$$R_{i,\mathrm{SEMS}} = \int_{-\infty}^{\infty} h_i(u) n(u) \mathrm{d}u. \tag{3.13}$$

We seek to determine the particle size distribution, $n(u) = n(\log D_\mathrm{p})$ from the counts recorded in the various time bins throughout the voltage scan, *i.e.*, from the signals $R_{i,\,\mathrm{SEMS}}$, $i = 1, 2, \cdots, I$. To do this, we need to discretize the particle size distribution, $n(u) = \frac{\mathrm{d}N}{\mathrm{d}u}$, where N denotes the total number concentration of particles of all sizes. Numerous representations of the particle size distribution have been employed in previous studies, including: (*i*) modal models in which $n(\log D_\mathrm{p})$ is described by a collection of log-normal modes, (*ii*) so-called nodal representations in which the size distribution is approximated by delta-functions at a set of J discrete sizes, (*iii*) sectional models (histograms), in which the size distribution is assumed to be constant within each size interval between discretization points, and (*iv*) linear-splines. As noted by Wolfenbarger and John H Seinfeld (1990), other basis functions such as cubic splines might be more realistic, but would introduce the need for nonlinear constraints to ensure non-negative size distributions, whereas linear splines require only linear constraints to obtain realistic results. For the nodal and sectional models, the size distribution can be taken outside the integral. On the other hand, modal or linear spline models require integration over the functional form of the discretized size distribution.

As the linear spline model allows good fidelity with the actual size distribution without imposing an arbitrary shape to the particle size distribution, we employ the linear-spline representation on discretization points $u_j^\dagger$, $j = 1, 2, \cdots, J$. The particle size distribution thus becomes

$$n(u) = n(u_j^\dagger) + \frac{n(u_{j+1}^\dagger) - n(u_j^\dagger)}{u_{j+1}^\dagger - u_j^\dagger}\left(u - u_j^\dagger\right) = n(u_j^\dagger)\frac{u_{j+1}^\dagger - u}{u_{j+1}^\dagger - u_j^\dagger} + n(u_{j+1}^\dagger)\frac{u - u_j^\dagger}{u_{j+1}^\dagger - u_j^\dagger}. \tag{3.14}$$

To improve accuracy, we discretize the integral in Eq. (3.13) over finer grid $u_k, k = 1, 2, \cdots, K$ than that used for the size distribution. The increment in particle size may be abbreviated as $\Delta u_k = u_{k+1} - u_k$. Using the linear-spline representation of the size distribution, and carrying out the integration over u using the trapezoidal rule over the integration diameter space, Equation (3.13) thus becomes

$$R_{i,\mathrm{SEMS}} = \sum_{k=1}^{K} \Delta u_k h_i(u_k) n(u_k), \tag{3.15}$$

where

$$\Delta u_k = \begin{cases} \dfrac{u_2 - u_1}{2}, & k = 1 \\ \dfrac{u_{k+1} - u_{k-1}}{2}, & k = 2, 3, \cdots, K-1 \\ \dfrac{u_K - u_{K-1}}{2}, & k = K \end{cases} \tag{3.16}$$

is the weighting factor arising from the trapezoidal integral. The instrument response as a function of size distribution thus becomes (See Supplementary Information for derivation)

$$R_{i,\,\mathrm{SEMS}} = \sum_{k=1}^{K} \Delta u_k \left[n(u_j^\dagger) \frac{u_{j+1}^\dagger - u_k}{u_{j+1}^\dagger - u_j^\dagger} + n(u_{j+1}^\dagger) \frac{u_k - u_j^\dagger}{u_{j+1}^\dagger - u_j^\dagger} \right] h_i(u_k), u_k \in [u_j^\dagger, \quad u_{j+1}^\dagger). \tag{3.17}$$

To determine the values of the size distribution at the discretization points, $u_j^\dagger$, we must solve the system of equations

$$R_{i,\mathrm{SEMS}} = \sum_{j=1}^{J} A_{i,j} n(u_j^\dagger), \qquad i = 1, 2, \cdots, I \tag{3.18}$$

where the kernel function $A_{i,j}$ is defined as

$$A_{i,j} = \sum_{u_k \geq u_{j-1}^\dagger}^{u_k < u_j^\dagger} \Delta u_k \frac{u_k - u_{j-1}^\dagger}{u_j^\dagger - u_{j-1}^\dagger} h_i(u_k) + \sum_{u_k \geq u_j^\dagger}^{u_k < u_{j+1}^\dagger} \Delta u_k \frac{u_{j+1}^\dagger - u_k}{u_{j+1}^\dagger - u_j^\dagger} h_i(u_k). \tag{3.19}$$

Thus, we seek to solve $\mathbf{R} = \mathbf{AN}$ for the values of the size distribution parameters $\mathbf{N} = [n(u_1^\dagger), n(u_2^\dagger), \cdots, n(u_J^\dagger)]$; $\mathbf{R}$ is the array of the count data, $R_i, \quad i = 1, 2, \ldots, I$. We employ a non-negative least squares algorithm (Merritt and Zhang, 2005), and compare results obtained using the DMA transfer functions obtained with three DMA models: (i) the geometric model (G-DMA) that is based upon the real instrument design (TSI Model 3081A long-column DMA, with instantaneous transfer function $\Omega_{\mathrm{DMA}}^{\mathrm{I,G}}$), (ii) the laminar, parallel-flow DMA model (transfer function: $\Omega_{\mathrm{DMA}}^{\mathrm{I,\,L}}$), and (iii) the uniform velocity (plug flow) model using the Stolzenburg (1988) transfer function evaluated at the mean voltage experienced by a particle during its passage through the classification region (transfer function: $\Omega_{\mathrm{DMA}}^{\mathrm{I,\,P}}$). One additional model is presented since a natural misinterpretation of SEMS/SMPS performance is to consider the classification voltage to be that at the instant when the particle leave the classifier; we have labeled this model the static-DMA transfer function, and evaluated it by applying the diffusional transfer function (Stolzenburg, 1988). Plumbing delays downstream of the DMA could further aggravate the biases associated with this misinterpretation of the scanning DMA method.

Experimental validation of integral intrument response function

Figure 3.2 illustrates the experimental system that was used to validate the integral instrument response function. Polystyrene latex (PSL) calibration particles were nebulized, neutralized using a TSI 3077 Kr-85 charge conditioner, and then classified using a TSI 3081A DMA (DMA_1) that was operated at constant voltage to produce a monodisperse calibration aerosol. The particle number

concentration downstream of DMA_1 was monitored with a TSI 3760 CPC (CPC_1), operated at a sample flow rate of 1.51 LPM (liters per minute). DMA_1 was operated with equal aerosol and classified sample flow rates (*i.e.*, balanced flows) of 1 LPM, and sheath and exhaust flow rates of 5 LPM. The voltage of DMA_1 was set to maximize the particle concentration. The classified PSL particles were subjected to bipolar diffusion charging using a home-made soft-X-ray charge conditioner, and then analyzed using a SEMS/SMPS system consisting of a TSI 3081A DMA (DMA_2) with a TSI 3010 CPC detector (CPC_2; sample flow rate 0.975 LPM); the operating parameters for these measurements are summarized in Table 3.1. The counting time for CPC_2 was $t_c = 0.5$ s, while the reference CPC (CPC_1) recorded the particle concentration at 1 s intervals. Prior to these measurements, the counting efficiencies of the two CPCs were compared and tuned to ensure consistent concentration measurements.

3.4 Results

CPC response time distribution

Figure 3.3 shows the measured response time distributions from 600 spark-pulse events, with cumulative counts exceeding 10^5. The CPC sample flow was 0.975 LPM, leading to an estimated mean residence time of particles in the downstream plumbing and CPC of 2.36 s. The time-response data were fitted to two different models that are described below. In each case, the fits were weighted according to the Poisson statistics based on the counts recorded in each time bin, i, such that $\sigma_i^2 = c_i$, where c_i is the number of counts in time bin i. Following Russell, Flagan, and John H. Seinfeld (1995), the first model treats the CPC response as a plug flow reactor (PFR) in series with a continuous stirred-tank reactor (CSTR). The residence time distribution for a plug-flow reactor is $E_p(t) = \delta(t - \tau_p)$, where $\delta(x)$ is the Dirac delta function that equals zero for all values of x other than zero, and $\int_{-\infty}^{\infty} \delta(x)\mathrm{d}x = 1$; τ_p is the mean residence time in the PFR. The CSTR has a delay time distribution of $E_c(t) = \frac{1}{\tau_c} e^{-\frac{t}{\tau_c}}$, where τ_c is the mean delay time in the CSTR. The delay time distribution of the combined system is the convolution of these two functions, *i.e.*, $E_{cp}(t) = E_c(t) \star E_p(t)$, which takes the form

$$E_{cp}(t) = E_p(t) \star E_c(t) = \int_{-\infty}^{\infty} E_c(t')E_p(t - t')\mathrm{d}t' = \begin{cases} 0, & t < \tau_p \\ \frac{1}{\tau_c} e^{-\frac{t-\tau_p}{\tau_c}}, & t \geq \tau_p. \end{cases} \tag{3.20}$$

Global optimization of the weighted least-squares fit between experimental data and $E_{cp}(t)$ yielded $\tau_c = 0.950 \pm 0.027$ s, and $\tau_p = 1.36 \pm 0.031$ s, though, as shown by the dashed line in Fig. 3.3, the PFR+CSTR model fails to capture the tail at long times.

The plumbing connections between the DMA and CPC, and parts of the flow within the CPC

employed in this study, can be described using a laminar-flow (LF) model, which has a residence time distribution of

$$E_{\mathrm{l}}(t) = \begin{cases} 0, & t < \frac{\tau_{\mathrm{l}}}{2} \\ \frac{\tau_{\mathrm{l}}^2}{2t^3}, & t \geq \frac{\tau_{\mathrm{l}}}{2}. \end{cases}$$

Passages within the CPC may add additional LF-like delay distributions. Adding a LF in series with the CSTR and PFR allows the model to capture the long-time tail of the response; the combined delay time distribution then becomes $E_{\mathrm{lcp}}(t) = E_{\mathrm{l}}(t) \star E_{\mathrm{c}}(t) \star E_{\mathrm{p}}(t)$, or

$$E_{\mathrm{lcp}}(t) = \begin{cases} 0, & t < \frac{\tau_{\mathrm{l}}}{2} + \tau_{\mathrm{p}} \\ \frac{\tau_{\mathrm{l}}^2 \exp\left(-\frac{t-\tau_{\mathrm{p}}}{\tau_{\mathrm{c}}}\right)\left[\mathrm{Ei}\left(\frac{t-\tau_{\mathrm{p}}}{\tau_{\mathrm{c}}}\right) - \mathrm{Ei}\left(\frac{\tau_{\mathrm{l}}}{2\tau_{\mathrm{c}}}\right)\right]}{4\tau_{\mathrm{c}}^3} & \\ \quad + \frac{4\left(t-\tau_{\mathrm{p}}\right)^2\left(\tau_{\mathrm{c}}+\frac{\tau_{\mathrm{l}}}{2}\right)\exp\left(-\frac{t-\tau_{\mathrm{p}}-\frac{\tau_{\mathrm{l}}}{2}}{\tau_{\mathrm{c}}}\right) - \tau_{\mathrm{l}}^2\left(t+\tau_{\mathrm{c}}-\tau_{\mathrm{p}}\right)}{4\tau_{\mathrm{c}}^2\left(t-\tau_{\mathrm{p}}\right)^2}, & t \geq \frac{\tau_{\mathrm{l}}}{2} + \tau_{\mathrm{p}} \end{cases} \tag{3.21}$$

where $\mathrm{Ei}(x) = \int_{-\infty}^{x} \frac{e^u}{u}\mathrm{d}u$ is the exponential integral. The time scales obtained by weighted fitting to the experimental data are $\tau_{\mathrm{l}} = 0.583 \pm 0.012$ s, $\tau_{\mathrm{c}} = 0.748 \pm 0.005$ s and $\tau_{\mathrm{p}} = 1.04 \pm 0.007$ s. This three-parameter delay time distribution captures the long-time tail in up-scan measurements, making it possible to properly attribute contributions of the tail of the response distribution to appropriate mobilities (or sizes) and, thereby, correct a potential overestimation of the aerosol mass that is very important to chamber measurements of aerosol yield.

Integrated SEMS response function

Substituting the CPC time response function, numerical result from direct measurement or empirical fit as shown in Eq. (5.3), into Eq. (3.8) yields the integrated SEMS system response function, $\Gamma_{\mathrm{SEMS}}\left(Z_{\mathrm{p}}(u,\phi),\beta,\delta,t\right)$. To examine how well the idealized laminar and plug-flow models, and the one based on the geometry of a real DMA, G-DMA, describe measurements, we seek to compare predicted particle counts for measurements of monodisperse PSL particles to experimental observations, using Eq. (3.11). The transmission efficiency of the flow system, $\eta_{\mathrm{F}}(D_{\mathrm{p}},\phi)$, remains unknown, however. The losses for which $\eta_{\mathrm{F}}(D_{\mathrm{p}},\phi)$ accounts are not directly associated with the scan, so they should not depend upon the scan rate. To enable comparison between models, we estimate this parameter by using it as the single parameter in fitting the time variation of ratio of the particle number concentration predicted for the G-DMA model to the particle number concentration that enters the DMA during a counting-time interval, *i.e.*, we find the value of $\eta_{\mathrm{F}}(D_{\mathrm{p}},\phi)$ for which $C_{\mathrm{CPC},2}/C_{\mathrm{CPC},1} \cong R_{i,\,\mathrm{SEMS}}/Q_{\mathrm{a}}t_{\mathrm{c}}N_{\mathrm{in}}$, where N_{in} is the number concentration of the monodisperse particles upstream of the SEMS system. The G-DMA model was selected for this fitting because, as will be shown below, it most closely approximates the observed time variation while other

models exhibit notable time shifts. The resulting concentration ratios are shown for both up-scans and down-scans and for a range of scan rates as discussed below.

Figure 3.4 compares measured and observed ratios for PSL particles of duration $10\,\mathrm{s} \le t_{\mathrm{ramp}} \le 90\,\mathrm{s}$ for 147 nm PSL particles. These correspond to exponential scan time constants τ_{s} ranging from 1.54 s to 13.9 s. The concentrations display two major peaks due to the presence of multiply-charged particles in the aerosol processed through the charge conditioner. The larger peak is associated with singly charged particles; the lower peak precedes it due to the higher mobility of the doubly charged ($\phi = 2$) particles. As the scan rate increases, peaks associated with particles of charge states $|\phi| > 1$ merge because resolution decreases due to the distribution of delays within components of the measurement system, particularly the CPC. The peak particle concentration ratio also decreases in the fast scan because the transmitted particles are redistributed among an increasing number of time bins. For example, the maximum concentration ratio for singly-charged 147 nm particles is 0.06 for $t_{\mathrm{ramp}} = 90$ s, but decreases to 0.03 for $t_{\mathrm{ramp}} = 10$ s. In short, fast scans come at a cost of reduced resolution and particle concentration ratio.

Using the charge distribution reported by Leppä et al. (2017) for $p_{\mathrm{charge}}(D_{\mathrm{p}}, \phi)$, each of the models predicts multiple peaks as observed experimentally, though the times at which they appear differ. For the slowest scan (90 s) the G-DMA model closely approximates the appearance time and magnitude of the experimentally observed count ratio for the singly charged peak; the $\phi = 2$ peak value is overestimated, suggesting that the charge distribution produced by the new soft x-ray charger used in these experiments may differ from that which we have assumed. The predictions of the G-DMA model capture the variation in the recorded signals for scans as short as 10 s, though the peaks are smeared poorly resolved for such fast scans.

The values of the particle-concentration ratios are low (< 0.1) due, in large part, to the charging probability that results from bipolar diffusion charging, though particle losses also contribute. The fitted values of $\eta_{\mathrm{F}}(D_{\mathrm{p}}, \phi)$, summarized in Table 3.2, include losses both in the plumbing upstream of the DMA classification region, and in the new charge conditioner. The values obtained were about 0.7 for each particle size examined (147 nm, 296 nm, and 498 nm). Any deviations from the assumed size-dependent charging probability will also be included in the values of $\eta_{\mathrm{F}}(D_{\mathrm{p}}, \phi)$ determined during the data fitting. The peak ratios predicted for singly-charged particles using the parallel-flow models are slightly higher than observed due to losses in the extended entrance region of the G-DMA model used in the fitting of η_{F} that do not occur in the PFDMA models. In addition, the predicted widths of the parallel-flow model peaks are narrower than for the G-DMA model, further enhancing the peak height. The apparent dependence of η_{F} on scan time likely results from

decreased resolution during fast scans; hence, values obtained in the slowest scans (t_{ramp} = 90 s) are most reliable, particularly since these losses occur upstream of the classification and, therefore, are not affected by the scanning operation. The fitted flow-system penetration efficiency does not show a significant dependence on particle size, which is not surprising since the PSL particle sizes are sufficiently large that diffusion does not significantly affect their transmission. The relatively low penetration efficiency is likely due to the prototype soft X-ray charge conditioner used in these tests.

The plug-flow version of the parallel-flow DMA model (PFDMA-P) predicts a peak that arrives about 1 s ($\sim$ 1%) later than observed for the slowest scan, while that for the laminar flow model (PFDMA-L) precedes the observed peak by about 1 s. The peak timing of the different DMA models show similar relative deviations for the faster scans through the peaks become broader and lower, and develop a tail to long times due to the tail in the delay-time distribution. The strong bias introduced by evaluating the plug-flow transfer function at the voltage corresponding to the particle exit (static-DMA model) rather than using the transit-mean value (PFDMA-P) is only slightly worse than the fully-developed laminar flow model for the slowest scan, but increases dramatically for the fastest (10 s) scan.

Figure 3.5 shows similar results for down-scan ramps with $20\,\text{s} \leq t_{\text{ramp}} \leq 90\,\text{s}$; 10 s down scans were not possible with the high voltage power supply used in these experiments. Down-scan results for 296 nm and 498 nm particles are shown in the Supplementary Information. Because the voltage deceases with time, high mobility particles exit the DMA later than low mobility ones. Moreover, Mai and Flagan (In review) found that the G-DMA transfer function for the down-scan exhibited a tail toward large times accentuating the tail caused by the delay time distribution in the CPC. The G-DMA model predicts arrival of the singly charged peak about 1 s later than observed experimentally in the 90 s scan. Both the laminar and plug-flow, parallel-flow models predict an additional 1 s delay. As the scan time is reduced, the plug-flow model peaks are further retarded. The static-DMA model assumes that the particles exit the DMA at a higher voltage (earlier) than observed experimentally. As with the up-scans, the geometric (G-DMA) model better approximates the experimental down-scan data at all scan rates than do either of the idealized, parallel-flow models, but even the G-DMA model slightly overestimates the time-in-scan at which particles are detected.

Figure 3.6 compares the instantaneous, integrated SEMS transfer functions $\Omega^{\text{I}}_{\text{SEMS}}$ and the cumulative system transfer functions Γ_{SEMS}, used in the data inversion, to the instantaneous scanning DMA transfer functions $\Omega^{\text{I}}_{\text{DMA}}$ for several sizes of singly-charged particles, ranging from the large, non-diffusive particles examined above to those classified at low voltage for which diffusion significantly

degrades instrument resolution. These transfer functions are shown only for the geometric model based upon the real instrument (G-DMA) and, due to the costly simulations required to produce these transfer functions, only for the scan and counting times used in our chamber measurements, *i.e.*, for t_{ramp} = 45 s and 240 s scans.

A fast ramp (t_{ramp} = 45 s) accentuates the CPC-induced broadening of the transfer function relative to that of a slow one (t_{ramp} = 240 s), as shown by the instantaneous SEMS transfer function Γ_{SEMS}. Moreover, the total number of particles detected during the ramp increases proportionally with the scan time t_{ramp}, as indicated by the plateau of the cumulative SEMS transfer function Γ_{SEMS}, which by definition represents the overall transmission in the system for particles of given size in an individual scan.

Previous studies have shown substantial differences between the total number of particles detected during up-scans verses down-scans of the same DMA (Collins, Cocker, et al., 2004; Mamakos, Ntziachristos, and Samaras, 2008). Figure 3.7 compares the model predictions of the ratio of the total number of particle counts in an up-scan to that in a down-scan for the three different scanning DMA transfer function models, and as observed experimentally. Three different ramp times, *i.e.*, t_{ramp} = 20, 45, 90 s are shown. Only the G-DMA transfer function model shows good agreement with the experimental data. The PFDMA-P transfer function model shows no bias for either up-scan or down-scan operation, so the response ratio based on this transfer function is identical for up- and down-scan operation. While the PFDMA-L transfer function model over-estimates the total concentration in the up-scan over the down-scan by 5% from the experimental data for t_{ramp} = 45 and 90 s, the over-estimation exceeds 10% for a 20 s ramp.

Data inversion

To recover the particle size distribution from the counts recorded in time bins requires solving the inversion problem expressed in Eq. (3.17) for the values of the size distribution at the discretization points $u_j^\dagger = \log D_{\text{p},j}^\dagger$. The results presented above reveal the superiority of the transfer function based on the actual DMA geometry (G-DMA) over those obtained using idealized, parallel-flow models of the DMA. Thus, we focus on inversion using the G-DMA model. Most previous SEMS data inversion has built upon the conclusions of Wang and Flagan (1990) that the transfer function for the SEMS is the same as that for the static DMA in the limit of plug flow, provided that the transfer function is evaluated at the mean electric field strength (or voltage) experienced by the particle during its transit through the DMA. The finite time response of the CPC detector is sometimes, but not always, taken into account. Therefore, we also perform the data inversion using the PFDMA-P transfer function. To illustrate the danger of evaluating the transfer function at the

voltage applied when particles leave the DMA rather than the transit-mean voltage, we also perform the inversion using the static transfer function.

Figure 3.8 shows the results for an *in silico* test of these three transfer functions for two bimodal particle size distribution for t_{ramp} = (a) 45 s and (b) 240 s scans. The signals have been generated using the G-DMA transfer function. As expected, inversion of the signals using that same G-DMA transfer function yields a size distribution that agrees well with that of the source aerosol. In contrast, the PFDMA-P transfer function underestimates particle size by 7% to 10% in the 45 s ramp, a result of having overestimated the delay time by ~1 s. The static DMA transfer function produces a much larger bias, overestimating the particle size by 35% to 40% in the 45 s ramp. These biases are reduced in a slow scan (240 s ramp), with PFDMA-P underestimating particle size by about 1%, and static DMA model overestimating particle size by about 6%. We did not compare the PFDMA-L model or other ramp times due to the high computational costs of performing sufficient simulations to fully map the transfer function over the full range of particle sizes.

3.5 Conclusions

This study has examined the integrated SEMS/SMPS instrument using transfer functions for different models of the scanned DMA. Idealized, parallel flow models of the cylindrical DMA assuming either plug flow as considered in the original model of Wang and Flagan (1990) were compared with results obtained using the transfer function for a real DMA, which was obtained finite element calculations of flow and electric fields within the instrument, and Brownian dynamics simulations of particle migration and transport (Mai and Flagan, In review). These scanning DMA models were combined with empirically derived models of the time response of the CPC detector and plumbing between the DMA and CPC. In order to capture the long-time tail of the combined plumbing and detector response, the plug flow plus continuously stirred tank reactor model used in previous studies was augmented with a laminar tube flow delay time distribution model.

The SEMS response function obtained with the geometrical model of the real DMA agrees well with that determined during measurements of monodisperse PSL calibration aerosols that were made with a SEMS/SMPS system consisting of a TSI Model 3081A long-column DMA coupled to a TSI model 3010 CPC as a detector during exponentially increasing voltage up-scans ranging from 10 to 240 s, and during down-scans ranging from 20 to 240 s. Full data inversion was demonstrated with 45 s and 240 s up-scans.

The results presented here reveal biases in the common approach of inverting SEMS data using the constant voltage (DMPS) transfer function leads in both up-scan and down-scan operation, even

when the finite time response of the detector is taken into account; these biases arise because the simplistic model does not accurately describe particle transmission through the scanning DMA. However, very slow scans allow accurate recovery of the size distribution to be obtained by inversion of measured counts using the idealized, parallel-flow DMA transfer function, and can be expected to approach that of properly made DMPS measurements. However, if the transfer function for the actual experimental system is known, the SEMS/SMPS should be able to accurately measure particle size distribution during both up-scans and down-scans.

In the present study, we obtained the real SEMS/SMPS instrument response function using computationally intensive Brownian dynamics simulations for one DMA design, one set of flow rates, one CPC, and a range of scan rates. Rigorous data inversion for other instruments or operating conditions will require that the appropriate scanning-mode transfer function be determined, a costly endeavor, or the use of scans that are sufficiently slow that the scanning instrument results approach those of DMPS measurements. Alternatively, the SEMS/SMPS instrument response function might be determined empirically by measurement of monodisperse calibration aerosols in a tandem differential mobility analyzer. Ideally, such empirical characterization would involve traceable particle size standards and the use of a well-calibrated reference particle detector that is identical to that used in the SEMS, and with a steady aerosol that can be scanned many times to attain good counting statistics. Because the instrument response function changes when operational parameters change, it needs to be determined for the conditions to be used during measurements. Parameters that need to be reproduced include flow rates, exponential scan time constant, $\tau_s = \frac{t_{ramp}}{\ln \frac{V_{high}}{V_{low}}}$, lengths, sizes, and geometry of all tubing and plumbing connection between the DMA outlet and CPC inlet, counting time, as well as the specific charge conditioner and CPC to be used in the measurements. Because of the sensitivity of the instrument response to details of the instrument, all operating parameters *and* the instrument response functions need to be well documented.

While the parallel flow models do not fully capture the performance of the scanned DMA, they have been extremely useful in the analysis of DMPS data, particularly using the semi-analytical transfer function that accounts for diffusion (Stolzenburg, 1988). It may be possible to develop hybrid models that combine the idealized parallel-flow models with description of the nonidealities that led to their present inclusion in the "extended classification region" of Mai and Flagan (In review). This might incorporate empirically-derived correction factors to account for perturbations to particle transit time, a transmission efficiency for the extended classification region, and a delay time distribution associated with the classification region. With care, the SEMS or SMPS can yield size distributions as faithfully as the DMPS, even in fast scans. However, for data from such

approximate descriptions of complex instruments, all of the corrections and approximations to the instrument response function need to be fully and openly documented with each dataset. Raw count data are essential if one is to assess measurement uncertainty.

Many size distributions have been measured with the commercial TSI SMPS and other SEMS systems in the two and a half decades since the method was introduced. Many users have wisely employed relatively slow scans that minimize the perturbations described here, but others have necessarily employed sufficiently fast scans that biases exist in the data. To the extent that the raw data have been preserved, and the operating conditions have been well documented, it may be possible to correct existing data for these biases. To do that will require developing a library of SEMS/SMPS instrument response functions for the range of operating conditions employed. Unfortunately, some data will not be recoverable due to incomplete documentation and preservation of key parameters.

Acknowledgements

The authors thank Dr. K. Beau Farmer of TSI Inc. for providing detailed design drawings of the TSI Model 3081A DMA that made it possible to simulate flows, fields, and particle trajectories in the real instrument. We thank Yuanlong Huang, Wilton Mui, Amandan Grantz, Johannes Leppä, Paula Popescu, and John Seinfeld for useful discussions. This material is based upon work supported by the National Science Foundation under Grant No. AGS-1602086.

Table 3.1: Operation parameters of the scanning DMA.

Parameter	Notation	Value
Length (cm)	L	44.38
Inner radius (cm)	R_1	0.937
Outer radius (cm)	R_2	1.961
Polydisperse flow rates (LPM)	Q_a	0.515
Monodisperse flow rates (LPM)	Q_c	0.515
Sheath flow rates (LPM)	Q_{sh}	2.510
Excess flow rate (LPM)	Q_{ex}	2.510
Low electrode voltage (V)	V_{low}	15
High electrode voltage (V)	V_{high}	9850
Up scan time (s)	$t_{ramp,u}$	10,20,45,90
Down scan time (s)	$t_{ramp,d}$	10,20,45,90
Holding time at V_{low}	t_{low}	20
Holding time at V_{high}	t_{high}	20

Table 3.2: Penetration efficiencies through the flow system for the geometric model (G-DMA) of instrument responses for various particle sizes.

D_p(nm)	Up-scan η_F	Down-scan η_F
147	0.706 ± 0.008	0.647 ± 0.016
296	0.722 ± 0.005	0.694 ± 0.012
498	0.669 ± 0.004	0.662 ± 0.011

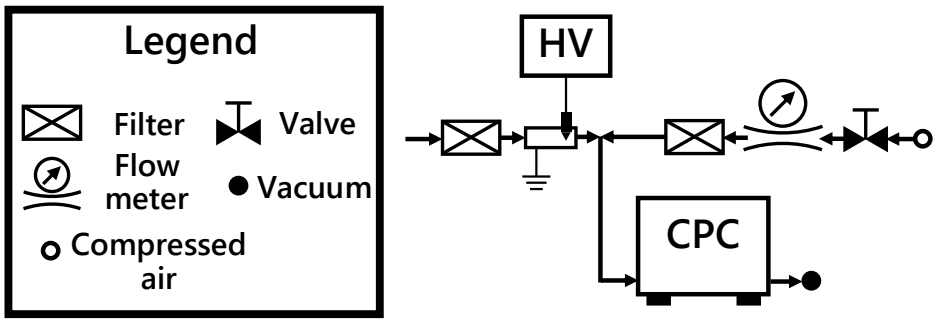

Figure 3.1: Experimental setup schematic to measure the CPC residence time distribution.

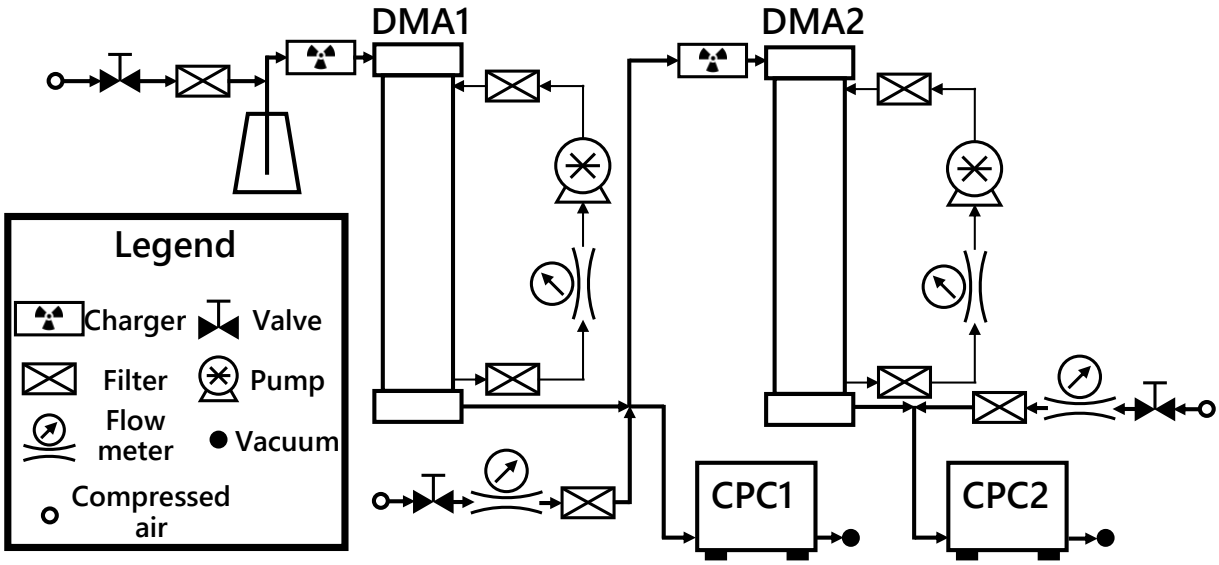

Figure 3.2: Experimental setup schematic to measure the DMA-CPC composite instrument response.

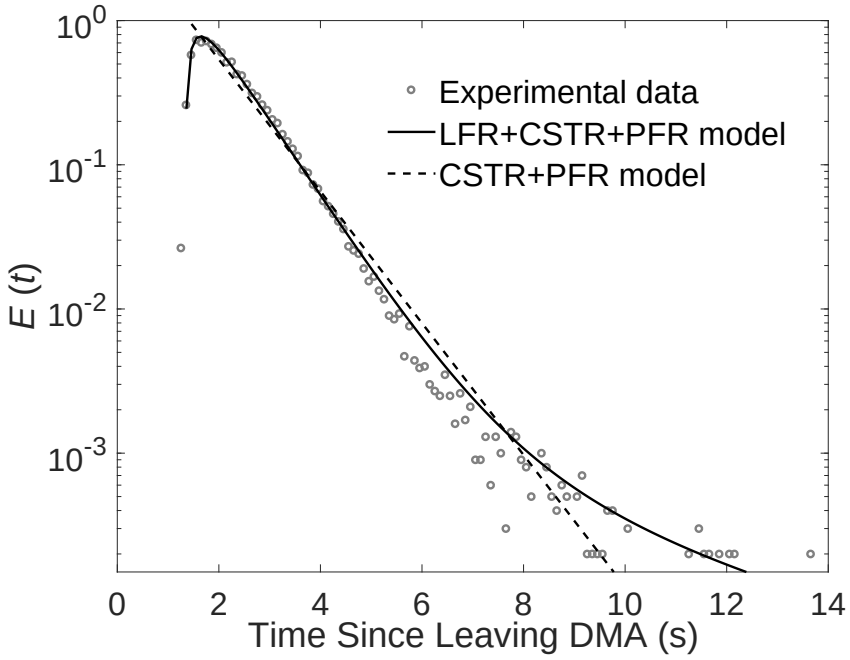

Figure 3.3: Residence time distribution of TSI 3010 CPC, with sampling flow rate of 0.975 LPM.

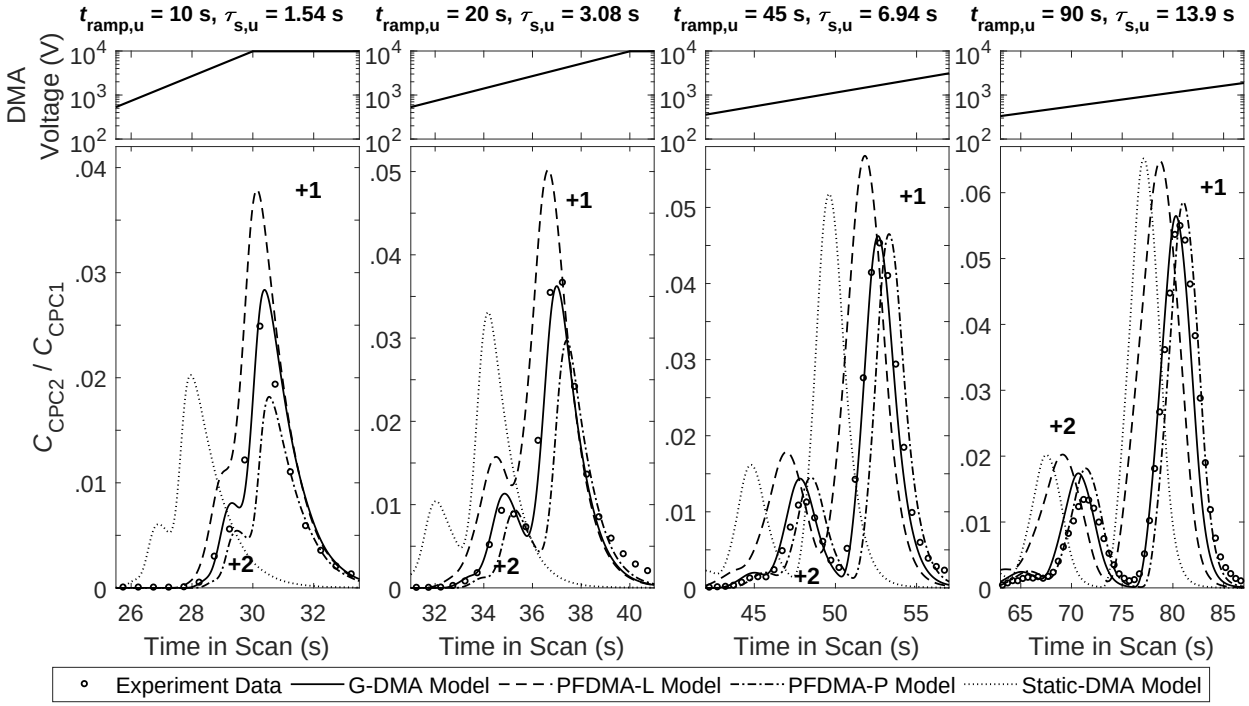

Figure 3.4: Up-scan experimental and modeling results for SEMS instrument response to monodisperse 147 nm particles with ramp duration t_{ramp} = 10, 20, 45 and 90 s (corresponding to scan time τ_{s} = 1.54, 3.08, 6.94 and 13.9 s).

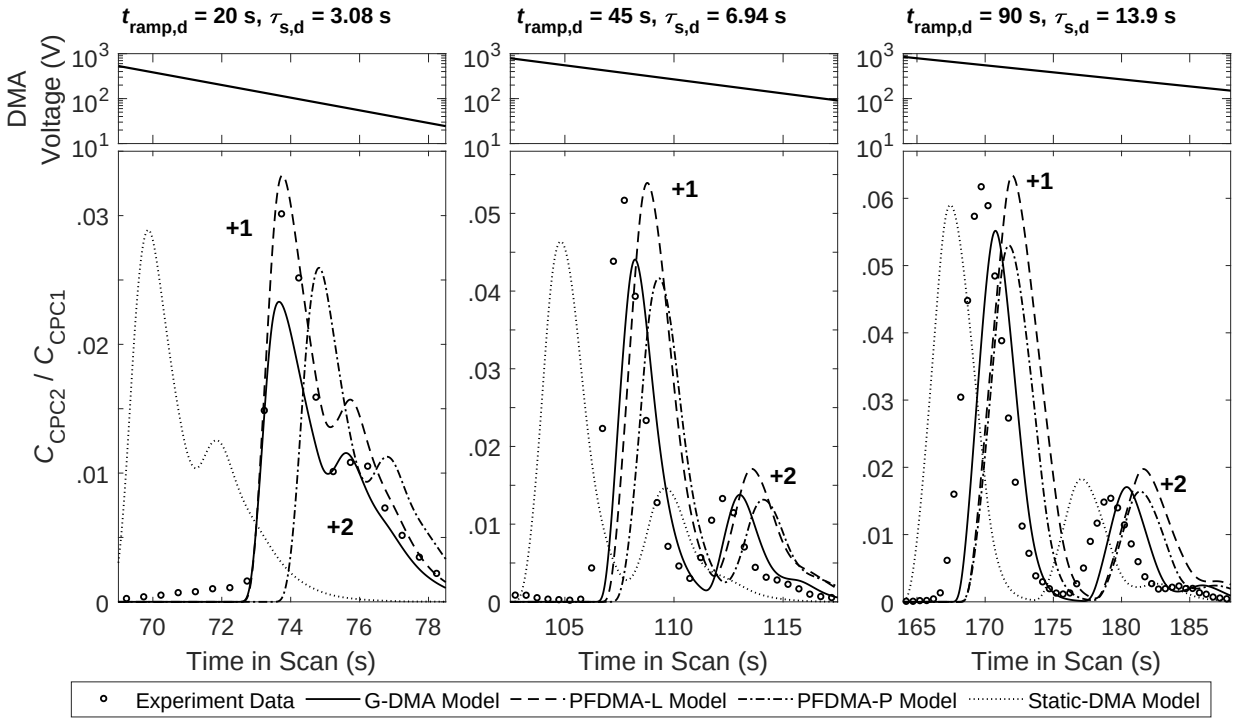

Figure 3.5: Down-scan experimental and modeling results for SEMS instrument response to monodisperse 147 nm particles with ramp duration t_{ramp} = 10, 20, 45 and 90 s (corresponding to scan time τ_s = 1.54, 3.08, 6.94 and 13.9 s).

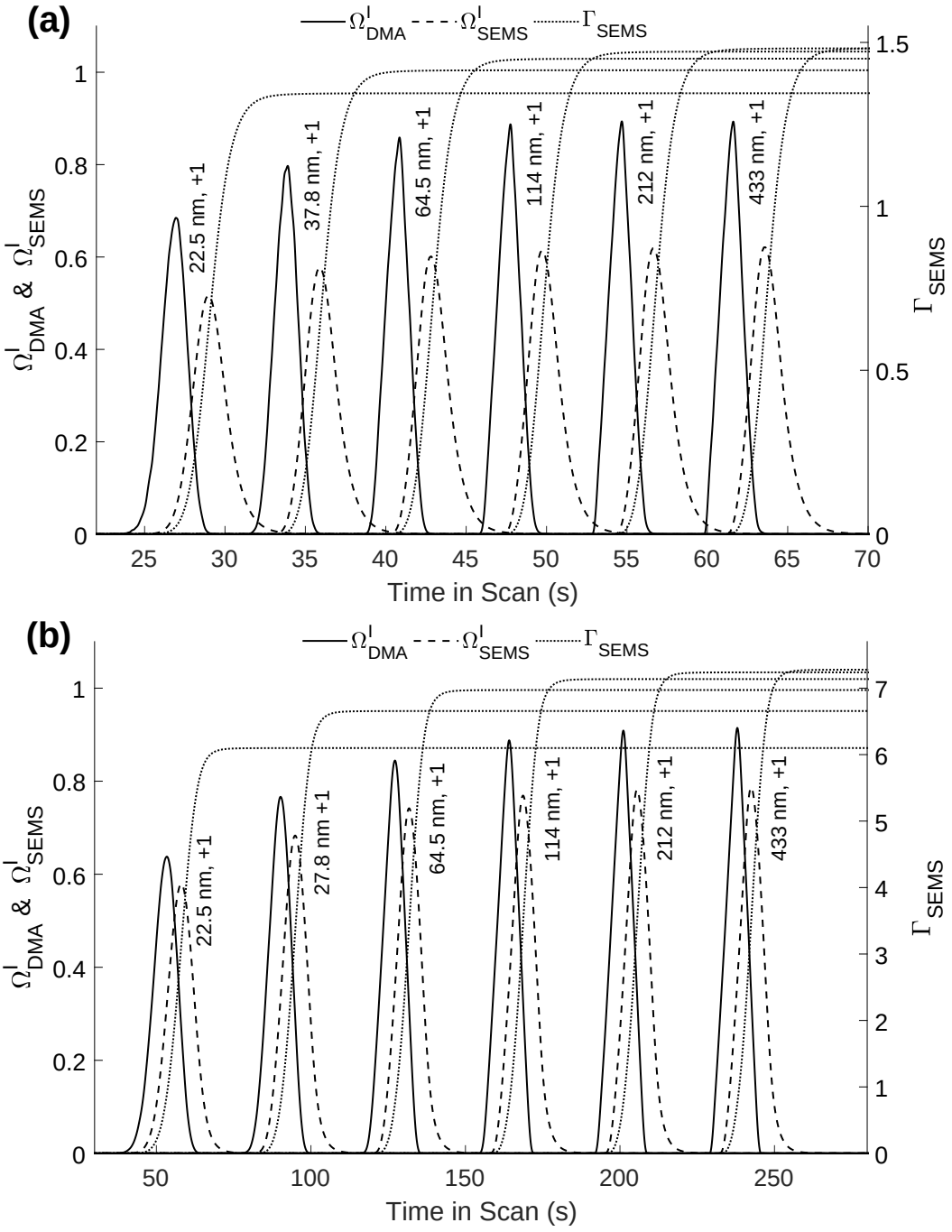

Figure 3.6: The instantaneous scanning DMA transfer functions Ω^I_{DMA}, the instantaneous SEMS transfer functions Ω^I_{SEMS} and the cumulative SEMS transfer functions $\Gamma_{C,\,SEMS}$ for up-scan operation with ramping durations t_{ramp} = (a) 45 s, (b) 240 s, which correspond to scanning time scales τ_s = 6.94 s, 37.00 s, respectively. Samples of the transfer functions are shown for singly-charged particles with electric mobility equivalent sizes ranging from 22.5 nm to 433 nm.

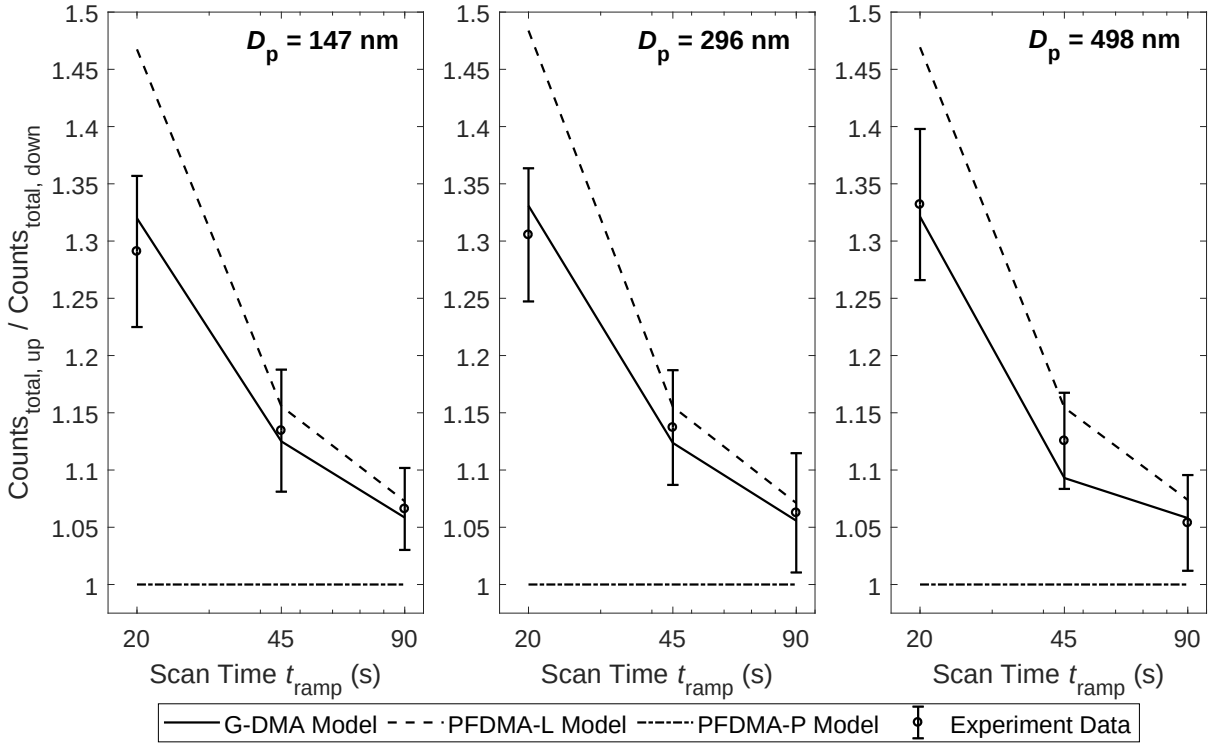

Figure 3.7: Comparison of the experimentally measured and the simulated total number concentration ratios between up- and down-scan operation. Error bars represents the standard deviations for the corresponding experimental measurement results.

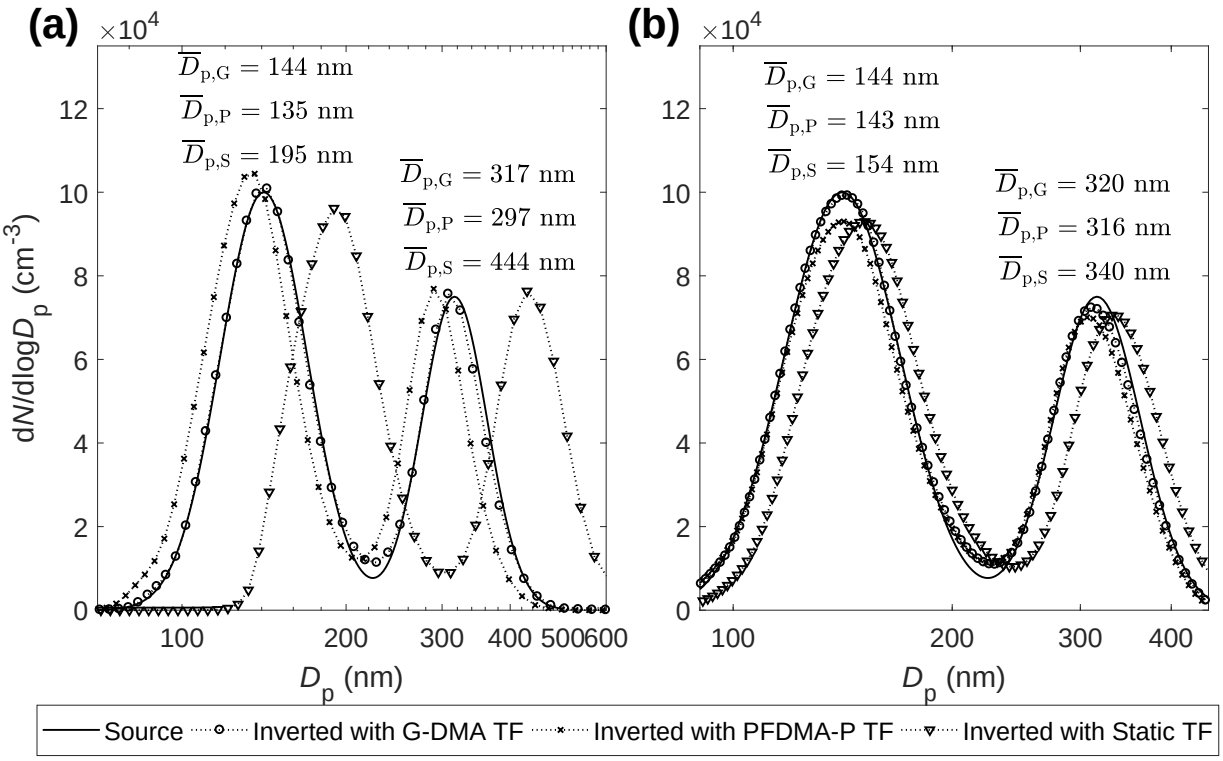

Figure 3.8: Comparison of the inverted size distribution with G-DMA model, PFDMA-F model, static DMA transfer function and the source particle size distribution in the (a) 45 s ramp and the (b) 240 s ramp. $\overline{D}_{\mathrm{p,G}}$, $\overline{D}_{\mathrm{p,P}}$ and $\overline{D}_{\mathrm{p,S}}$ denote the mean particle sizes from G-DMA model, PFDMA-F model, static DMA transfer function based inversion and for different modes of the size distribution, respectively.

References

Collins, Don R., David R. Cocker, et al. (2004). "The Scanning DMA Transfer Function". In: *Aerosol Science and Technology* 38.8, pp. 833–850.

Collins, Don R., Richard C. Flagan, and John H. Seinfeld (2002). "Improved Inversion of Scanning DMA Data". In: *Aerosol Science and Technology* 36.1, pp. 1–9.

Dubey, Praney and Suresh Dhaniyala (2008). "Analysis of scanning DMA transfer functions". In: *Aerosol Science and Technology* 42.7, pp. 544–555.

– (2011). "A New Approach to Calculate Diffusional Transfer Functions of Scanning DMAs". In: *Aerosol Science and Technology* 45.8, pp. 1031–1040. eprint: `http://dx.doi.org/10.1080/02786826.2011.579644`.

Knutson, E. O. and K. T. Whitby (1975). "Aerosol classification by electric mobility: apparatus, theory, and applications". In: *Journal of Aerosol Science* 6.6, pp. 443–451.

Leppä, J et al. (2017). "Charge distribution uncertainty in differential mobility analysis of aerosols". In: *Aerosol Science and Technology* 14, pp. 1–22.

Mai, Huajun and Richard C. Flagan (In review). "Scanning DMA Data Analysis I. Classification Transfer Function". In: *Aerosol Science and Technology*.

Mamakos, Athanasios, Leonidas Ntziachristos, and Zissis Samaras (2008). "Differential mobility analyser transfer functions in scanning mode". In: *Journal of Aerosol Science* 39.3, pp. 227–243.

Merritt, M. and Y. Zhang (2005). "Interior-Point Gradient Method for Large-Scale Totally Nonnegative Least Squares Problems". In: *Journal of Optimization Theory and Applications* 126.1, pp. 191–202.

Russell, Lynn M., Richard C. Flagan, and John H. Seinfeld (1995). "Asymmetric Instrument Response Resulting from Mixing Effects in Accelerated DMA-CPC Measurements". In: *Aerosol Science and Technology* 23.4, pp. 491–509.

Stolzenburg, Mark Richard (1988). "An ultrafine aerosol size distribution measuring system". In: *Ph. D. thesis, Univ. Minnesota*.

Wang, Shih Chen and Richard C. Flagan (1990). "Scanning Electrical Mobility Spectrometer". In: *Aerosol Science and Technology* 13.2, pp. 230–240.

Wolfenbarger, Kenneth and John H Seinfeld (1990). "Inversion of aerosol size distribution data". In: *Journal of Aerosol Science* 21.2, pp. 227–247.

SCANNING OPPOSED MIGRATION AEROSOL CLASSIFIER (OMAC)

By Huajun Mai, and Richard C. Flagan

4.1 Introduction

The opposed migration aerosol classifier (OMAC) can maintain its ideal resolution at much lower electrode voltages than the differential mobility analyzer (DMA) (Flagan, 1999; Flagan, 2004). A radial-flow version of this instrument, called the radial opposed migration ion and aerosol classifier (ROMIAC) can classify sub-2 nm ions (Mui, Thomas, et al., 2013), and even to separate peptide stereoisomers (Mui, Mai, et al., 2017). The ROMIAC has been used as a particle classifier in the measurement of particle size distributions during atmospheric nucleation events owing to its high resolving power in the nucleated particles domain. To measure particle size distributions, the classification voltage was stepped to obtain particle concentration over a range of discrete mobilities. Voltage stepping makes size distribution measurements slow due to the time one must wait between channels; by continuously scanning the voltage, Wang and Flagan (1990) accelerated DMA measurements in the scanning electrical mobility spectrometers (SEMS).

Because scanning alters the ideal trajectory the successfully classified particles follow in the OMAC, voltage scanning of the OMAC can be expected to increase losses relative to constant voltage classification. One could vary the field or flow along the classification channel, but this would significantly complicate instrument design and operation. Hence, the OMAC has been limited to stepping mode operation to date.

In this chapter, we explore the potential of scanning the OMAC through Monte Carlo simulation of particle trajectories using COMSOL Multiphysics^{TM}, following an approach similar to that used to derive the scanning mode transfer function of a commercial DMA. Individual particle trajectories and the mean trajectory of the transmitted particles are compare with those from the stepping-mode operation to elucidate the difference between these measurements modes over a wide range of scan rates with duration of voltage ramping ranging from 3 to 100 s.

4.2 Methods

Particle trajectory simulation in COMSOL

Mai and Flagan (In review) derived the DMA transfer function by dividing the DMA into three regions: (*i*) entrance region, where only particle loss is concerned; (*ii*) "extended classification region", where the time-varying electric field affects the particle motion; (*iii*) exit region, where the residence time distribution and the penetration efficiency are both required for the size distribution data inversion. In that paper, the diffusive particle trajectories in both the entrance region and the exit region were simulated by applying the Monte Carlo method in COMSOL Multiphysics^{TM}, while the particle trajectories and the associated classification transfer function were obtained using the Monte Carlo simulation in Igor Pro, but with the steady fluid flow and electric field solution imported from the finite-element-analysis from COMSOL Multiphyscis^{TM}. This method provides comprehensive understanding and detail insight of the performances of each component of the instrument, but it poses challenges for further application given the difficulty of subdividing the instrument into multiple regions, and evaluating the instrument performance individually for each part.

Here, the performance of the ROMIAC is evaluated in COMSOL Multiphyscis^{TM} as a whole, with the basic geometry described by Mui, Mai, et al. (2017). Since the ROMIAC is designed for classifying particles ranging from 1 to 100 nm in size, inertia effects can be assumed to have negligible influences on the diffusive particle trajectories; non-inertial particle simulations were performed using the "massless" formulation in the particle tracing module in COMSOL Multiphyscis^{TM}. In contrast, Mai and Flagan (In review) used the "Newtonian" formulation that takes particle inertia into account. Intuitively, neglecting inertia accelerates particle trajectory calculations, so long as the error tolerance level is not changed. Following Mai and Flagan (In review), steady-state fluid flows and electric fields were solved numerically using the laminar flow and electrostatic modules, respectively, for the operating parameters given in Table 4.1. The time-varying electric field is then defined as $E(x, y, z, t) = E_0(x, y, z)f(t)$, where $E_0(r, z)$ is the electric field obtained by finite element simulations at an electrode potential of $V_0 = 1$ V, and $f(t)$ is the time variation factor, defined as (Mai, Kong, et al., In review),

$$f(t) = \begin{cases} \dfrac{V_{\text{low}}}{V_0}, & 0 \le t < t_{\text{low}} \\ \dfrac{V_{\text{low}}}{V_0} e^{\frac{t-t_{\text{low}}}{\tau_{\text{s, u}}}}, & t_{\text{low}} \le t < t_{\text{low}} + t_{\text{ramp,u}} \\ \dfrac{V_{\text{high}}}{V_0}, & t_{\text{low}} + t_{\text{ramp,u}} \le t < t_{\text{low}} + t_{\text{ramp,u}} + t_{\text{high}} \\ \dfrac{V_{\text{high}}}{V_0} e^{-\frac{t-t_{\text{low}}-t_{\text{ramp,u}}-t_{\text{high}}}{\tau_{\text{s, d}}}}, & t_{\text{low}} + t_{\text{ramp,u}} + t_{\text{high}} \le t < t_{\text{low}} + t_{\text{ramp,u}} + t_{\text{high}} + t_{\text{ramp,d}}. \end{cases} \tag{4.1}$$

Eq. 4.1 can be incorporated into the COMSOL simulation by defining a Analytic function with 4 step functions under "Definitions" in the "Model Builder" interface. The 3-dimensional particle trajectories are then implemented with the mathematical particle tracing module by defining the particle velocity as follows

$$v_\chi = u_\chi + E_{0,\chi} f(t) Z_\mathrm{p} + \frac{g(\sqrt{2\mathcal{D}\mathrm{d}t})}{\mathrm{d}t}, \tag{4.2}$$

where χ denotes one of the Cartesian coordinates, x, y or z, and u_χ and $E_{0,\chi}$ are the fluid flow velocity and the steady-state electric field intensity of χ coordinates from the finite element calculations. $\mathrm{d}t$ denotes the time step for the trajectory simulation, which is chosen to be 0.5 ms for this study.

To enable comparison with the prior stepping-mode approach, particle trajectories in the stepping mode ROMIAC are also simulated by setting the time variation factor $f(t)$ as constant in the particle motion equation (Eq. (4.2)).

Mean particle trajectory

In order to show the instrument performance from a integrated perspective, the mean trajectory of the transmitted particles is introduced. The particle trajectories from the 3-dimensional COMSOL simulation are interpolated onto axisymmetric coordinates (r, z). To quantitatively compare the stepping mode to the scanning mode, mean trajectories for both modes of operation are calculated.

To get an unbiased representation of the mean trajectory of particles of a given mobility, all possible transmitted particle trajectories are collected. In the scanning mode, we first release particle in each time interval and then identify all time intervals when any such particles are successfully transmitted through the instrument. These intervals for the scanning ROMIAC are shown in Table 4.2 for scan times t_ramp ranging from 3 to 100 s for singly-charged particles of two sizes, D_p = 2.67 and 20.8 nm. For the 2.67 nm particles, 100 particles are released at each time step, while for the 20.8 nm particle, only 50 particles are released per step since the transmission efficiency for 20.8 nm is around twice of that at 2.67 nm.

To generate an unbiased mean particle trajectory in the stepping mode, particle trajectories are simulated for different electrode voltages, at which any such particles are transmitted. For the 2.67 nm singly-charged particle, the voltage range is 81 to 97 V, which was simulated with voltage step of 2 V. For singly-charged, 20.8 nm particles, voltages ranging from 4700 to 5700 V were simulated, with voltage steps of 100 V.

Transfer function

Following Mai and Flagan (In review), the scanning ROMIAC transfer function is defined as

$$\Omega^{\mathrm{I}}_{\mathrm{ROMIAC}}(Z_{\mathrm{p}}(D_{\mathrm{p}}, \phi), t) = \frac{Q_{\mathrm{a,\,out}} N_{\mathrm{a,\,out}}(t)}{Q_{\mathrm{a,\,in}} N_{\mathrm{a,\,in}}}, \tag{4.3}$$

where $Q_{\mathrm{a,\,in}}$ and $Q_{\mathrm{a,\,out}}$ are the flow rates of the polydisperse and the monodisperse aerosol, respectively, and $N_{\mathrm{a,\,in}}$ and $N_{\mathrm{a,\,out}}$ are the corresponding particle number concentrations.

To determine the scanning ROMIAC transfer function with adequate time resolution, particles were released in the simulation at 2.5 ms intervals for voltage ramp times of t_{ramp} = 25, 50, and 100 s, and for both up- and down-scans. Simulations were performed for 12 electrical mobility-equivalent particle sizes ranging from 1.61 nm (electrical mobility $Z_{\mathrm{p}} = 8.03\times10^{-5}$ m^2/s/V) to 27.1 nm ($Z_{\mathrm{p}} = 3.02\times10^{-7}$ m^2/s/V). For fast scans, *i.e.*, t_{ramp} = 3, 6, and 12 s, transfer functions are only explored for two particle sizes: 2.67 nm ($Z_{\mathrm{p}} = 4.83\times10^{-5}$ m^2/s/V) and 20.8 nm ($Z_{\mathrm{p}} = 5.01\times10^{-7}$ m^2/s/V), since these fast scans raise challenges for particle size distribution inversion.

4.3 Results

Particle trajectories in ROMIAC

Figure 4.1 shows trajectories for the D_{p} = 20.8 nm particle in the fast scans. The particles trajectories are projected on the axisymmetric (r, z) coordinates for visualization purposes. In the fast scans, few particles are transmitted through the classified aerosol exit; most of the particles are deposited on the upper- or lower-electrodes, particularly for t_{ramp} = 3 s, as shown in Fig. 4.1 (a) and (b). During the fast up-scan, particles are deposited over a wide range of radial positions ($0 < r < 1.4$ cm) on both electrodes. In contrast, particles are deposited over a much narrower range of radii (1.0 cm $< r <$ 1.4 cm) in the 3 s down scan, as shown in Fig. 4.1 (b). The area of which particles deposit on the electrodes increases as the down-scan slows. As shown in Fig. 4.1 (f), when t_{ramp} = 12 s, particles deposit on the lower electrode from 0.4 cm$< r <$1.4 cm. For the slow scans shown in Fig. 4.2, the difference of trajectories between up- and down-scans is less significant than that for the fast scans.

With the operating parameters given in Table 5.1 for the ROMIAC, singly-charged, D_{p} = 20.8 nm particles can be considered to be non-diffusive since their trajectories closely follow the kinematic trajectories determined by the fluid motion and electric field. By comparison, particle trajectories for singly-charged, D_{p} = 2.67 nm particles show the role of diffusion in the particle motion. This is as shown in Figures 4.3 and 4.4 for fast and slow scans, respectively.

The particle trajectories for the stepping-mode ROMIAC are shown in Figure 4.5. For a "non-diffusive" particle (D_{p} = 20.8 nm), particle trajectories are simulated for 11 different voltages

ranging from 4.7 kV to 5.7 kV, which approximately covers the full range of the stepping mode transfer functions as shown in Fig. 4.5 (c). The peak penetration efficiency is around 0.6 for D_p = 20.8 nm particles, with an electrode voltage of 5.2 kV. For "diffusive" 2.67 nm particles, the peak penetration efficiency is about 0.3 as electrode voltage of 91 V. During stepping mode, particles deposit on the electrodes from $0 < r < 1.0$ cm, which is a smaller area than for any scanning mode conditions, because the changes of voltage during the particles' transit increases the range variation in the particle trajectories.

Transmitted particle trajectories and transfer function of scanning ROMIAC

As the transmitted particles, rather the deposited ones, contribute to the classifier output signal, only the transmitted particle trajectories and the associated transfer function of the scanning ROMIAC are discussed in this section. The times at which the transmitted particles enter and exit the scanning ROMIAC are recorded. Figure 4.6 (a) and (b) show particle trajectories for the transmitted D_p = 20.8 nm particles and the corresponding entrance and exit time distributions in the t_{ramp} = 3 s up-scan, respectively. The particle trajectories are colored by the time they leave the instrument (or particle exit time). Figure 4.6 and 4.7 show the particle trajectories and the transfer functions for fast (t_{ramp} = 3, 6, and 12 s) and slow (t_{ramp} = 25, 50, and 100 s) up-scans, respectively. The down-scan results are shown in Figures 4.8 and 4.9 for fast and slow scans, respectively. The smoothed transfer functions in Figures 4.6 - 4.9 are obtained using locally-weighted regression and smoothing on the raw simulation data (Cleveland, 1979).

For 20.8 nm particles, the peak transmission efficiency increases from 0.4 to 0.5 as the the scan time duration t_{ramp} is increased from 3 s to 12 s, shown in Fig. 4.6. The peak transmission efficiency is around 0.6 for the slow t_{ramp} = 25, 50 and 100 s conditions. For these slow scans, the transfer function contains only one mode. During both fast- and slow up scans, particles that exit late in the scan (red particle trajectories) tend to enter the ROMIAC classification region near the top boundary of the inlet. These particles also tend to leave the classification region near the center of the aerosol outlet. By contrast, those particles that exit early (blue particle trajectories) enter the classification region near the bottom boundary of the inlet. This particle trajectory pattern can be explained by the configuration of the ROMIAC. To avoid losses associated with the adverse potential gradient in DMAs, aerosol both enters and leaves the ROMIAC at the electrically grounded top electrode. The cross-flow enters from the bottom electrode (z = 0 cm), and exits at the top electrode (z = 1.14 cm). Thus, the counter-balanced electric force pushes particles away from the top electrode. As a result, particles that exit late are pulled towards the bottom electrode due to the high electric field strength late in the up-scan.

The down-scan transfer functions are distorted from the expected single-mode form, particularly for scan times of 6, 12, 25 and 50 s, as shown in Figures 4.8 and 4.9. This down-scan transfer function distortion can be explained with the corresponding particle trajectories. When t_{ramp} = 25 s, the transfer function shows a long tail (Fig. 4.9 (b)) between 40.0 s and 40.5 s, due to the late-exiting particles (red particle trajectories in Fig. 4.9 (a)). This group of particles first approaches the bottom electrode within the classification region, and is then pushed toward the top electrode as the electric field strength decreases in the down-scan. The rapid change of the electrostatic force leads to the abrupt change in particle motion in the z-direction, with particle trajectories initially approaching the bottom electrode but then reversing direction to exit through the classified aerosol outlet at the top. This effect is significant when t_{ramp} = 6 and 12 s, with large fraction of "reverse" particle trajectories.

Mean trajectory of scanning ROMIAC

Figures 4.10 and 4.11 show the mean trajectories of the transmitted D_{p} = 20.8 nm particles, and the corresponding standard deviations for the fast and slow scans, respectively. In the fast up-scan, as shown in Fig. 4.10 (a), (c) and (e), the mean particle trajectories are close to the top electrode due to the low electric field strength when the transmitted particles enter the classification region, particularly for t_{ramp} = 3 s. By contrast, the mean particle trajectory is close to the bottom electrode for the fast down-scan, as shown in Fig. 4.10 (b), (d) and (f). The mean particle trajectories in stepping-mode measurements are also shown for comparison. As expected, the mean particle trajectory during scanning approach that during stepping mode when the scan is slow (large t_{ramp}). This is clearly shown in Figures 4.11 (e) and (f), for t_{ramp} = 100 s during up- and down-ramps, respectively; in these very slow scans, the scanning-mode trajectory overlaps with that during stepping-mode (constant voltage) classification.

The standard deviation of the mean up-scan trajectory is smaller than that during the down-scan. We attribute this behavior to the "reverse" particle trajectories discussed above since the reversal increases the variability of the transmitted particle trajectories, which exacerbates the distortion of the down-scan transfer function. The increased variability in the mean particle trajectory is significant for t_{ramp} = 6, 12 s down-scan operation, as shown in Figure 4.10 (d) and (f). Instrument design also contributes to the asymmetry in the ROMIAC transfer function between up- and down-scans, as the polydisperse aerosol is introduced close the top electrode, thereby constraining the particle trajectories during up-scans.

The mean trajectory is also shown for the diffusive particles, *i.e.*, ones with 2.67 nm electrical mobility equivalent diameter for both fast and slow scans in Figures 4.12 and 4.13, respectively.

The mean trajectory of the 2.67 nm diameter particles is less smooth less than that of 20.8 nm particles due to increased particle diffusion.

4.4 Average transmission efficiency of ROMIAC and DMA

Counting statistics, a major source of uncertainty in size distribution measurements, are aggravated by low transmission efficiencies at small particle size. Any increase in the overall probability that the particles of given size are transmitted into the classified sample reduces this uncertainty by increasing the downstream particle counts. The average transmission efficiency is defined as the integral over the instantaneous fraction of particles that are transmitted, normalized with respect to the ramp time,

$$\bar{\eta}(Z_\mathrm{p}, t_\mathrm{ramp}) = \frac{R_\mathrm{nd} \int_0^{t_\mathrm{end}} \Omega^\mathrm{I}(Z_\mathrm{ramp}(D_\mathrm{ramp}, \phi), t)\mathrm{d}t}{t_\mathrm{ramp}} \tag{4.4}$$

where $\Omega^\mathrm{I}(Z_\mathrm{p}(D_\mathrm{p}, \phi), t)$ is the instantaneous classifier transfer function (either up-scan or down-scan) for the scan classifier, and $t_\mathrm{end} = t_\mathrm{low} + t_\mathrm{ramp,u} + t_\mathrm{high} + t_\mathrm{ramp,d}$. R_nd is the non-diffusive resolution, defined as $R_\mathrm{nd} = \dfrac{1}{\beta(1+|\delta|)}$ (Flagan, 1999). For the ROMIAC, $\beta = \dfrac{Q_\mathrm{a,in} + Q_\mathrm{a,out}}{Q_\mathrm{c,in} + Q_\mathrm{c,out}}$, $\delta = \dfrac{Q_\mathrm{a,out} - Q_\mathrm{a,in}}{Q_\mathrm{a,in} + Q_\mathrm{a,out}}$. For the DMA, $\beta = \dfrac{Q_\mathrm{a} + Q_\mathrm{c}}{Q_\mathrm{sh} + Q_\mathrm{ex}}$, $\delta = \dfrac{Q_\mathrm{c} - Q_\mathrm{a}}{Q_\mathrm{c} + Q_\mathrm{a}}$, where Q_a, Q_s, Q_sh and Q_e are the aerosol inlet, aerosol outlet, sheath in and excess out flow rates in DMA. The average transmission is normalized with the scanning time duration t_ramp since, in a long scan (increased t_ramp), the number of transmitted particles is also increased. The non-diffusive classifier resolution R_nd also needs to be taken into account, since low resolution results in a broad transfer function, at least for stepping-mode operation, and increases the overall particle transmission efficiency. The transfer function can be determined from simulations of the particle trajectories, with the integral $\int_0^{t_\mathrm{end}} \Omega^\mathrm{I}(Z_\mathrm{p}(D_\mathrm{p}, \phi), t)\mathrm{d}t$ being approximated by the summation based on Eq. (4.3),

$$\int_0^{t_\mathrm{end}} \Omega^\mathrm{I}(Z_\mathrm{p}(D_\mathrm{p}, \phi), t)\mathrm{d}t \approx \frac{Q_\mathrm{a,\,out}}{Q_\mathrm{a,\,in} N_\mathrm{a,in}} \sum_0^{t_\mathrm{end}} N_\mathrm{a,\,out}(t)\delta t = \frac{Q_\mathrm{a,\,out} N_\mathrm{transmitted} \delta t}{Q_\mathrm{a,\,in} N_\mathrm{a,in}}, \tag{4.5}$$

where $N_\mathrm{transmitted}$ is the total number of the transmitted particles in the simulation, and δt is the time step of particle release in the simulation.

Figure 4.14 shows the average transmission efficiencies for the OMAC (a) and the DMA (b), respectively, as a function of the dimensionless scan time scale, defined as follows

$$\rho_\tau = \frac{\tau_s}{\tau_f}, \tag{4.6}$$

where $\tau_s = t_{ramp}/\ln(V_{high}/V_{low})$ is the ramping time scales, and $\tau_f = V_{class}/Q_{class}$ denotes the mean residence time within the classification region, with V_{class} and Q_{class} as the volume and the effective flow rate in the classification region, respectively. For the ROMIAC, $V_{class} = \pi R^2 b$, where R = 1.613 cm and b = 1 cm are the radius and the gap between two electrodes, respectively, and $Q_{class} = \frac{Q_{a,\,in} + Q_{a,\,out}}{2}$. For the DMA, the volume of the classification region is $V_{class} = \pi(R_2^2 - R_1^2)L$, and the effective flow rate is $Q_{class} = Q_a + Q_{sh} = Q_c + Q_{ex}$ (Mai and Flagan, In review).

Figure 4.14 (a) shows the average transmission efficiency $\bar{\eta}$ for two different particle sizes, D_p = 2.67 and 20.8 nm, with scan durations t_{ramp} ranging from 3 s (ρ_τ = 0.89) to 100 s (ρ_τ = 29.6) for both up- and down-scans. For 20.8 nm singly-charged particles, the average transmission efficiency, $\bar{\eta}$, is consistently higher than that for 2.67 nm singly-charged particles due to the lower particle diffusivity of the 20.8 nm particles. The up-scans (down-scans) transmission efficiency of the ROMIAC decreases with ρ_τ since a large fraction of the particles deposit on the cross-flow outlet (inlet) electrode during fast scans (small ρ_τ), as shown in Figure 4.15. The counter-balanced cross-flow and the electrical migration make it possible for particles to impinge on the electrode during a scan even without diffusion.

During ROMIAC down-scans, the average transmission efficiency $\bar{\eta}$ increases as t_{ramp} decreases from 100 s (ρ_τ = 29.6) to 6 s (ρ_τ = 1.78) because the particle is introduced close to the upper electrode, allowing particles that enter over a wide range of times to be transmitted through the classifier owing to the large distance between the polydisperse sample inlet and the lower electrode. However, $\bar{\eta}$ decreases as t_{ramp} decreases further from 6 s (ρ_τ = 1.78) to 3 s (ρ_τ = 0.89), since the lower electrode then becomes a constraint for the particle transmission, as shown in Fig. 4.15 (b). In contrast, the average transmissions for up- and down-scans asymptotically approaches that for constant voltage as the scan slows. For D_p = 20.8 nm particle, $\bar{\eta}$ = 0.084 and 0.088 for slow up- and down-scan (t_{ramp} = 100 s, ρ_τ = 29.6). For D_p = 2.67 nm particle, $\bar{\eta}$ = 0.045 and 0.046 for slow up- and down-scan (t_{ramp} = 100 s, ρ_τ = 29.6).

For comparison, we also examine the average transmission efficiency for the widely-used DMA, as Figure 4.14, based upon the data from Mai and Flagan (In review) for three different, non-diffusive particle sizes D_p = 147, 296, 498 nm. As with the ROMIAC, $\bar{\eta}$ approaches the stepping-mode limit for slow scans, with the penetration efficiencies $\bar{\eta}$ ranging from 0.144 to 0.152 for the different particle sizes in the 240 s scan (ρ_τ = 4.51). The average transmission efficiency increases as the DMA scan is accelerated, because some of the particles are transmitted during the transition

between ramp period and the constant-voltage periods at the beginning and end of the measurement cycle. This effect is observed at $\rho_\tau < 1$ in the scanning DMA; the ROMIAC scans discussed above were relatively slow, $\rho_\tau > 0.89$. As a result, any enhancement in the transmission efficiency of the ROMIAC should be small due to short residence time t_f within the scanning ROMIAC under the conditions of the present study.

4.5 Conclusions

This study demonstrates that the ROMIAC can be scanned enabling rapid classification of sub-nanometer particles approaching molecular region. Trajectory of transmitted particles were simulated using Brownian dynamics, with the flow- and electric fields calculated with finite-element simulation; the results of these simulations provided the scanning ROMIAC transfer functions for both increasing and decreasing voltage scans. Distortions of the scanning ROMIAC transfer function from that at constant voltage, and asymmetric performance between up- and down-scans were determined using the individual trajectories of the transmitted particles.

Despite the non-ideality of the instrument transfer function, this analysis shows the scanning ROMIAC is able to classify particles in very fast scans, with t_{ramp} = 3 s (corresponding to τ_s =0.44 s), aided by the short residence time within the instrument. Thus, the scanning ROMIAC can measure the nanometer particles when high time-resolution is desired, as in atmospheric nucleation experiments or flight measurements.

Acknowledgements

The authors thank Wilton Mui for providing the design and the COMSOL model of the ROMIAC that made it possible to simulate the particle trajectories in the instrument. The authors gratefully acknowledge support for this work by the National Science Foundation under Grant No. AGS-1602086.

Table 4.1: Operating parameters used for the scanning OMAC

Parameter	Notation	Value
Polydisperse flow rate (LPM)	$Q_{\text{a, in}}$	1.00
Monodisperse flow rate (LPM)	$Q_{\text{a, out}}$	1.00
Incoming cross-flow flow rate (LPM)	$Q_{\text{c, in}}$	10.0
Outgoing cross-flow flow rate (LPM)	$Q_{\text{c, out}}$	10.0
Low electrode voltage (V)	V_{low}	10.0
High electrode voltage (V)	V_{high}	9800
Up/down scan times (s)	$t_{\text{ramp,u/d}}$	3, 6, 12, 25, 50, 100
Holding time at V_{low} (s)	t_{low}	6
Holding time at V_{high} (s)	t_{high}	6

Table 4.2: Time intervals and time steps used for scanning ROMIAC particle trajectory generation; the data format is [Start time : Time step : End time]

t_{ramp} (s)	D_{p} = 2.67 nm		D_{p} = 20.8 nm	
	up scan	down scan	up scan	down scan
3	[5.85:0.025:6.85]	[15.80:0.025:16.90]	[7.50:0.025:8.60]	[13.90:0.025:15.10]
6	[6.80:0.025:7.80]	[20.90:0.025:22.00]	[10.20:0.025:11.30]	[17.20:0.025:18.40]
12	[8.50:0.025:9.80]	[30.90:0.025:32.10]	[15.50:0.025:16.80]	[23.70:0.025:25.10]
25	[12.40:0.05:14.20]	[52.50:0.05:54.30]	[26.80:0.05:28.70]	[37.60:0.05:39.40]
50	[20.0:0.1:22.5]	[94.3:0.1:96.8]	[49.6:0.1:51.6]	[64.5:0.1:67.0]
100	[35.3:0.2:39.1]	[177.8:0.2:181.8]	[94.4:0.2:97.6]	[118.3:0.2:122.3]

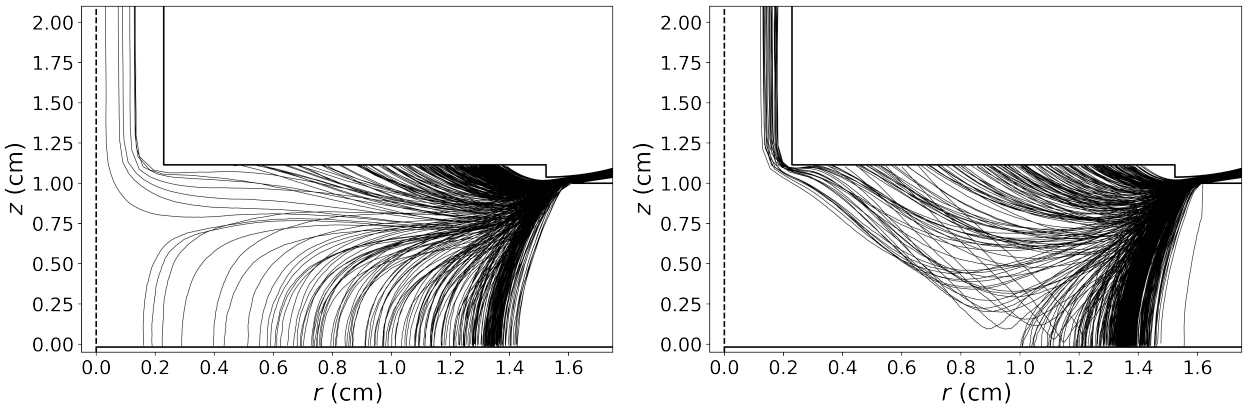

(a) Up scan, $t_{\text{ramp, u}}$ = 3 s

(b) Down scan, $t_{\text{ramp, d}}$ = 3 s

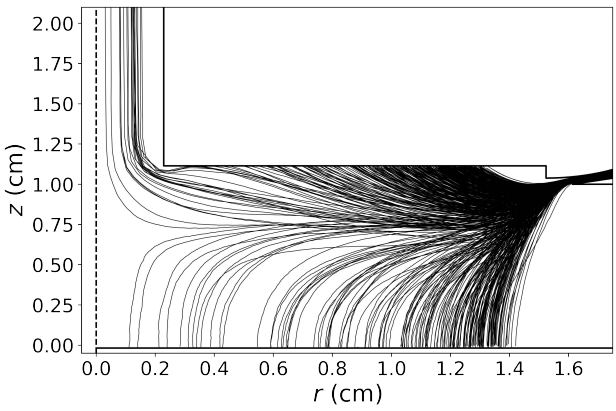

(c) Up scan, $t_{\text{ramp, u}}$ = 6 s

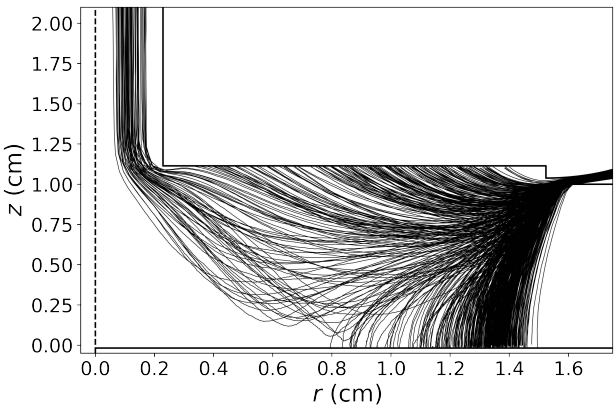

(d) Down scan, $t_{\text{ramp, d}}$ = 6 s

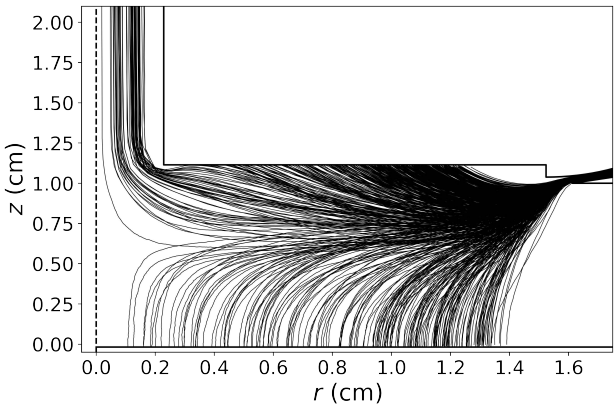

(e) Up scan, $t_{\text{ramp, u}}$ = 12 s

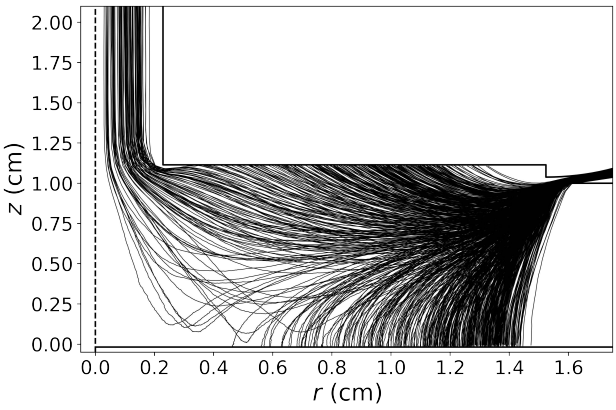

(f) Down scan, $t_{\text{ramp, d}}$ = 12 s

Figure 4.1: Simulated trajectories for 20.8 nm diameter particles during fast 3, 6, 12 s ROMIAC scans (τ_s = 0.436, 0.871, 1.74 s).

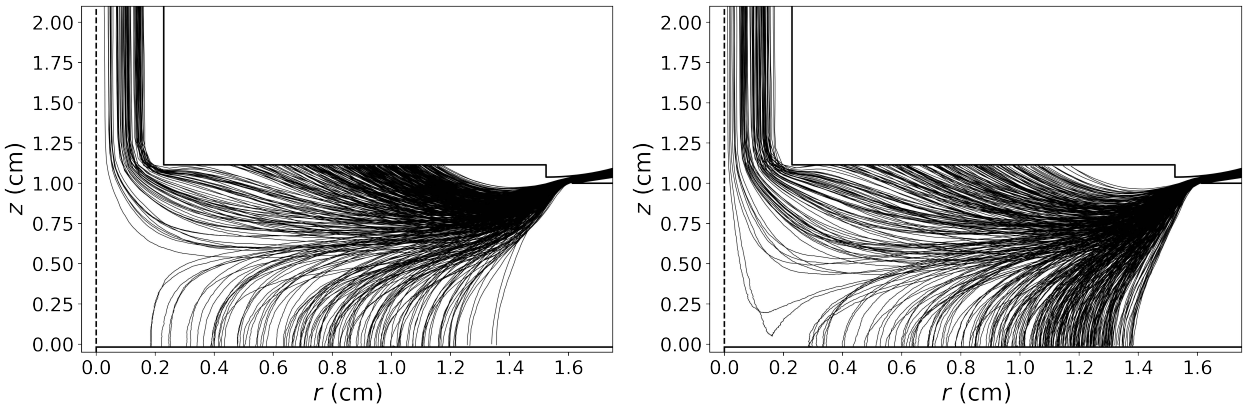

(a) Up scan, $t_{\text{ramp, u}}$ = 25 s

(b) Down scan, $t_{\text{ramp, d}}$ = 25 s

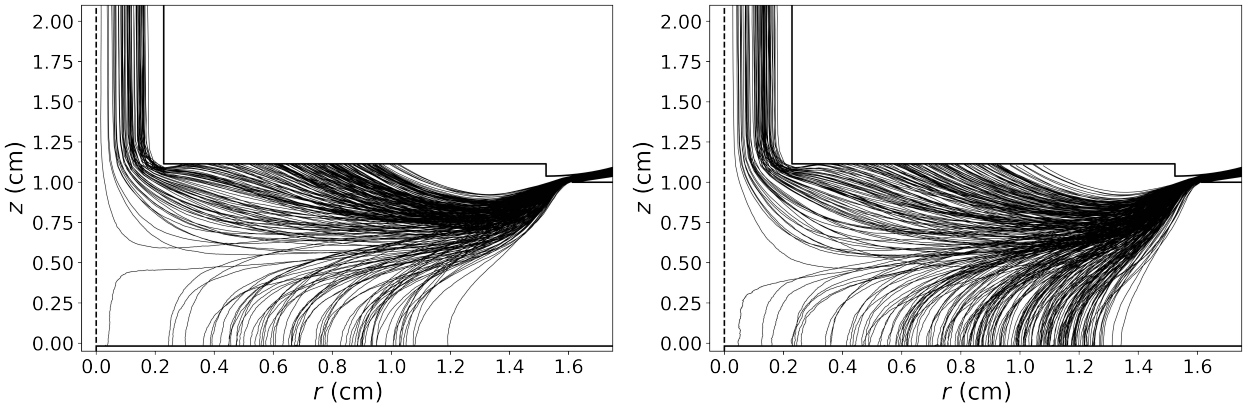

(c) Up scan, $t_{\text{ramp, u}}$ = 50 s

(d) Down scan, $t_{\text{ramp, d}}$ = 50 s

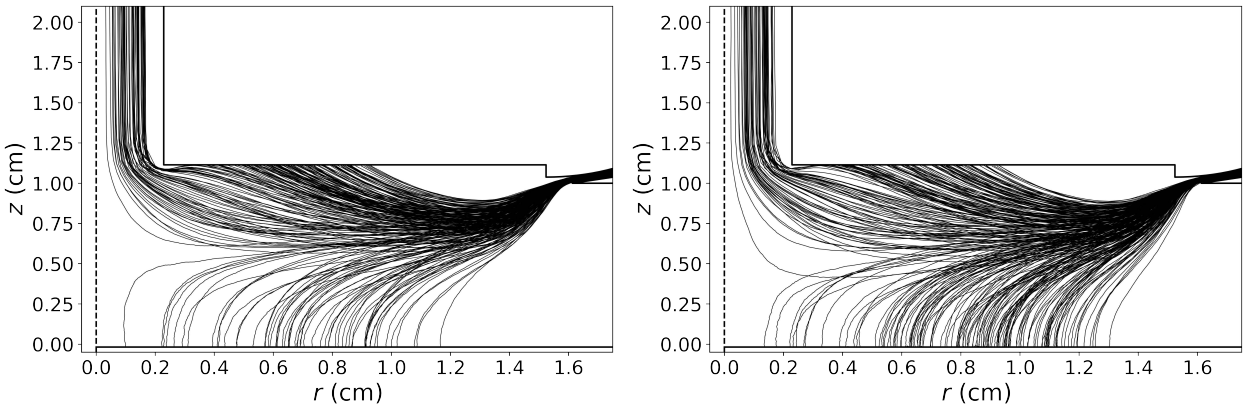

(e) Up scan, $t_{\text{ramp, u}}$ = 100 s

(f) Down scan, $t_{\text{ramp, d}}$ = 100 s

Figure 4.2: Simulated trajectories for 20.8 nm diameter particles during slow 25, 50, 100 s ROMIAC scans (τ_s = 3.63, 7.26, 14.5 s).

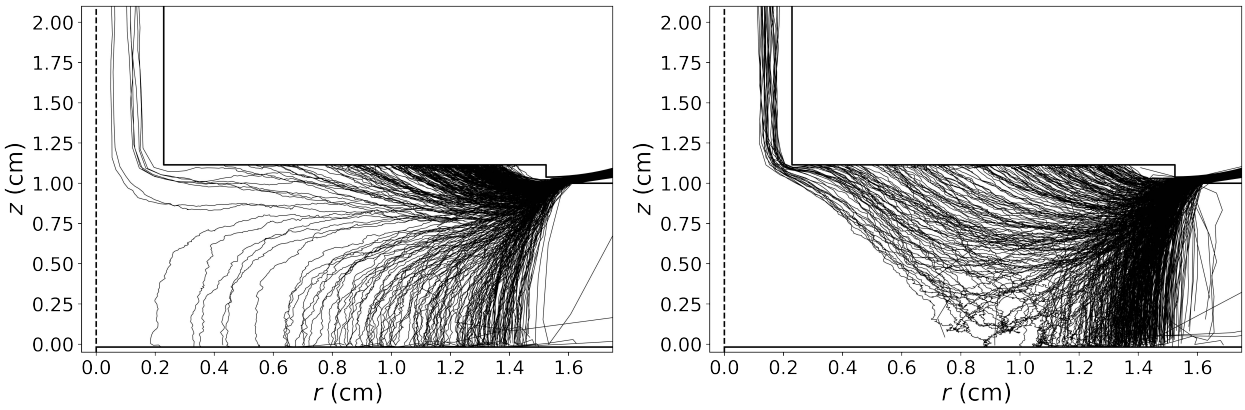

(a) Up scan, $t_{\text{ramp, u}}$ = 3 s

(b) Down scan, $t_{\text{ramp, d}}$ = 3 s

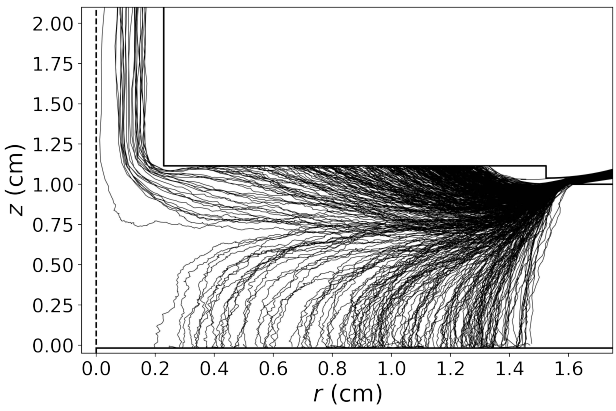

(c) Up scan, $t_{\text{ramp, u}}$ = 6 s

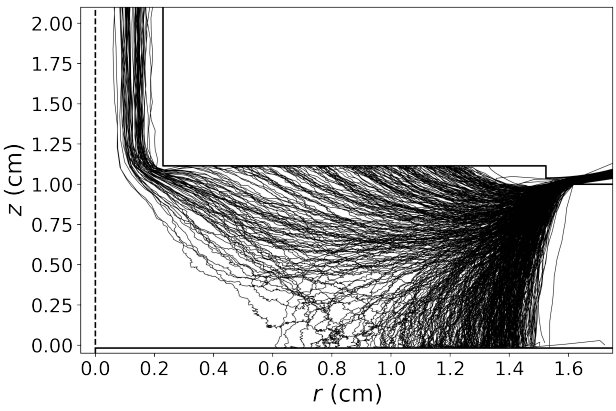

(d) Down scan, $t_{\text{ramp, d}}$ = 6 s

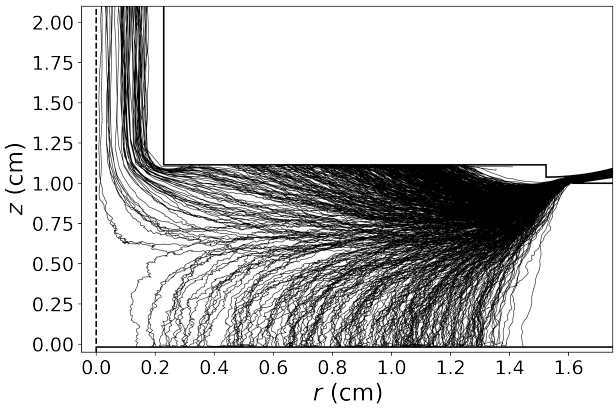

(e) Up scan, $t_{\text{ramp, u}}$ = 12 s

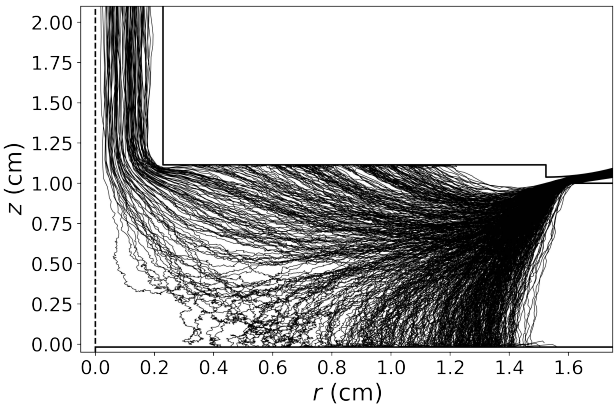

(f) Down scan, $t_{\text{ramp, d}}$ = 12 s

Figure 4.3: Simulated trajectories for 2.67 nm diameter particles during fast 3, 6, 12 s ROMIAC scans (τ_s = 0.436, 0.871, 1.74 s).

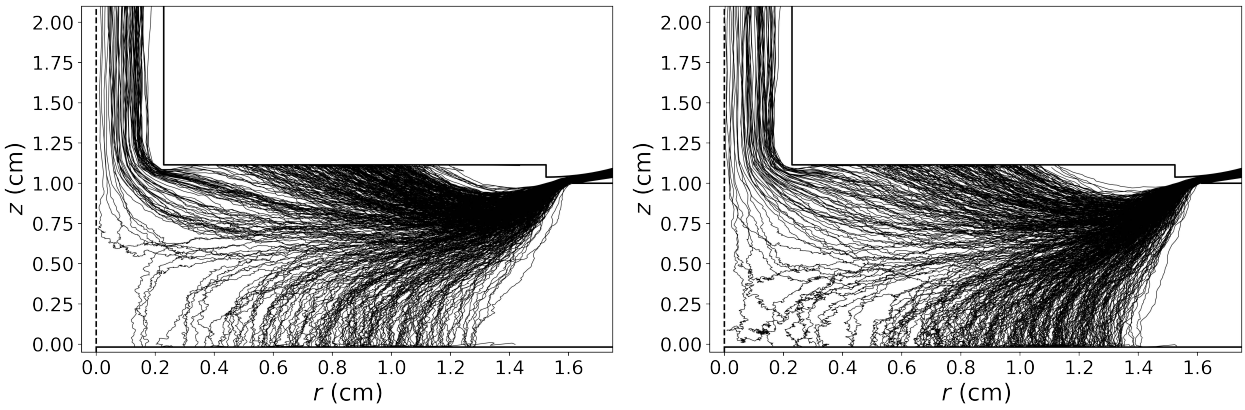

(a) Up scan, $t_{\text{ramp, u}}$ = 25 s

(b) Down scan, $t_{\text{ramp, d}}$ = 25 s

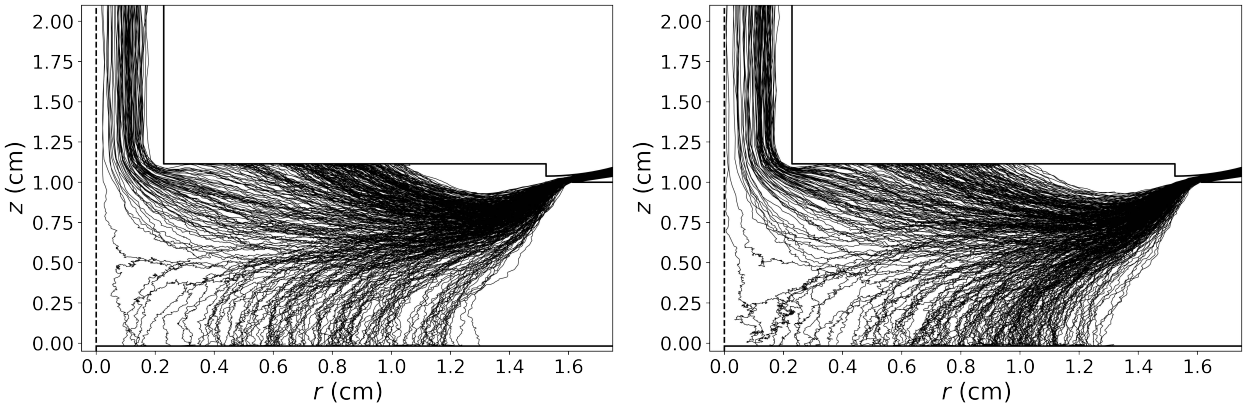

(c) Up scan, $t_{\text{ramp, u}}$ = 50 s

(d) Down scan, $t_{\text{ramp, d}}$ = 50 s

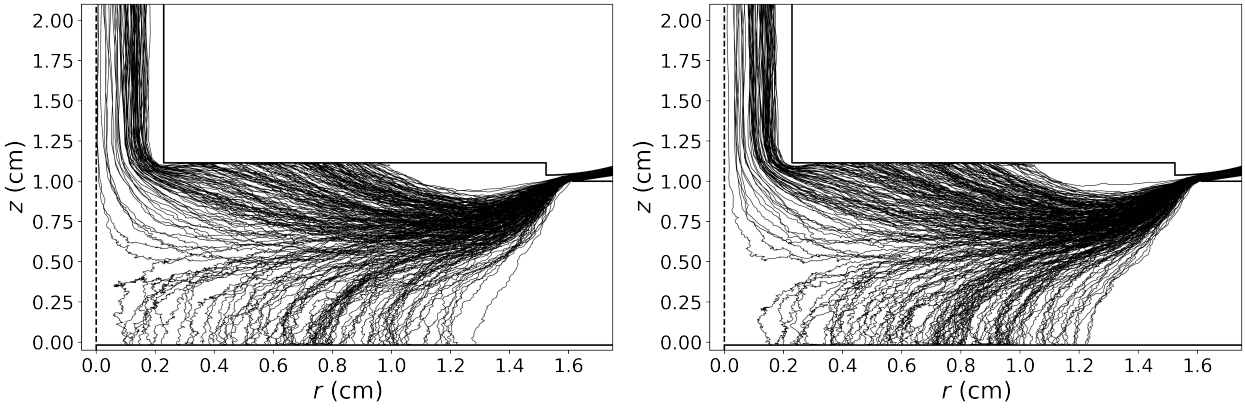

(e) Up scan, $t_{\text{ramp, u}}$ = 100 s

(f) Down scan, $t_{\text{ramp, d}}$ = 100 s

Figure 4.4: Simulated trajectories for 2.67 nm diameter particles during slow 25, 50, 100 s ROMIAC scans (τ_s = 3.63, 7.26, 14.5 s).

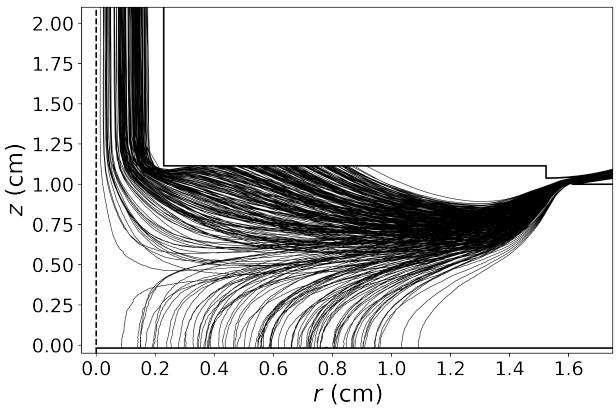

(a) Particle trajectory, D_p = 20.8 nm

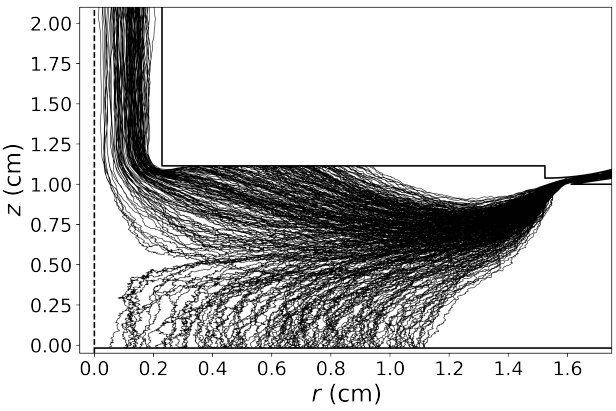

(b) Particle trajectory, D_p = 2.67 nm

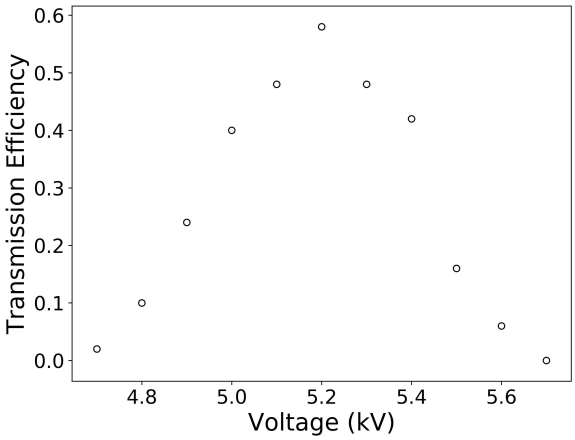

(c) Transfer function, D_p = 20.8 nm

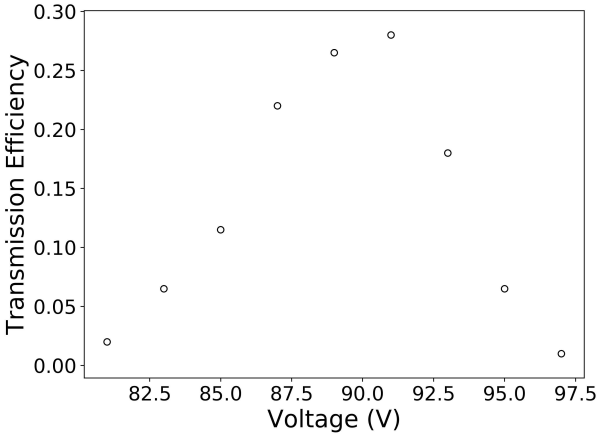

(d) Transfer function, D_p = 2.67 nm

Figure 4.5: Simulated particle trajectories, both successful and unsuccessful, in the stepping-mode (constant voltage) ROMIAC for (a) D_p = 20.8 nm and (b) D_p = 2.67 nm; the corresponding transfer functions are shown in (c) D_p = 20.8 nm and (d) D_p = 2.67 nm.

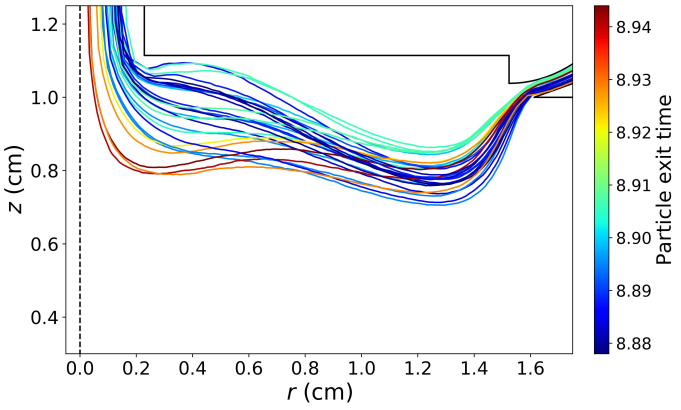

(a) Particle trajectory, $t_{\text{ramp, u}}$ = 3 s

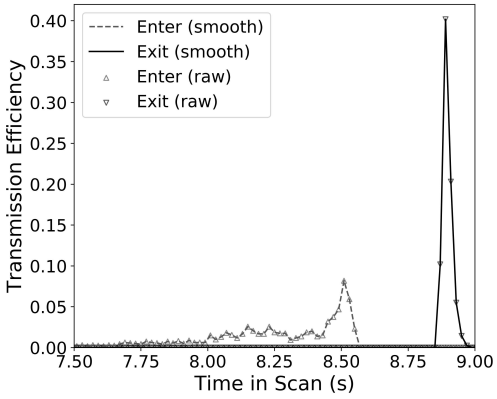

(b) Transfer function, $t_{\text{ramp, u}}$ = 3 s

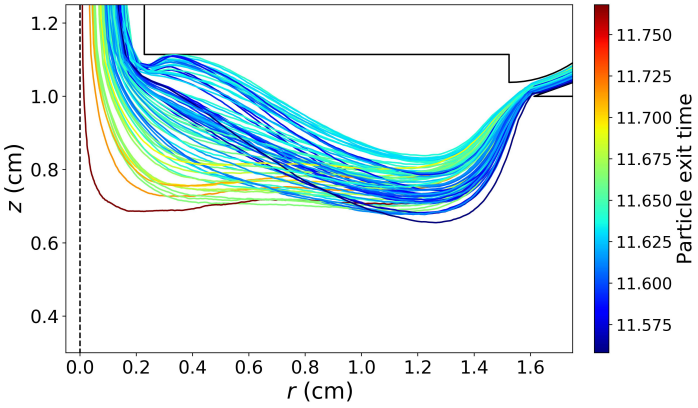

(c) Particle trajectory, $t_{\text{ramp, u}}$ = 6 s

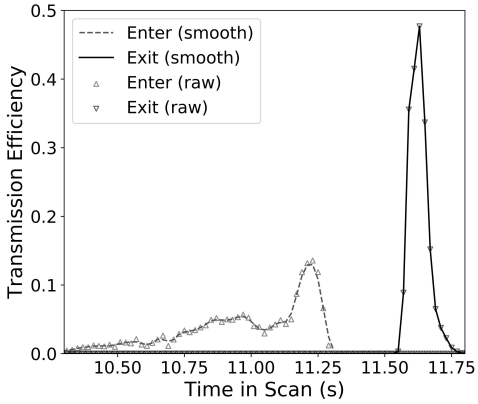

(d) Transfer function, $t_{\text{ramp, u}}$ = 6 s

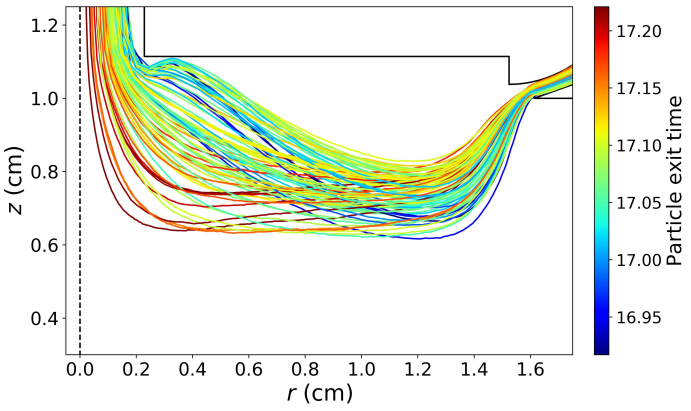

(e) Particle trajectory, $t_{\text{ramp, u}}$ = 12 s

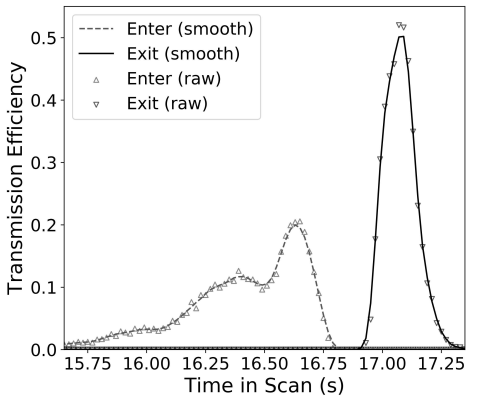

(f) Transfer function, $t_{\text{ramp, u}}$ = 12 s

Figure 4.6: Simulated trajectories of 20.8 nm particles that were successfully transmitted during fast t_{ramp} / τ_s = (a) 3 / 0.436 s, (c) 6 / 0.871 s, and (e) 12 / 1.74 s up-scans; the color bar denotes the time at which the particle exited the classification region. The corresponding up-scan transfer function are shown in (b) t_{ramp} = 3, (d) t_{ramp} = 6, (f) t_{ramp} = 12 s.

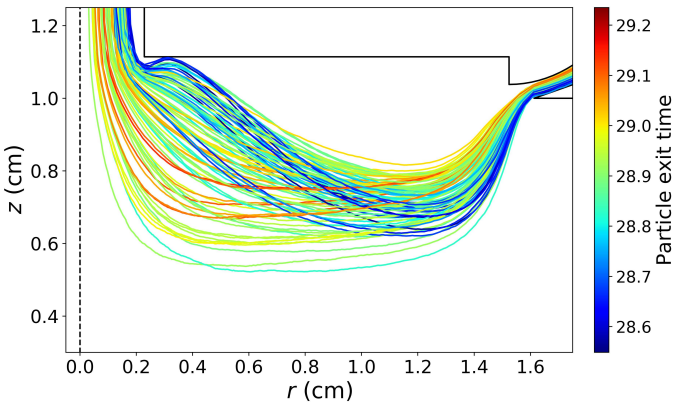

(a) Particle trajectory, $t_{\text{ramp, u}}$ = 25 s

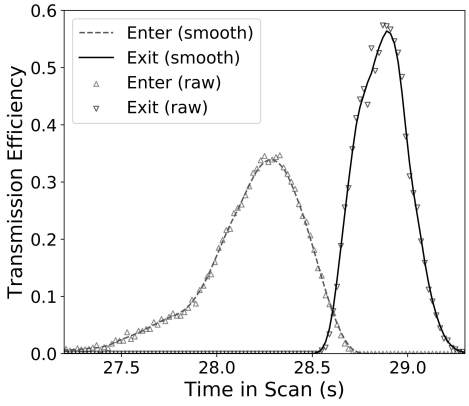

(b) Transfer function, $t_{\text{ramp, u}}$ = 25 s

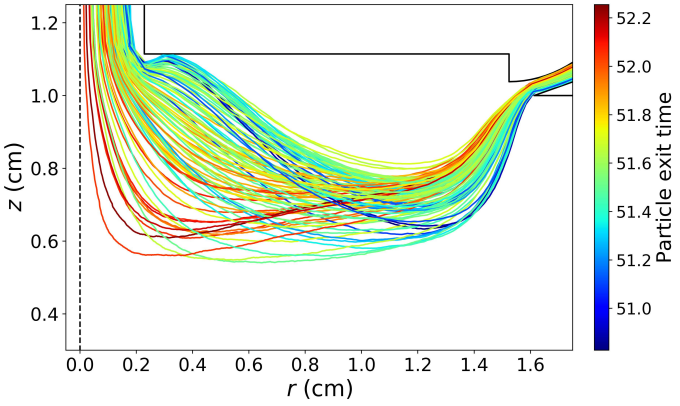

(c) Particle trajectory, $t_{\text{ramp, u}}$ = 50 s

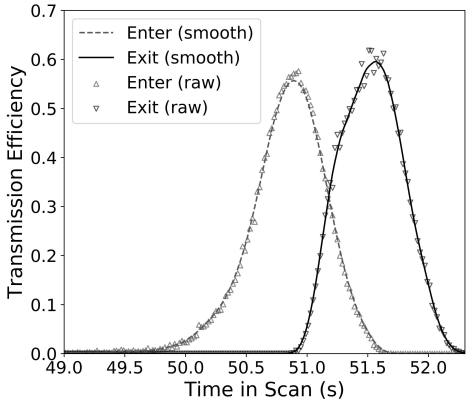

(d) Transfer function, $t_{\text{ramp, u}}$ = 50 s

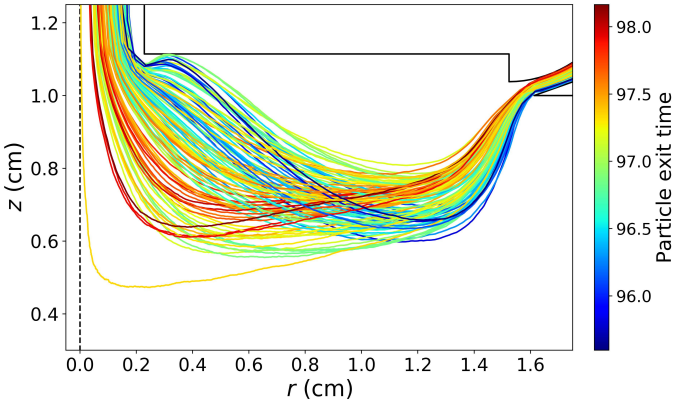

(e) Particle trajectory, $t_{\text{ramp, u}}$ = 100 s

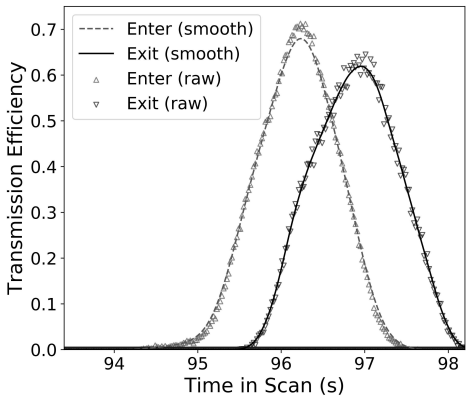

(f) Transfer function, $t_{\text{ramp, u}}$ = 100 s

Figure 4.7: Simulated trajectories of 20.8 nm particles that were successfully transmitted during slow t_{ramp} / τ_s = (a) 25 / 3.63 s, (c) 50 / 7.26 s, and (e) 100 / 14.5 s up-scans; the color bar denotes the time at which the particle exited the classification region. The corresponding up-scan transfer function are shown in (b) t_{ramp} = 25, (d) t_{ramp} = 50, (f) t_{ramp} = 100 s.

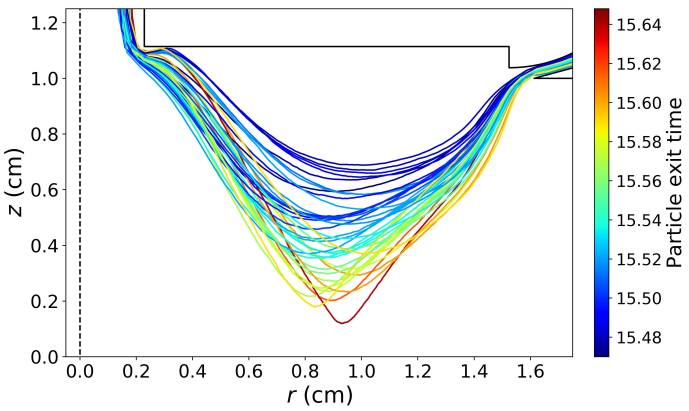

(a) Particle trajectory, $t_{\text{ramp, d}}$ = 3 s

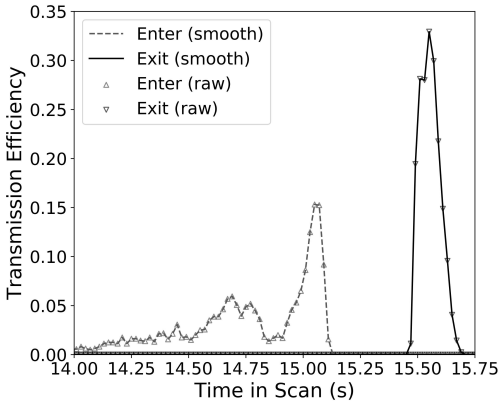

(b) Transfer function, $t_{\text{ramp, d}}$ = 3 s

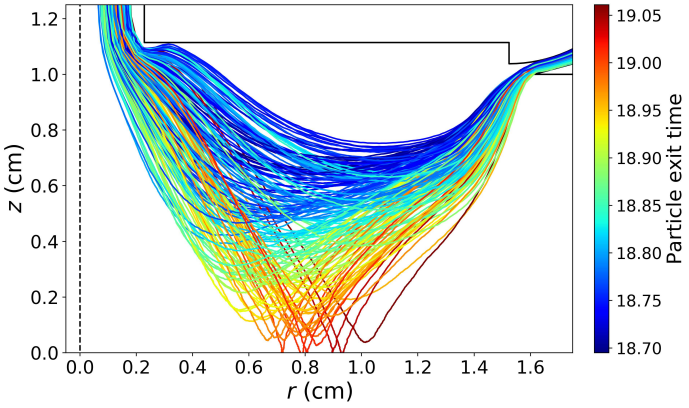

(c) Particle trajectory, $t_{\text{ramp, d}}$ = 6 s

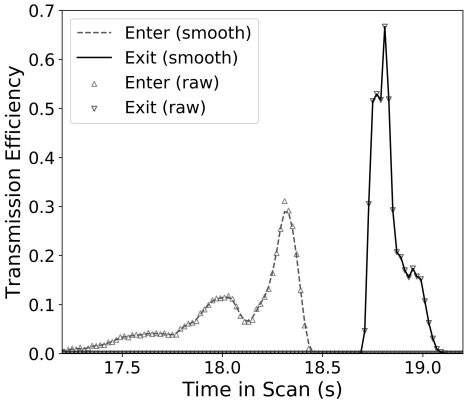

(d) Transfer function, $t_{\text{ramp, d}}$ = 6 s

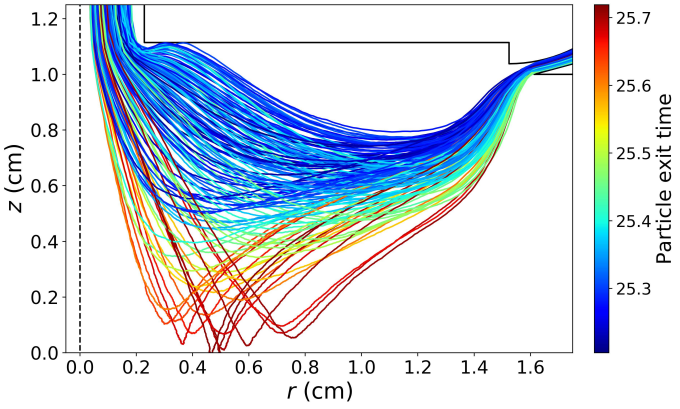

(e) Particle trajectory, $t_{\text{ramp, d}}$ = 12 s

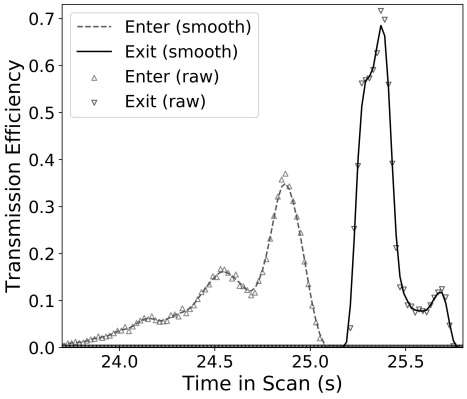

(f) Transfer function, $t_{\text{ramp, d}}$ = 12 s

Figure 4.8: Simulated trajectories of 20.8 nm particles that were successfully transmitted during fast t_{ramp} / τ_s = (a) 3 / 0.436 s, (c) 6 / 0.871 s, and (e) 12 / 1.74 s down-scans; the color bar denotes the time at which the particle exited the classification region. The corresponding down-scan transfer function are shown in (b) t_{ramp} = 3, (d) t_{ramp} = 6, (f) t_{ramp} = 12 s.

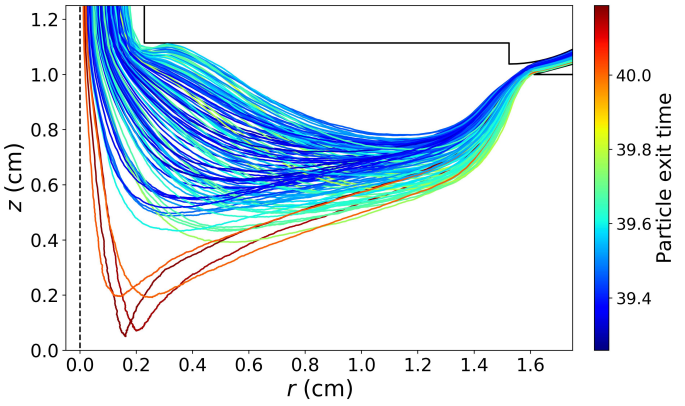

(a) Particle trajectory, $t_{\text{ramp, d}}$ = 25 s

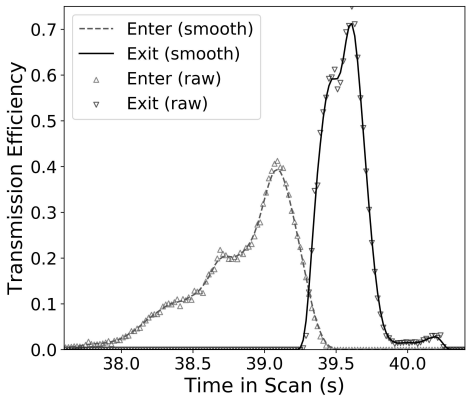

(b) Transfer function, $t_{\text{ramp, d}}$ = 25 s

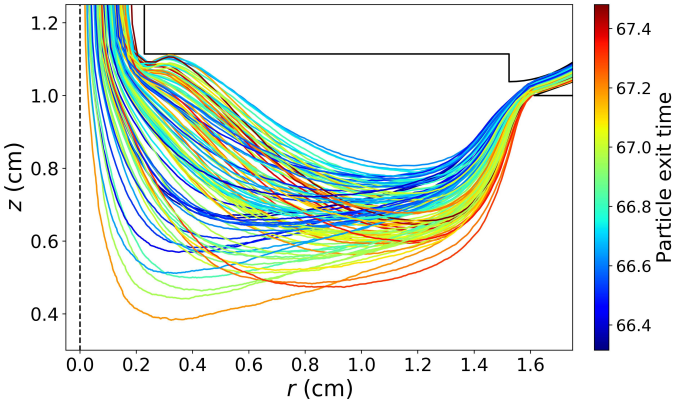

(c) Particle trajectory, $t_{\text{ramp, d}}$ = 50 s

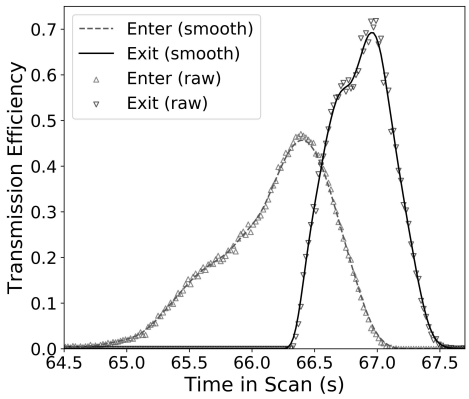

(d) Transfer function, $t_{\text{ramp, d}}$ = 50 s

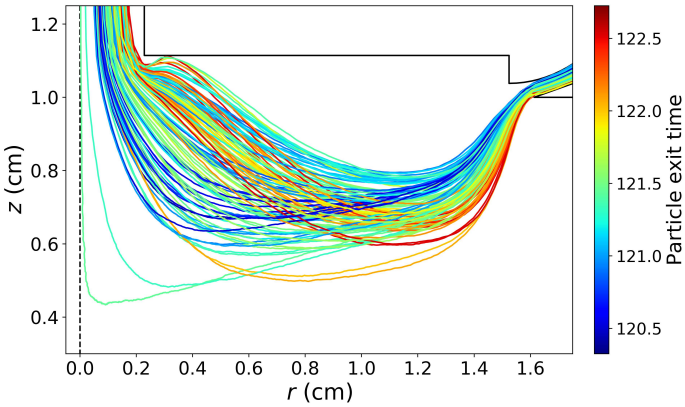

(e) Particle trajectory, $t_{\text{ramp, d}}$ = 100 s

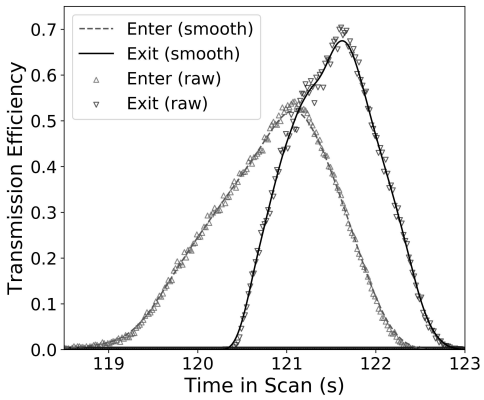

(f) Transfer function, $t_{\text{ramp, d}}$ = 100 s

Figure 4.9: Simulated trajectories of 20.8 nm particles that were successfully transmitted during slow t_{ramp} / τ_s = (a) 25 / 3.63 s, (c) 50 / 7.26 s, and (e) 100 / 14.5 s down-scans; the color bar denotes the time at which the particle exited the classification region. The corresponding up-scan transfer function are shown in (b) t_{ramp} = 25, (d) t_{ramp} = 50, (f) t_{ramp} = 100 s.

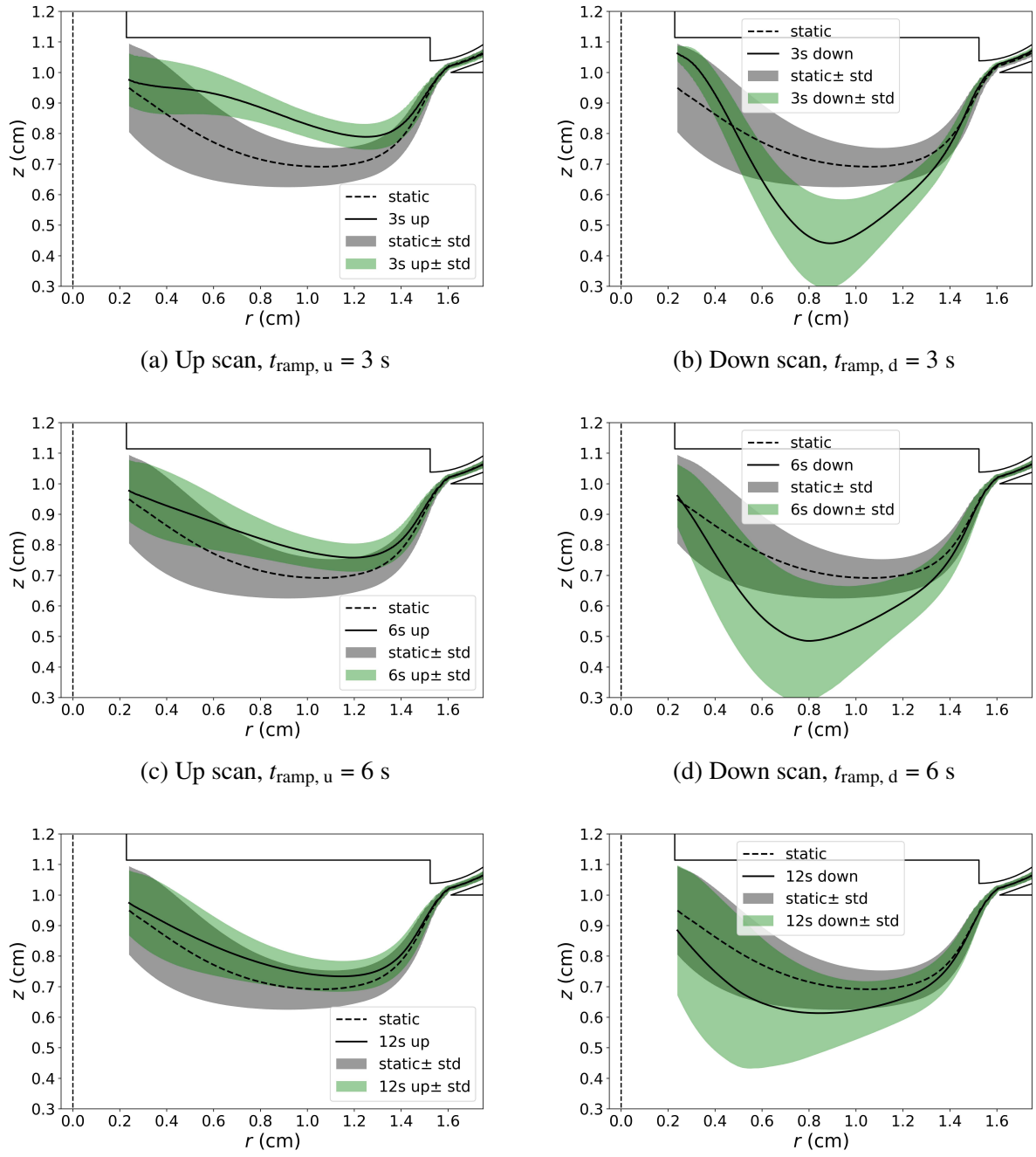

(a) Up scan, $t_{\text{ramp, u}}$ = 3 s

(b) Down scan, $t_{\text{ramp, d}}$ = 3 s

(c) Up scan, $t_{\text{ramp, u}}$ = 6 s

(d) Down scan, $t_{\text{ramp, d}}$ = 6 s

(e) Up scan, $t_{\text{ramp, u}}$ = 12 s

(f) Down scan, $t_{\text{ramp, d}}$ = 12 s

Figure 4.10: Mean particle trajectories (solid lines) and corresponding standard deviations (green shaded area) for 20.8 nm particles that were successfully transmitted during fast t_{ramp} / τ_{s} = (a) 3 / 0.436 s, (c) 6 / 0.871 s, and (e) 12 / 1.74 s scans. For comparison, trajectories (dashed lines) and corresponding standard deviations (gray shaded area) from steady-state operation are plotted for each scan time rate.

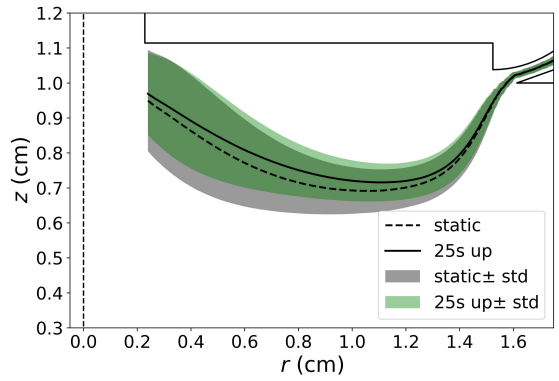

(a) Up scan, $t_{\text{ramp, u}}$ = 25 s

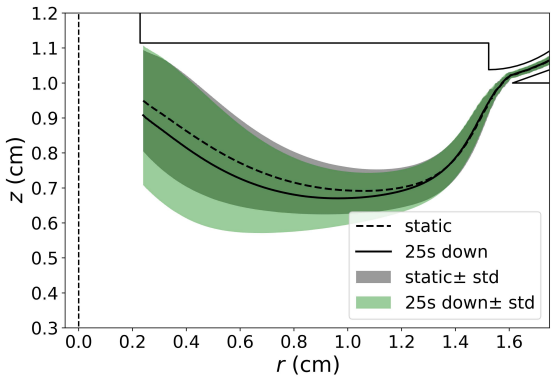

(b) Down scan, $t_{\text{ramp, d}}$ = 25 s

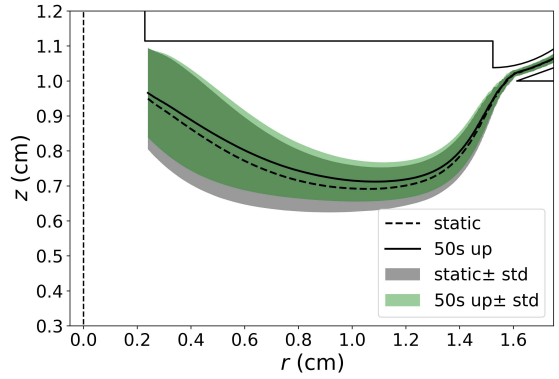

(c) Up scan, $t_{\text{ramp, u}}$ = 50 s

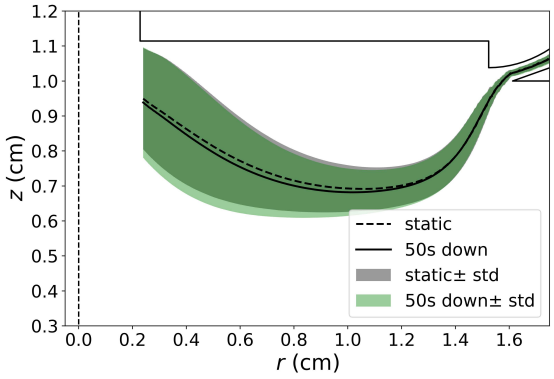

(d) Down scan, $t_{\text{ramp, d}}$ = 50 s

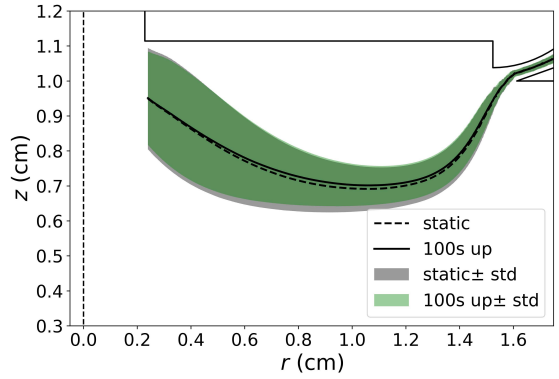

(e) Up scan, $t_{\text{ramp, u}}$ = 100 s

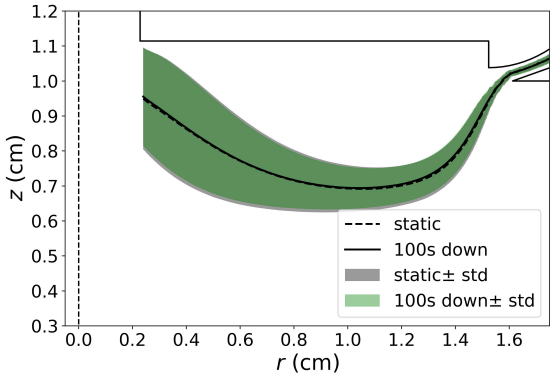

(f) Down scan, $t_{\text{ramp, d}}$ = 100 s

Figure 4.11: Mean particle trajectories (solid lines) and corresponding standard deviations (green shaded area) for 20.8 nm particles that were successfully transmitted during slow t_{ramp} / τ_s = (a) 25 / 3.63 s, (c) 50 / 7.26 s, and (e) 100 / 14.5 s scans. For comparison, trajectories (dashed lines) and corresponding standard deviations (gray shaded area) from steady-state operation are plotted for each scan time rate.

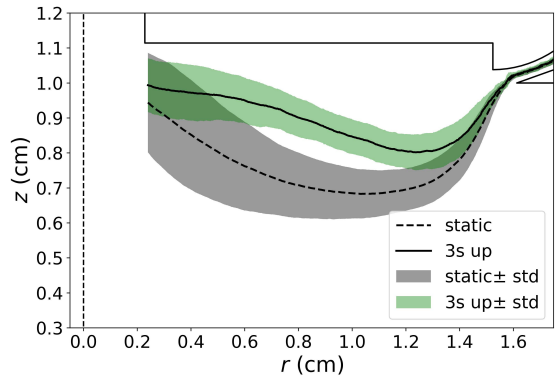

(a) Up scan, $t_{\text{ramp, u}}$ = 3 s

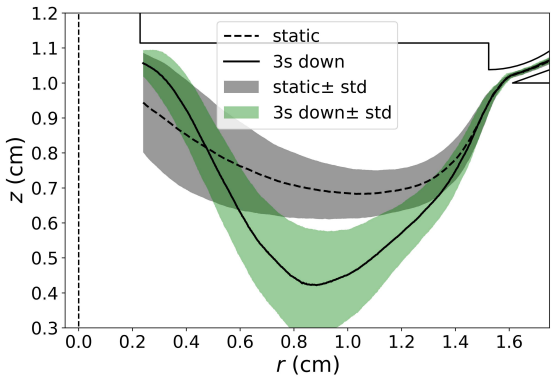

(b) Down scan, $t_{\text{ramp, d}}$ = 3 s

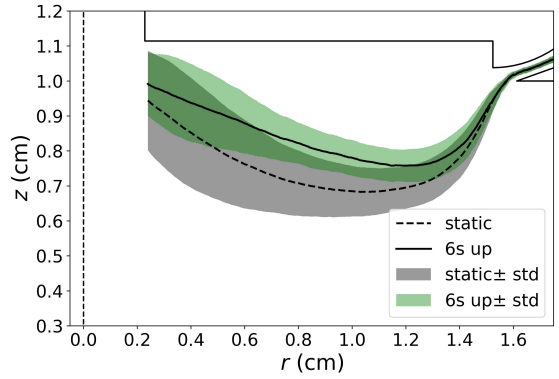

(c) Up scan, $t_{\text{ramp, u}}$ = 6 s

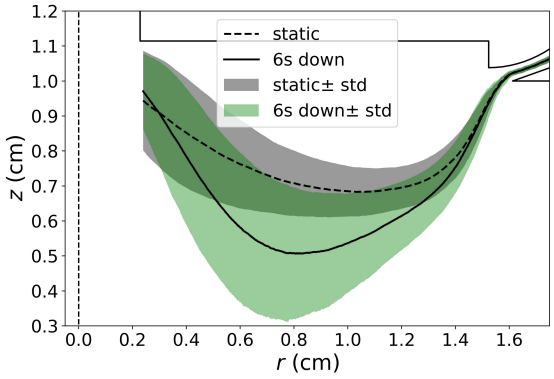

(d) Down scan, $t_{\text{ramp, d}}$ = 6 s

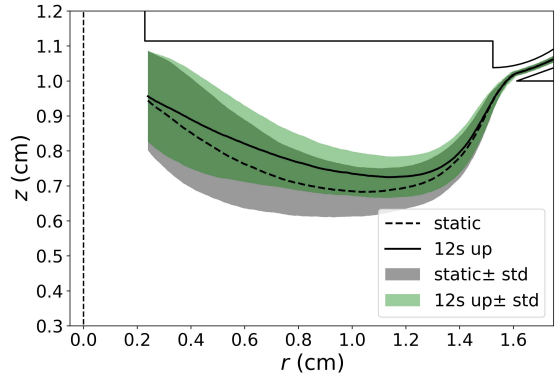

(e) Up scan, $t_{\text{ramp, u}}$ = 12 s

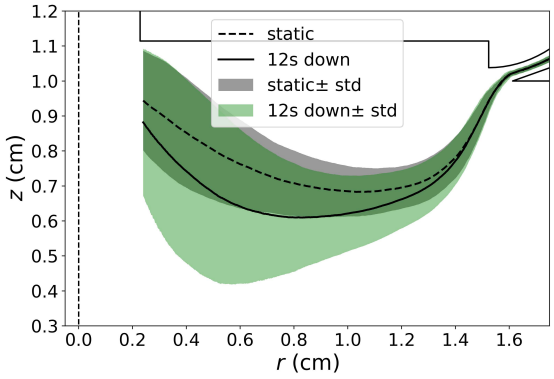

(f) Down scan, $t_{\text{ramp, d}}$ = 12 s

Figure 4.12: Mean particle trajectories (solid lines) and corresponding standard deviations (green shaded area) for 2.67 nm particles that were successfully transmitted during fast t_{ramp} / τ_{s} = (a) 3 / 0.436 s, (c) 6 / 0.871 s, and (e) 12 / 1.74 s scans. For comparison, trajectories (dashed lines) and corresponding standard deviations (gray shaded area) from steady-state operation are plotted for each scan time rate.

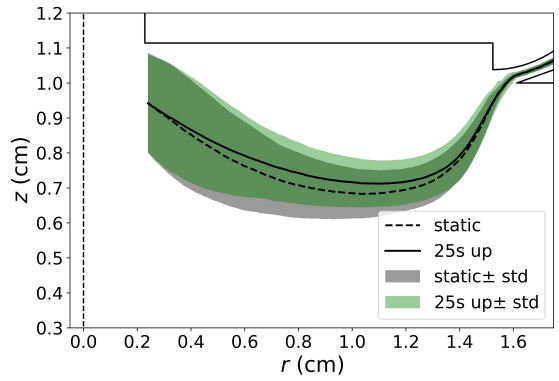

(a) Up scan, $t_{\text{ramp, u}}$ = 25 s

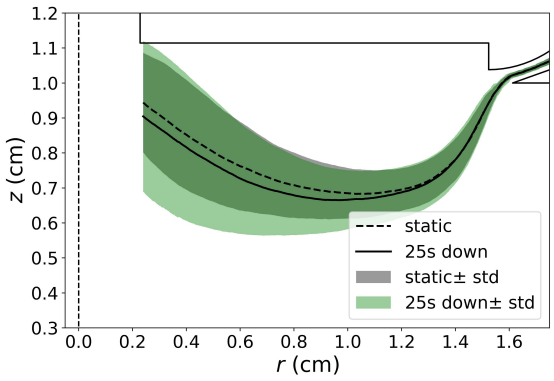

(b) Down scan, $t_{\text{ramp, d}}$ = 25 s

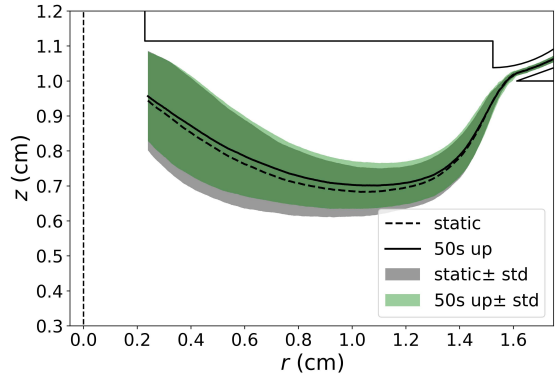

(c) Up scan, $t_{\text{ramp, u}}$ = 50 s

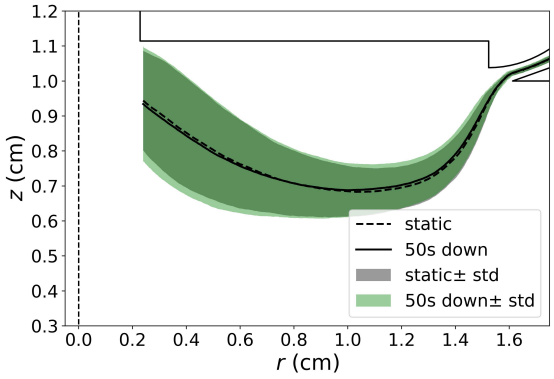

(d) Down scan, $t_{\text{ramp, d}}$ = 50 s

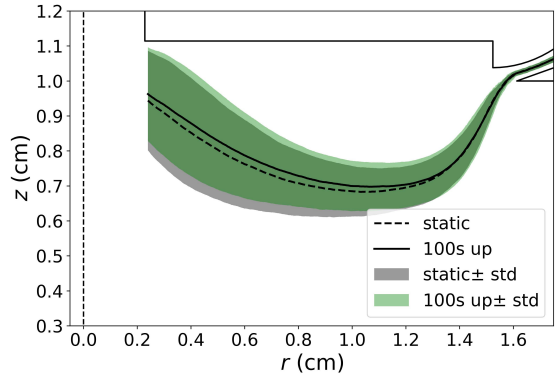

(e) Up scan, $t_{\text{ramp, u}}$ = 100 s

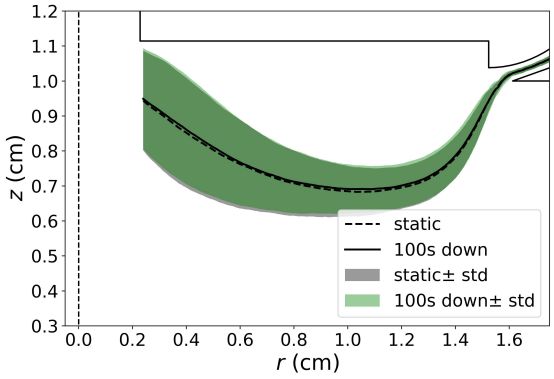

(f) Down scan, $t_{\text{ramp, d}}$ = 100 s

Figure 4.13: Mean particle trajectories (solid lines) and corresponding standard deviations (green shaded area) for 2.67 nm particles that were successfully transmitted during slow t_{ramp} / τ_s = (a) 25 / 3.63 s, (c) 50 / 7.26 s, and (e) 100 / 14.5 s scans. For comparison, trajectories (dashed lines) and corresponding standard deviations (gray shaded area) from steady-state operation are plotted for each scan time scale.

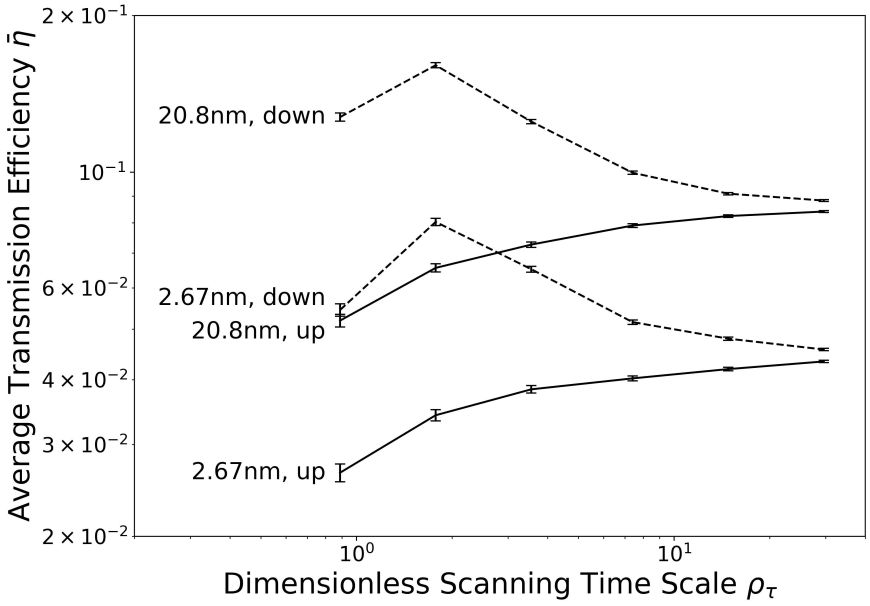

(a) OMAC

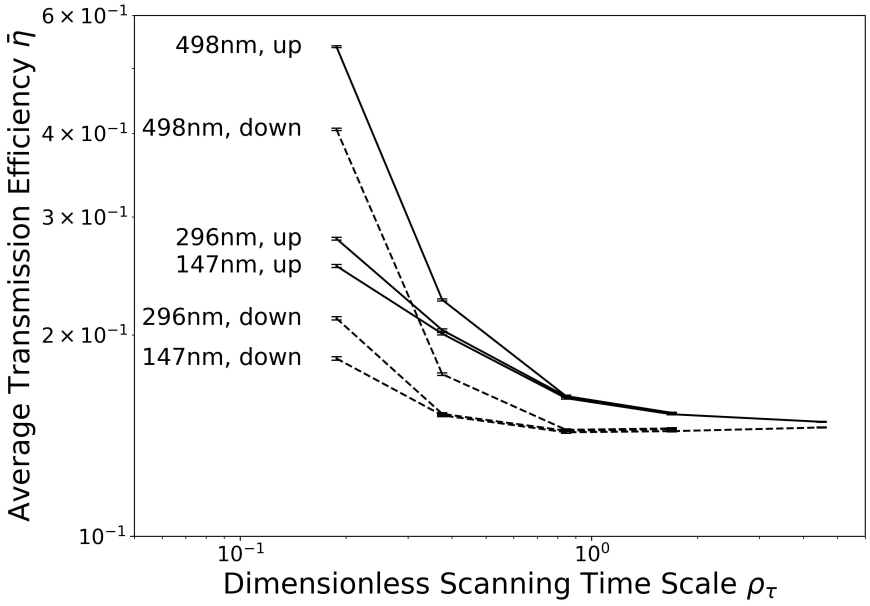

(b) DMA

Figure 4.14: Average transmission efficiency $\bar{\eta}$ variation with the dimensionless scan time, $\rho_\tau = \tau_s/\tau_f$ for (a) the ROMIAC and (b) the DMA. Solid lines show up-scan results, while dashed lines show down-scan results.

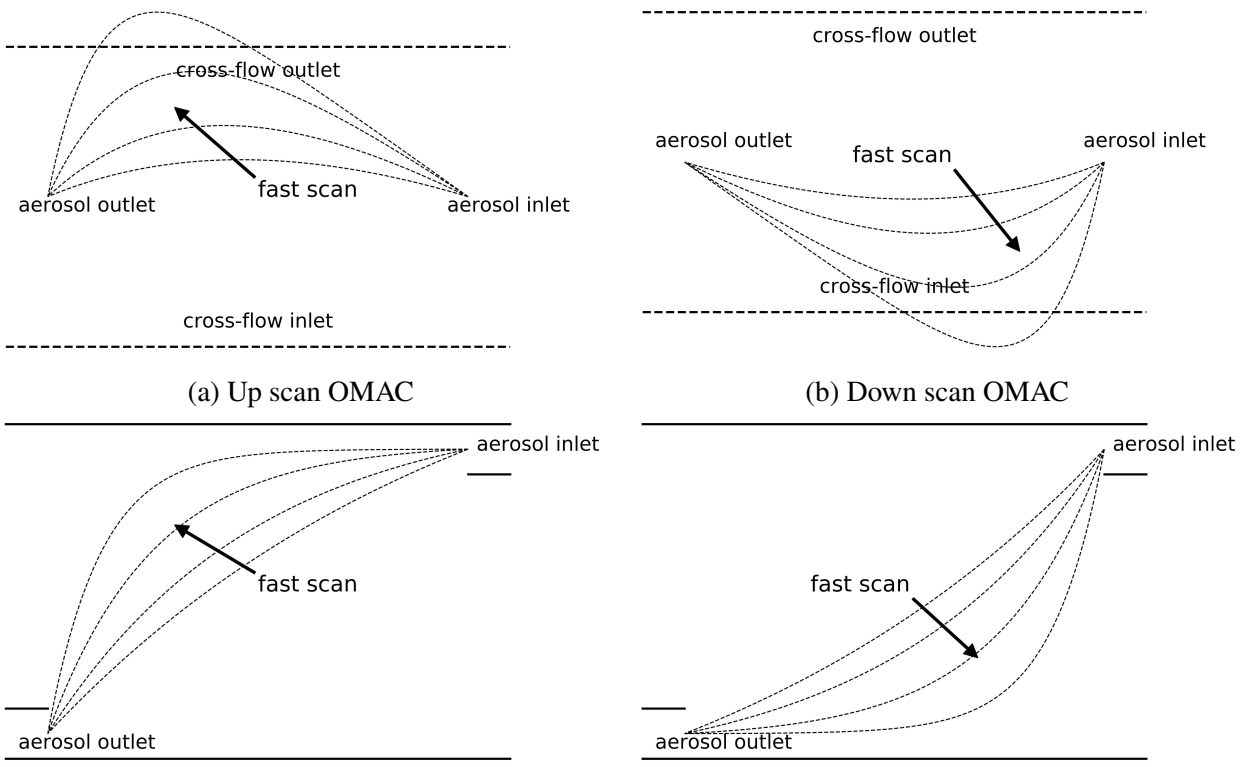

Figure 4.15: Conceptual particle trajectories to illustrate the effects of scanning on the transmission efficiency in the scanning OMAC ((a) up scan, (b) down scan) and the scanning DMA ((c) up scan, (d) down scan).

References

Cleveland, William S (1979). "Robust locally weighted regression and smoothing scatterplots". In: *Journal of the American Statistical Association* 74.368, pp. 829–836.

Flagan, Richard C. (1999). "On differential mobility analyzer resolution". In: *Aerosol Sci Tech* 30.6, pp. 556–570.

– (2004). "Opposed Migration Aerosol Classifier (OMAC)". In: *Aerosol Science and Technology* 38.9, pp. 890–899. DOI: 10.1080/027868290505242. eprint: https://doi.org/10.1080/027868290505242. URL: https://doi.org/10.1080/027868290505242.

Mai, Huajun and Richard C. Flagan (In review). "Scanning DMA Data Analysis I. Classification Transfer Function". In: *Aerosol Science and Technology*.

Mai, Huajun, Weimeng Kong, John H. Seinfeld, and Richard C. Flagan (In review). "Scanning DMA data analysis. II. Integrated DMA-CPC instrument response and data inversion". In: *Aerosol Science and Technology*.

Mui, Wilton, Huajun Mai, et al. (2017). "Design, simulation, and characterization of a radial opposed migration ion and aerosol classifier (ROMIAC)". In: *Aerosol Science and Technology* 51.7, pp. 801–823.

Mui, Wilton, Daniel A. Thomas, et al. (2013). "Ion Mobility-Mass Spectrometry with a Radial Opposed Migration Ion and Aerosol Classifier (ROMIAC)". In: *Analytical Chemistry* 85.13. PMID: 23730869, pp. 6319–6326. DOI: 10.1021/ac400580u. eprint: https://doi.org/10.1021/ac400580u. URL: https://doi.org/10.1021/ac400580u.

Wang, Shih Chen and Richard C. Flagan (1990). "Scanning Electrical Mobility Spectrometer". In: *Aerosol Science and Technology* 13.2, pp. 230–240.

SCANNING OPPOSED MIGRATION AEROSOL CLASSIFIER (OMAC) SYSTEM AND DATA INVERSION

By Huajun Mai, Michel Attoui, and Richard C. Flagan

5.1 Introduction

This chapter introduces a new method for retrieval of the particle size distributions from scanning differential mobility measurement data. Mai and Flagan (In review) derived the transfer function for the scanning differential mobility analyzer (DMA) by using finite element calculations to obtain the flow field and electric field within a real DMA, and then simulating particle trajectories within the instrument during scanning mobility measurements. That transfer function was integrated with an empirical model of the time response of a condensation particle counter (CPC) detection. The integrated DMA-CPC instrument response was validated with the experimentally measured instrument responses to monodisperse polystyrene latex (PSL) calibration particles (Mai, Kong, et al., In review). Although the simulated scanning mobility analyzer transfer function proved very effective at recovering the particle size distributions, the use of Brownian dynamics simulations renders the method impractical for routine use due to the high computational cost. Moreover, measuring the instrument response for a wide range of monodisperse PSL particles is also costly. While generating monodisperse aerosols may not be practical, a polydisperse aerosol can be generated in a number of ways, such as atomizing the salt solution, evaporation and condensation of semi-volatile or even refractory material in a furnace, or evaporation of metal from a hot wire. Any such stable source of particles can then be used with a tandem differential mobility classifier system to empirically deduce the integrated instrument transfer functions as will be shown in the chapter. Traditionally, differential mobility analyzers (DMAs) are employed in such tandem systems, but we will employ an alternate form of classifier in this study.

This tandem differential mobility analysis protocol has been well established for DMA calibration and other instrument characterization studies, but our purpose here is to deduce the instrument response function with sufficient fidelity to enable data inversion directly from the experimental results. The method for determining the instrument response function and extracting particle size distribution distributions involves the following steps: (*i*) measure the instrument response using mobility-classified particles from a polydisperse aerosol with known size distribution; (*ii*) compute

the kernel for the size distribution inversion based on the data from step (*i*).

We demonstrate this method by determining the integrated instrument response function of the scanning ROMIAC (radial opposed migration ion and aerosol classifier, Mui, Thomas, et al. (2013) and Mui, Mai, et al. (2017)) system in this chapter. The polydisperse aerosol for measuring the instrument response is generated from the heated Nichrome wire (hot wire source particles).

5.2 Methods

Scanning ROMIAC size distribution measurement system

Figure 5.1 shows the experimental system used for scanning ROMIAC particle size distribution measurement in the range of 1-20 nm. The ROMIAC, which is described in detail by Mui, Thomas, et al. (2013) and Mui, Mai, et al. (2017), is used as the particle classifier in the present study. Its operating parameters are given in Table 5.1. To detect nanometer particles to sizes below 3 nm in diameter, a two-stage CPC is used as the particle counter. The first-stage of the detector, which uses diethylene glycol (DEG) as the working fluid to activate the sampled particles, with a saturator flow rate of 0.2 liter per minute (LPM), and a cold aerosol sample flow rate of 1.0 LPM. The activated sampled particles are passed through a condenser, where the particle size increases due to condensation of the DEG vapor on the activated particles. A TSI 3760 CPC is used as the second stage for further particle growth and the final particle detection. The sample flow rate of the TSI 3760 CPC used here is 1.56 LPM at a laboratory temperature of T = 295 K. Since the detection CPC requires a larger flow than is supplied by the first stage, a dilution flow of 0.36 LPM is needed between the condenser and the TSI 3760 CPC.

The detection efficiency of the two-stage CPC is calibrated with an aerosol electrometer. The two-stage CPC and aerosol electrometer are each supplied with classified particles generated from the hot wire source. The experimental set-up for the CPC calibration is shown in Figure 5.2. The hot wire source aerosol generator is powered by a DC power supply with voltage set at 7.5 V, and the current running through the Nichrome wire is around 5.2 A for this experiment. ROMIAC alpha is operated with balanced (equal aerosol and classified sample) flow rates of Q_{a} = 2.5 LPM ; the cross-flow flow rate is Q_{c} = 35.5 LPM. The aerosol electrometer (AE) samples at 2.36 LPM, which is controlled by the critical orifice at its exhaust port. The two-stage CPC samples aerosol at 1.0 LPM; the saturator and condensor temperatures are 70 °C and 4 °C, respectively. The CPC counting efficiency relative to that of the aerosol electrometer is shown in Figure 5.3 for measurements of classified particles from the hot-wire source. The 50% cut-off size is around 1.6 nm. The counting efficiency reaches plateau for the electrical mobility equivalent particle sizes larger than 2.1 nm. The experimentally-measured, two-stage CPC counting efficiency has been

fitted with logistic equation, *i.e.*,

$$\eta = \frac{\eta_{\max}}{1 + e^{-k(D_{\mathrm{p}} - D_{\mathrm{p},0})}}, \tag{5.1}$$

where $\eta_{\max} = 0.841$, $k = 6.30\ \mathrm{nm}^{-1}$ and $D_{\mathrm{p},0} = 1.54$ nm are the parameters determined by fitting.

The residence time distribution of the two-stage CPC is determined using the method of Mai, Kong, et al. (In review) by measuring the particle counts following spark-pulse events. The experimentally measured residence time distribution, $E(t)$, from the two-stage CPC is shown in Figure 5.4; the mean residence time was found to be 1.183 s. The CPC residence time distribution, $E(t)$, has been fitted with two models. The first model describes the flow system as a plug flow reactor (PFR) in series with a continuous stirred-tank reactor (CSTR), with the residence time distribution function that is determined by the convolution of the time response functions of the two modules, *i.e.*,

$$E_{\mathrm{cp}}(t) = E_{\mathrm{p}}(t) \star E_{\mathrm{c}}(t) = \int_{-\infty}^{\infty} E_{\mathrm{c}}(t') E_{\mathrm{p}}(t - t') \mathrm{d}t' = \begin{cases} 0, & t < \tau_{\mathrm{p}} \\ \frac{1}{\tau_{\mathrm{c}}} e^{-\frac{t-\tau_{\mathrm{p}}}{\tau_{\mathrm{c}}}}, & t \geq \tau_{\mathrm{p}}, \end{cases} \tag{5.2}$$

where τ_{c} and τ_{p} are the mean residence times of the CSTR and PFR, respectively. The optimized time scales determined using a weighted least-sequres fit are $\tau_{\mathrm{c}} = 0.354$ s and $\tau_{\mathrm{p}} = 0.778$ s. The second model adds a laminar flow reactor (LFR) to the first model, with the following residence time distribution function, following Mai, Kong, et al. (In review),

$$E_{\mathrm{lcp}}(t) = \begin{cases} 0, & t < \frac{\tau_{\mathrm{l}}}{2} + \tau_{\mathrm{p}} \\ \dfrac{\tau_{\mathrm{l}}^2 \exp\left(-\frac{t-\tau_{\mathrm{p}}}{\tau_{\mathrm{c}}}\right) \left[\mathrm{Ei}\left(\frac{t-\tau_{\mathrm{p}}}{\tau_{\mathrm{c}}}\right) - \mathrm{Ei}\left(\frac{\tau_{\mathrm{l}}}{2\tau_{\mathrm{c}}}\right)\right]}{4\tau_{\mathrm{c}}^3} & \\ \quad + \dfrac{4\left(t - \tau_{\mathrm{p}}\right)^2 \left(\tau_{\mathrm{c}} + \frac{\tau_{\mathrm{l}}}{2}\right) \exp\left(-\frac{t-\tau_{\mathrm{p}}-\frac{\tau_{\mathrm{l}}}{2}}{\tau_{\mathrm{c}}}\right) - \tau_{\mathrm{l}}^2 \left(t + \tau_{\mathrm{c}} - \tau_{\mathrm{p}}\right)}{4\tau_{\mathrm{c}}^2 \left(t - \tau_{\mathrm{p}}\right)^2}, & t \geq \frac{\tau_{\mathrm{l}}}{2} + \tau_{\mathrm{p}} \end{cases} \tag{5.3}$$

where $\mathrm{Ei}(x) = \int_{-\infty}^{x} \frac{e^u}{u} \mathrm{d}u$ is the exponential integral, and τ_{l} is residence time scales of the LFR. The fitted time scales of the LFR + CSTR + PFR model are $\tau_{\mathrm{l}} = 0.431$ s, $\tau_{\mathrm{c}} = 0.151$ s and $\tau_{\mathrm{p}} = 0.616$ s. The fitted residence-time-distribution models are compared with the observations in Figure 5.4; clearly model 2 captures the tail at long time better than model 1.

Particle size distribution inversion kernel for the scanning ROMIAC

The particle size distribution inversion for the scanning classifier is to retrieve the size distribution of the source particles $\mathbf{n}$ from the particle count sequence $\mathbf{r}_{\mathrm{scan}} = \mathbf{A}_{\mathrm{scan}}\mathbf{n}$, where $\mathbf{A}_{\mathrm{scan}}$ is the inversion kernel for the scanning system. Mai, Kong, et al. (In review) calculated the inversion kernel $\mathbf{A}_{\mathrm{scan}}$ by

simulating the transfer function of the scanning aerosol classifier. Here, we calculate the inversion kernel $\mathbf{A}_{\text{scan}}$ from the experimentally measured instrument response $\mathbf{r}_{\text{scan}}$ and the source particle size distribution $\mathbf{n}$. This method is applied to the scanning ROMIAC system described in the previous section.

The experiment to measure the scanning ROMIAC instrument response $\mathbf{r}_{\text{scan}}$ is completed in two steps: (*i*) the stepping mode classifier was used to measure the size distribution of the aerosol from the hot wire source, as shown in Figure 5.5 (a); (*ii*) the tandem ROMIAC system was used to measure the scanning ROMIAC instrument response $\mathbf{r}_{\text{scan}}$ of the polydisperse aerosol with the size distribution $\mathbf{n}$, as shown in Figure 5.5 (b).

Particle size distribution inversion for the stepping ROMIAC

To measure the particle size distribution from the hot wire generator, the ROMIAC beta is operated in stepping mode, with an aerosol flow rate of $Q_{\text{a}} = 1$ LPM, and a cross-flow flow rate of $Q_{\text{c}} = 10$ LPM. The saturator and condenser temperatures for the DEG stage are 70 °C and 4 °C, respectively. The hot wire particles generator for these experiments was operated under the same conditions as in the CPC detection efficiency measurements shown in Figure 5.2.

The particle size distribution from the hot wire source is obtained with the ROMIAC operated in the stepping mode, as shown in Figure 5.5 (a). Assuming a steady-state size distribution from the hot wire source $n(\log D_{\text{p}})$, the CPC counts recorded in a time bin with the classifier operated at constant voltage V_i are

$$\begin{aligned} R_{\text{step},i} &= Q_{\text{a}} t_{\text{c}} \int_{-\infty}^{\infty} n(\log D_{\text{p}}) \sum_{\phi} \Omega_{\text{OMAC}}(Z_{\text{p}}(D_{\text{p}}, \phi), Z_{\text{p}}^{*}(V_i), \beta, \delta) p_{\text{charge}}(D_{\text{p}}, \phi) \\ &\times \eta_{\text{F}}(D_{\text{p}}, \phi) \eta_{\text{CPC}}(D_{\text{p}}, \phi) \mathrm{d} \log D_{\text{p}}, \quad i = 1, 2, \ldots, I, \end{aligned} \tag{5.4}$$

where $\Omega_{\text{OMAC}}(Z_{\text{p}}(D_{\text{p}}, \phi), Z_{\text{p}}^{*}(V_i), \beta, \delta)$ is the *transfer function* of the ROMIAC when operated at constant voltage, V_i, with the entrance and exit penetration efficiencies taken into account (Mui, Mai, et al., 2017). t_{c} is the counting time of a time bin. $p_{\text{charge}}(D_{\text{p}}, \phi)$, $\eta_{\text{F}}(D_{\text{p}}, \phi)$ and $\eta_{\text{CPC}}(D_{\text{p}}, \phi)$ are the charging probability, penetration efficiency in the plumbing system, CPC detection efficiency, respectively. Following Mai, Kong, et al. (In review), a linear spline approximation of the source particle size distribution is applied on discretization points $u_j^{*} = \log D_{\text{p},j}^{*}$, $j = 1, 2, \cdots, J$. The particle size distribution is

$$n(u) = n(u_j^{\dagger}) + \frac{n(u_{j+1}^{\dagger}) - n(u_j^{\dagger})}{u_{j+1}^{\dagger} - u_j^{\dagger}} \left(u - u_j^{\dagger}\right) = n(u_j^{\dagger}) \frac{u_{j+1}^{\dagger} - u}{u_{j+1}^{\dagger} - u_j^{\dagger}} + n(u_{j+1}^{\dagger}) \frac{u - u_j^{\dagger}}{u_{j+1}^{\dagger} - u_j^{\dagger}}. \tag{5.5}$$

Following the derivation of the scanning DMA data inversion from Mai, Kong, et al. (In review), the instrument response in the stepping ROMIAC can be obtained with the same method. The integral in Eq. (5.4) is approximated by summation over finer grid u_k, $k = 1, 2, \cdots, K$ than that for the size distribution representation, and becomes

$$R_{\text{step},i} = \sum_{k=1}^{K} \Delta u_k g_i(u_k) n(u_k), \tag{5.6}$$

where

$$\Delta u_k = \begin{cases} \dfrac{u_2 - u_1}{2}, & k = 1 \\ \dfrac{u_{k+1} - u_{k-1}}{2}, & k = 2, 3, \cdots, K-1 \\ \dfrac{u_K - u_{K-1}}{2}, & k = K \end{cases} \tag{5.7}$$

is the weighting factor arising from the trapezoidal integral. $g_i(u)$ denotes the kernel function for the stepping mode data inversion, which is defined as

$$g_i(u) \quad = \quad Q_\text{a} t_\text{c} \sum_{\phi} \Omega_\text{OMAC}(u, u^*(V_i), \beta, \delta) p_\text{charge}(u, \phi) \eta_\text{F}(u, \phi) \eta_\text{CPC}(u, \phi). \tag{5.8}$$

The instrument response in the stepping mode becomes

$$R_{\text{step},i} = \sum_{k=1}^{K} \Delta u_k \left[n(u_j^\dagger) \frac{u_{j+1}^\dagger - u_k}{u_{j+1}^\dagger - u_j^\dagger} + n(u_{j+1}^\dagger) \frac{u_k - u_j^\dagger}{u_{j+1}^\dagger - u_j^\dagger} \right] g_i(u_k), u_k \in [u_j^\dagger, \quad u_{j+1}^\dagger). \tag{5.9}$$

Alternatively, the instrument response can be rewritten in a matrix form

$$R_{\text{step},i} = \sum_{j=1}^{J} A_{\text{step},i,j} n(u_j^\dagger), \qquad i = 1, 2, \cdots, I \tag{5.10}$$

where the kernel function $A_{i,j}$ is defined as

$$A_{\text{step},i,j} = \sum_{u_k \geq u_{j-1}^\dagger}^{u_k < u_j^\dagger} \Delta u_k \frac{u_k - u_{j-1}^\dagger}{u_j^\dagger - u_{j-1}^\dagger} g_i(u_k) + \sum_{u_k \geq u_j^\dagger}^{u_k < u_{j+1}^\dagger} \Delta u_k \frac{u_{j+1}^\dagger - u_k}{u_{j+1}^\dagger - u_j^\dagger} g_i(u_k). \tag{5.11}$$

To solve the inversion problem $\mathbf{r}_\text{step} = \mathbf{A}_\text{step}\mathbf{n}$ for the values of the size distribution parameters $\mathbf{n} = [n(u_1^\dagger), n(u_2^\dagger), \cdots, n(u_J^\dagger)]^\text{T}$, with $\mathbf{r}_\text{step} = [R_{\text{step},1}, R_{\text{step},2}, \cdots, R_{\text{step},I}]^\text{T}$ as the array of the CPC data in the stepping mode measurement, a non-negative least squares algorithm (Merritt and Zhang, 2005) is used.

Instrument response of tandem ROMIAC and scanning ROMIAC data inversion

In the tandem ROMIAC experiments, the size distribution of the particles downstream of the stepping-mode ROMIAC is

$$n_{\mathrm{mc}}(u) = n(u)\Omega_{\mathrm{OMAC}}(u, u(V_i'), \beta, \delta)p_{\mathrm{charge}}(u, \phi). \tag{5.12}$$

where V_i' is the voltage of the stepping mode ROMIAC. The subscript "mc" in n_{mc} represents the *mobility-classified* particles that get transmitted through the stepping ROMIAC. Following Mai, Kong, et al. (In review), the downstream instrument response in the scanning mode is $\mathbf{r}_{\mathrm{scan}} = \mathbf{A}_{\mathrm{scan}}\mathbf{n}_{\mathrm{mc}}$, where $\mathbf{r}_{\mathrm{scan}} = [R_{\mathrm{scan},1}, R_{\mathrm{scan},2}, \cdots, R_{\mathrm{scan},I}]^{\mathrm{T}}$ is the time series of the instrument response on the source particle distribution $\mathbf{n}_{\mathrm{mc}} = [n_{\mathrm{mc}}(u_1^{\dagger}), n_{\mathrm{mc}}(u_2^{\dagger}), \cdots, n_{\mathrm{mc}}(u_J^{\dagger})]^{\mathrm{T}}$. Unlike (Mai, Kong, et al., In review), which calculate the kernel function of the scanning instrument $\mathbf{A}_{\mathrm{scan}}$ by simulating the scanning DMA transfer function and incorporating it with the CPC delay effect, here we obtain the kernel function $\mathbf{A}_{\mathrm{scan}}$ given the instrument response $\mathbf{r}_{\mathrm{scan}}$ and the particle size distribution $\mathbf{n}_{\mathrm{mc}}$. To reduce the uncertainty of the calculated kernel function $\mathbf{A}_{\mathrm{scan}}$, it is desired to measure the instrument response $\mathbf{r}_{\mathrm{scan}}$ for various upstream particle size distribution $\mathbf{n}_{\mathrm{mc}}$. Assuming we have a number of L instrument responses that corresponds to L different upstream particle size distributions, the composite instrument matrix is

$$\mathbf{R}_{\mathrm{scan}} = \mathbf{A}_{\mathrm{scan}}\mathbf{N}_{\mathrm{mc}}, \tag{5.13}$$

where $\mathbf{R}_{\mathrm{scan}} = [\mathbf{r}_{\mathrm{scan},1}, \mathbf{r}_{\mathrm{scan},2}, \cdots, \mathbf{r}_{\mathrm{scan},L}]$ is a $I \times L$ matrix (I instrument responses and L experiments). The $\mathbf{N}_{\mathrm{mc}} = [\mathbf{n}_{\mathrm{mc},1}, \mathbf{n}_{\mathrm{mc},2}, \cdots, \mathbf{n}_{\mathrm{mc},L}]$ ($J \times L$ matrix) denotes the composite upstream particle size distributions for L experiments.

To retrieve the kernel matrix $\mathbf{A}_{\mathrm{scan}}$, we seek to solve the inversion problem from the matrix-matrix multiplication relationship shown in Eq. (5.13). The non-negative least squares (NNLS) algorithm (Merritt and Zhang, 2005) that was introduced above aims to solve the inversion problem by matrix-vector multiplication. To utilize the NNLS inversion algorithm, Eq. (5.13) can be transformed into matrix-vector problems via the following decomposition,

$$\mathbf{A}_{\mathrm{scan}} = \begin{bmatrix} \mathbf{A}_{\mathrm{scan},1} \\ \mathbf{A}_{\mathrm{scan},2} \\ \vdots \\ \mathbf{A}_{\mathrm{scan},I} \end{bmatrix}, \quad \mathbf{R}_{\mathrm{scan}} = \begin{bmatrix} \mathbf{R}_{\mathrm{scan},1} \\ \mathbf{R}_{\mathrm{scan},2} \\ \vdots \\ \mathbf{R}_{\mathrm{scan},I} \end{bmatrix} \tag{5.14}$$

where $\mathbf{A}_{\text{scan},i}$ is the ith row of matrix $\mathbf{A}_{\text{scan}}$, and $\mathbf{R}_{\text{scan},i}$ is the ith row of matrix $\mathbf{R}_{\text{scan}}$. With these decomposition, Eq. (5.13) becomes

$$\begin{bmatrix} \mathbf{A}_{\text{scan},1} \\ \mathbf{A}_{\text{scan},2} \\ \vdots \\ \mathbf{A}_{\text{scan},I} \end{bmatrix} = \begin{bmatrix} \mathbf{R}_{\text{scan},1}\mathbf{N}_{\text{mc}} \\ \mathbf{R}_{\text{scan},2}\mathbf{N}_{\text{mc}} \\ \vdots \\ \mathbf{R}_{\text{scan},I}\mathbf{N}_{\text{mc}} \end{bmatrix}. \tag{5.15}$$

Thus, we can apply the NNLS algorithm for every inversion problem $\mathbf{A}_{\text{scan},i} = \mathbf{R}_{\text{scan},i}\mathbf{N}_{\text{mc}}$ (or applying transpose for both sides to get the standard form of the inversion problem, $\mathbf{A}^{\text{T}}_{\text{scan},i} = {\mathbf{N}_{\text{mc}}}^{\text{T}}\mathbf{R}^{\text{T}}_{\text{scan},i}$), $i = 1, 2, \cdots, I$ in Eq. (5.15).

5.3 Results

Figure 5.6 (a) shows the CPC counts and the ROMIAC voltage as a function of time in the experiment in which the particle size distribution from the hot wire source generator was measured. The voltage of the ROMIAC was changed after 15 s of the steady- state CPC signal was acquired. To demonstrate the steady-state during the measurement, Figure 5.6 (b) shows the delay between the CPC counts and the ROMIAC voltage. Only the steady-state signal is extracted from the experimental data; it is averaged for each ROMIAC voltage. The mean CPC counts in a time bin are plotted versus the ROMIAC voltage in Figure 5.7 (a); the error bar represents the standard error of the particle counts. Using the non-negative-least-squares algorithm (Merritt and Zhang, 2005), the inverted particle size distribution of the aerosol from the hot wire source generator is shown in Figure 5.7 (b).

The tandem ROMIAC instrument response is shown in Fig. 5.8, for the stepping mode ROMIAC set at voltages V = 331, 529, 1349, 2154, and 3139 V. In the tandem ROMIAC experiment, flows in both classifiers were balanced, with an aerosol flow rate of Q_{a} = 1 LPM and a cross-flow flow rate of Q_{c} = 10 LPM.

Inversion kernels were obtained from the experimental instrument response measurements, for both up- and down-scans, as shown in Fig. 5.9. The inversion kernels obtained from finite-element simulated scanning ROMIAC transfer function following the method of Mai, Kong, et al. (In review) are shown in Figure 5.10 for comparison. The experimental based inversion kernel is noisier than that based on the simulation owing to: (*i*) the intrinsic uncertainty in the experimental data, and (*ii*) the additional error that arises in deriving the kernel by inverting Eq. (5.15).

Figure 5.11 shows the particle size distributions obtained from the same scanning ROMIAC data gathered in an experiment that measured the particle wall loss rate in the environmental chamber

after inversion using these two different kernels. Details of this experiment is presented in the following chapter. The total particle number concentration and the mean particle diameters from this analysis are shown in Figure 5.12. The differences in the total particle number concentration and the mean particle using the experimentally generated inversion kernel are around 10 %.

5.4 Discussion and Conclusion

The distortions of the scanning classifier transfer function, and the time delay effect associated with particle detection pose challenges for data inversion of scanning measurements. Mai, Kong, et al. (In review) addressed these non-idealities wusing Brownian dynamics simulations of the exact scanning classifier transfer function, combined with experiment measurements of the residence-time-distribution of the particle counter. Instead of deriving the inversion kernel by using the computationally expensive Monte Carlo simulations, the present study provides a method for determining the inversion kernel for scanning measurements via measurement of the instrument responses on mobility-classified particles from a polydisperse aerosol. Although the work presented here focuses on particles in the nanometer domain, with particle diameters ranging from 1 to 20 nm, the method provided in this study can be applied to other size distribution measurement systems that probe other size ranges.

The particle size distribution obtained with this experimentally-measured kernel is compared with that derived using the kernels based on computational simulations. Uncertainties on the order of 10 % were observed in both total particle number concentration estimates and the mean particle diameter. This error can be attributed to uncertainties in determining the inversion kernel from experimental measurements. First, the method presented here requires a steady size distribution of the source particles. This assumption could be compromised given the time it takes to complete the whole experiment. Second, the inversion kernel is derived by measuring the instrument response by counting particles into finite time bin, followed by least-squares data inversion. To improve the accuracy of the methods used in this study, one can measure the size distribution of the source particles periodically during the experiment. The uncertainty can be also reduced by increasing the instrument measurement signal. For example, particle chargers can be removed in the experiment set-up, which increases the number of transmitted particles in the downstream instrument.

Acknowledgements

The authors gratefully acknowledge support for this work by the National Science Foundation under Grant No. AGS-1602086.

Table 5.1: Operation parameters of the scanning OMAC (balanced flow)

Parameter	Notation	Value
Polydisperse flow rate (LPM)	$Q_{\text{a, in}}$	1.00
Monodisperse flow rate (LPM)	$Q_{\text{a, out}}$	1.00
Incoming cross-flow flow rate (LPM)	$Q_{\text{c, in}}$	10.0
Outgoing cross-flow flow rate (LPM)	$Q_{\text{c, out}}$	10.0
Low electrode voltage (V)	V_{low}	20.0
High electrode voltage (V)	V_{high}	5000
Up/down scan times (s)	$t_{\text{ramp,u/d}}$	50
Holding time at V_{low} (s)	t_{low}	6
Holding time at V_{high} (s)	t_{high}	6
Time bin duration (s)	t_{c}	0.5

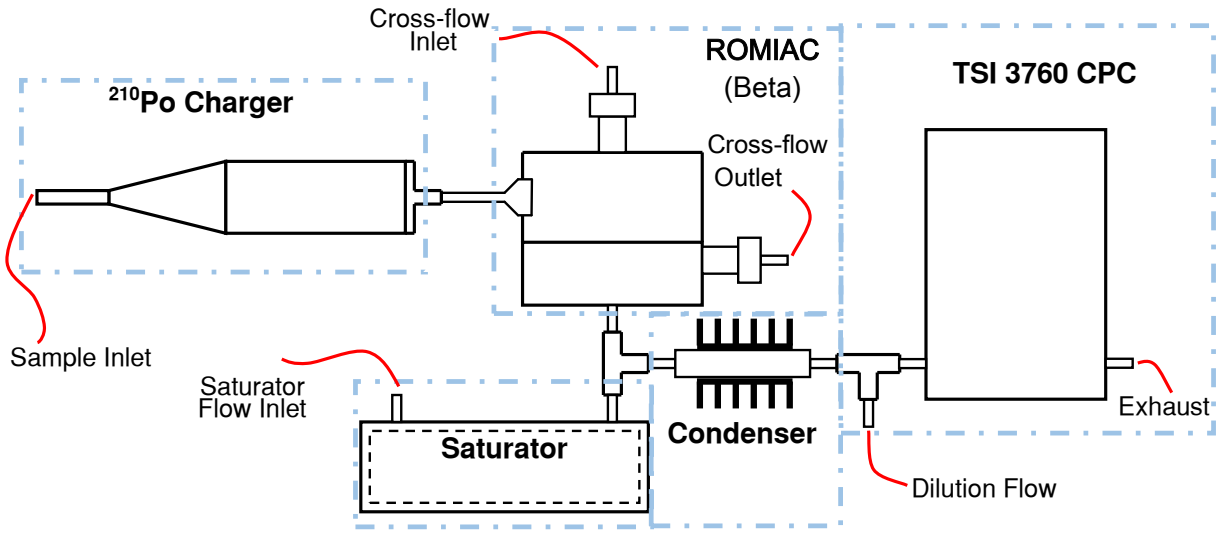

Figure 5.1: Schematic of scanning ROMIAC system with a two-stage CPC as the particle detector. The saturator in the first stage is used to provided diethylene glycol (DEG) vapor for particle activation. The particle size increases in the downstream condenser due to the DEG vapor condensation.

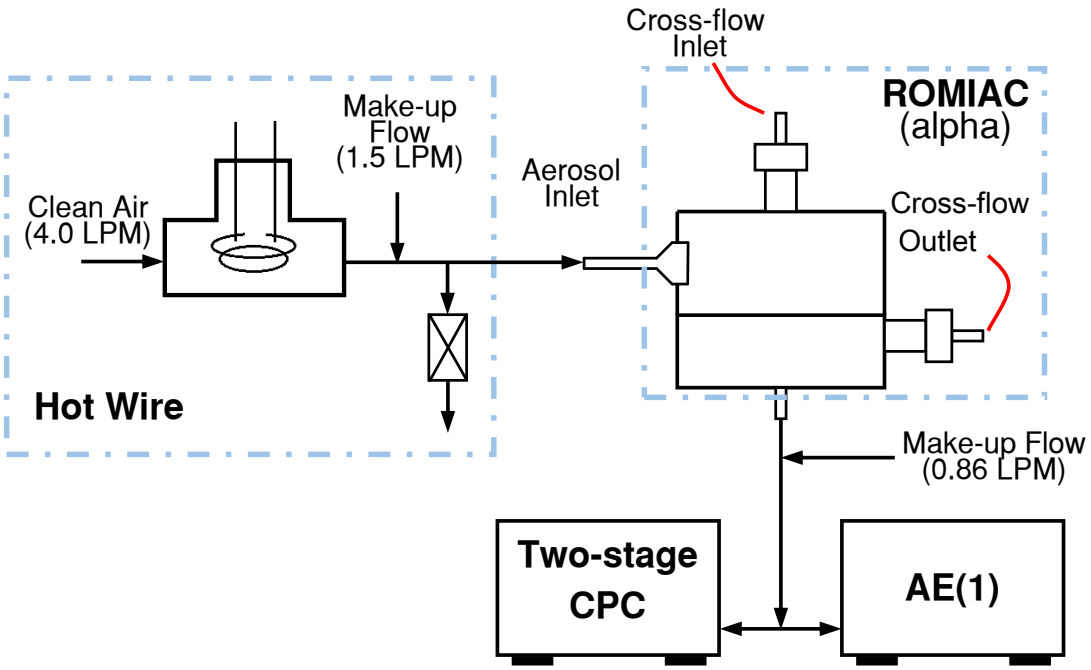

Figure 5.2: Experiment set-up for the CPC calibration. AE represents the aerosol electrometer. (Notice Prof. Michel Attoui developed two aerosol electrometers, one is labeled as "1", and the other is "2". Here, the aerosol electrometer labeled "1" is used in the experiment.)

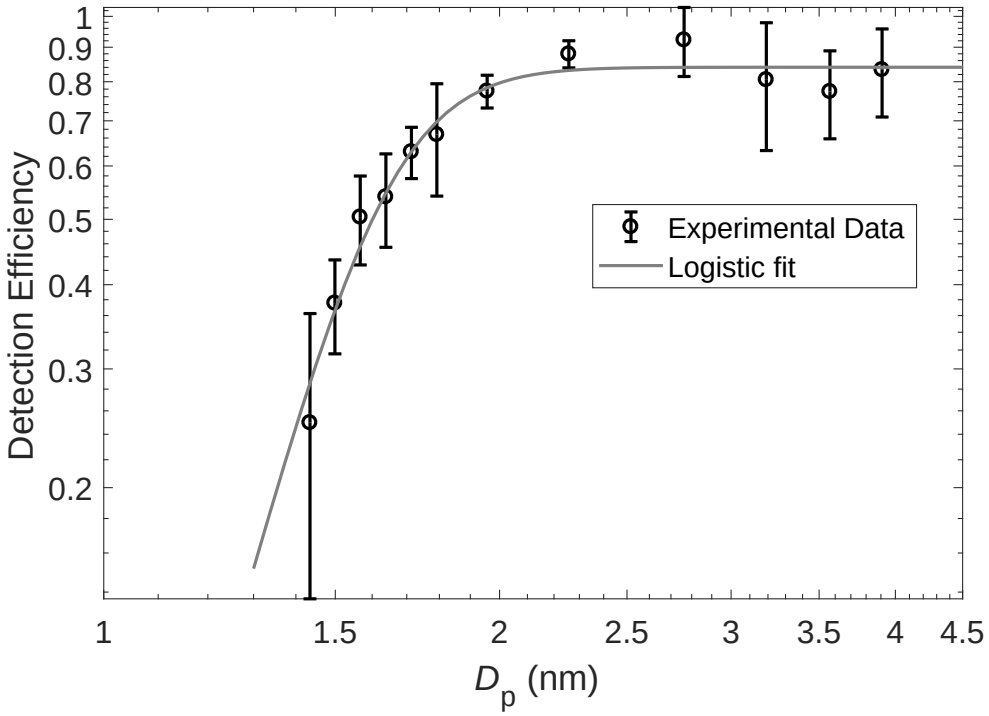

Figure 5.3: Detection efficiency of the two-stage CPC as a function of electrical mobility equivalent particle diameter D_p, with the saturator and condensor temperatures at 70 °C and 4 °C, respectively.

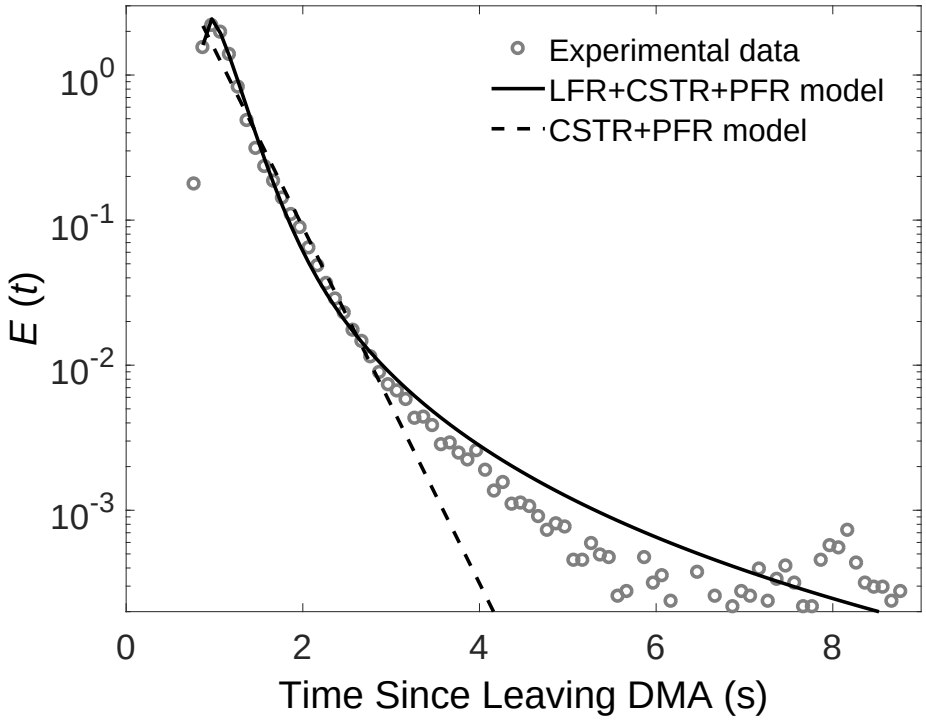

Figure 5.4: Residence time distribution of the two-stage CPC. The experimental measured results are fitted with two models: (1) LFR + CSTR + PFR model; (2) CSTR + PFR model.

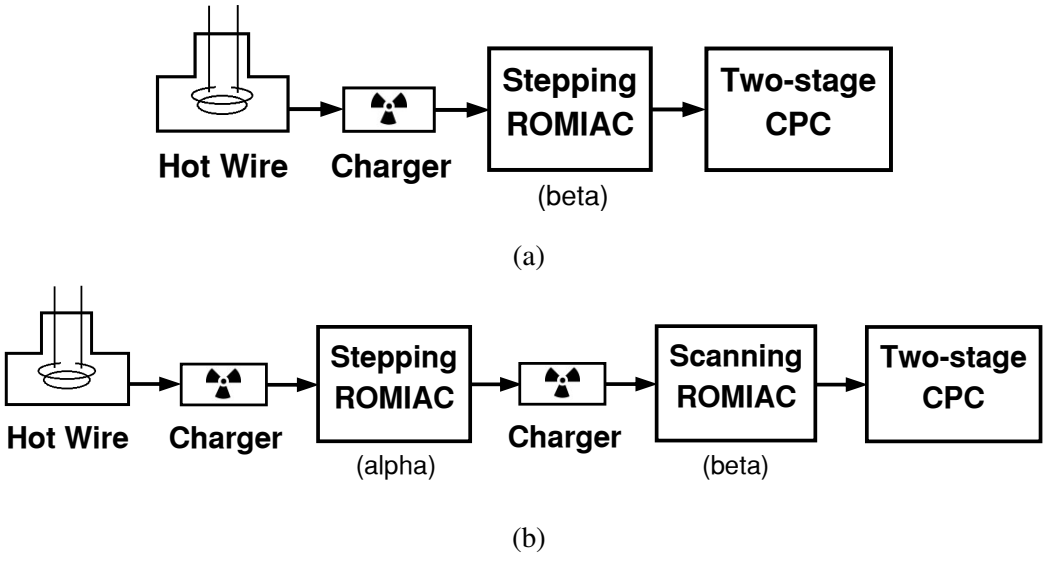

Figure 5.5: (a) Schematic of stepping mode ROMIAC to measure the size distribution generated from the hot wire source. (b) Schematic of the tandem ROMIAC experiment to measure the instrument response of the polydisperse particles.

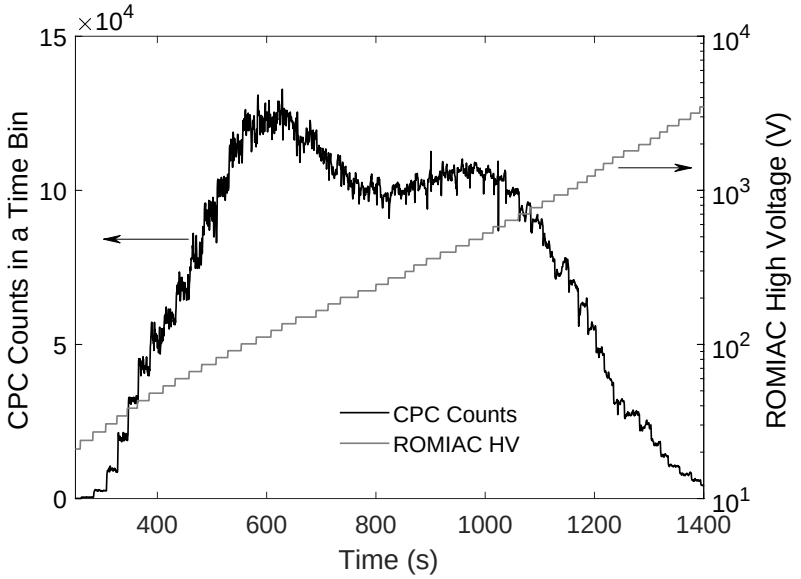

(a)

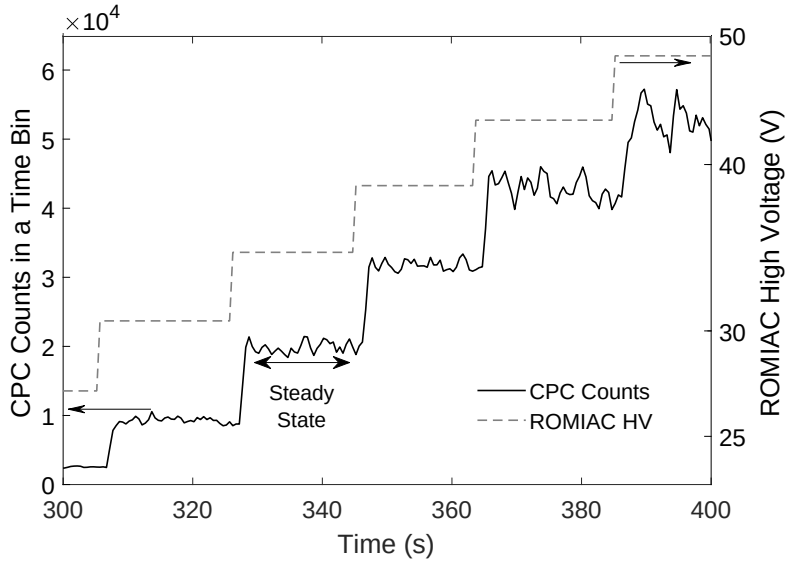

(b)

Figure 5.6: (a) CPC counts and the ROMIAC voltage as function of time during a size distribution measurement with the ROMIAC operated at the stepping mode. (b) The delay between the CPC counts and the ROMIAC voltage change in the measurement.

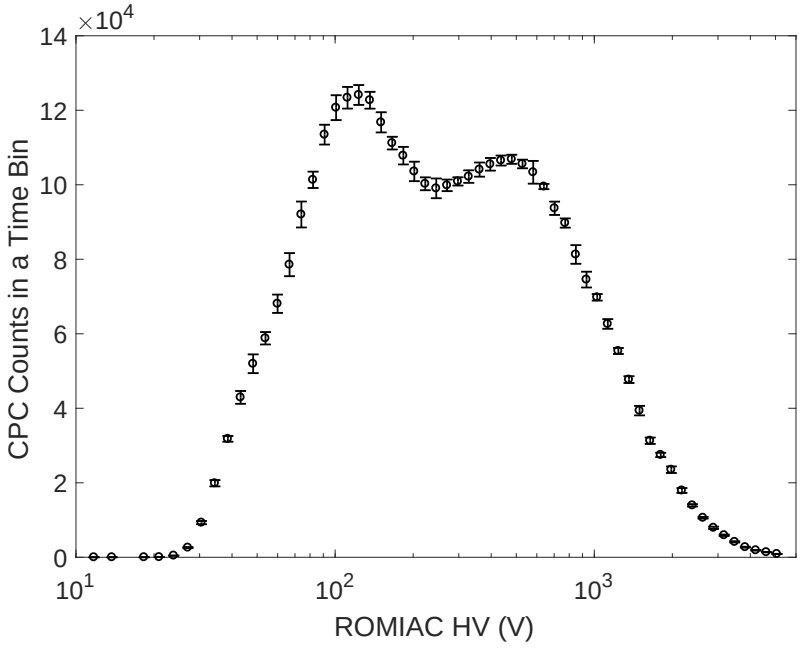

(a)

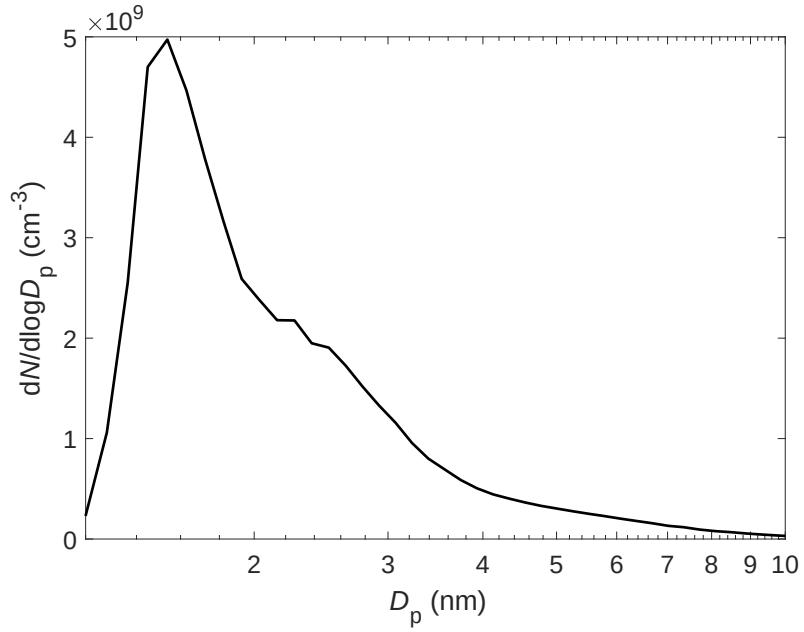

(b)

Figure 5.7: (a) Average CPC particle counts as a function of the ROMIAC HV in the stepping mode measurement. (b) Inverted size distribution of the hot wire source particles from the particle counts and ROMIAC HV.

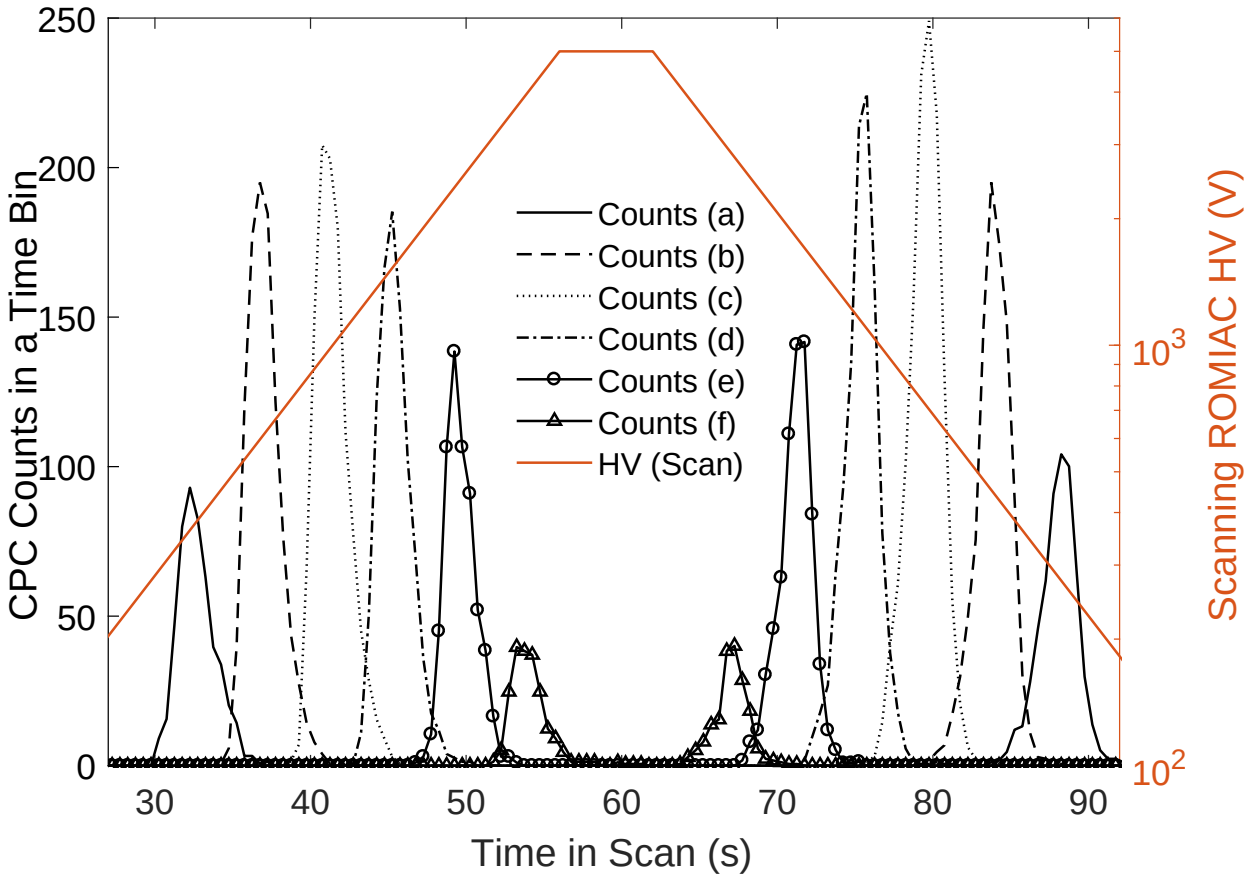

Figure 5.8: CPC counts of the tandem ROMIAC measurement as a function of the time in scan, with the stepping ROMIAC (first classifier) set at different voltages: (a) 331 V, (b) 529 V, (c) 845 V, (d) 1349 V, (e) 2154 V, (f) 3439 V.

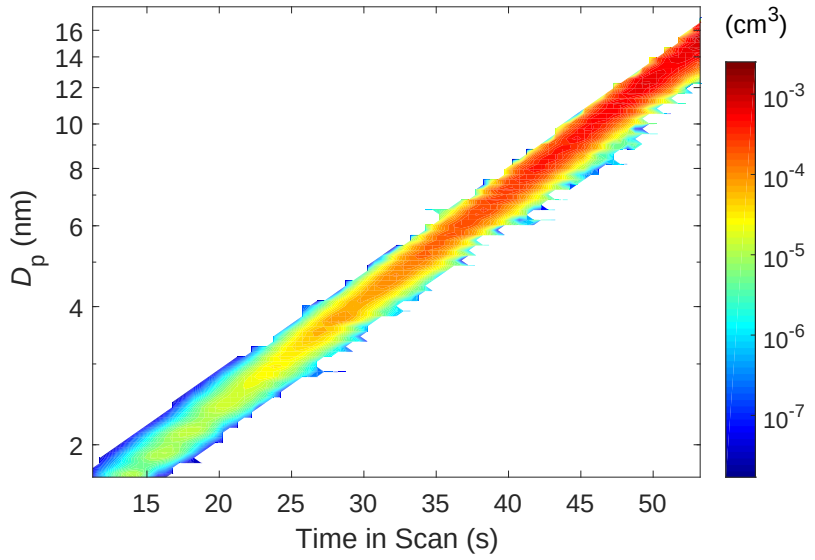

(a)

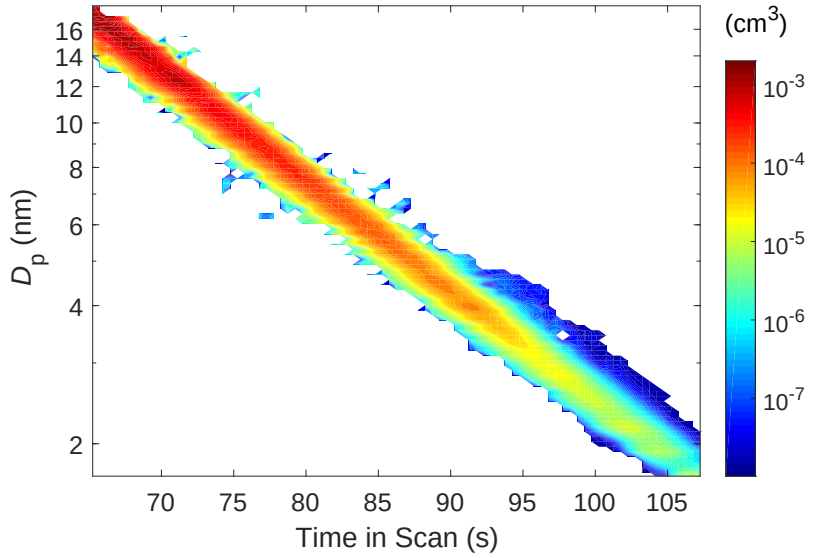

(b)

Figure 5.9: Contours of inversion kernel based on the experimental instrument response for (a) up- and (b) down-scan.

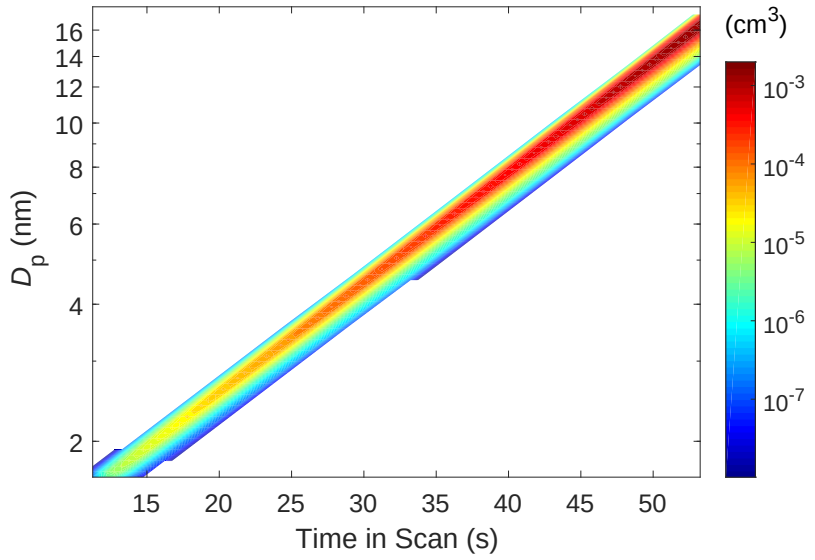

(a)

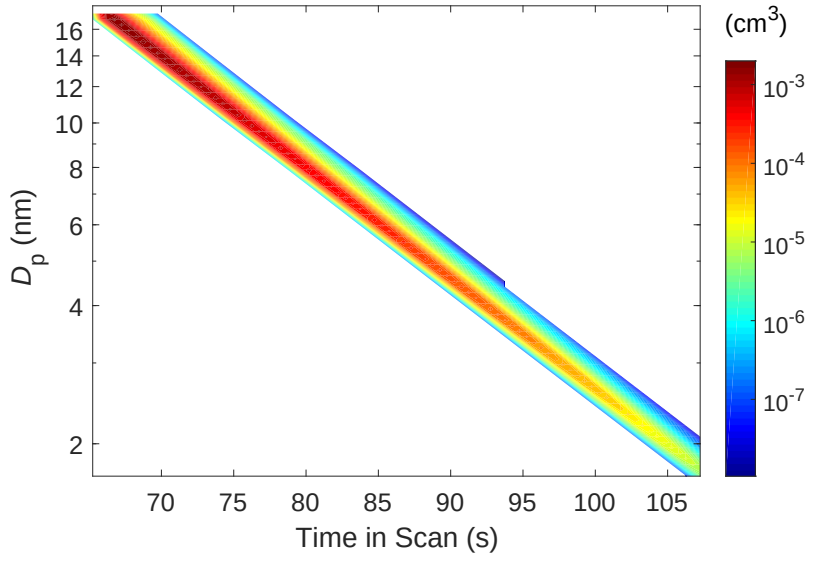

(b)

Figure 5.10: Contours of inversion kernel based on the finite-element simulated ROMIAC transfer functions for (a) up- and (b) down-scan.

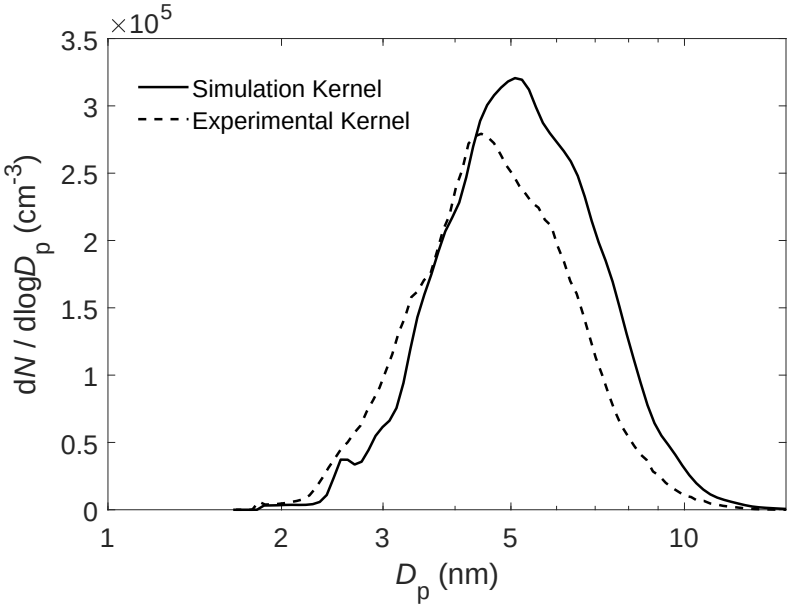

(a)

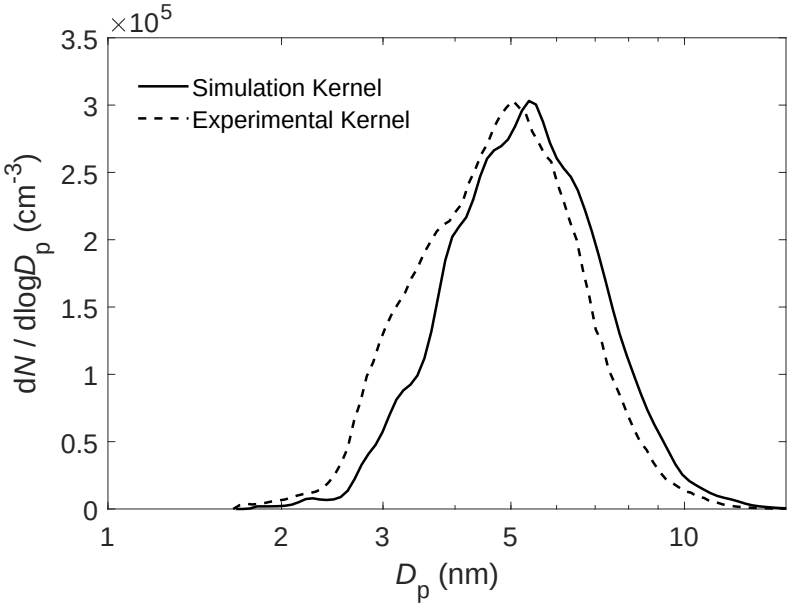

(b)

Figure 5.11: Inverted particle size distributions with kernel from the experimental measured instrument response and the one based on the simulated transfer function for (a) up- and (b) down-scan.

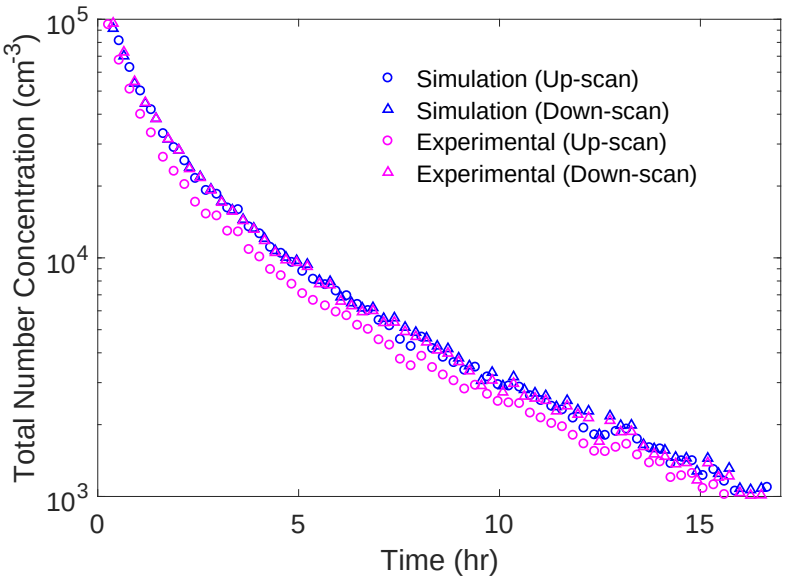

(a)

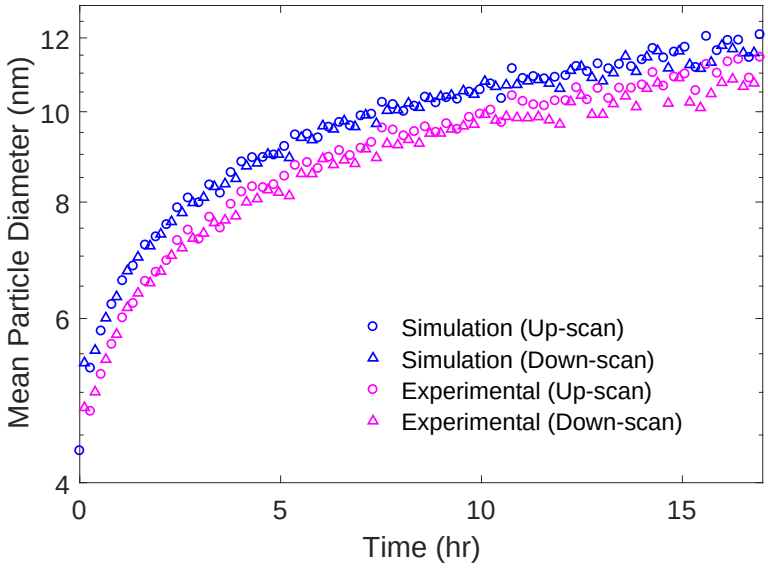

(b)

Figure 5.12: (a) Total number concentration and (b) mean particle diameter biases between the experimental measured kernel inversion and the simulated kernel inversion.

References

Mai, Huajun and Richard C. Flagan (In review). "Scanning DMA Data Analysis I. Classification Transfer Function". In: *Aerosol Science and Technology*.

Mai, Huajun, Weimeng Kong, John H. Seinfeld, and Richard C. Flagan (In review). "Scanning DMA data analysis. II. Integrated DMA-CPC instrument response and data inversion". In: *Aerosol Science and Technology*.

Merritt, M. and Y. Zhang (2005). "Interior-Point Gradient Method for Large-Scale Totally Non-negative Least Squares Problems". In: *Journal of Optimization Theory and Applications* 126.1, pp. 191–202.

Mui, Wilton, Huajun Mai, et al. (2017). "Design, simulation, and characterization of a radial opposed migration ion and aerosol classifier (ROMIAC)". In: *Aerosol Science and Technology* 51.7, pp. 801–823.

Mui, Wilton, Daniel A. Thomas, et al. (2013). "Ion Mobility-Mass Spectrometry with a Radial Opposed Migration Ion and Aerosol Classifier (ROMIAC)". In: *Analytical Chemistry* 85.13. PMID: 23730869, pp. 6319–6326. DOI: 10.1021/ac400580u. eprint: https://doi.org/10.1021/ac400580u. URL: https://doi.org/10.1021/ac400580u.

PARTICLE-WALL DEPOSITION IN THE ENVIRONMENTAL CHAMBER

By Huajun Mai, Yuanlong Huang, Sophia M. Charan, John H. Seinfeld, Richard C. Flagan

6.1 Introduction

New particle formation in the atmosphere has an important impact on aerosol particle size distribution and on the energy budget of global climate. Due to the limited understanding of the new particle formation mechanisms, recent research have attempted to quantify the nucleation rate in the atmosphere. Controlled experiments with environmental chambers shows that sulphuric acid, ammonia, amines, and highly oxygenated modelcules play important roles in the new particle formation and subsequent growth (Kirkby, Duplissy, et al., 2016; Kirkby, Curtius, et al., 2011; Almeida et al., 2013). To determine the new particle formation rates and the initial particle growth rates from the environmental chamber measurements, particle-wall deposition is an important process that needs to be taken into account. In this chapter, we focus on wall losses of particles in the sub-20 nm diameter range. The particles injected into the environmental chamber are generated by evaporation and condensation of ammonium sulfate (Scheibel, Porstendo, et al., 1983), and the particle size distribution of the chamber is monitored by the scanning radial opposed migration ion and aerosol classifier (ROMIAC) system.

6.2 Methods

Sub-20 nm ammonium sulfate particles were generated using a tube furnace (Scheibel, Porstendo, et al., 1983). Clean filtered air with a flow rate of 2.5 liters per minute (LPM) is supplied to a quartz tube containing ammonium sulfate; the tube was heated to 170 °C to evaporate the salt into the carrier gas. At the end of the tube furnace, the vapor was quenched with 2.5 LPM of cold filtered air injected through four opposing jets. The aerosol formed by nucleation was passed through an aerosol charge neutralizer. The nucleated ammonium sulfate particles were then injected to the environmental chamber for 25 minutes at a total flow rate of 5 LPM.

The particle size distribution was measured with the scanning ROMIAC system using a two-stage condensation particle counter (CPC) that was built at Caltech. The ROMIAC voltage was scanned from 20 to 5000 V in a 50 s ramp time for both up- and down-scan. The ROMIAC was operated with equal aerosol inlet and classified sample flows of 1 LPM aerosol flow rate, with a 10 LPM

cross-flow flow rate. These operating conditions result in a measurement particle size range of 1.7 - 17 nm. Particle size distributions were obtained using inversion method described in Chapter 5; the scanning ROMIAC transfer function used in this inversion was obtained by finite element simulations of the flow- and electric-fields, and particle trajectories within the scanning ROMIAC.

6.3 Results

The evolution of the particle size distribution in the wall loss experiment is shown in Figure 6.1. The ammonium sulfate particles were injected into the chamber for the first 25 minutes in the experiments, with particle size ranging from 1.7 to 15 nm. The particles in the range of 1.7 - 3 nm has been depleted since the fifth hour. The time variation of the total particle number concentration and the mean particle diameter during the experiment are shown in Figure 6.2. During the first four hours of the experiment, the total particle number concentration decreased by an order of magnitude, while the mean particle diameter increases from 5 nm to 8 nm. From hours 6 to 17, the total number concentration decays exponentially as the mean particle diameter increases from 9 nm to 12 nm. Particle coagulation appears to be the dominant particle loss mechanism for the first four hours of the experiment when the total number concentration is above 10^4 cm^{-3}. The rapid increase of the mean particle diameter during this time period is consistent with loss by coagulation. In contrast, from 6 to 17 hour of the experiment, the first order of exponential decay of the total number concentration suggests that the wall deposition is the dominant process as the wall loss rate is independent of particle number concentration. The observed increase of mean particle diameter in this period of time can be attributed to the fast rate of diffusional loss of small particles relative to that of the large particles (Crump and Seinfeld, 1981), rather than to actual particle growth.

Here, we assume that wall deposition is the dominant process during hour 6 - 17 of the experiment, and fit the particle number concentration data for the different particle size bins during this time using the first order exponential decay model to produce the results shown in Figure 6.3. The variation of fitted wall deposition rate with particle diameter is shown in Figure 6.4. Crump and Seinfeld (1981) predict that, in the diffusion dominated regime, the wall loss rate should scale as $\beta \propto \mathcal{D}^{1/2}$, where $\mathcal{D}$ is the Brownian diffusivity of the particles. For sub-20 nm particles, the particle diffusivity is proportional to the square of the particle diameter D_p, *i.e.*, $\mathcal{D} \propto D_\mathrm{p}^2$. Thus, the wall loss rate should decrease with particle size as D_p^{-1}, as is observed in Figure 6.4.

6.4 Discussion and Conclusions

This study investigates wall deposition of sub-20 nm particle in the Caltech environmental chamber. Since the chamber is used to measure the yield of the secondary aerosol for most of the experiments,

the particle wall deposition has previously only been examined for particles larger than 20 nm. Nah et al. (2017) reported particle-wall deposition rates for 20 nm particles between 10^{-4} and 10^{-3}, while the present study found that the deposition rate of 13 nm particles is as low as 3×10^{-4}. Although the particle size ranges of these two studies do not overlap, the extrapolated deposition rate from this study is approximately an order of magnitude lower than that of Nah et al. (2017).

As this study focused on sub-20 nm particles, we generated the ammonium sulfate particles by the evaporation and condensation method, while the previous study nebulized a solution to produce ammonium sulfate particles in the size range from 20 to 1000 nm. Nah et al. (2017) fitted theis size distribution data using an aerosol dynamics model to determine the wall deposition rate, taking into account particle coagulation, while the present study estimates the particle wall-loss rate from that time within the experiment, in which coagulation is negligible. Following Seinfeld and Pandis (2016), the characteristic time scale of coagulation is $\tau_c = \frac{2}{k_c N}$, where k_c and N are the coagulation coefficient and particle number concentration, respectively. In the 10^{th} hour examined in the experiment reported here, the number concentration was $N = 3\times10^3$ cm^{-3}, and the mean particle size was $D_p = 10$ nm, leading to a coagulation coefficient of $k_c = 2\times10^{-9}$ cm^{3}s^{-1}. The corresponding characteristic coagulation time is 3×10^5 s; the observed wall deposition rate from this study is around 0.5×10^{-4} s^{-1} for 10 nm particles, corresponding to a deposition time of $t_d = \frac{1}{\beta} = 2\times10^4$ s, which is an order of magnitude shorter than that for coagulation. This suggests that neglecting the coagulation may lead to an error of order 10 % in the wall deposition rate. It is clear that the coagulation mechanism can not resolve the discrepancy between these studies.

Kiyoura and Urano (1970) reveals that, when ammonium sulfate is heated above 100 °C, it decomposes into ammonium bisulfate and ammonia. This suggests ammonia may also be injected into the chamber during the wall deposition experiment along with the nucleated particles that contain ammonium sulfate and ammonium bisulfate particles. Injected ammonia might possibly condense on or react heterogeneouly with the nucleated particles. If condensation or heterogeneous reaction occurs, the resulting growth would reduce the concentration of small particles, while increasing that of large particles. Thus, the wall loss rate for small particle could be over-estimated, while that for large particle might be under-estimated in Figure 6.4. Although the effect of condensation or heterogeneous reaction is not quantified, significant growth in the particle size was not observed during the experiments presented in this study, *i.e.*, the mean particle size only increases from 10 nm to 11 nm in 5 hours. As described above, this apparent particle growth could be an artifact of the increasing rate of particle losses with decreasing size.

To fully understand the wall deposition of sub-20 nm particle, further experiments or aerosol

dynamics modeling is required. Improvements in the experimental method could include reducing the temperature within the tube-furnace to reduce the amount of ammonia injected to the chamber, thereby minimizing potential condensation within the environmental chamber. An alternative approach would be to replace the ammonium sulfate that was used to generate particles with some chemically inert species, such as sodium chloride.

Acknowledgements

The authors gratefully acknowledge support for this work by the National Science Foundation under Grant No. AGS-1602086.

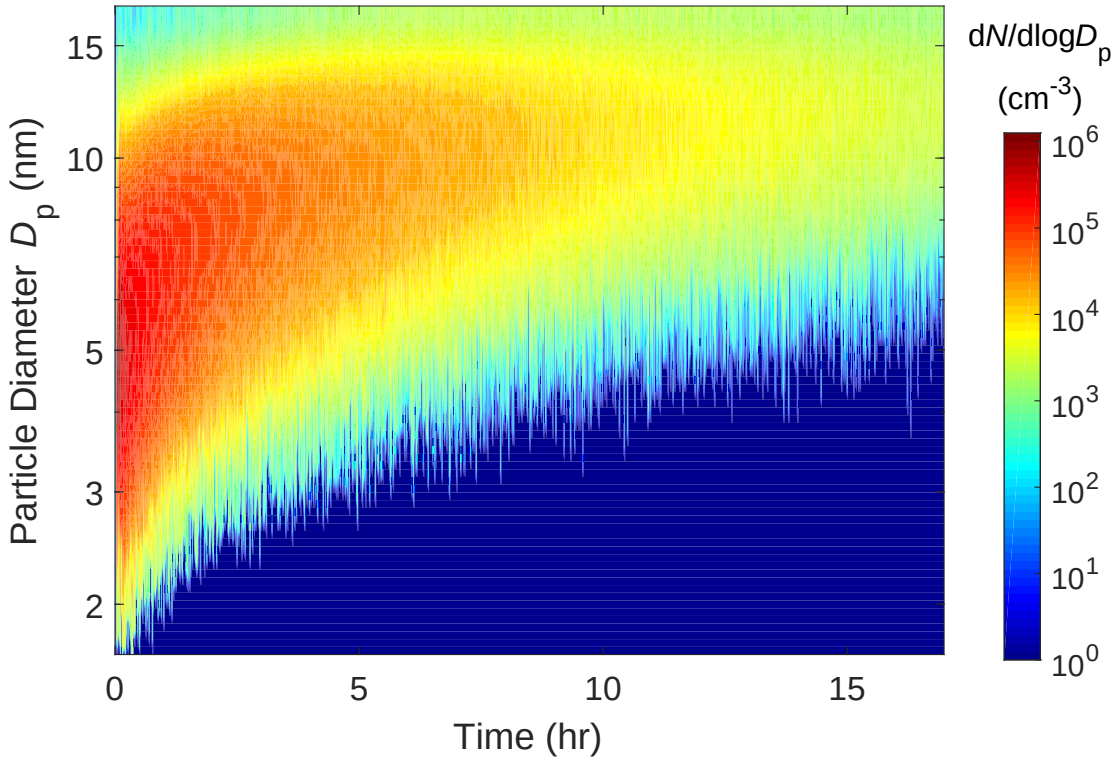

Figure 6.1: Evolution of the particle size distribution in the sub-20 nm particle wall loss experiment.

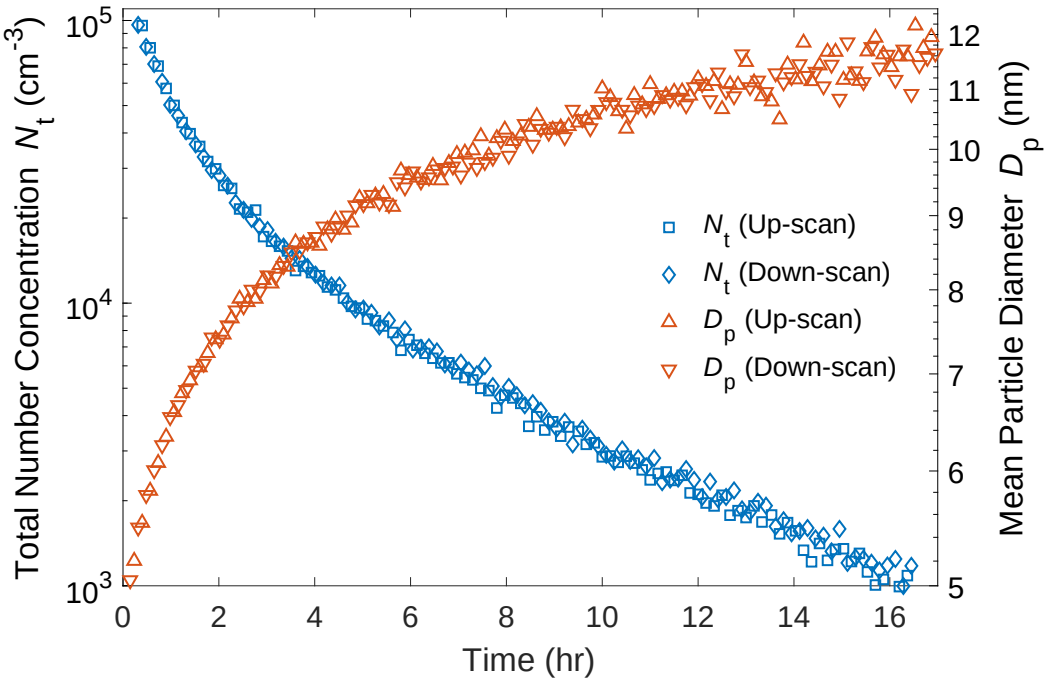

Figure 6.2: Total particle number concentration and mean particle diameter as a function of time in the sub-20 nm particle wall loss experiment.

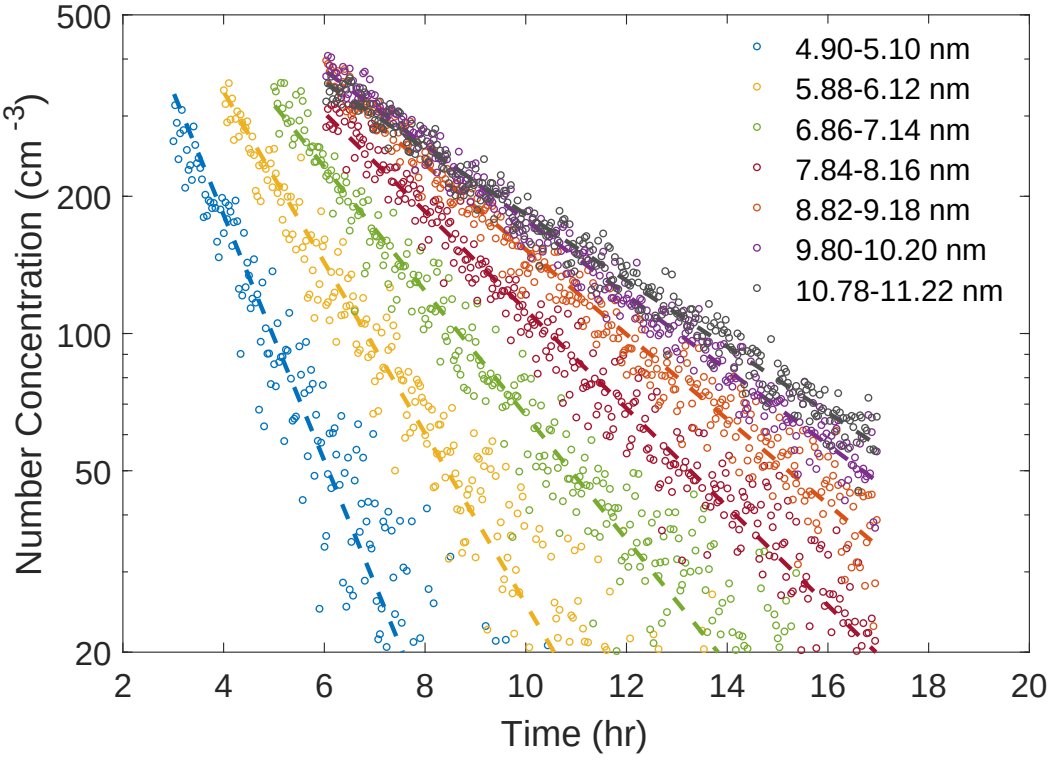

Figure 6.3: Evolution of the particle number concentrations at 7 particle size bins: 4.90 - 5.10 nm, 5.88 - 6.12 nm, 6.86 - 7.14 nm, 7.84 - 8.16 nm, 8.82 - 9.18 nm, 9.80 - 10.20 nm and 10.78 - 11.22 nm.

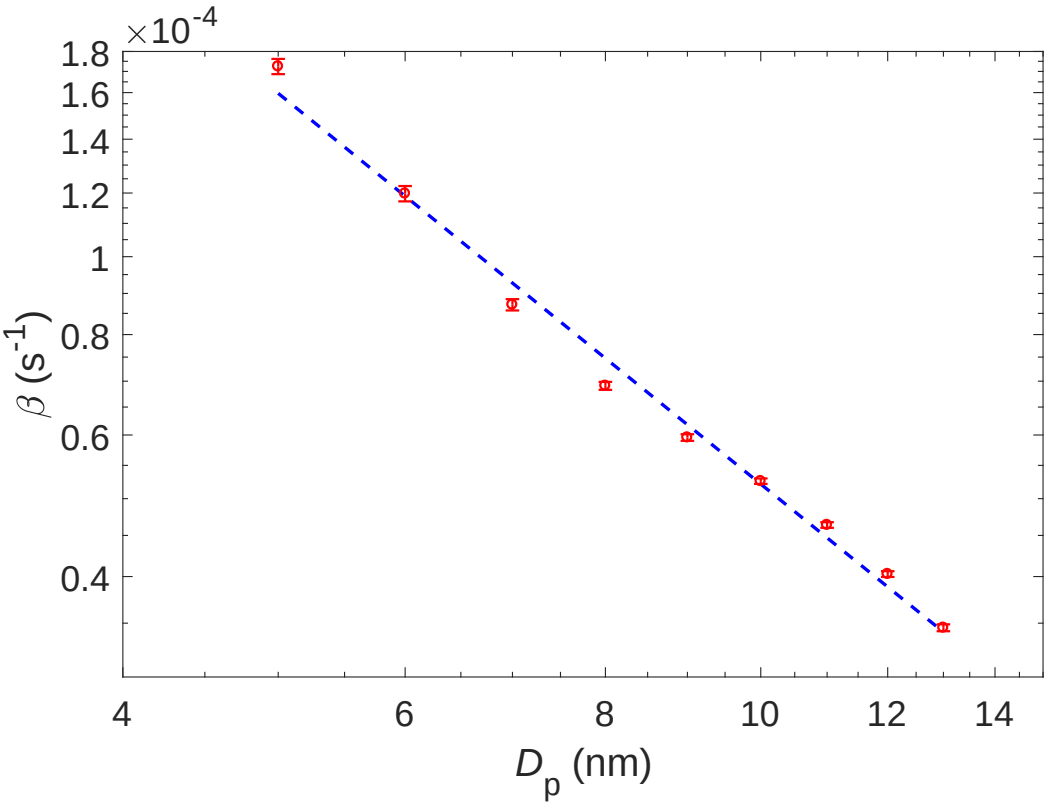

Figure 6.4: Particle wall deposition rate as a function of particle diameter. The dash line is the linear fitting curve on log-log scale. Error bars represent the standard deviation of the fitted deposition rates.

References

Almeida, João et al. (2013). "Molecular understanding of sulphuric acid–amine particle nucleation in the atmosphere". In: *Nature* 502.7471, p. 359. DOI: 10.1038/nature12663.

Crump, James G and John H Seinfeld (1981). "Turbulent deposition and gravitational sedimentation of an aerosol in a vessel of arbitrary shape". In: *Journal of Aerosol Science* 12.5, pp. 405–415.

Kirkby, Jasper, Joachim Curtius, et al. (2011). "Role of sulphuric acid, ammonia and galactic cosmic rays in atmospheric aerosol nucleation". In: *Nature* 476.7361, p. 429. DOI: 10.1038/nature10343.

Kirkby, Jasper, Jonathan Duplissy, et al. (2016). "Ion-induced nucleation of pure biogenic particles". In: *Nature* 533.7604, p. 521. DOI: 10.1038/nature17953.

Kiyoura, Raisaku and Kohei Urano (1970). "Mechanism, kinetics, and equilibrium of thermal decomposition of ammonium sulfate". In: *Industrial & Engineering Chemistry Process Design and Development* 9.4, pp. 489–494.

Nah, T. et al. (2017). "Constraining uncertainties in particle-wall deposition correction during SOA formation in chamber experiments". In: *Atmospheric Chemistry and Physics* 17.3, pp. 2297–2310. DOI: 10.5194/acp-17-2297-2017. URL: https://www.atmos-chem-phys.net/17/2297/2017/.

Scheibel, HG, J Porstendo, et al. (1983). "Generation of monodisperse Ag-and NaCl-aerosols with particle diameters between 2 and 300 nm". In: *Journal of Aerosol Science* 14.2, pp. 113–126.

Seinfeld, John H and Spyros N Pandis (2016). *Atmospheric chemistry and physics: from air pollution to climate change*. John Wiley & Sons.

UNDER WHAT CONDITIONS CAN EQUILIBRIUM GAS-PARTICLE PARTITIONING BE EXPECTED TO HOLD IN THE ATMOSPHERE?

By Huajun Mai, Manabu Shiraiwa, Richard C. Flagan, and John H. Seinfeld

This chapter was originally published in *Environmental science & technology* as:

Mai, Huajun, Manabu Shiraiwa, Richard C. Flagan, and John H. Seinfeld (2015). "Under what conditions can equilibrium gas–particle partitioning be expected to hold in the atmosphere?" In: *Environmental science & technology* 49.19, pp. 11485–11491. DOI: 10.1021/acs.est.5b02587.

7.1 Abstract

The prevailing treatment of secondary organic aerosol formation in atmospheric models is based on the assumption of instantaneous gas-particle equilibrium for the condensing species. Yet, compelling experimental evidence indicates that organic aerosols can exhibit the properties of highly viscous, semi-solid particles, for which gas-particle equilibrium may be achieved slowly. The approach to gas-particle equilibrium partitioning is controlled by gas-phase diffusion, interfacial transport, and particle-phase diffusion. Here we evaluate the controlling processes and the time scale to achieve gas-particle equilibrium as a function of the volatility of the condensing species, its surface accommodation coefficient, and its particle-phase diffusivity. For particles in the size range of typical atmospheric organic aerosols (50 nm to 500 nm), the timescale to establish gas-particle equilibrium is generally governed either by interfacial accommodation or particle-phase diffusion. The rate of approach to equilibrium differs depending on whether the bulk vapor concentration is constant, typical of an open system, or decreasing as a result of condensation into the particles, typical of a closed system.

Keywords: Secondary Organic Aerosol; Gas-particle Partitioning; Diffusion; Aerosol Phase State; Interfacial Transport

7.2 Introduction

Mounting evidence indicates that organic aerosols can exhibit the properties of viscous, semi-solid particles (Seinfeld and Pankow, 2003; Grieshop, Donahue, and Robinson, 2007; Vaden, Song,

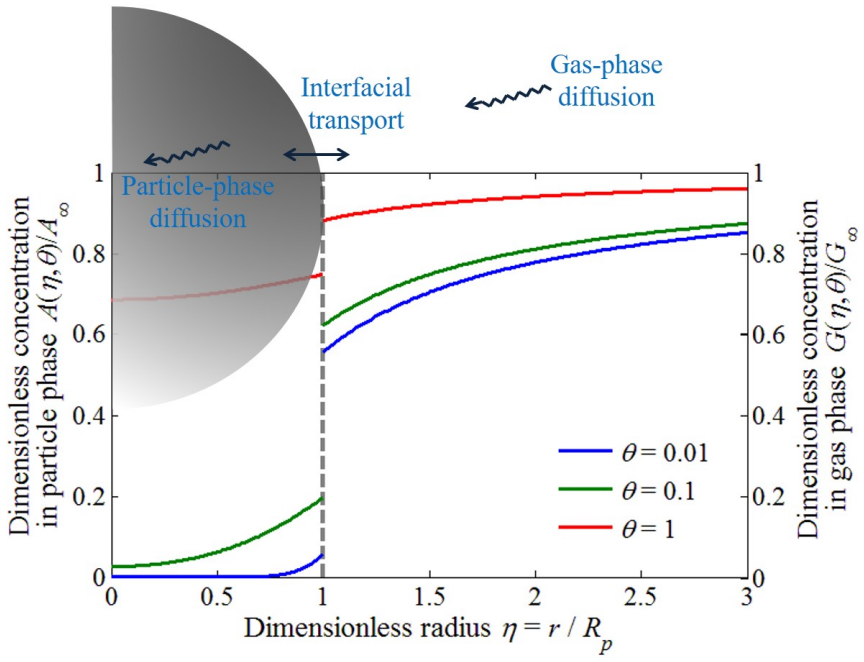

TOC figure.

et al., 2010; Virtanen et al., 2010; Pierce et al., 2011; Vaden, Imre, et al., 2011; Kuwata and Martin, 2012; Perraud et al., 2012; Abramson et al., 2013; Saukko et al., 2012; L Renbaum-Wolff, Grayson, and Bertram, 2013; Lindsay Renbaum-Wolff et al., 2013). In describing the process of formation of secondary organic aerosol (SOA) it has traditionally been assumed that condensing, low-volatility oxidation products partition according to instantaneous gas-particle equilibrium (Loza et al., 2013). The assumption of instantaneous gas-particle equilibrium implies that the timescale to achieve that equilibrium is short when compared to the timescales over which other processes, such as gas- and particle-phase dynamics, are occurring. Moreover, most current atmospheric chemical transport models incorporate the assumption of instantaneous gas-particle equilibrium in describing SOA formation. A consequence of a highly viscous aerosol phase is that gas-particle equilibrium for condensing species may not be established instantaneously, owing to the time associated with the transport processes in the gas phase, across the gas-particle interface, and within the particle itself. In this case, a dynamic, rather than equilibrium, formulation of the SOA formation process is required. Since the computational implications of dynamic versus equilibrium model formulations are significant, it is important to assess the conditions under which such a dynamic formulation is needed.

Several recent studies have addressed the time scales associated with the establishment of atmo-

spheric gas-aerosol equilibrium. Manabu Shiraiwa and Seinfeld (2012) estimated the equilibration time scale of SOA gas-particle partitioning using a state-of-the-art numerical gas- and particle-phase transport model. Zaveri et al. (2014) developed a comparable framework for describing gas-particle SOA partitioning that accounts for diffusion-reaction in the particle phase and includes the size distribution dynamics of the aerosol population. Liu, Zaveri, and Seinfeld (2014) presented an exact analytical solution of the transient equations of gas-phase diffusion of a condensing vapor to, and diffusion and first-order reaction in, a particle. These three studies provide the theoretical and computational framework to estimate the timescale for establishment of gas-particle equilibrium. The present work assesses the regimes of parameter values associated with various limiting cases of gas-particle transport. Based on the analytical solution of Liu, Zaveri, and Seinfeld (2014), we derive expressions for the time scales associated with the transport steps involved in SOA growth. We evaluate the overall time scale to achieve gas-particle equilibrium in both open and closed systems and compare it to that obtained from the full numerical solution of Manabu Shiraiwa and Seinfeld (2012).

7.3 Analytical solution for transient gas-particle partitioning

Transport of a vapor molecule to a particle involves three mass transfer processes that occur in series: (1) diffusion from the bulk of the gas phase to the particle surface; (2) transport across the gas-particle interface; and (3) diffusion into the interior of the particle. (If reactions are occurring in the particle phase, these occur simultaneously with particle-phase diffusion. In the present work we do not explicitly consider the effect of chemical reactions.) Any of these three processes can be rate-determining, depending on the particular set of conditions, and the rate-determining step will govern the time scale for achieving gas-particle equilibrium. The mathematical statement of the transport problem couples gas-phase diffusion, accommodation at the particle surface, and diffusion into the particle bulk. It is assumed that at $t = 0$ the particle is free of the condensing species and that the bulk gas-phase concentration of the condensing species is maintained constant for $t > 0$. This latter condition restricts the analytical solution to a so-called open system, one in which the bulk vapor concentration is maintained at a constant level. In the corresponding closed system, the total amount of vapor available is fixed, so that as condensation occurs, the vapor concentration decreases. The exact analytical solution of the transport problem allows one to derive expressions for the timescales associated with each of these three processes, from which one can infer which transport step controls the overall approach to equilibrium. A general numerical simulation that treats both open and closed systems, such as that used by Manabu Shiraiwa and Seinfeld (2012), can account for change of particle size with condensation and generation or depletion of the vapor

by chemical reaction.

We consider the analytical formulation for transient gas-particle partitioning of a species with a fixed concentration in the bulk gas phase into a particle free of that species at $t = 0$. Letting $G(r, t)$ and $A(r, t)$ be the gas- and particle-phase concentrations of the transporting species, the transient boundary value problem describing the approach to equilibrium is (Liu, Zaveri, and Seinfeld, 2014)

$$\frac{\partial A(r,t)}{\partial t} = D_b \left[\frac{\partial^2 A(r,t)}{\partial r^2} + \frac{2}{r} \frac{\partial A(r,t)}{\partial r} \right] \tag{7.1}$$

$$D_g \left(\frac{\partial G}{\partial r} \right)_{r=R_p} = \frac{1}{4} \alpha \bar{v} \left[G(R_p, t) - \frac{A(R_p, t)}{H'} \right] = D_b \left(\frac{\partial A}{\partial r} \right)_{r=R_p} \tag{7.2}$$

$$G(r,t) = G_\infty - \frac{R_p}{r} \left[G_\infty - G(R_p, t) \right] \tag{7.3}$$

$$A(r, 0) = 0 \tag{7.4}$$

$$\left(\frac{\partial A(r,t)}{\partial r} \right)_{r=0} = 0 \tag{7.5}$$

where G_∞ = bulk gas-phase concentration of the condensing species, R_p = particle radius, α = accommodation coefficient of the condensing species on the particle surface, $\bar{v}$ = mean molecular speed of the condensing species in the gas phase, D_g = molecular diffusion coefficient of the condensing species in the gas phase, D_b = molecular diffusivity of the condensing species in the particle phase, and H' = dimensionless Henry's law constant for the condensing species ($H' = H_A RT$). Equation (7.3) expresses the steady-state diffusion profile in the gas phase; under any circumstances the time scale to establish a steady-state concentration profile in the gas phase is extremely short and therefore the steady-state gas-phase profile for the condensing species holds at all time (Seinfeld and Pandis, 2016).

The use of a Henry's law constant is customary when describing the equilibrium of a dissolved solute in a relatively dilute cloud droplet. Here, our primary interest concerns the equilibrium of a solute between the gas phase and a sub-micrometer aerosol particle, for which a gas-particle equilibrium constant formulation is customary (Seinfeld and Pankow, 2003). The two formulations for equilibrium can be related as follows. Assuming an ideal mixture, the equilibrium partial pressure of condensing species A is $p_A = x_A p_A^\circ$, where p_A° = saturation vapor pressure of species A, and x_A = mole fraction of A in the particle phase. The mole fraction of the condensing species A is related to the mass fraction in the gas-phase, $x_A = \dfrac{A^g}{c^*}$, where A^g = the mass concentration of condensing species A in the gas-phase, g (m^3 of air)$^{-1}$ and c^* is the saturation mass concentration of the condensing species. Assuming the molecular weight of the condensing species A is identical

to that of the absorbing particle-phase and individual condensing species A is one of many in the particle-phase, the mole fraction of A can be written as

$$x_A \approx \frac{A^p}{c_{OA} + A^p} \approx \frac{A^p}{c_{OA}},$$

where A^p = the mass concentration of condensing species A in the particle-phase, g (m^3 of air)$^{-1}$, and c_{OA} = the mass concentration of absorbing-phase, g (m^3 of air)$^{-1}$. Thus, the distribution factor f_A, the ratio of particle-phase mass concentration to the gas-phase mass concentration, is

$$f_A = \frac{A^p}{A^g} = \frac{c_{OA}}{c^*},$$

and

$$f_A = H_A RT w_L = H' w_L,$$

where H_A = Henry's law constant in M atm^{-1}, w_L = volume fraction of particle in the air, (m^3 of particle) (m^3 of air)$^{-1}$. Thus, the partitioning equilibrium constant is

$$K_p = \frac{A^p / c_{OA}}{A^g} = \frac{1}{c^*},$$

and the dimensionless Henry's law constant H' is formally related to the gas-particle partitioning equilibrium constant by

$$H' = K_p \frac{c_{OA}}{w_L} = K_p \rho_p,$$

where ρ_p = the density of particle, g (m^3 of air)$^{-1}$. The equilibrium fraction of organic material in the particle phase is $(1 + c^*/c_{OA})^{-1}$. Thus, for $c_{OA} = 1$ μg m^{-3}, a condensing substance with $c^* = 1$ μg m^{-3} will reside 50% in the particle phase at equilibrium; a substance with $c^* = 0.01$ μg m^{-3} will reside 99% in the particle phase.

The solution for the normalized particle-phase concentration of the condensing species defined by equations (7.1) - (7.5) is (Liu, Zaveri, and Seinfeld, 2014)

$$\phi(\eta, \theta) = 1 - \frac{2}{\eta} \sum_{n=1}^{\infty} \frac{L e^{-\beta_n^2 \theta} \sin(\beta_n \eta)}{[\beta_n^2 + L(L-1)] \sin \beta_n} \tag{7.6}$$

where $\phi = \frac{A(r,t)}{A_\infty}$, $\eta = \frac{r}{R_p}$, $\theta = \frac{D_b t}{R_p^2}$, $A_\infty = H' G_\infty$ and where A_∞ is the particle-phase concentration of the condensing species at equilibrium with the gas-phase concentration G_∞. β_n is the n^{th} positive root of

$$\beta \cot \beta + L - 1 = 0 \tag{7.7}$$

where

$$L = \frac{v_b^{-1}}{v_i^{-1} + v_g^{-1}} \tag{7.8}$$

and where the transport velocities for gas-phase diffusion, interfacial transport, and particle-phase diffusion are

$$v_g = \frac{D_g}{R_p H'}, v_i = \frac{\alpha \bar{v}}{4H'}, v_b = \frac{D_b}{R_p}. \tag{7.9}$$

Physically, L is the ratio of the gas-phase + interfacial transport velocities to the particle-phase transport velocity. Thus, a limit of $L \gg 1$ implies that transport in the particle phase is much slower than that in the gas phase or across the interface, and a limit of $L \ll 1$ corresponds to the case in which particle-phase diffusion is rapid relative to either gas-phase diffusion or interfacial accommodation.

The time-dependent gas-phase concentration profile of the condensing species is obtained from equation (7.6) based on equality of fluxes, equation (7.2),

$$\frac{G(\eta, \theta)}{G_\infty} = 1 - \frac{1}{\eta}\left[2\sum_{n=1}^{\infty} \frac{L e^{-\beta_n^2 \theta}}{\beta_n^2 + L(L-1)} - \frac{8H' D_b}{\alpha \bar{v} R_p} \sum_{n=1}^{\infty} \frac{L^2 e^{-\beta_n^2 \theta}}{\beta_n^2 + L(L-1)}\right]. \tag{7.10}$$

The e-folding timescale to achieve overall gas-particle equilibrium partitioning is approximated by the exponent in the first term of the infinite series in equation (7.6),

$$\tau_{eq} = \frac{R_p^2}{\beta_1^2 D_b}. \tag{7.11}$$

This timescale represents that for the entire particle to achieve equilibrium with the bulk gas-phase concentration, G_∞. Three important limits can be identified on the basis of equation (7.11).

If the transport resistance is dominated by gas-phase diffusion, *i.e.*, $v_g \ll v_i$ and $v_g \ll v_b$, then

$$L \cong \frac{D_g}{H' D_b} \ll 1 \tag{7.12}$$

and $\beta_1 \cong \sqrt{3L} \ll 1$. In this case, both interfacial equilibrium and a uniform particle-phase concentration are established (Figure 7.2a). Letting $L \to 0$ in equation (7.6), $\lim_{L \to 0^+} \phi(\eta, \theta) = 1 - e^{-3L\theta}$, the time-dependent dimensionless concentration of the condensing species in the particle phase is

$$\phi(\eta, \theta) = 1 - \exp\left(-\frac{3D_g}{H' R_p^2} t\right), \tag{7.13}$$

and the equilibrium partitioning timescale is governed by diffusion in the particle phase,

$$\tau_{eq} = H' \frac{R_p^2}{3D_g}. \tag{7.14}$$

If the transport resistance is dominated by interfacial accommodation, *i.e.*, $v_i \ll v_g$ and $v_i \ll v_b$, the parameter L can be approximated as

$$L \cong \frac{\alpha \bar{v} R_p}{4H' D_b} \ll 1. \tag{7.15}$$

In this limiting case, the concentration profiles of the condensing species in both the gas and particle phases are essentially uniform, owing to relatively rapid particle-phase diffusion (Figure 7.2b). The form of the dimensionless concentration of the condensing species in the particle phase in this limit is

$$\lim_{L \to 0^+} \phi(\eta, \theta) = 1 - \exp\left(-\frac{3\alpha\bar{v}}{4H' R_p} t\right), \tag{7.16}$$

and the equilibrium partitioning timescale in this case is

$$\tau_{eq} = H' \frac{4R_p}{3\alpha\bar{v}}. \tag{7.17}$$

If the overall transport resistance is dominated by particle-phase diffusion, *i.e.*, $v_b \ll v_g$ and $v_b \ll v_i$, then equation (7.7) reduces to,

$$\beta_n = n\pi \left(1 - \frac{1}{L-1}\right), \tag{7.18}$$

and

$$\lim_{L \to 0^+} \phi(\eta, \theta) = 1 - \frac{2}{\eta} \sum_{n=1}^{\infty} \frac{(-1)^{n-1}}{n\pi} e^{-n^2\pi^2\theta} \sin(n\pi\eta). \tag{7.19}$$

The equilibrium partitioning timescale in this limit, depicted in Figure 7.2c, is simply that associated with diffusion in the particle phase,

$$\tau_{eq} = \frac{R_p^2}{\pi^2 D_b}. \tag{7.20}$$

Table 7.1 presents parameter values that illustrate the three limiting regimes of gas-particle equilibration. In each case we consider an organic species with saturation mass concentration $c^* = 10\mu$g m^{-3}, molecular weight $M = 200$ g mol^{-1}, and a gas-phase molecular diffusivity $D_g = 10^{-1}$ cm^{2}s^{-1}. Gas-phase diffusion limited partitioning is likely to occur for large liquid particles (*i.e.*, droplets) with a vapor accommodation coefficient α close to 1.0. Interfacial transport limited partitioning will hold for small, somewhat viscous particles with a relatively small vapor accommodation coefficient. Finally, particle-phase diffusion limited partitioning is expected to occur for highly viscous (*e.g.* semi-solid) aerosols.

7.4 Results and Discussion

Analytical timescales

Figure 7.3 shows the dependence of the analytical gas-particle partitioning timescale τ_{eq} on particle-phase diffusivity D_b and accommodation coefficient α for cloud droplets (Panel (a): D_p = 20 μm) and fine-mode aerosols (Panel (b): D_p = 100 nm). The dashed lines in Figure 7.3 are intended to give a rough indication of the location of the transition regions between those representing different controlling mechanisms. Although our principal interest in this work is the equilibration behavior of organic atmospheric aerosols, it is informative to examine the implications of the theory for typical cloud droplets, as well. The equilibration timescale for a solute dissolving in a cloud droplet with typical aqueous-phase diffusivities is gas-phase diffusion controlled for values of $\alpha \gtrsim 0.01$. Because of the relatively large size of cloud droplets, theoretical gas-droplet equilibration timescales are much longer than the typical lifetime of a cloud droplet. Most relevant for the present work is Panel (b) of Figure 7.3. For particles in the size range of typical atmospheric organic aerosols (50 nm to 500 nm), the gas-particle equilibration timescale is governed either by interfacial accommodation or particle-phase diffusion. For $\alpha \gtrsim 0.01$ and $D_b \lesssim 10^{-13}$ cm^{2}s^{-1}, gas-particle equilibration is controlled by particle-phase diffusion; when $\alpha \lesssim 0.01$, interfacial accommodation is controlling, and τ_{eq} is asymptotically proportional to α. For $\alpha \gtrsim 0.1$, the timescale for a fine mode aerosol particle to achieve gas-particle equilibrium is of order minutes for all but the smallest particle-phase diffusion coefficients. For sub-micrometer atmospheric aerosols, gas-phase diffusion of the condensing species is not a limiting process to achieve gas-particle equilibrium. The transitional boundaries between limiting regimes can be defined approximately by the intersection of the corresponding asymptotic solutions. For example, a rough indication of the particle size range where the transition between gas-phase diffusion-limited and interfacial-transport limited regimes occurs can be obtained by combining equations (7.14) and (7.17),

$$R_p = \frac{4D_g}{\alpha \bar{v}}. \tag{7.21}$$

Figure 7.4 shows τ_{eq} as a function of particle diameter D_p and Henry's law constant and c^* with α = 1.0. Panel (a) is for $D_b = 10^{-8}$cm^2 s^{-1}, and Panel (b) is for $D_b = 10^{-13}$cm^{2}s^{-1}. For SOA, the gas-particle equilibrium state is commonly characterized by the gas-phase saturation mass concentration c^* and the gas-particle partitioning equilibrium constant K_p, which as we have shown can be related to H'. τ_{eq}, increases with particle diameter, since the smaller surface area per unit volume for larger particles is less efficient for vapor uptake. Gas-particle partitioning between a highly volatile organic compound ($c^* \gtrsim 10^6 \mu$g m^{-3}) and a liquid particle (Panel (a)) is rapid. If the condensing species is less volatile, more material ultimately condenses into the particle

at equilibrium. The larger amount of condensing material must be transported into the particle through the gas phase and the interface, which leads to a longer equilibration time. Since particle-phase diffusion alone does not depend on the volatility of the condensing species, the limiting step changes from particle-phase diffusion towards interfacial transport or gas-phase diffusion for low volatility species. Panel (b) presents the comparable calculation for a highly viscous particle. Owing to hindered diffusion in the particle phase, equilibration times are longer than in the liquid particle for the same particle size and species volatility.

Numerical simulation in open and closed systems

An alternative to the analytical evaluation of equilibration timescales is detailed numerical simulation of the process of vapor molecule diffusion to and uptake in a particle, or a population of particles. The kinetic multi-layer model (KM-GAP, U Pöschl, Rudich, and Ammann (2007) and M Shiraiwa et al. (2012)) for gas-particle interactions in aerosols and clouds allows evaluation of τ_{eq} by numerically simulating the evolution of the condensing species concentrations in gas and particle phases (Manabu Shiraiwa and Seinfeld, 2012). The model is general in terms of whether the overall system is open (vapor concentration maintained constant) or closed (finite amount of vapor). The analytical solution above assumes an open system, *i.e.*, the bulk gas-phase concentration of the condensing species is constant. In a closed system the bulk gas-phase concentration decreases as condensation into the aerosol phase proceeds.

It is instructive to compare the analytical approximation for τ_{eq} based on equation (7.11) with that derived from numerical simulation using KM-GAP. We consider numerical simulation of a population of particles growing in open and closed systems. For simplicity, gas and particle-phase chemical reactions are not considered in this comparison. Figure 7.5a shows the equilibrium partitioning timescale as a function of saturation mass concentration c^* at different particle number concentrations, c_{aer}, in a closed system. The analytical approximation and the numerical simulation are essentially identical for relatively volatile species, $c^* \gtrsim 10^3 \mu\text{g m}^{-3}$. The analytical prediction based on the assumption of a fixed bulk gas-phase concentration of the condensing species and the numerical simulation based on a closed system in which the bulk concentration declines with time begin to diverge for $c^* \lesssim 10^3 \mu\text{g m}^{-3}$. This divergence is the result of two effects that are not explicitly treated in the analytical solution: (1) Particle size change - the KM-GAP model tracks the change of particle size due to condensation of vapor and; (2) Vapor depletion - in a closed system, as vapor condenses on the particle, the bulk gas-phase concentration decreases. Each of these two effects becomes negligible for a sufficiently volatile condensing species ($c^* \gtrsim 10^3 \mu\text{g m}^{-3}$), since less overall amount of vapor species condenses into the particles. Consequently, the

gas-particle equilibrium timescale computed from KM-GAP shows no dependence on the aerosol number concentration caer in this region. For condensing species saturation mass concentration in the range $2 \times 10^2 \mu$g m$^{-3} \lesssim c^* \lesssim 10^3 \mu$g m^{-3}, the discrepancy between the open and closed system arises from the effect of particle growth. The equilibrium particle size increases dramatically in this region, as shown in Figure 7.5b, so the actual time for the system to achieve gas-particle equilibrium can be considerably longer than that estimated based on the initial particle size. For decreasing particle concentration c_{aer}, the equilibrium particle size increases, since a greater amount of vapor condenses into each particle. For number concentrations characteristic of urban conditions ($c_{aer} = 10^5$cm^{-3}), the condensing vapor is distributed over a relatively large number of particles, and the effect of particle size change on the equilibration timescale is negligible, as shown in Figure 4b. However, in the closed system, the effect of gas-phase depletion begins to dominate the equilibrium timescale; as the vapor becomes depleted, a progressively smaller amount of vapor transfers into the particle phase, and the equilibrium timescale decreases.

For less volatile vapor, $c^* \lesssim 2 \times 10^3 \mu$g m^{-3}, in the closed system, gas-particle partitioning is dominated by gas-phase depletion of the condensing species. Less volatile condensing species transfer predominantly into the particle phase, and as volatility decreases, τ_{eq} and the equilibrium particle size eventually become independent of the volatility of the condensing species since virtually all of it effectively condenses.

Implications for atmospheric models

Atmospheric models simulate the formation and growth of organic aerosols. At present, these processes are assumed in most models to be the result of instantaneous gas-particle equilibrium. In addition, most atmospheric models do not resolve the ambient aerosol size distribution. Under a number of ambient situations the rate at which that equilibrium is achieved can be slower than the rates at which other atmospheric processes are changing. The numerical machinery needed to resolve these microscopic gas-particle interactions would add substantially to an already heavy computational load. Using a combination of analytical transport theory and numerical modeling, the present work delineates the broad conditions governing the timescales for establishing gas-particle equilibrium. These conditions depend on the surface accommodation coefficient and volatility of the species in question, the diffusivity of the condensing organic species in the particle phase, and the particle size. In most ambient modeling circumstances, surface accommodation coefficients for condensing species and viscosities of particles (from which diffusion coefficients have to be inferred) are not known with precision. Thus, a high degree of uncertainty will attend any computation based on microscopic particle dynamics; nonetheless, the results of the present work

provide a framework for estimation of the possible effect of non-equilibrium growth in atmospheric models of organic aerosols.

Acknowledgements

This work was supported by National Science Foundation grant AGS-1523500.

Table 7.1: Examples of Three Limiting Cases [a]

	Gas-phase diffusion limited partitioning	Interfacial transport limited partitioning	Particle-phase diffusion limited partitioning
R_p (μ m)	10	0.05	0.05
D_b ($cm^2 s^{-1}$)	10^{-5}	10^{-9}	10^{-18}
α	1	10^{-3}	10^{-2}
	$v_g/v_i = 2.25 \times 10^{-2}$	$v_i/v_g = 2.2 \times 10^{-4}$	$v_b/v_g = 10^{-6}$
	$v_g/v_b = 10^{-7}$	$v_i/v_b = 2.2 \times 10^{-7}$	$v_b/v_i = 4.5 \times 10^{-4}$

[a] $c^* = 10\mu g\ m^{-3}$; $M = 200 g\ mol^{-1}$; $D_g = 0.1 cm^2\ s^{-1}$; $H' = 10^{11}$. Since H' and c^* are related by $H' = \rho_p/c^*$, where ρ_p is the density of the particle, $c^* = 10\mu g\ m^{-3}$ corresponds to $H' = 10^{11}$.

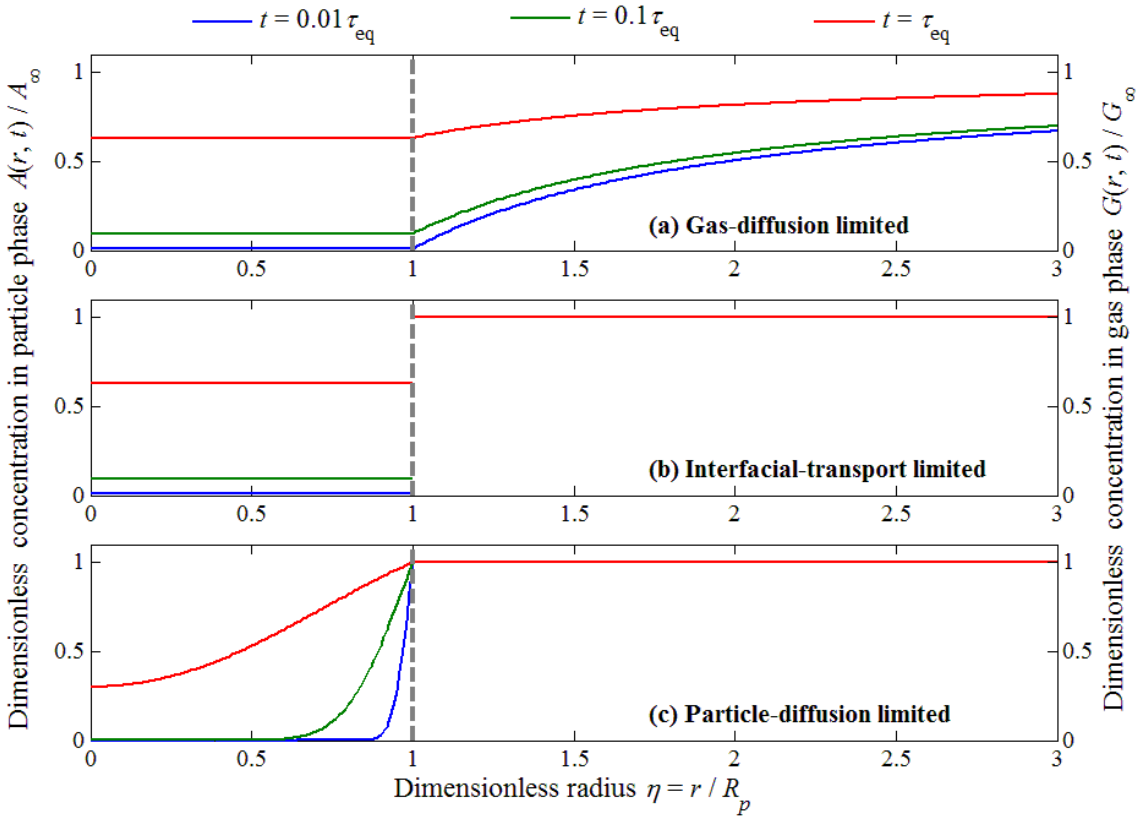

Figure 7.2: Dimensionless concentration profiles in the particle and gas phase for three limiting cases: (a) Gas-phase diffusion-limited partitioning; (b) Interfacial-transport limited partitioning; (c) Particle-phase diffusion-limited partitioning. The region $\eta \leq 1$ corresponds to the particle phase.

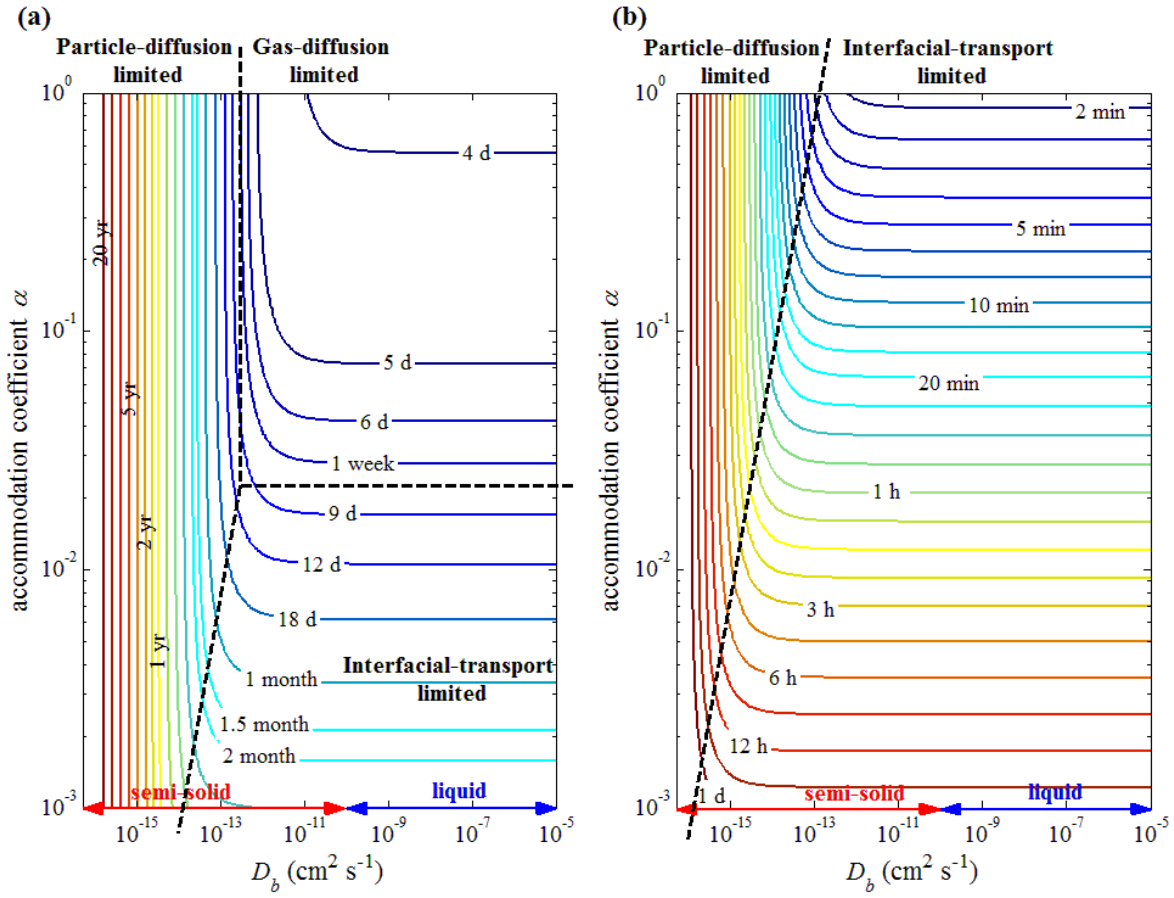

Figure 7.3: Analytical equilibrium partitioning time scale as a function of particle-phase diffusivity D_b and accommodation coefficient α for two particle diameters: Panel (a) 20 μm; Panel (b) 100 nm. Other physical parameters are identical for the two panels: M = 200 g mol^{-1}, D_g = 10^{-1} cm^2 s^{-1}, H' = 10^{11}.

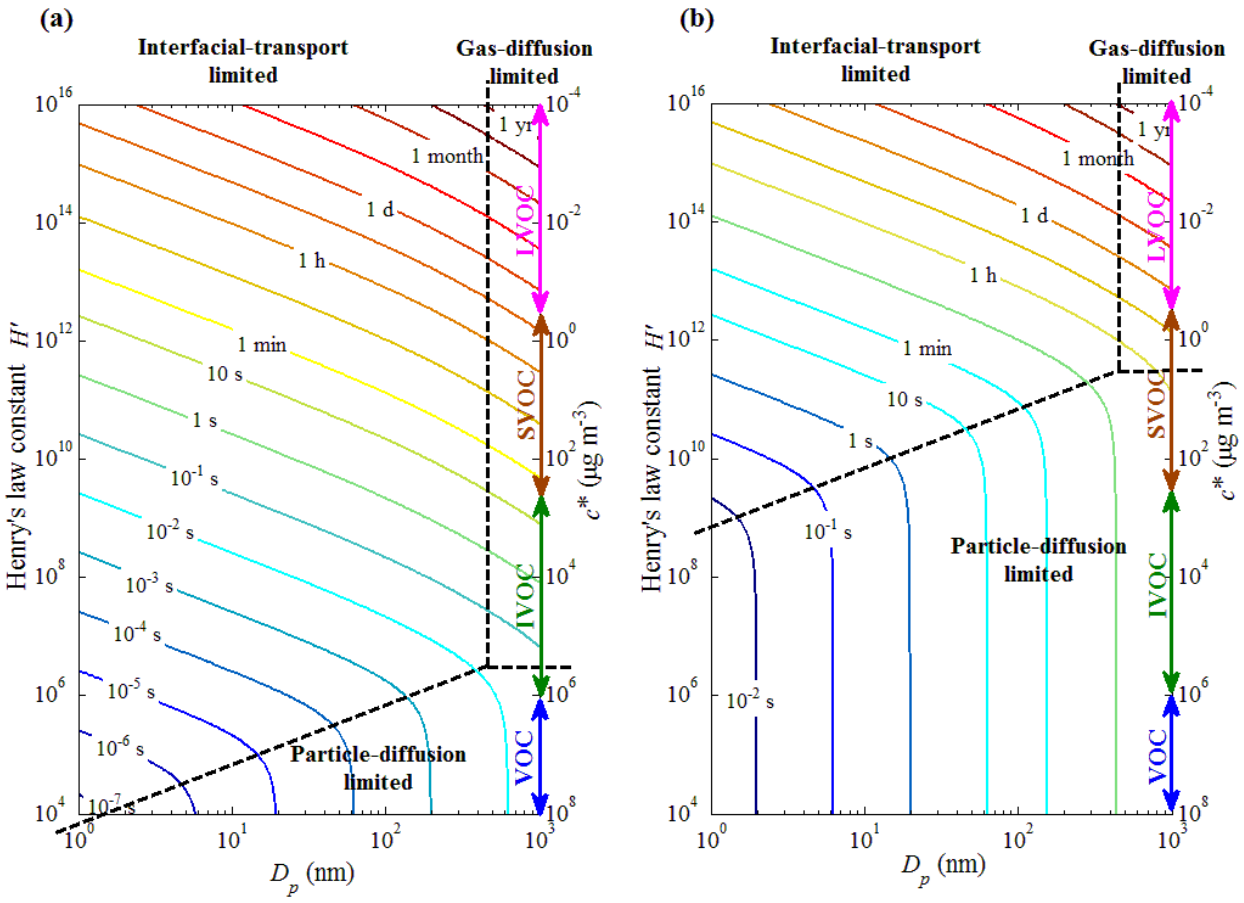

Figure 7.4: Analytical equilibrium partitioning timescale as a function of particle diameter D_p and Henry's law constant H' (or equivalent saturation mass concentration c^*) (ρ_p = 1 g cm^{-3}, α = 1). Panel (a): liquid particles: $D_b = 10^{-8}$ cm^2 s^{-1}. Panel (b): highly viscous particles: $D_b = 10^{-13}$ cm^2 s^{-1}.

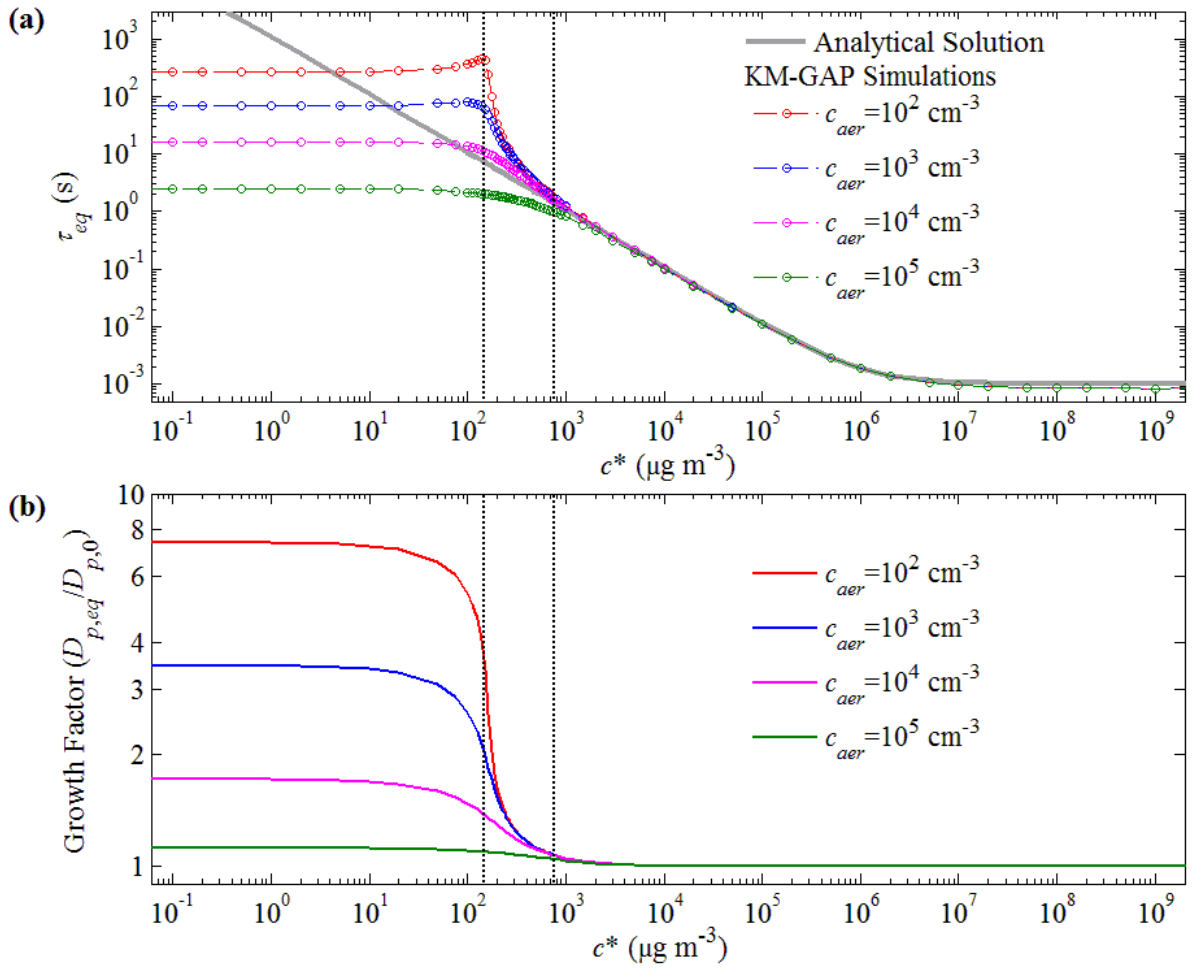

Figure 7.5: Effect of an open vs. closed system. The analytical equilibration timescale for the open system is given by equation (11). The equilibration timescale for the closed system is computed by the KM-GAP numerical model. Panel (a): Equilibrium partitioning timescale as a function of saturation mass concentration c^* at different particle number concentrations, c_{aer}, for both open and closed systems. Panel (b): Equilibrium particle growth factor in the closed system as a function of particle number concentration from KM-GAP. Physical parameters used in the KM-GAP model simulations are: α = 1.0, $\tau_d = 10^{-9}$ s, ρ_p =1 g cm^{-3}, $D_b = 10^{-8}$ cm^2 s^{-1}, $D_g = 10^{-1}$ cm^2 s^{-1}, M = 200 g mol^{-1}, $D_{p,0}$ = 200 nm.

References

Abramson, Evan et al. (2013). "Experimental determination of chemical diffusion within secondary organic aerosol particles". In: *Physical Chemistry Chemical Physics* 15.8, pp. 2983–2991.

Grieshop, Andrew P, Neil M Donahue, and Allen L Robinson (2007). "Is the gas-particle partitioning in alpha-pinene secondary organic aerosol reversible?" In: *Geophysical Research Letters* 34.14.

Kuwata, Mikinori and Scot T Martin (2012). "Phase of atmospheric secondary organic material affects its reactivity". In: *Proceedings of the National Academy of Sciences* 109.43, pp. 17354–17359.

Liu, Albert Tianxiang, Rahul A Zaveri, and John H Seinfeld (2014). "Analytical solution for transient partitioning and reaction of a condensing vapor species in a droplet". In: *Atmospheric Environment* 89, pp. 651–654.

Loza, Christine L et al. (2013). "On the mixing and evaporation of secondary organic aerosol components". In: *Environmental science & technology* 47.12, pp. 6173–6180.

Perraud, Véronique et al. (2012). "Nonequilibrium atmospheric secondary organic aerosol formation and growth". In: *Proceedings of the National Academy of Sciences* 109.8, pp. 2836–2841.

Pierce, JR et al. (2011). "Quantification of the volatility of secondary organic compounds in ultrafine particles during nucleation events". In: *Atmospheric Chemistry and Physics* 11.17, pp. 9019–9036.

Pöschl, U, Y Rudich, and M Ammann (2007). "Kinetic model framework for aerosol and cloud surface chemistry and gas-particle interactions–Part 1: General equations, parameters, and terminology". In: *Atmospheric Chemistry and Physics* 7.23, pp. 5989–6023.

Renbaum-Wolff, L, JW Grayson, and AK Bertram (2013). "New methodology for measuring viscosities in small volumes characteristic of environmental chamber particle samples". In: *Atmospheric Chemistry and Physics* 13.2, pp. 791–802.

Renbaum-Wolff, Lindsay et al. (2013). "Viscosity of α-pinene secondary organic material and implications for particle growth and reactivity". In: *Proceedings of the National Academy of Sciences* 110.20, pp. 8014–8019.

Saukko, E et al. (2012). "Humidity-dependent phase state of SOA particles from biogenic and anthropogenic precursors". In: *Atmospheric Chemistry and Physics* 12.16, pp. 7517–7529.

Seinfeld, John H and Spyros N Pandis (2016). *Atmospheric chemistry and physics: from air pollution to climate change*. John Wiley & Sons.

Seinfeld, John H and James F Pankow (2003). "Organic atmospheric particulate material". In: *Annual review of physical chemistry* 54.1, pp. 121–140.

Shiraiwa, Manabu and John H Seinfeld (2012). "Equilibration timescale of atmospheric secondary organic aerosol partitioning". In: *Geophysical Research Letters* 39.24.

Shiraiwa, M et al. (2012). “Kinetic multi-layer model of gas-particle interactions in aerosols and clouds (KM-GAP): linking condensation, evaporation and chemical reactions of organics, oxidants and water”. In: *Atmospheric Chemistry and Physics* 12.5, pp. 2777–2794.

Vaden, Timothy D, Dan Imre, et al. (2011). “Evaporation kinetics and phase of laboratory and ambient secondary organic aerosol”. In: *Proceedings of the National Academy of Sciences* 108.6, pp. 2190–2195.

Vaden, Timothy D, Chen Song, et al. (2010). “Morphology of mixed primary and secondary organic particles and the adsorption of spectator organic gases during aerosol formation”. In: *Proceedings of the National Academy of Sciences* 107.15, pp. 6658–6663.

Virtanen, Annele et al. (2010). “An amorphous solid state of biogenic secondary organic aerosol particles”. In: *Nature* 467.7317, p. 824.

Zaveri, Rahul A et al. (2014). “Modeling kinetic partitioning of secondary organic aerosol and size distribution dynamics: representing effects of volatility, phase state, and particle-phase reaction”. In: *Atmospheric Chemistry and Physics* 14.10, pp. 5153–5181.

SUPPLEMENTARY INFORMATION FOR SCANNING DMA DATA ANALYSIS I. CLASSIFICATION TRANSFER FUNCTION

A.1 COMSOL simulation

Fluid flow field and electric field simulations

The configuration of the TSI Model 3081A long-column DMA, shown in the Figure 1 of the main text, was subdivided into entrance, classification and exit regions to perform particle trajectories simulations individually. Both the entrance and exit regions are grounded; the fluid flow field in these regions, which have non-axisymmetric elements, were simulated with a 3-dimensional, steady-state, laminar flow model in COMSOL Multiphysics^{TM}, respectively. Fig. A.1 shows the sectional view of the fluid flow profile for an aerosol flow of Q_a = 0.51 LPM (liters per minute) through the DMA entrance region. To simulate the flow field, the DMA polydisperse inlet was defined as the fluid inflow boundary, with the flow, Q_a, assumed to be fully-developed and laminar. An atmospheric pressure boundary condition was prescribed at the annular outflow boundary. The no slip condition is applied to all the other boundaries.

Fig. A.2 shows flow field within the the DMA exit, downstream of the adverse potential gradient region. The flow field simulation extends part of the way into the central tube flow region where at the end of the extended classification region so that the fully developed fluid flow is reproduced at the entrance to the exit region. Recirculation can be observed at the bottom of the cone where the incoming flow impinge on the wall before entering the classified aerosol outlet section.

To facilitate the Brownian dynamics simulations of the particle trajectories within the DMA, the flow region of the two-dimensional simulation in COMSOL^{TM} was subdivided into 11 zones shown in Fig. A.3; the data obtained from COMSOL^{TM} simulations on the triangular mesh in each of these sections were interpolated onto a quadrilateral grid to facilitate efficient evaluation of the local velocity and electric field in the Brownian dynamics simulations. As shown in the top inset, grid spacings were nonuniform to capture the boundary layer regions of the flow, and non-rectilinear where necessary to follow the shapes of the boundaries, as illustrated in the lower inset.

Particle trajectory simulation

The particle trajectory simulations in the DMA entrance and exit regions were completed by applying the COMSOL Multiphysics^{TM} 5.0 particle tracing module to the fluid flow fields and

quasi-steady-state electric fields that had previously been obtained. The COMSOL Multiphysics^{TM} 5.0 particle tracing module does not account for non-continuum effects, *i.e.*, there is provision for including a slip correction factor. Therefore, an equivalent particle size method was used to account for the non-continuum effects of drag force and Brownian diffusion simultaneously, *i.e.*, the pseudo particle diameter as simulation input is $D_{p,sim} = D_p/C_c(D_p)$, where D_p is actual particle diameter, and $C_c(D_p)$ is the Cunningham correction factor.

The efficiency of penetration through the entrance region was evaluated as

$$\eta_{ent}(D_p) = \frac{N_{out}}{N_{in}}, \tag{A.1}$$

where D_p is the electric mobility equivalent particle diameter, N_{out} is number of particles reaching the outflow boundary, and N_{in} is the number of particles injected to the inflow boundary. For simulations at each particle size, 10^5 particles were supplied to the inflow boundary, with a particle density proportional to the fluid volumetric flux.

The time-dependent penetration efficiency for each size and time was evaluated at the time when particles leave the exit region, *i.e.*,

$$\eta_{exit}(D_p, t) = \frac{N_{out}(t)}{N_{in}}, \tag{A.2}$$

where $N_{out}(t)$ is number of particles reaching the outlet boundary at time t since the particles enter the DMA exit region. Due to the wall deposition, the overall penetration for a given particle size can not exceed unity, *i.e.*, $\int_0^\infty \eta_{exit}(D_p, t)\mathrm{d}t \leq 1$ for any D_p.

A.2 Brownian dynamics in cylindrical coordinates

Eq. (7) in the main text shows the radial component of particle motion in cylindrical coordinates, based on the sketch shown in Fig. A.4. The radial motion combines the Brownian contributions in the x and y directions, $\mathrm{d}\sigma_x^2 = \mathrm{d}\sigma_y^2 = 2\mathcal{D}\mathrm{d}t$, into the r component. The radial position of the particle as a function of time is, therefore,

$$r(t + \mathrm{d}t) = \sqrt{\left[r(t) + \int_t^{t+\mathrm{d}t} v_r(r, z, t)\mathrm{d}t + g\left(\sqrt{\mathrm{d}\sigma_x^2}\right)\right]^2 + g\left(\sqrt{\mathrm{d}\sigma_y^2}\right)^2}. \tag{A.3}$$

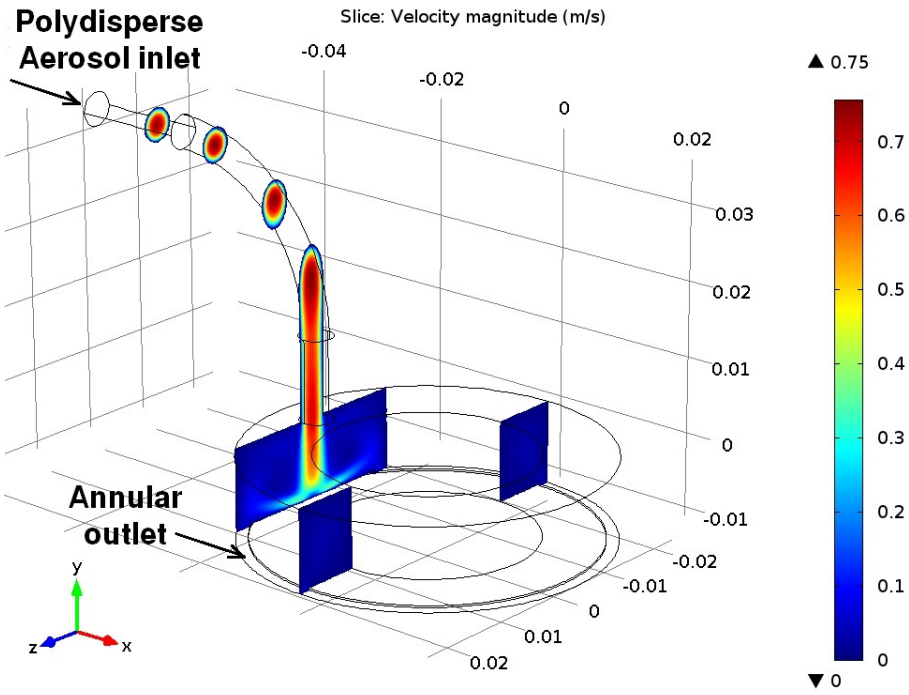

Figure A.1: Section view of fluid flow velocity magnitude within the DMA entrance region at $z = -0.045, -0.035, -0.025, -0.019, 0$ m.

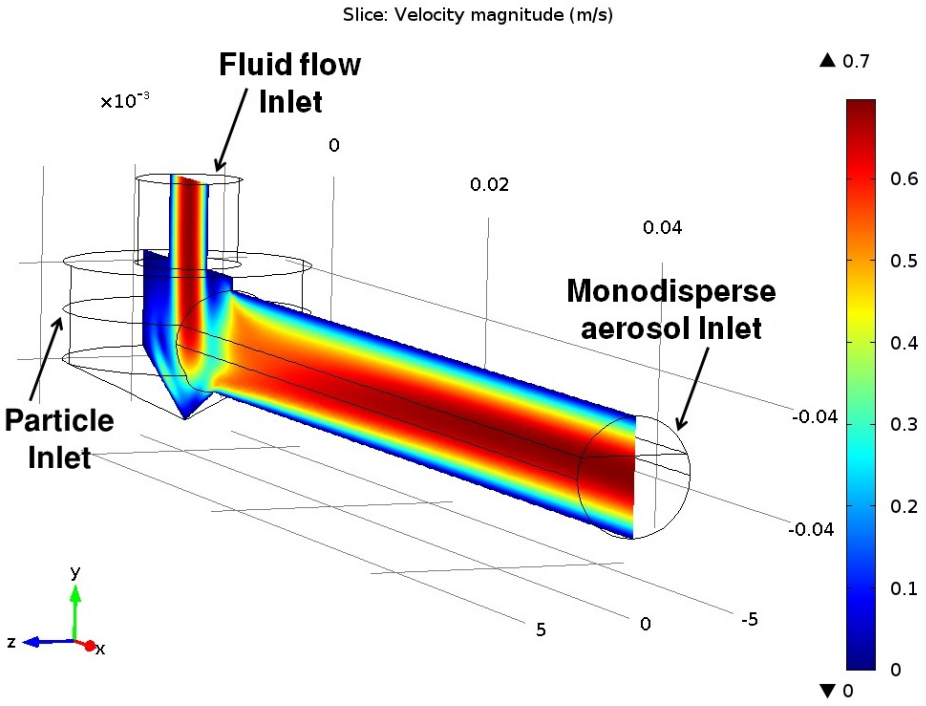

Figure A.2: Section view of fluid flow velocity magnitude within the DMA exit region at $z = 0$ m. Notice that the fluid flow simulation is extended into the classification region to calculate the accurate fluid flow field within the exit region.

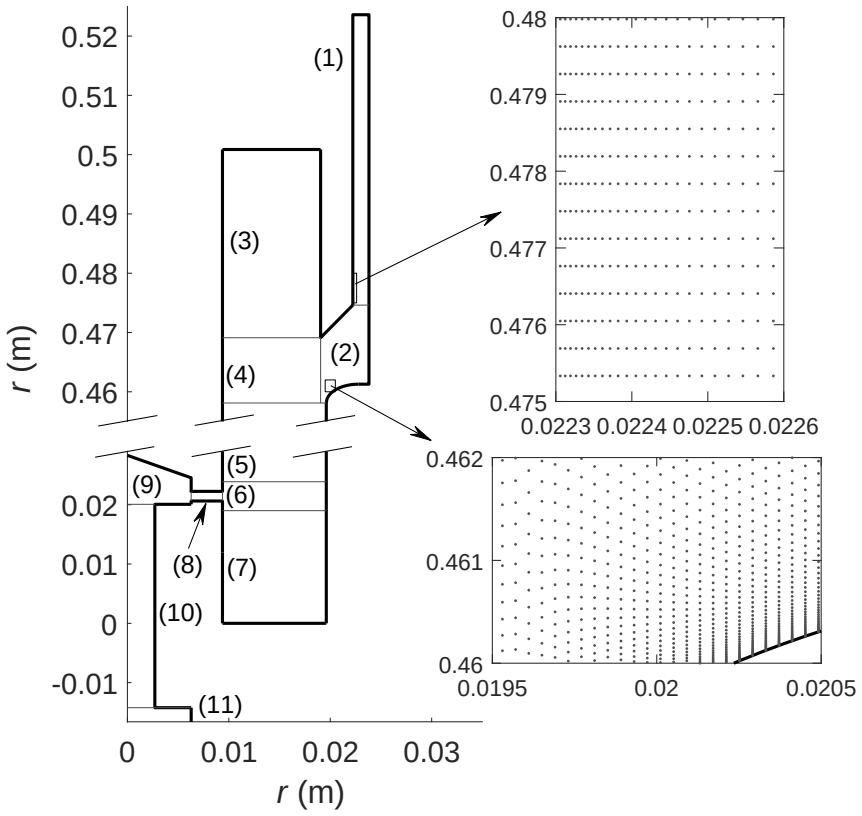

Figure A.3: Segmentation of the exact classification region, with zone indices labled. Inset shows the interpolation grids for the fluid flow field and the electric field.

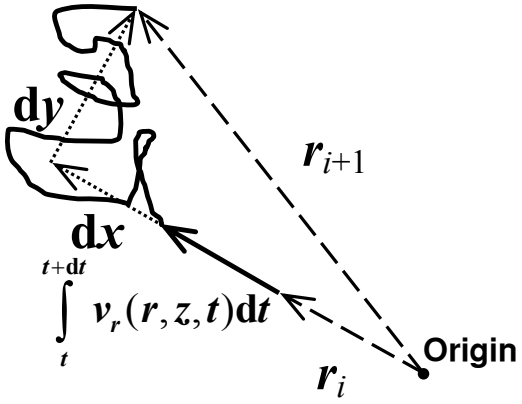

Figure A.4: Particle motion in radial direction. $\int_t^{t+dt} v_r(r,z,t)dt$ denotes the migration in the fluid flow field and electric field, and dx and dy denote the displacement due to Brownian motion.

SUPPLEMENTARY INFORMATION FOR SCANNING DMA DATA ANALYSIS II. INTEGRATED DMA-CPC INSTRUMENT RESPONSE AND DATA INVERSION

B.1 Integrated DMA-CPC instrument response

The total number of particles recorded in the SEMS in the time bin i is

$$\begin{aligned} R_{i,\mathrm{SEMS}} &= Q_\mathrm{a} \int_{(i-1)t_\mathrm{c}}^{it_\mathrm{c}} \int_{-\infty}^{\infty} n(u) \sum_{\phi} p_\mathrm{charge}(u,\phi)\eta_\mathrm{F}(u,\phi)\eta_\mathrm{CPC}(u,\phi) \\ &\times \left[\Gamma_\mathrm{SEMS}(Z_\mathrm{p}(u,\phi),\beta,\delta,it_\mathrm{c}) - \Gamma_\mathrm{SEMS}(Z_\mathrm{p}(u,\phi),\beta,\delta,(i-1)t_\mathrm{c})\right] \mathrm{d}u, \end{aligned} \tag{B.1}$$

where Q_a is the incoming aerosol sample flow rate, and $n(u)$ is the size distribution of the source particles with the $u = \log D_\mathrm{p}$. $p_\mathrm{charge}(u,\phi)$, $\eta_\mathrm{F}(u,\phi)$ and $\eta_\mathrm{CPC}(u,\phi)$ are the probability that a particle of size u will acquire ϕ charges in the charge conditioner, the particle penetration efficiency, and the CPC counting efficiency, respectively. For convenience, the overall detection efficiency for particles with diameter u and ϕ charges can be expressed concisely as $\eta(u,\phi) = p_\mathrm{charge}(u,\phi)\eta_\mathrm{F}(u,\phi)\eta_\mathrm{CPC}(u,\phi)$. $\Gamma_\mathrm{SEMS}(Z_\mathrm{p}(u,\phi),\beta,\delta,t)$ is the cumulative transfer function for the SEMS.

With the definition of the kernel function

$$h_i(u) = Q_\mathrm{a} \sum_{\phi} \eta(u,\phi) \left[\Gamma_\mathrm{SEMS}(Z_\mathrm{p}(u,\phi),\beta,\delta,it_\mathrm{c}) - \Gamma_\mathrm{SEMS}(Z_\mathrm{p}(u,\phi),\beta,\delta,(i-1)t_\mathrm{c})\right], \tag{B.2}$$

the instrument reponse in Eq. (B.1) becomes

$$R_{i,\mathrm{SEMS}} = \int_{-\infty}^{\infty} h_i(u) n(u) \mathrm{d}u. \tag{B.3}$$

The inversion problem is to retrieve the size distribution function $n(u)$ on the targeted particle size node $u_j^\dagger = \log D_{\mathrm{p},j}^\dagger$ ($j = 1, 2, \cdots, J$). The functional form of $n(u)$ is assumed to be linear spline over each targeted particle size interval $[u_j^\dagger, u_{j+1}^\dagger)$,

$$n(u) = n(u_j^\dagger) + \frac{n(u_{j+1}^\dagger) - n(u_j^\dagger)}{u_{j+1}^\dagger - u_j^\dagger}\left(u - u_j^\dagger\right) = n(u_j^\dagger)\frac{u_{j+1}^\dagger - u}{u_{j+1}^\dagger - u_j^\dagger} + n(u_{j+1}^\dagger)\frac{u - u_j^\dagger}{u_{j+1}^\dagger - u_j^\dagger}. \tag{B.4}$$

The Fredholm integral, Eq.(B.3), is numerically evaluated by applying the trapezoidal rule on a particle-size grid $u_k = \log D_{\mathrm{p},k}$ ($k = 1, 2, \cdots, K$). To improve the accuracy of the kernel calculation,

the integration grid is much finer than the targeted size node, *i.e.*, $K \gg J$. In practice, the particle size grid u_k is created by slicing the targeted particle size interval $[u_j^\dagger, u_{j+1}^\dagger)$ into smaller size bins. Using trapezoidal-rule integration, Eq.(B.3) can be written in form of summation,

$$R_{i,\,\mathrm{SEMS}} = \sum_{k=1}^{K} \Delta u_k h_i(u_k) n(u_k), \tag{B.5}$$

where

$$\Delta u_k = \begin{cases} \dfrac{u_2 - u_1}{2}, & k = 1 \\ \dfrac{u_{k+1} - u_{k-1}}{2}, & k = 2, 3, \cdots, K-1 \\ \dfrac{u_K - u_{K-1}}{2}, & k = K \end{cases} \tag{B.6}$$

is the weighting factor arising from the trapezoidal integral. Combining Eqs.(B.4) and (B.5), the instrument response becomes

$$R_{i,\,\mathrm{SEMS}} = \sum_{k=1}^{K} \Delta u_k \left[n(u_j^\dagger) \frac{u_{j+1}^\dagger - u_k}{u_{j+1}^\dagger - u_j^\dagger} + n(u_{j+1}^\dagger) \frac{u_k - u_j^\dagger}{u_{j+1}^\dagger - u_j^\dagger} \right] h_i(u_k), u_k \in [u_j^\dagger, u_{j+1}^\dagger). \tag{B.7}$$

Equation (B.7) requires that, for each u_k, we must first determine which targeted size interval $[u_j^\dagger, u_{j+1}^\dagger)$ it belongs to, and then calculate the $h_i(u_k)$ values, and perform the summation. This process can be viewed from another perspective, in which we focus on the targeted size interval $[u_j^\dagger, u_{j+1}^\dagger)$ and then we find out all u_k within the interval, *i.e.*, $u_k \in [u_j^\dagger, u_{j+1}^\dagger)$. In the latter method, the summation index is changed from k to j,

$$\begin{aligned} R_{i,\,\mathrm{SEMS}} &= \sum_{j=1}^{J} \left[\sum_{u_k \geq u_j^\dagger}^{u_k < u_{j+1}^\dagger} \Delta u_k \frac{u_k - u_j^\dagger}{u_{j+1}^\dagger - u_j^\dagger} n(u_{j+1}^\dagger) h_i(u_k) + \sum_{u_k \geq u_j^\dagger}^{u_k < u_{j+1}^\dagger} \Delta u_k \frac{u_{j+1}^\dagger - u_k}{u_{j+1}^\dagger - u_j^\dagger} n(u_j^\dagger) h_i(u_k) \right] \\ &= \sum_{j=1}^{J} \left[\sum_{u_k \geq u_{j-1}^\dagger}^{u_k < u_j^\dagger} \Delta u_k \frac{u_k - u_{j-1}^\dagger}{u_j^\dagger - u_{j-1}^\dagger} n(u_j^\dagger) h_i(u_k) + \sum_{u_k \geq u_j^\dagger}^{u_k < u_{j+1}^\dagger} \Delta u_k \frac{u_{j+1}^\dagger - u_k}{u_{j+1}^\dagger - u_j^\dagger} n(u_j^\dagger) h_i(u_k) \right] \\ &= \sum_{j=1}^{J} \left[\sum_{u_k \geq u_{j-1}^\dagger}^{u_k < u_j^\dagger} \Delta u_k \frac{u_k - u_{j-1}^\dagger}{u_j^\dagger - u_{j-1}^\dagger} h_i(u_k) + \sum_{u_k \geq u_j^\dagger}^{u_k < u_{j+1}^\dagger} \Delta u_k \frac{u_{j+1}^\dagger - u_k}{u_{j+1}^\dagger - u_j^\dagger} h_i(u_k) \right] n(u_j^\dagger), \end{aligned} \tag{B.8}$$

As shown in Eq.(B.8), the instrument response can be cast into the form of matrix $\mathbf{R} = \mathbf{AN}$, in which $\mathbf{R} = [R_{1,\mathrm{SEMS}}, R_{2,\mathrm{SEMS}}, \cdots, R_{I,\mathrm{SEMS}}]^{\mathrm{T}}$ is the time-series instrument response, $\mathbf{N} = [n(u_1^\dagger), n(u_2^\dagger), \cdots, n(u_J^\dagger)]^{\mathrm{T}}$, and the $\mathbf{A}$ is the kernel matrix with elements

$$\mathbf{A}_{i,j} = \sum_{u_k \geq u^\dagger_{j-1}}^{u_k < u^\dagger_j} \Delta u_k \frac{u_k - u^\dagger_{j-1}}{u^\dagger_j - u^\dagger_{j-1}} h_i(u_k) + \sum_{u_k \geq u^\dagger_j}^{u_k < u^\dagger_{j+1}} \Delta u_k \frac{u^\dagger_{j+1} - u_k}{u^\dagger_{j+1} - u^\dagger_j} h_i(u_k). \tag{B.9}$$

B.2 Integrated SEMS system response plots

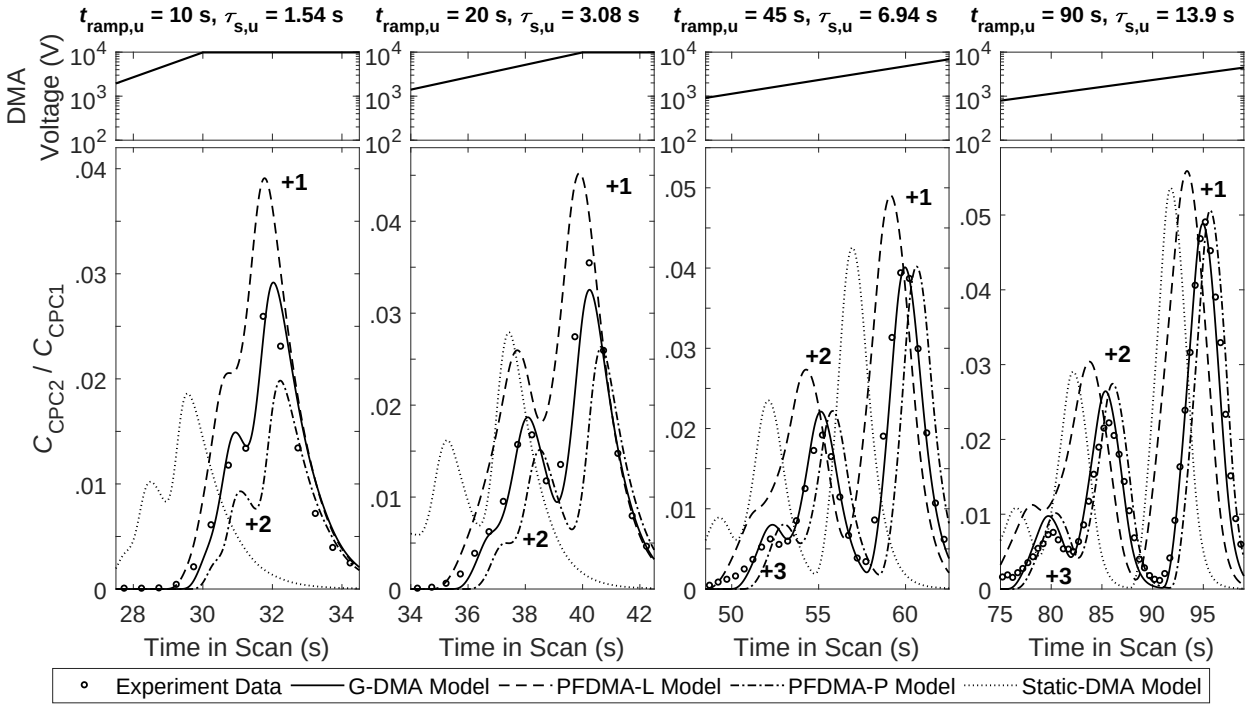

Figure B.1: Up-scan experimental and modeling results for SEMS instrument response to monodisperse 296 nm particles with ramp duration t_{ramp} = 10, 20, 45 and 90 s (corresponding to scan time τ_{s} = 1.54, 3.08, 6.94 and 13.9 s).

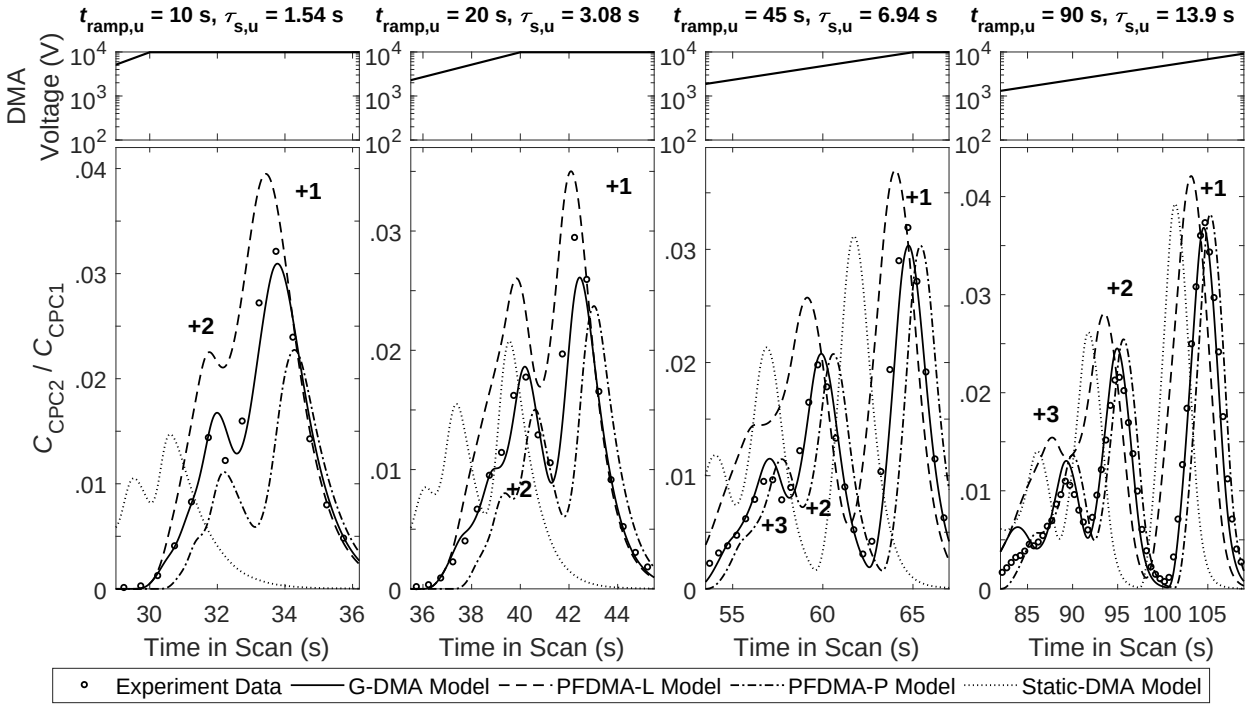

Figure B.2: Up-scan experimental and modeling results for SEMS instrument response to monodisperse 498 nm particles with ramp duration t_{ramp} = 10, 20, 45 and 90 s (corresponding to scan time τ_{s} = 1.54, 3.08, 6.94 and 13.9 s).

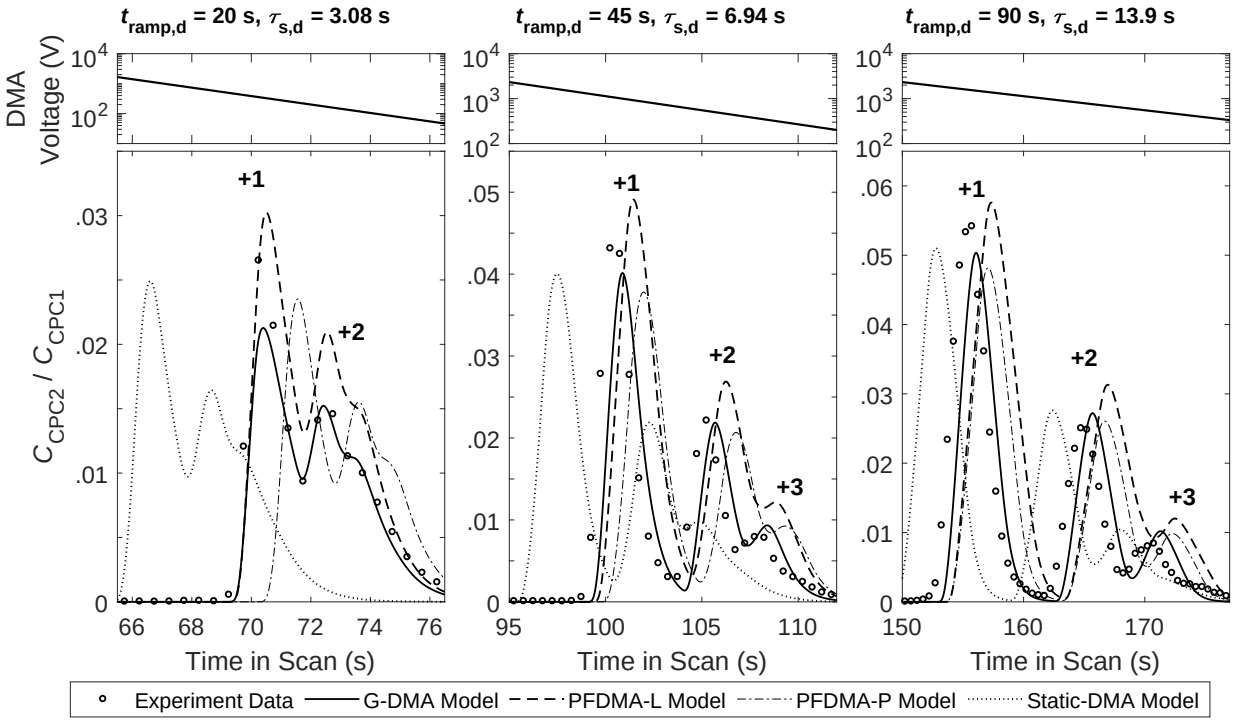

Figure B.3: Down-scan experimental and modeling results for SEMS instrument response to monodisperse 296 nm particles with ramp duration t_{ramp} = 10, 20, 45 and 90 s (corresponding to scan time τ_s = 1.54, 3.08, 6.94 and 13.9 s).

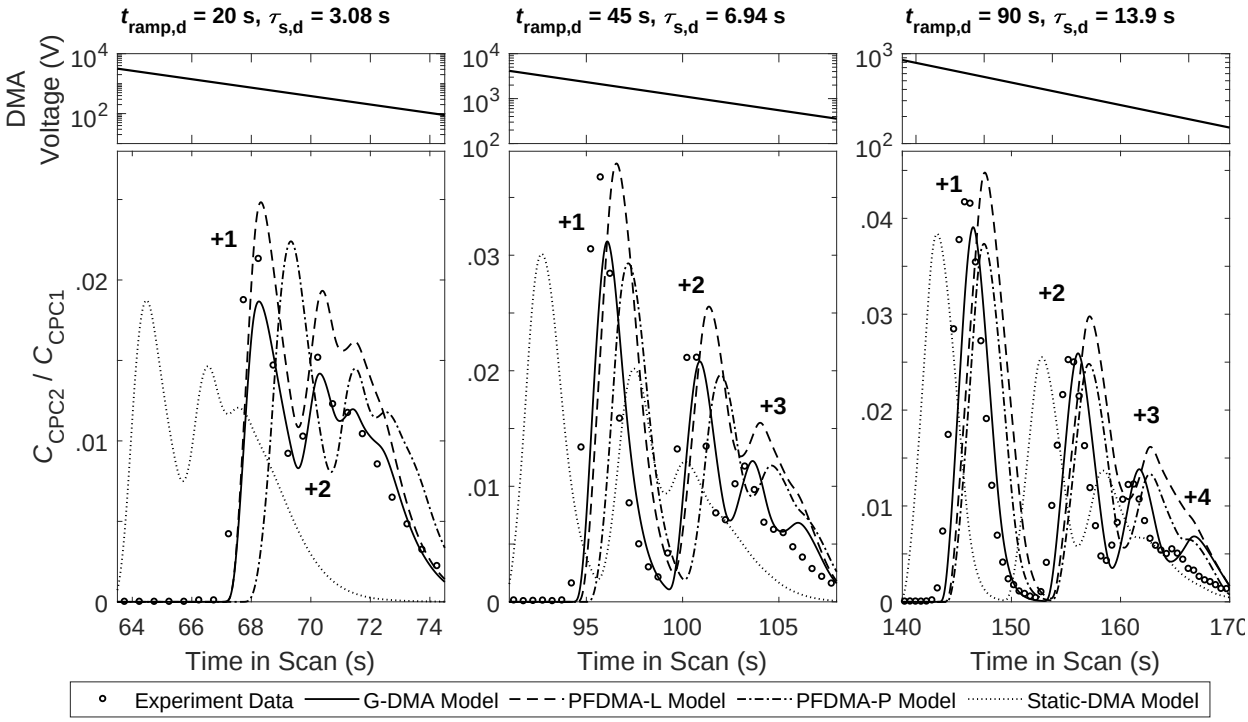

Figure B.4: Down-scan experimental and modeling results for SEMS instrument response to monodisperse 498 nm particles with ramp duration t_{ramp} = 10, 20, 45 and 90 s (corresponding to scan time τ_s = 1.54, 3.08, 6.94 and 13.9 s).

TWO-STEP INVERSION OF SCANNING DMA DATA

C.1 Instrument Response Function

Following (3.19), the total number of particles recorded in the SEMS is related with the particle size distribution in matrix form by $\mathbf{R} = \mathbf{AN}$, where

$$\mathbf{A}_{i,j} = \sum_{u_k \geq u_{j-1}^{\dagger}}^{u_k \leq u_j^{\dagger}} \Delta u_k \frac{u_k - u_{j-1}^{\dagger}}{u_j^{\dagger} - u_{j-1}^{\dagger}} h_i(u_k) + \sum_{u_k \geq u_j^{\dagger}}^{u_k \leq u_{j+1}^{\dagger}} \Delta u_k \frac{u_{j+1}^{\dagger} - u_k}{u_{j+1}^{\dagger} - u_j^{\dagger}} h_i(u_k). \tag{C.1}$$

$h_i(u)$ is the kernel function,

$$h_i(u) = Q_{\mathrm{a}} \sum_{\phi} \eta(u,\phi) \left[\Gamma^{\mathrm{C}}_{\mathrm{SEMS}}(Z_{\mathrm{p}}(u,\phi),\beta,\delta,it_{\mathrm{c}}) - \Gamma^{\mathrm{C}}_{\mathrm{SEMS}}(Z_{\mathrm{p}}(u,\phi),\beta,\delta,(i-1)t_{\mathrm{c}}) \right]. \tag{C.2}$$

$\Gamma^{\mathrm{c}}_{\mathrm{SEMS}}(Z_{\mathrm{p}}(u,\phi),\beta,\delta,t)$ is the cumulative transfer function of the integrated SEMS, given as $\Gamma^{\mathrm{C}}_{\mathrm{SEMS}}(Z_{\mathrm{p}}(u,\phi),\beta,\delta,t) = \int_{-\infty}^{t} \Gamma^{\mathrm{I}}_{\mathrm{SEMS}}(Z_{\mathrm{p}}(u,\phi),\beta,\delta,t)\mathrm{d}t$, where $\Gamma^{\mathrm{I}}_{\mathrm{SEMS}}(Z_{\mathrm{p}}(u,\phi),\beta,\delta,t)$ is the instantaneous transfer function of the SEMS.

The kernel function can be expressed as

$$\begin{aligned} h_i(u) &= Q_{\mathrm{a}} \sum_{\phi} \eta(u,\phi) \int_{(i-1)t_{\mathrm{c}}}^{it_{\mathrm{c}}} \Gamma^{\mathrm{I}}_{\mathrm{SEMS}}(Z_{\mathrm{p}}(u,\phi),\beta,\delta,t)\mathrm{d}t \\ &= Q_{\mathrm{a}} \sum_{\phi} \eta(u,\phi) \int_{(i-1)t_{\mathrm{c}}}^{it_{\mathrm{c}}} \Omega^{\mathrm{I}}_{\mathrm{DMA}}(Z_{\mathrm{p}}(u,\phi),\beta,\delta,t) \star E(t), \end{aligned} \tag{C.3}$$

where $\Omega^{\mathrm{I}}_{\mathrm{DMA}}(Z_{\mathrm{p}}(u,\phi),\beta,\delta,t)$ and $E(t)$ are the instantaneous transfer function of DMA and the resident time distribution of CPC. The convolution operator $\star$ is defined as

$$f(t) \star g(t) = \int_{-\infty}^{\infty} f(t')g(t-t')dt' = \int_{-\infty}^{\infty} f(t-t')g(t')dt'. \tag{C.4}$$

Thus, the integrated SEMS transfer function is (only the dependence on t is shown for convenience)

$$\begin{aligned} \int_{(i-1)t_{\mathrm{c}}}^{it_{\mathrm{c}}} \Gamma^{\mathrm{I}}_{\mathrm{SEMS}}(t)\mathrm{d}t &= \int_{(i-1)t_{\mathrm{c}}}^{it_{\mathrm{c}}} \left[\int_{-\infty}^{\infty} \Omega^{\mathrm{I}}_{\mathrm{DMA}}(t')E(t-t')\mathrm{d}t' \right] \mathrm{d}t \\ &= \int_{-\infty}^{\infty} \left[\int_{(i-1)t_{\mathrm{c}}}^{it_{\mathrm{c}}} E(t-t')\mathrm{d}t \right] \Omega^{\mathrm{I}}_{\mathrm{DMA}}(t')\mathrm{d}t'. \end{aligned} \tag{C.5}$$

Define the cumulative CPC residence time distribution as

$$F(t) = \int_0^t E(t')\mathrm{d}t' \tag{C.6}$$

the integrated SEMS transfer function is

$$\int_{(i-1)t_\mathrm{c}}^{it_\mathrm{c}} \Gamma^\mathrm{I}_\mathrm{SEMS}(t)\mathrm{d}t = \int_{-\infty}^{\infty} \left[F(it_\mathrm{c} - t') - F((i-1)t_\mathrm{c} - t')\right] \Omega^\mathrm{I}_\mathrm{DMA}(t')\mathrm{d}t', \tag{C.7}$$

C.2 Discretization and Deconvolution

The instrument transfer function from Eq. (C.7) can be evaluated numerically. Here, the DMA transfer function is approximated as constant in every time bin $t \in [(m-1)t_\mathrm{c}, mt_\mathrm{c}]$. Thus, the instantaneous DMA transfer function is given in a form of step function, *i.e.*,

$$\Omega^\mathrm{I}_\mathrm{DMA}(t) = \sum_{m=1}^{\infty} \Omega^\mathrm{c}_{\mathrm{DMA},m} \frac{H(t-(m-1)t_\mathrm{c}) - H(t-mt_\mathrm{c})}{t_\mathrm{c}}, \tag{C.8}$$

where $\Omega^\mathrm{c}_{\mathrm{DMA},m} = \int_{(m-1)t_\mathrm{c}}^{mt_\mathrm{c}} \Omega^\mathrm{I}_\mathrm{DMA}(t)\mathrm{d}t$ is the cumulative DMA transfer function for time bin m, and $H(x)$ is the Heaviside step function.

Therefore, Eq. (C.7) is

$$\begin{aligned}
\int_{(i-1)t_\mathrm{c}}^{it_\mathrm{c}} \Gamma^\mathrm{I}_\mathrm{SEMS}(t)\mathrm{d}t &= \sum_{m=1}^{\infty} \frac{\Omega^\mathrm{c}_{\mathrm{DMA},m}}{t_\mathrm{c}} \int_{(m-1)t_\mathrm{c}}^{mt_\mathrm{c}} \left[F(it_\mathrm{c} - t') - F((i-1)t_\mathrm{c} - t')\right] \mathrm{d}t' \\
&= \sum_{m=1}^{\infty} \frac{\Omega^\mathrm{c}_{\mathrm{DMA},m}}{t_\mathrm{c}} \left[\int_{(i-m)t_\mathrm{c}}^{(i-m+1)t_\mathrm{c}} F(t')\mathrm{d}t' - \int_{(i-m-1)t_\mathrm{c}}^{(i-m)t_\mathrm{c}} F(t')\mathrm{d}t' \right]
\end{aligned} \tag{C.9}$$

The residence time distribution $E(t)$ becomes negligible when t is sufficiently large. Thus, the summation in Eq. (C.9) is evaluated up to $i - m = \Delta b - 1$ bins, where Δb can be defined by the tolerance ϵ, *i.e.*, $\int_0^{\Delta bt_\mathrm{c}} E(t')\mathrm{d}t' = 1 - \epsilon$. Then, (C.9) is normalized by a factor of $\frac{\int_{(\Delta b-1)t_\mathrm{c}}^{(\Delta b)t_\mathrm{c}} F(t')\mathrm{d}t'}{t_\mathrm{c}}$, and becomes

$$\begin{aligned}
\int_{(i-1)t_\mathrm{c}}^{it_\mathrm{c}} \Gamma^\mathrm{I}_\mathrm{SEMS}(t)\mathrm{d} &= \sum_{m=1}^{\infty} \Omega^\mathrm{c}_{\mathrm{DMA},m} \frac{\int_{(i-m)t_\mathrm{c}}^{(i-m+1)t_\mathrm{c}} F(t')\mathrm{d}t' - \int_{(i-m-1)t_\mathrm{c}}^{(i-m)t_\mathrm{c}} F(t')\mathrm{d}t'}{\int_{(\Delta b-1)t_\mathrm{c}}^{\Delta bt_\mathrm{c}} F(t')\mathrm{d}t'} \\
&= \sum_{m=1}^{i-\Delta b+1} \Omega^\mathrm{c}_{\mathrm{DMA},m} \Theta_{i-m},
\end{aligned} \tag{C.10}$$

where

$$\Theta_{i-m} = \begin{cases} \dfrac{\int_{(i-m)t_c}^{(i-m+1)t_c} F(t')\mathrm{d}t' - \int_{(i-m-1)t_c}^{(i-m)t_c} F(t')\mathrm{d}t'}{\int_{(\Delta b-1)t_c}^{\Delta b t_c} F(t')\mathrm{d}t'}, & m \le i \le m + \Delta b - 1 \\ 0, & \text{elsewhere} \end{cases}. \tag{C.11}$$

or expressed in the matrix form

$$\boldsymbol{\Theta} = \begin{bmatrix} \Theta_0 & 0 & \cdots & 0 & 0 \\ \Theta_1 & \Theta_0 & \cdots & \vdots & \vdots \\ \Theta_2 & \Theta_1 & \cdots & \vdots & \vdots \\ \vdots & \Theta_2 & \cdots & \vdots & \vdots \\ \Theta_{\Delta b-2} & \vdots & \ddots & \vdots & \vdots \\ \Theta_{\Delta b-1} & \Theta_{\Delta b-2} & \ddots & 0 & 0 \\ 0 & \Theta_{\Delta b-1} & \ddots & 0 & 0 \\ \vdots & 0 & \cdots & \vdots & \vdots \\ \vdots & \vdots & \cdots & \vdots & \vdots \end{bmatrix} \tag{C.12}$$

To make Eq. (C.11) in a compact formula, another residence time distribution function can be defined as

$$G(t) = \int_0^t F(t')\mathrm{d}t' = \int_0^t \int_0^{t'} E(t'')\mathrm{d}t''\mathrm{d}t'. \tag{C.13}$$

Thus, Eq. (C.11) becomes

$$\Theta_{i-m} = \begin{cases} \dfrac{G((i-m+1)t_c) - 2G((i-m)t_c) + G((i-m-1)t_c)}{G(\Delta b t_c) - G((\Delta b - 1)t_c)}, & m \le i \le m + \Delta b - 1 \\ 0, & \text{elsewhere} \end{cases}. \tag{C.14}$$

C.3 Size Distribution Inversion

Substitute Eq. (C.2) and (C.10) into Eq. (C.1), we have

$$\begin{aligned}\mathbf{A}_{i,j} &= Q_{\mathrm{a}} \sum_{m=1}^{i-\Delta b+1} \left\{ \sum_{u_k \geq u_{j-1}^{\dagger}}^{u_k \leq u_j^{\dagger}} \Delta u_k \frac{u_k - u_{j-1}^{\dagger}}{u_j^{\dagger} - u_{j-1}^{\dagger}} \sum_{\phi} \eta(u_k, \phi) \Omega_{\mathrm{DMA},m}^{\mathrm{c}}(u_k) \right. \\ &+ \left. \sum_{u_k \geq u_j^{\dagger}}^{u_k \leq u_{j+1}^{\dagger}} \Delta u_k \frac{u_{j+1}^{\dagger} - u_k}{u_{j+1}^{\dagger} - u_j^{\dagger}} \sum_{\phi} \eta(u_k, \phi) \Omega_{\mathrm{DMA},m}^{\mathrm{c}}(u_k) \right\} \Theta_{i-m}. \end{aligned} \tag{C.15}$$

The size distribution inversion can be written in a new matrix form,

$$\mathbf{R} = \mathbf{\Theta}\mathbf{\Phi}\mathbf{N}, \tag{C.16}$$

where $\mathbf{\Phi}$ is a $m \times j$ matrix, with

$$\begin{aligned}\Phi_{m,j} &= \sum_{u_k \geq u_{j-1}^{\dagger}}^{u_k \leq u_j^{\dagger}} \Delta u_k \frac{u_k - u_{j-1}^{\dagger}}{u_j^{\dagger} - u_{j-1}^{\dagger}} \sum_{\phi} \eta(u_k, \phi) \Omega_{\mathrm{DMA},m}^{\mathrm{c}}(u_k) \\ &+ \sum_{u_k \geq u_j^{\dagger}}^{u_k \leq u_{j+1}^{\dagger}} \Delta u_k \frac{u_{j+1}^{\dagger} - u_k}{u_{j+1}^{\dagger} - u_j^{\dagger}} \sum_{\phi} \eta(u_k, \phi) \Omega_{\mathrm{DMA},m}^{\mathrm{c}}(u_k). \end{aligned} \tag{C.17}$$

The two-step size distribution inversion is to complete inversion $\mathbf{\Theta}^{-1}\mathbf{R} = \mathbf{\Phi}\mathbf{N}$ and $\mathbf{\Phi}^{-1}\mathbf{\Theta}^{-1}\mathbf{R} = \mathbf{N}$ in sequential steps. Notice that, the Matlab™ script "SMPS_Inversion.m" is written in the form of Eq. (C.16), but implements the inversion in one step with kernel matrix as $\mathbf{\Theta}\mathbf{\Phi}$.

INTERPOLATION OF SCANNING DMA TRANSFER FUNCTION

D.1 Introduction

To invert the particle size distribution from scanning electrical mobility measurement, the calculation of the kernel matrix $\mathbf{A}_{i,j}$ requires the evaluation of the cumulative scanning DMA transfer function $\Omega^{\mathrm{C}}_{\mathrm{DMA}}(Z_{\mathrm{p}}(u,\phi),\beta,\delta,t)$ for various sizes $u = \log D_{\mathrm{p}}$ and time bins $[(i-1)t_{\mathrm{C}}, it_{\mathrm{C}}]$, which is defined by Eq. (C.15), *i.e.*,

$$\begin{aligned}\mathbf{A}_{i,j} &= Q_{\mathrm{a}} \sum_{m=1}^{i-\Delta b+1} \left\{ \sum_{u_k \geq u_{j-1}^{\dagger}}^{u_k \leq u_j^{\dagger}} \Delta u_k \frac{u_k - u_{j-1}^{\dagger}}{u_j^{\dagger} - u_{j-1}^{\dagger}} \sum_{\phi} \eta(u_k,\phi)\Omega^{\mathrm{C}}_{\mathrm{DMA},m}(u_k) \right. \\ &+ \left. \sum_{u_k \geq u_j^{\dagger}}^{u_k \leq u_{j+1}^{\dagger}} \Delta u_k \frac{u_{j+1}^{\dagger} - u_k}{u_{j+1}^{\dagger} - u_j^{\dagger}} \sum_{\phi} \eta(u_k,\phi)\Omega^{\mathrm{C}}_{\mathrm{DMA},m}(u_k) \right\} \Theta_{i-m}. \end{aligned} \tag{D.1}$$

However, the scanning DMA transfer function is only evaluated for finite number of particle sizes via particle trajectory simulations. To evaluate the kernel function, we have to interpolate the simulated scanning DMA transfer function for different particle sizes and time bins. In this appendix, the method to store the simulated DMA transfer function and the implementation of interpolation are documented.

D.2 Transform and Interpolation

The scanning DMA transfer function is simulated for 52 particle sizes, with entrance, classification and exit regions simulated individually. The integrated scanning DMA transfer function is

$$\Omega_{\mathrm{DMA}}(Z_{\mathrm{p}}(D_{\mathrm{p}},\phi),t) = \eta_{\mathrm{ent}}(D_{\mathrm{p}}) \left[\Omega(Z_{\mathrm{p}}(D_{\mathrm{p}},\phi),t) \star \eta_{\mathrm{exit}}(D_{\mathrm{p}},t)\right], \tag{D.2}$$

where $\eta_{\mathrm{ent}}(D_{\mathrm{p}})$, $\Omega(Z_{\mathrm{p}}(D_{\mathrm{p}},\phi),t)$ and $\eta_{\mathrm{exit}}(D_{\mathrm{p}},t)$ are the entrance penetration efficiency, classification transfer function and delay distribution in the exit region, respectively. The $\star$ denotes the convolution operator, *i.e.*, $f(t) \star g(t) = \int_{-\infty}^{\infty} f(\tau)g(t-\tau)d\tau$. The entrance penetration efficiencies $\eta_{\mathrm{ent}}(D_{\mathrm{p}})$ for 52 simulated particle sizes is fitted with logistic equation and stored as a Matlab$^{\mathrm{TM}}$ structure.

The simulated classification transfer functions for 103, 139, 190 and 266 nm singly charged particles are shown in Figure D.1. The time in a scan when the classification region transfer function reaches

maximum for each simulated particle size is denoted as $t^*(Z_p)$, and shown in Figure D.2 (a). Then each simulated scanning DMA transfer function is centralized with $t^*(Z_p)$, as shown in Figure D.2 (b) and (c) for 103 and 266 nm singly charge particles.

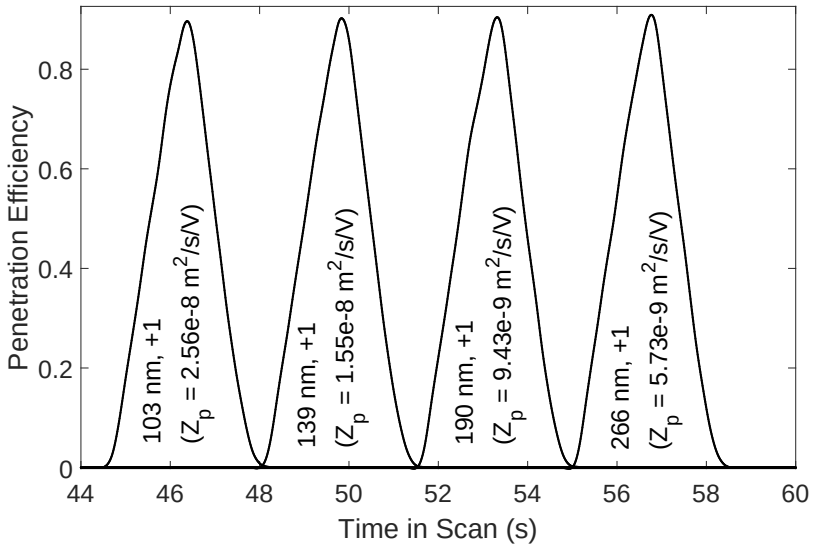

Figure D.1: Transfer function of TSI 3081 DMA classification region for 103, 139, 190 and 266 nm singly charged particles.

The cumulative scanning DMA transfer function $\Omega^{C}_{DMA}(Z_p(u,\phi),\beta,\delta,t)$ is derived by numerically integrating the centralized transfer function. In other words, the cumulative scanning DMA transfer function is stored as $\Omega^{C}_{DMA}(t^*(Z_p),\beta,\delta,t-t^*(Z_p))$ in practice. This enables the proper linear interpolation on the transfer function for different electric mobilities Z_p and times in scan t.

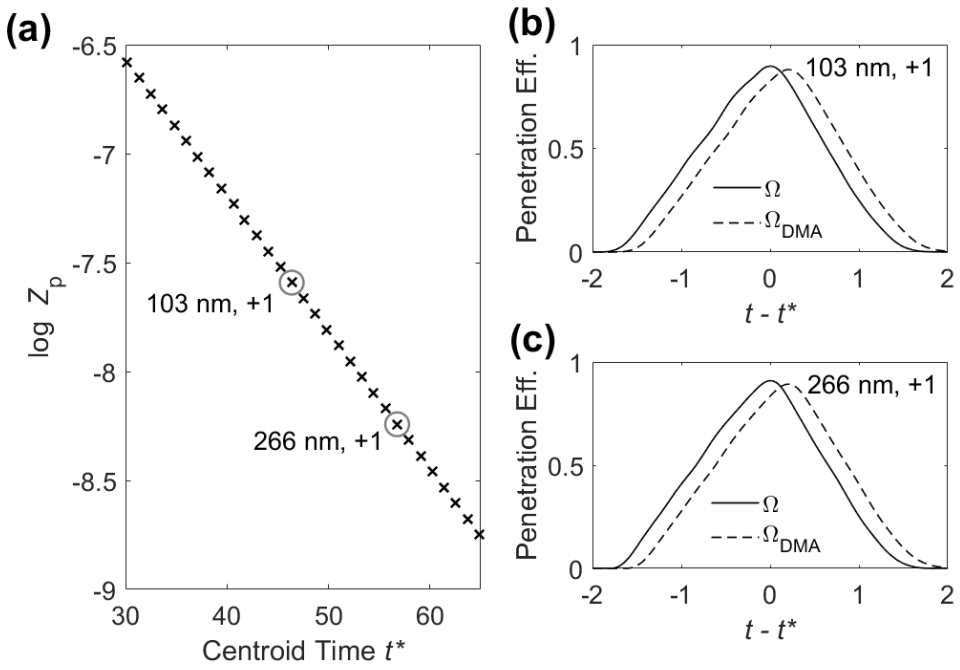

Figure D.2: (a) The centroid time t^* as a function of electric mobility and the centralized scanning transfer function for singly charged (b) 103nm and (c) 266nm particle.